

# **Microstructural characterization of Cu/ZnO/Al<sub>2</sub>O<sub>3</sub> catalysts for the synthesis and steam reforming of methanol**

vorgelegt von  
Diplom-Ingenieur (Chemie)  
Patrick Kurr  
aus Potsdam

Von der Fakultät II - Mathematik und Naturwissenschaften  
der Technischen Universität Berlin  
zur Erlangung des akademischen Grades

Doktor der Ingenieurwissenschaften  
- Dr. Ing. -

genehmigte Dissertation

Promotionsausschuss:

Vorsitzender: Prof. Dr. rer. nat. S. Blechert

Berichter/ Gutachter: Prof. Dr. rer. nat. R. Schlögl

Berichter/ Gutachter: Prof. Dr. rer. nat. T. Ressler

Tag der wissenschaftlichen Aussprache: 10.09.2008

Berlin, 2008

D 83







---

**Microstructural characterization of Cu/ZnO/Al<sub>2</sub>O<sub>3</sub> catalysts  
for the synthesis and steam reforming of methanol**

---

Ph.D. Thesis by Patrick Kurr

Berlin, 2008



## Danksagung

Die vorliegende Doktorarbeit wurde im Zeitraum vom Januar 2005 bis Juni 2008 in der Abteilung Anorganische Chemie des Fritz-Haber-Instituts der Max-Planck-Gesellschaft sowie in der Abteilung Analytische Chemie der Technischen Universität Berlin angefertigt.

Mein Dank gilt Herrn Prof. Dr. Robert Schlögl für die interessante wissenschaftliche Fragestellung, die mit dieser Arbeit verbunden war, sein stetes Interesse an der Arbeit und schließlich den vielen entscheidenden Anregungen.

Herrn Prof. Dr. Thorsten Ressler danke ich für sein Vertrauen, seine fachliche Betreuung, die weit reichenden Freiheiten bei der Durchführung der experimentellen Arbeiten sowie die stete Diskussionsbereitschaft während meiner Promotionszeit.

Ferner gilt mein herzlicher Dank Dr. Annette Trunschke sowie Dr. Malte Behrens für die tatkräftige und kompetente Unterstützung, das Korrekturlesen sowie die kritischen Diskussionen gerade zum Ende dieser Arbeit.

Insbesondere bedanke ich mich bei Dr. Igor Kasatkin für seine detaillierten elektronenmikroskopischen Untersuchungen sowie für die zahlreichen, anregenden Diskussionen im Laufe dieser Arbeit.

Bei Dr. Rolf Jentoft sowie Dr. Frank Girgsdies bedanke ich mich ganz herzlich für die vielen Hilfestellungen zur Interpretation von Messdaten insbesondere zu Beginn dieser Arbeit.

Ferner bedanke ich mich insbesondere bei Dr. Benjamin Frank sowie Juan Milano, die mich Demut beim Pool Billard gelehrt haben, bei Semitha Schwarz für die vielen (nicht wissenschaftlichen) Gespräche, bei Gisela Lorenz für die moralische Unterstützung sowie den interessanten Unterhaltungen während unserer gemeinsamen Raucherpausen sowie bei Dr. Hary Soerijanto, dessen Optimismus mich stets verblüfft hat.

Des Weiteren danke ich bei allen anderen, nicht namentlich genannten Mitarbeitern des Fritz-Haber-Instituts sowie der Technischen Universität, für die ausgesprochen angenehme und kollegiale Arbeitsatmosphäre.

Abschließend gilt mein Dank all denjenigen, die im Rahmen des BMBF Projektes „Entwicklung von Methanolsynthesekatalysatoren als Basis für nachhaltige Ressourcennutzung - New Generation Methanol“ (BMBF - Projektnummer: 01RI05029) zum Gelingen dieser Arbeit mit beigetragen haben: Prof. Dr. Martin Muhler, Dr. Wilma Busser, Dr. Raoul Naumann, Dr. Marie Katrin Schröter, Stefan Kaluza, Holger Ruland von der Ruhr-Universität Bochum, Dr. Richard Fischer, Dr. Benjamin Kniep, Dr. Nora Schiefenhövel, Tobias Henkel von der Südchemie AG sowie Prof. Dr. Sharifah Bee Abd Hamid und Nur Fadhila Idris von NanoC SDN, Kuala Lumpur (Malaysia).

Berlin, 2008.

## “Mikrostrukturelle Charakterisierung von Cu/ZnO/Al<sub>2</sub>O<sub>3</sub> Katalysatoren für die Synthese und Dampfreformierung von Methanol”

Dissertation vorgelegt von Patrick Kurr

### Zusammenfassung

Cu/ZnO/Al<sub>2</sub>O<sub>3</sub> Katalysatoren stellen ein vielseitig einsetzbares Katalysatorsystem, wie z.B. für die Methanol Synthese sowie für die Methanol Dampfreformierung, dar. Letztere Reaktion kann formal auch als die Rückreaktion der Methanol Synthese ausgehend von CO<sub>2</sub> und H<sub>2</sub> betrachtet werden. In der vorliegenden Arbeit wurden unterschiedlich präparierte Cu/ZnO/Al<sub>2</sub>O<sub>3</sub> Katalysatoren mittels *in situ* Röntgenbeugung sowie Röntgenabsorptionsspektroskopie hinsichtlich ihrer Mikrostruktur untersucht. Zusätzlich sind die Cu/ZnO/Al<sub>2</sub>O<sub>3</sub> Katalysatoren zur Bestimmung ihrer Morphologie mittels Transmissionselektronenmikroskopie sowie zur Charakterisierung ihrer Reduzierbarkeit mittels temperaturprogrammierten Methoden (Reduktion, Oxidation) untersucht worden. Die hier charakterisierten Cu/ZnO/Al<sub>2</sub>O<sub>3</sub> Katalysatoren wiesen eine Elementzusammensetzung von Cu/Zn/Al = 60:30:10 auf, welche dem im technischen Großmaßstab optimierten und eingesetzten System für die Methanol Synthese entspricht. Das Ziel dieser Arbeit war es, Zusammenhänge zwischen der Mikrostruktur der Cu/ZnO/Al<sub>2</sub>O<sub>3</sub> Katalysatoren sowie deren katalytischem Verhalten sowohl in der Synthese als auch in der Dampfreformierung von Methanol (Methanol Chemie) kausal zu ergründen. Diese Struktur-Aktivitäts-Korrelationen stellen die Basis für eine rationale Entwicklung von neuen, effizienteren Kupfer Katalysatoren dar.

Die Aktivität der untersuchten Cu/ZnO/Al<sub>2</sub>O<sub>3</sub> Katalysatoren in der Synthese sowie in der Dampfreformierung von Methanol war in erster Näherung durch die Höhe der Gesamtkupferoberfläche bestimmt. Darüber hinaus konnte gezeigt werden, dass der Anteil von Nicht-Gleichgewichtsstrukturen im Kupfer, wie z.B. planare Defekte sowie Gitterverspannung, quantitativ mit der Aktivität der Cu/ZnO/Al<sub>2</sub>O<sub>3</sub> Katalysatoren korrelierte. Die Präsenz dieser geometrischen Defekte war ursächlich für die beobachtete Abweichung vom linearen Zusammenhang zwischen Gesamtkupferoberfläche und Aktivität in beiden Reaktionen. Katalytisch aktives Kupfer in Cu/ZnO/Al<sub>2</sub>O<sub>3</sub> Katalysatoren war eine hoch defektreiche, Gitterverspannte Modifikation des makrokristallinen Metalls. Diese Defektstruktur wurde durch eine homogene Mikrostrukturierung der Kupferphase in der ZnO/Al<sub>2</sub>O<sub>3</sub> Matrix kinetisch stabilisiert. Im Unterschied dazu, zeigen die Cu/ZnO/Al<sub>2</sub>O<sub>3</sub> Katalysatoren, welche durch eine ausgeprägte heterogene Mikrostruktur bestehend aus unterschiedlich großen sowie unregelmäßig geformten Kupferpartikeln charakterisiert waren, eine deutlich geringe Aktivität in beiden Reaktionen.

Des Weiteren konnte gezeigt werden, dass Cu/ZnO Katalysatoren mit oder ohne Al<sub>2</sub>O<sub>3</sub> als zusätzliche stabilisierende Phase mittels Kalzinierung in CO<sub>2</sub> mikrostrukturell derart modifiziert werden konnten, dass verbesserte katalytische Eigenschaften erhalten wurden. Kalzinieren unter geeigneten O<sub>2</sub>/CO<sub>2</sub>- Partialdrücken resultierte in einer Einlagerung von Karbonat in die Kupferphase, was eine höhere Defektdichte im Kupfer zur Folge hatte. Entsprechend zeigten die modifizierten Cu/ZnO/(Al<sub>2</sub>O<sub>3</sub>) Katalysatoren eine deutlich verbesserte Selektivität in der Methanol Dampfreformierung. Somit konnte



---

durch Kohlendioxid Kalzinierung der Anteil an CO, einem Nebenprodukt der Methanol Dampfreformierung, signifikant vermindert werden. Insbesondere für den Einsatz in Brennstoffzellen, in denen CO als Katalysatorgift der dort verwendeten Platinanode wirkt, stellt die Kalzinierung in CO<sub>2</sub> eine aussichtsreiche Alternative für die Entwicklung von hoch selektiven Cu/ZnO/Al<sub>2</sub>O<sub>3</sub> Katalysatoren für die Methanol Dampfreformierung dar. Auf der anderen Seite konnte mittels Kalzinierung in CO<sub>2</sub> keine Verbesserung der katalytischen Aktivität der hier untersuchten Cu/ZnO/Al<sub>2</sub>O<sub>3</sub> Katalysatoren sowohl in der Synthese als auch der Dampfreformierung von Methanol erzielt werden („Prinzip der mikroskopischen Reversibilität“).

**“Microstructural characterization of Cu/ZnO/Al<sub>2</sub>O<sub>3</sub> catalysts for the synthesis and steam reforming of methanol”**

Dissertation by Patrick Kurr

**Abstract**

Cu/ZnO/Al<sub>2</sub>O<sub>3</sub> catalysts represent a versatile catalyst system for methanol chemistry, including the synthesis and steam reforming of methanol. Formally, the steam reforming of methanol is the reverse of methanol synthesis from CO<sub>2</sub> and H<sub>2</sub>. In the present work a set of differently prepared Cu/ZnO/Al<sub>2</sub>O<sub>3</sub> catalysts with a fixed composition of Cu/Zn/Al = 60:30:10 were investigated by *in situ* bulk techniques, X-ray diffraction, and X-ray absorption spectroscopy. Additionally, microscopic and morphological structural characteristics have been examined by electron microscopy (TEM). Temperature programmed techniques (TPR, TPO) were used to study the reducibility of the derived catalysts. The objective was to elucidate structure - activity correlations of Cu/ZnO/Al<sub>2</sub>O<sub>3</sub> catalysts employed for the synthesis and steam reforming of methanol. These correlations provide the basic principles for a rational design of superior Cu/ZnO/Al<sub>2</sub>O<sub>3</sub> catalysts for methanol chemistry.

The activity of Cu/ZnO/Al<sub>2</sub>O<sub>3</sub> catalysts in methanol chemistry was roughly determined by the overall copper surface area. Additionally, it was shown that the abundance of non-equilibrium structures in Cu, such as planar defects, lattice strain, and subsurface oxygen correlated with the catalytic activity in the synthesis as well as steam reforming of methanol. The presence of microstructural imperfections in the bulk accounted for the deviations from a linear Cu surface area - activity correlation observed. Thus, catalytically active copper in the Cu/ZnO/Al<sub>2</sub>O<sub>3</sub> catalysts for both reactions (methanol synthesis, methanol steam reforming) was a highly defective, strained form of the metal originating from an appropriate nanostructuring of Cu and the ZnO/Al<sub>2</sub>O<sub>3</sub> matrix. The latter were a direct consequence of an advanced Cu-ZnO/Al<sub>2</sub>O<sub>3</sub> interface predominately found in those samples exhibiting a pronounced homogeneous microstructure. Conversely, a heterogeneous microstructure with variously sized and textured copper particles was observed for the less active Cu/ZnO/Al<sub>2</sub>O<sub>3</sub> catalysts studied.

Moreover, it was shown that Cu/ZnO catalysts with or without alumina as an additional refractory phase could be microstructurally modified by carbon dioxide calcination. Calcination under proper CO<sub>2</sub>/O<sub>2</sub> partial pressures resulted in incorporation of carbonates into the bulk of the Cu/ZnO/(Al<sub>2</sub>O<sub>3</sub>) catalyst leading to more defective microstructure of the copper phase. These structurally modified Cu/ZnO/(Al<sub>2</sub>O<sub>3</sub>) catalysts featured a considerably lower selectivity to CO, an undesired consecutive by-product of the methanol steam reforming reaction, even at high methanol conversions. Considering the low CO levels obtained carbon dioxide calcination is a promising alternative for the preparation of highly selective Cu/ZnO/Al<sub>2</sub>O<sub>3</sub> catalysts for methanol steam reforming reaction to be applied for fuel cells. Conversely, activities in methanol steam reforming and methanol synthesis were not improved by carbon dioxide calcination (“principle of microscopic reversibility”).

## List of Figures

|  |    |
|--|----|
| Fig. 2-1: Powder X-ray diffraction pattern of a Cu/ZnO/Al <sub>2</sub> O <sub>3</sub> methanol synthesis catalyst measured at ambient temperature. ....  | 9  |
| Fig. 2-2: X-ray absorption spectra (XAS) of a Cu/ZnO/Al <sub>2</sub> O <sub>3</sub> methanol synthesis catalyst measured at the Zn K -edge (E = 9.659 keV). ....   | 12 |
| Fig. 2-3: Measured EXAFS function, $\chi(k)$ , of a Cu/ZnO/Al <sub>2</sub> O <sub>3</sub> methanol synthesis catalyst measured at the Zn K -edge (left) and the corresponding pseudo radial distribution function (FT{ $\chi(k)$ }) obtained after Fourier- transformation (right). ....   | 13 |
| Fig. 2-4: High resolution transmission electron microscopic image of a Cu particle (left) and the corresponding power spectrum (right). ....   | 16 |
| Fig. 3-1: Comparison of the normalized H <sub>2</sub> production rates obtained from in situ experiments (XRD, XAS) and measured in a fixed bed micro-reactor (FBR) at 523 K, $WHSV_{MeOH} = (86-96) s^{-1}$ . ....  | 24 |
| Fig. 3-2: H <sub>2</sub> production rate obtained in a fixed-bed reactor in dependence on the specific copper surface area determined by N <sub>2</sub> O surface titration (RFC). ....  | 24 |
| Fig. 3-3: Hydrogen consumption during temperature programmed reduction (TPR) of the CZA catalysts. Bold lines are experimental curves and thin lines are deconvoluted curves. ....   | 25 |
| Fig. 3-4: Bright field transmission electron micrographs of the in hydrogen activated Cu/ZnO/Al <sub>2</sub> O <sub>3</sub> catalysts: (a) CZA-1, (b) CZA-2, (c) CZA-3, (d) CZA-4, (e) CZA-5, and (f) CZA-6. ....  | 27 |
| Fig. 3-5: Characteristic high resolution electron micrograph (scale bars: 10 nm and 5 nm) and detailed Cu particle size distribution obtained for the activated (reduced) Cu/ZnO/Al <sub>2</sub> O <sub>3</sub> catalysts: CZA-1 (a and c) and CZA-5 (b and d). ....   | 28 |
| Fig. 3-6: <i>In situ</i> powder X-ray diffraction patterns recorded at ambient temperature of the (a) calcined precursors, and (b) of the reduced catalysts ( $\circ$ ZnO; $\square$ Malachite {Cu <sub>2</sub> CO <sub>3</sub> (OH) <sub>2</sub> }). ....   | 29 |
| Fig. 3-7: Crystallite sizes of CuO and Cu determined from the XRD line broadening of the calcined precursor, the reduced and the Cu/Zn/Al- catalyst under MSR conditions. ....   | 30 |
| Fig. 3-8: Experimental Cu K -edge FT( $\chi(k) \cdot k^3$ ) of the in 5 vol.-% H <sub>2</sub> (He) reduced Cu/ZnO/Al <sub>2</sub> O <sub>3</sub> catalysts recorded at ambient temperature. The inset shows the real amplitude of the 1 <sup>st</sup> Cu-Cu shell (without offset). ....   | 31 |
| Fig. 3-9: Refinement of theoretical Cu EXAFS function (dashed line) to the experimental Cu K -edge FT( $\chi(k) \cdot k^3$ ) (solid line) of CZA-1 catalyst measured after MSR reaction at 313 K. ....   | 33 |
| Fig. 3-10: Correlation of Cu crystallite size (XRD) with the DWF of the 1 <sup>st</sup> Cu-Cu shell (XAS) derived from a refinement of theoretical Cu functions to the corresponding experimental data. ....   | 34 |
| Fig. 3-11: Experimental FT( $\chi(k) \cdot k^3$ ) of the Cu/ZnO/Al <sub>2</sub> O <sub>3</sub> catalysts measured after the reduction (activation) treatment at ambient temperature. For comparison the Radial Distribution Function (RDF) of ZnO measured as reference is also depicted. ....   | 34 |
| Fig. 3-12: Experimental Zn K -edge FT( $\chi(k) \cdot k^3$ ) measured before and after reduction in hydrogen of the sample CZA-1: calcined oxide precursor (bottom) and reduced catalyst (top) with refinement of theoretical ZnO EXAFS function (dashed line) to the experimental Zn K -edge FT( $\chi(k) \cdot k^3$ ) (solid line). .... | 35 |
| Fig. 4-1: Characteristic TEM overview images (a), and the corresponding Cu particle size distribution (b), and Cu/Zn/Al- elementary composition (c) of an activated (reduced) Cu/ZnO/Al <sub>2</sub> O <sub>3</sub> catalyst. ....   | 46 |
| Fig. 4-2: Metal composition determined by Energy Disperse X-ray spectroscopy (EDX) of the activated Cu/ZnO/Al <sub>2</sub> O <sub>3</sub> catalysts studied. ....  | 47 |
| Fig. 4-3: Typical morphologies of Cu and ZnO particles of the Cu/ZnO/Al <sub>2</sub> O <sub>3</sub> catalysts investigated by means of high resolution electron microscopy (HRTEM). ....   | 47 |
| Fig. 4-4: Dependency of the local Zn concentration on the Al content in the analyzed TEM images, shown in Fig. 4-1a. The bold line corresponds to a theoretical Zn to Al ratio which is characteristic for ZnAl <sub>2</sub> O <sub>4</sub> Spinel. ....   | 48 |
| Fig. 4-5: Microstructural parameters of the Cu phase obtained by TEM and XRD in dependence on the relative catalytic activity in methanol synthesis. ....  | 49 |

- Fig. 4-6: Measured contact angle  $\theta$  as a function of the size of Cu particles supported on ZnO (black symbols) and on ZnO/Al<sub>2</sub>O<sub>3</sub> (open symbols). Right axis shows the apparent work of adhesion:  $W_{adh.} = \gamma_{Cu} \cdot (1 + \cos\theta)$ , where  $\gamma_{Cu}$  is the surface energy of the Cu phase [4.17]. ..... 50
- Fig. 4-7: (a) High resolution TEM image of a typical Cu particle in the Cu/ZnO/Al<sub>2</sub>O<sub>3</sub> catalysts exhibiting a stacking faults ( $\alpha$ ) in the (111) direction and a twin boundary ( $\beta$ ) between the (111) and (200) direction, (b) corresponding Fourier-filtered TEM image, and (c) corresponding d-spacing of the Cu phase present. .... 51
- Fig. 4-8: Refinement of the corresponding ICSD model structures of *fcc* Cu and *hcp* ZnO to the experimental XRD pattern of a reduced Cu/ZnO/Al<sub>2</sub>O<sub>3</sub> catalyst. .... 52
- Fig. 4-9: Hydrogen consumption during temperature programmed reduction (TPR) of the calcined and re-oxidized CuO/ZnO/Al<sub>2</sub>O<sub>3</sub> catalysts (TPR-TPO-TPR-TPO-TPR). .... 57
- Fig. 4-10: Oxygen consumption during temperature programmed oxidation (TPO) of the reduced Cu/ZnO/Al<sub>2</sub>O<sub>3</sub> catalysts (TPR-TPO-TPR-TPO-TPR). .... 58
- Fig. 4-11: Evolution of copper phase during (a) TPR of the calcined catalyst (TPR-1), and (b) during TPR of the re-oxidized sample (TPR-2). The TPR profiles have been calculated by differentiation of the concentration profile (as a function of the temperature) of the CuO phase. The quantitative phase analysis is based on a least-squares fit of Cu K -edge XANES during TPR using suitable reference spectra of Cu, Cu<sub>2</sub>O, and CuO as described in the text. .... 58
- Fig. 4-12: Evolution of the Cu K -edge XANES position obtained from its first derivative during temperature programmed oxidation (TPO). The energy offset (edge position) has been determined as the position of the inflection point of the continuum. .... 60
- Fig. 4-13: Experimental Cu K -edge FT( $\chi(k) \cdot k^3$ ) spectra recorded during temperature programmed oxidation. The spectra were taken after each oxidation event observed during temperature programmed oxidation of (a) the re-oxidized (TPO-1), and (b) re-re-oxidized sample (TPO-2). .... 61
- Fig. 4-14: Experimental FT( $\chi(k) \cdot k^3$ ) measured at (a) Cu K -edge, and at (b) Zn K -edge. The spectra were recorded after each temperature programmed reduction cycle at ambient temperature. .... 62
- Fig. 4-15: Cu K -edge XANES spectra measured at ambient temperature for the calcined (as prepared) and re-oxidized catalysts (TPO-1, TPO-2). Insert shows the Cu K -edge XANES spectra of bulk CuO and Malachite (Cu<sub>2</sub>CO<sub>3</sub>(OH)<sub>2</sub>; [4-41]) measured as references. .... 63
- Fig. 4-16: Powder X-ray diffraction patterns recorded at ambient temperature after (a) reduction (TPR-1, TPR-2, TPR-3), and (b) of the calcined and re-oxidized (TPO-1, TPO-2) catalyst (M: Malachite {(Cu<sub>2</sub>CO<sub>3</sub>(OH)<sub>2</sub>} [4-41]). .... 64
- Fig. 4-17: Schematic model for the impact of successive reduction and re-oxidation (TPR/ O) on the microstructure of the derived Cu/Zn/Al- catalysts. Reduction of the as prepared CuO/ZnO/Al<sub>2</sub>O<sub>3</sub> catalyst (TPR-1) results in a reduction of copper from primary CuO particles and, in addition, in a decomposition of residual Cu/Zn/(Al)- hydroxycarbonates which is accompanied by a considerable change of the microstructure of the derived Cu/ZnO/Al<sub>2</sub>O<sub>3</sub> catalyst. Consequently, a {Cu(Al)}<sub>x</sub>Zn<sub>1-x</sub>O pseudo solid solution is formed. Finally, during TPR-2 the copper dissolved in the ZnO host lattice is reduced to its metallic form resulting in a superior interface between this Cu fraction and the ZnO/(Al<sub>2</sub>O<sub>3</sub>) matrix. Conversely to TPR-1, further re-oxidation and subsequent reduction (TPR-3) only results in reversible changes and some thermal sintering leading to a decreased overall Cu surface area. .... 68
- Fig. 5-1: XRD pattern of the precipitated, washed, and subsequently dried (Cu,Zn)- hydroxycarbonate precursor material used for the calcination experiments: (a) as prepared (Cu,Zn)- precursor, (b) powder X-ray diffraction file of Rosasite, (Cu,Zn)<sub>2</sub>(OH)<sub>2</sub>CO<sub>3</sub>, and (c) powder X-ray diffraction file of Aurichalcite, (Cu,Zn)<sub>5</sub>(OH)<sub>6</sub>(CO<sub>3</sub>)<sub>2</sub>. .... 76
- Fig. 5-2: XRD pattern of the differently calcined and *in situ* reduced Cu/Zn catalysts: (a) calcined CuO/ZnO catalyst precursors (from bottom to top: CZ-1, CZ-2, CZ-3, CZ-4), (b) powder X-ray diffraction file of CuO, (c) powder X-ray diffraction file of ZnO, (d) reduced Cu/ZnO catalysts (from bottom to top: CZ-1, CZ-2, CZ-3, CZ-4), (e) powder X-ray diffraction file of Cu, and (f) powder X-ray diffraction file of ZnO. .... 77
- Fig. 5-3: Experimental Cu K -edge Fourier- transformed spectra, FT{ $\chi(k) \cdot k^3$ }, of the differently calcined (left), and subsequently reduced (right) Cu/ZnO catalysts. CZ-1: a) and f); CZ-2: b) and g); CZ-3: c) and h); CZ-4: d) and k); macro-crystalline CuO: e); and macro-crystalline Cu: l). .... 78
- Fig. 5-4: (a) Dependency of the overall distance of the 2<sup>nd</sup> Cu-O shell of the Cu K -edge FT( $\chi(k) \cdot k^3$ ) of the differently calcined catalysts on the fraction of CO<sub>2</sub> employed during catalyst calcination. The

- corresponding Cu-O shell is indicated by an arrow in Fig. 5-3 a-e. (b) Cu K -edge  $FT(\chi(k) \cdot k^3)$  of bulk CuO and Malachite  $\{Cu_2CO_3(OH)_2\}$  measured as references. The characteristic displacement of the corresponding Cu-O shell, located at  $R \approx 2.5 \text{ \AA}$  in the RDF, is highlighted in the inset. .... 79
- Fig. 5-5: Dependency of the *Debye-Waller* factors (DWF) determined for the (a) 4<sup>th</sup> ( $R_{Cu-Cu} = 5.1 \text{ \AA}$ ), (b) 5<sup>th</sup> ( $R_{Cu-Cu} = 5.8 \text{ \AA}$ ) Cu-Cu shell, and fraction of residual carbonates in the activated (reduced) Cu/ZnO catalysts on the fraction of CO<sub>2</sub> (O<sub>2</sub>) employed during catalyst calcinations, respectively. DWF's have been determined from refinement of theoretical Cu model structure to the experimental Cu K -edge EXAFS function measured for the *in situ* reduced Cu/ZnO catalysts..... 80
- Fig. 5-6: Temperature programmed reduction (TPR) profiles obtained during catalyst activation in 5 vol.-% H<sub>2</sub> ( $\beta = 2 \text{ K} \cdot \text{min}^{-1}$ ) of the differently calcined CuO/ZnO catalysts: a). CZ-1, b). CZ-2, c). CZ-3, and d). CZ-4. .... 81
- Fig. 5-7: MS spectra obtained during temperature programmed reduction (TPR) of sample CZ-1 ( $\beta = 6 \text{ K} \cdot \text{min}^{-1}$ ). The mass-to-charge:  $m/e = 2$  corresponds to hydrogen,  $m/e = 18$  corresponds to water, and  $m/e = 44$  corresponds to carbon dioxide. .... 82
- Fig. 5-8: Evolved CO<sub>2</sub> profiles observed during reduction (TPR) of the differently calcined Cu/ZnO catalysts ( $\beta = 6 \text{ K} \cdot \text{min}^{-1}$ ). For comparison the spectra were normalized to the maximum of the CO<sub>2</sub>-release during catalyst activation. .... 83
- Fig. 5-9: Apparent activation energy as a function of the degree of CO<sub>2</sub>- release upon catalyst activation of the differently calcined CuO/ZnO catalysts. The EGA profiles of CO<sub>2</sub> during reduction (TPR) are shown in Figure 5-8. The activation energy has been determined by model-free isoconversional method according to *Friedman* [5.12]. .... 84
- Fig. 5-10: Apparent activation energies and order of reactions of the first step in the CO<sub>2</sub>- release upon catalyst reduction (see Fig. 5-8). The kinetic parameters derived from a refinement of a series of CO<sub>2</sub>- EGA spectra during catalyst activation are summarized in Table 5-3. .... 85
- Fig. 5-11: Dependency of the MeOH conversion on the residence time ( $WHSV^{-1}$ ) in methanol steam reforming reaction of the differently calcined Cu/ZnO catalysts ( $T = 250 \text{ }^\circ\text{C}$ ;  $p = 1 \text{ bar}$ ;  $H_2O/MeOH = 1$ ). .... 87
- Fig. 5-12: Dependency of the CO concentration at the reactor outlet on MeOH conversion during methanol steam reforming reaction of the differently calcined Cu/ZnO catalysts ( $T = 250 \text{ }^\circ\text{C}$ ;  $p = 1 \text{ bar}$ ;  $H_2O/MeOH = 1$ ). .... 88

## List of Tables

|   |    |
|---|----|
| Table 3-1: Methanol conversion and product composition for methanol steam reforming over various Cu/ZnO/Al <sub>2</sub> O <sub>3</sub> (CZA) catalysts determined in a fixed-bed reactor (reaction temperature 523 K; ambient pressure; catalyst mass 0.05 g; total gas flow rate 100 ml·min <sup>-1</sup> ; feed concentration: 3.5 vol.-% CH <sub>3</sub> OH + 3.5 vol.-% H <sub>2</sub> O).....  | 23 |
| Table 3-2: Metal composition of the investigated CZA catalysts determined by X-ray fluorescence analysis (XRF) and Cu to Zn ratio determined from the edge jump at the Cu K and the Zn K -edge (XAS).....   | 26 |
| Table 3-3: Specific Cu surface area determined by N <sub>2</sub> O frontal chromatography (RFC) and bulk structural characteristics of the reduced Cu/ZnO/Al <sub>2</sub> O <sub>3</sub> catalysts determined by XRD: Cu crystallite size, Cu lattice strain, and Cu dispersion. ....   | 26 |
| Table 3-4: Comparison of Cu lattice constant <i>a</i> ( <i>in situ</i> XRD), Cu K -edge position <i>E</i> <sub>0</sub> , Cu-Cu distance <i>R</i> , and the <i>Debye Waller</i> factor ( $\sigma_{\text{Cu}}^2$ ) obtained from fitting theoretical <i>fcc</i> Cu to the experimental EXAFS of the 1 <sup>st</sup> Cu-Cu shell ( <i>in situ</i> XAS) measured under working conditions (MSR feed, 523 K).....  | 28 |
| Table 3-5: Structural parameters obtained from refinement of theoretical <i>fcc</i> copper metal to the experimental Cu K -edge EXAFS function recorded after MSR reaction at 313 K ( $k = 3 \text{ \AA}^{-1}$ to $13 \text{ \AA}^{-1}$ ; $R = 1.7 \text{ \AA}$ to $6 \text{ \AA}$ ; Refinement includes 5 single and 9 multi scattering paths; $N_{\text{ind}} = 27$ ; $N_{\text{free}} = 11$ ). ....  | 32 |
| Table 3-6: Zn K -edge position ( <i>E</i> <sub>0</sub> ) of the calcined precursor (313 K), the reduced catalyst (523 K), and the catalyst under MSR conditions (523 K). Energy offset has been determined as the position of the inflection point of the continuum absorption curve. The edge position of macro-crystalline ZnO measured as reference amounts to <i>E</i> <sub>0</sub> = 9.662 keV.....  | 33 |
| Table 4-1: Comparison of the characteristics of the temperature programmed reduction profile obtained by conventional TPR, and by <i>in situ</i> studies (XRD, XAS), and abundance of CO <sub>2</sub> released during reduction of the derived Cu/Zn/Al- catalysts. ....  | 57 |
| Table 4-2: Structural parameters obtained from refinement of theoretical Cu model structure to the experimental Cu K -edge EXAFS function measured for the calcined and re-oxidized samples at ambient temperature. ....  | 59 |
| Table 4-3: Structural parameters obtained from refinement of theoretical CuO model structure to the experimental Cu K -edge EXAFS function measured for the calcined and re-oxidized samples at ambient temperature. ....   | 60 |
| Table 4-4: Structural parameters obtained from refinement of theoretical ZnO model structure to the experimental Zn K -edge EXAFS function recorded after each reduction and re-oxidation cycle at ambient temperature. ....  | 61 |
| Table 4-5: Structural parameters of the reduced samples obtained from refinement of theoretical Cu and ZnO model structures to the experimental XRD pattern recorded after each reduction at ambient temperature. ....  | 62 |
| Table 4-6: Specific Cu surface areas, <i>S</i> <sub>0</sub> (Cu), determined from N <sub>2</sub> O titration and normalized reaction rate in methanol synthesis determined at different temperatures, and 60 bar of the calcined and re-oxidized CuO/ZnO/Al <sub>2</sub> O <sub>3</sub> catalysts. The rates in methanol synthesis were normalized to the rate of the as prepared Cu/ZnO/Al <sub>2</sub> O <sub>3</sub> catalyst. Prior to the catalytic testing, the derived CuO/ZnO/Al <sub>2</sub> O <sub>3</sub> catalysts have been <i>in situ</i> reduced according to the procedure described in chapter 4.2.2. .... | 64 |
| Table 5-1: Structural parameters, i.e. lattice constants, mean crystallite sizes of the Cu and ZnO phases present and characteristic intensity ratio of the Cu ( <i>111</i> ) to Cu ( <i>311</i> ) Bragg diffraction reflexes, of the reduced Cu/ZnO catalysts obtained from a refinement of theoretical Cu and ZnO model structures to the experimental XRD pattern recorded at ambient temperature. ....  | 77 |
| Table 5-2: Characteristics, such as specific Cu surface area, overall abundance of residual carbonates and apparent activation energies for the activation process, of the activated (reduced) Cu/ZnO catalysts studied.....  | 81 |
| Table 5-3: Kinetic parameters determined from a refinement of a series of MS spectra of the CO <sub>2</sub> - release during TPR of the differently calcined Cu/ZnO catalysts measured with different heating rates.....  | 85 |

---

|   |    |
|---|----|
| Table 5-4: Apparent activation energies ( $E_A$ ), frequency factors ( $A$ ) determined for methanol steam reforming of the differently calcined Cu/ZnO catalysts obtained from <i>Arrhenius</i> plot, normalized reaction rate, and hydrogen yield during methanol steam reforming reaction. The rates obtained in methanol steam reforming were normalized to the rate of the Cu/ZnO catalyst which was derived by conventional calcination in synthetic air (CZ-1).....  | 88 |
| Table 5-5: Normalized reaction rate and apparent activation energy in methanol synthesis obtained from the differently calcined Cu/ZnO catalysts ( $T = 250\text{ }^\circ\text{C}$ ; $p = 60\text{ bar}$ ; feed: 59.5 vol.-% $\text{H}_2$ , 19.5 vol.-% $\text{CH}_4$ , 8 vol.-% $\text{CO}_2$ , 6 vol.-% $\text{CO}$ , and balance $\text{N}_2$ ). The rates in methanol synthesis were normalized to the rate of the Cu/ZnO catalyst which was derived by conventional calcination in synthetic air (CZ-1).....   | 89 |
| Table 5-6: Apparent activation energies, normalized reaction rate, and $\text{H}_2$ yield in MSR reaction obtained from the differently calcined Cu/ZnO/ $\text{Al}_2\text{O}_3$ catalysts ( $T = 250\text{ }^\circ\text{C}$ ; $p = 1\text{ bar}$ ; $\text{WHSV} = 9.0 \cdot 10^{-5}\text{ h}$ ; $\text{H}_2\text{O/MeOH} = 1$ ). The rates in MSR were normalized to the rate of the Cu/ZnO/ $\text{Al}_2\text{O}_3$ catalyst which was derived by conventional calcination in synthetic air (20 vol.-% $\text{O}_2$ in $\text{N}_2$ ). .....  | 91 |
| Table 5-7: Normalized reaction rates and apparent activation energies ( $E_A$ ) obtained in methanol synthesis of the differently calcined Cu/ZnO/ $\text{Al}_2\text{O}_3$ catalysts ( $T = 250\text{ }^\circ\text{C}$ ; $p = 60\text{ bar}$ ; feed: 59.5 vol.-% $\text{H}_2$ , 19.5 vol.-% $\text{CH}_4$ , 8 vol.-% $\text{CO}_2$ , 6 vol.-% $\text{CO}$ , and balance $\text{N}_2$ ). The rates in methanol synthesis were normalized to the rate of the Cu/ZnO/ $\text{Al}_2\text{O}_3$ catalyst which was derived by conventional calcination in synthetic air (20 vol.-% $\text{O}_2$ in $\text{N}_2$ )..... | 92 |
| Table 5-8: Specific Cu surface area of the differently calcined Cu/ZnO/ $\text{Al}_2\text{O}_3$ catalysts measured by $\text{N}_2\text{O}$ surface titration (RFC). Prior to each experiment the catalysts were <i>in situ</i> reduced in 5 vol.-% $\text{H}_2$ (He) at 523 K. ....   | 92 |





# Table of Contents

|                        |      |
|------------------------|------|
| Danksagung.....        | I    |
| Zusammenfassung.....   | II   |
| Abstract.....          | IV   |
| List of Figures.....   | V    |
| List of Tables.....    | VIII |
| Table of Contents..... | XI   |

## Chapter One

|   |   |
|---|---|
| Introduction .....  | 1 |
| 1.1 General.....  | 1 |
| 1.2 Cu/ZnO/Al <sub>2</sub> O <sub>3</sub> catalysts in methanol chemistry ..... | 2 |
| 1.3 Outline of work.....  | 5 |
| 1.4 References cited.....   | 7 |

## Chapter Two

|   |    |
|---|----|
| Fundamentals and theoretical details.....   | 9  |
| 2.1 X-ray diffraction .....                 | 9  |
| 2.2 X-ray absorption spectroscopy .....     | 11 |
| 2.3 Temperature programmed techniques ..... | 14 |
| 2.4 Transmission electron microscopy .....  | 15 |
| 2.5 References cited.....                   | 16 |

## Chapter Three

### Role of Defects in Cu/ZnO/Al<sub>2</sub>O<sub>3</sub> Catalysts for Methanol Steam Reforming..... 18

|   |           |
|---|-----------|
| <b>3.1 Introduction .....</b>   | <b>18</b> |
| <b>3.2 Experimental .....</b>   | <b>19</b> |
| 3.2.1 Sample preparation .....  | 19        |
| 3.2.2 Activity screening and Cu surface area determination .....  | 20        |
| 3.2.3 Temperature programmed reduction .....  | 21        |
| 3.2.4 Transmission electron microscopy .....  | 21        |
| 3.2.5 <i>In situ</i> X-ray diffraction .....  | 21        |
| 3.2.6 <i>In situ</i> X-ray absorption spectroscopy .....  | 22        |
| <b>3.3 Results .....</b>  | <b>23</b> |
| 3.3.1 Catalytic activity in methanol steam reforming .....  | 23        |
| 3.3.2 General characterization of Cu/ZnO/Al <sub>2</sub> O <sub>3</sub> catalysts .....                                 | 25        |
| 3.3.3 Bulk structural <i>in situ</i> investigations .....   | 29        |
| <b>3.4 Discussion .....</b>   | <b>35</b> |
| 3.4.1 Microstructure of Cu in Cu/ZnO/Al <sub>2</sub> O <sub>3</sub> catalysts .....                                     | 35        |
| 3.4.2 Microstructure of ZnO and Al <sub>2</sub> O <sub>3</sub> in Cu/ZnO/Al <sub>2</sub> O <sub>3</sub> catalysts ..... | 38        |
| 3.4.3 Thermal stability of Cu/ZnO/Al <sub>2</sub> O <sub>3</sub> catalysts .....  | 40        |
| <b>3.5 Summary .....</b>  | <b>41</b> |
| <b>3.6 References cited .....</b>   | <b>41</b> |

## Chapter Four

### Role of Defects in Cu/ZnO/Al<sub>2</sub>O<sub>3</sub> Catalysts for Methanol Synthesis..... 44

|  |           |
|--|-----------|
| <b>4.1 Role of defects in the activated Cu/ZnO/Al<sub>2</sub>O<sub>3</sub> catalyst .....</b>    | <b>44</b> |
| 4.1.1 Introduction .....   | 44        |
| 4.1.2 Experimental details .....   | 44        |
| 4.1.3 Results and discussion .....   | 45        |
| 4.1.4 Summary .....  | 53        |
| <b>4.2 Redox behavior of Cu/ZnO/Al<sub>2</sub>O<sub>3</sub> methanol synthesis catalyst.....</b> | <b>53</b> |
| 4.2.1 Introduction .....   | 53        |
| 4.2.2 Experimental techniques.....   | 54        |
| 4.2.3 Results .....  | 56        |
| 4.2.4 Discussion .....   | 64        |
| 4.2.5 Conclusions .....  | 69        |
| <b>4.3 References cited .....</b>  | <b>70</b> |

**Chapter Five**

|   |           |
|---|-----------|
| <b>Catalyst Modification by Carbon Dioxide Calcination.....</b>   | <b>73</b> |
| <b>5.1 Introduction .....</b>   | <b>73</b> |
| <b>5.2 Experimental details .....</b>   | <b>74</b> |
| <b>5.3 Results and Discussion .....</b>   | <b>75</b> |
| 5.3.1 Microstructure of the derived CuO/ZnO catalysts.....  | 75        |
| 5.3.2 Reducibility of the derived CuO/ZnO catalysts.....  | 80        |
| 5.3.3 Effect of CO <sub>2</sub> calcination on methanol steam reforming activity .....  | 87        |
| 5.3.4 Effect of CO <sub>2</sub> calcination on methanol synthesis activity.....   | 89        |
| <b>5.4 Implication of carbon dioxide calcination on ternary Cu/ZnO/Al<sub>2</sub>O<sub>3</sub> catalysts:<br/>    methanol steam reforming vs. methanol synthesis .....</b> | <b>90</b> |
| <b>5.5 Mechanistic considerations of the effect of carbon dioxide calcination on methanol steam<br/>    reforming and synthesis reaction .....</b>                          | <b>93</b> |
| <b>5.6 Summary .....</b>  | <b>95</b> |
| <b>5.7 References cited .....</b>   | <b>96</b> |

**Chapter Six**

|  |            |
|--|------------|
| <b>Conclusions .....</b>   | <b>98</b>  |
| <b>6.1 Methanol steam reforming vs. Methanol synthesis .....</b>                                   | <b>98</b>  |
| 6.1.1 Role of the defects and the support in Cu/ZnO/Al <sub>2</sub> O <sub>3</sub> catalysts ..... | 98         |
| 6.1.2 Role of the calcination gas atmosphere .....   | 100        |
| <b>6.2 Summary and perspectives.....</b>   | <b>103</b> |
| <b>6.3 References cited .....</b>  | <b>105</b> |
| <b>Appendix .....</b>  | <b>107</b> |
| <b>7.1 Curriculum vitae .....</b>  | <b>107</b> |
| <b>7.2 Publication index.....</b>  | <b>108</b> |



“I believe that water will one day be employed as fuel, that hydrogen and oxygen which constitute it, used singly or together, will furnish an inexhaustible source of heat and light, of an intensity of which coal is not capable. I believe then that when the deposits of coal are exhausted, we shall heat and warm ourselves with water. Water will be the coal of the future.”

- Jules Verne, *L'île mystérieuse* (1874) -

to my family with love.



# Chapter One

## Introduction

### 1.1 General

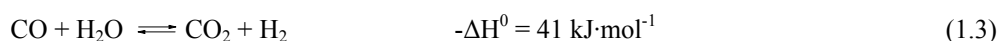
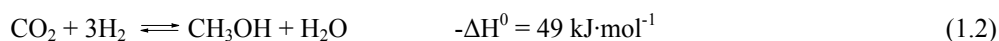
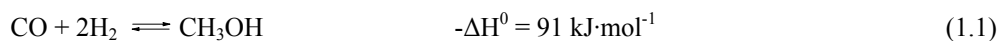
Catalysis plays a key role in nature and environment since almost every (bio-) chemical reaction requires a certain catalytic material. Generally, a catalyst is a species that accelerates a reaction by providing an energetically favorable reaction pathway which is characterized by lower activation energy than the path it replaces. Additionally, catalysts can direct a reaction that influences the selectivity of a (bio-) chemical process. Especially the latter property of catalysts makes that catalysis significantly contributes to the development of a sustainable society. Generally, a (heterogeneous) catalytic reaction starts with the adsorption of the reactants which is accompanied by weakening or cleavage of intermolecular chemical bonds on the surface of the catalyst. The adsorbed species react to the products in one or several consecutive steps and, finally, the products desorb from the surface regenerating the active site on the catalyst surface. Thereby, the surface of the working catalysts is covered to a minor by active sites which can catalyze a (bio-) chemical reaction, and to a major by spectator sites which do not participate in the catalytic reaction.

For a long time catalyst development was exclusively based on chemical intuition and on trial and error procedures. Such empirical discoveries will, certainly, continue leading to optimized and/ or new industrial catalytic processes. Nevertheless, rational catalyst design is the most challenging field of catalysts science since it allows the development of innovative catalysts which, most probably, never had been invented just by chance. The detailed knowledge of the dependencies between reaction mechanism and the microstructure of the catalyst helps to optimize processes and catalysts and, hence, helps to minimize costs, and to save energy and natural resources in a rational manner (rational catalyst design). In order to accomplish this, tools are required, which can be utilized to identify those physiochemical processes taking place in an active catalyst under working (*in situ*) conditions. Therefore, the economically employed and structurally complex catalyst is replaced by simplified and well known models in order to study the working principle of a catalyst. Such model catalysts range from single crystals, via well defined particles deposited on planar substrates to supported particles from which structural promoters were (partially) removed. However, science often faces a dilemma between the level of information which was gained from *in situ* spectroscopy of a catalyst under working conditions and the relevance about this information for the real, industrially employed catalytic process. Thus, the wealth

of working concepts obtained can not always directly transferred to commercially employed catalysts systems owing to the inherent complexity of usually multiphase mixtures of various compounds (e.g. mixed metal oxides). A solution can be derived by combination of advanced theoretical tools for calculating spectroscopic data which in addition to experimental data allows a detailed description of the structure of the active site of a catalyst. Based on this knowledge, a catalytic reaction cycle can be proposed and, hence, a mechanistic insight into the catalytic process can be obtained.

## 1.2 *Cu/ZnO/Al<sub>2</sub>O<sub>3</sub> catalysts in methanol chemistry*

Methanol is a technical important feedstock for the production of formaldehyde, acetic acid, methyl tertiary butyl ether (MTBE), methyl methacrylate (MMA) and other organic compounds, and is used as a solvent or gasoline extender [1.1]. Due to its high hydrogen-to-carbon ratio and its unproblematic handling, methanol is also an alternative candidate to petroleum based fuels [1.2]. Industrially, methanol is produced from synthesis gas over Cu/ZnO/Al<sub>2</sub>O<sub>3</sub> catalysts [1.3]. Feed stocks for industrial methanol synthesis on Cu based catalysts consist of a mixture of CO<sub>2</sub>, CO and H<sub>2</sub> with or without inert components (N<sub>2</sub>, CH<sub>4</sub>). Thereby, synthesis gas can be produced from partial oxidation or steam reforming of natural gas predetermining the CO to CO<sub>2</sub> ratio in the gas feed. Methanol synthesis is an exothermic ( $\Delta H^0 < 0$ ) and, as a result of the entropy decrease, an endergonic ( $\Delta G^0 > 0$ ) reaction and, hence, favored at low reaction temperature ( $T < 300$  °C) and high reaction pressure {p = (35-55) bar} [1.4]. In principle methanol synthesis involves the following reaction network:

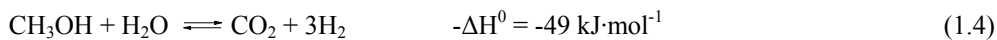


In the framework of methanol synthesis, the water-gas-shift reaction (WSG; Eq. 1.3) is not an independent reaction, as it is, at least formally, the difference of reactions Eq. 1.2 and Eq. 1.1. The WGS reaction is industrially applied to achieve appropriate H<sub>2</sub> to CO ratios in the production of bulk chemicals, such as ammonia, methanol, and alternative hydrocarbon fuels through *Fischer–Tropsch* synthesis [1.5]. Commercially, water-gas-shift reaction is performed via two separated stages of a high temperature shift using a Fe<sub>2</sub>O<sub>3</sub> catalyst and a subsequent low temperature shift using a Cu/ZnO/Al<sub>2</sub>O<sub>3</sub> catalyst [1.5].

Methanol, as a chemical carrier of hydrogen to be applied in fuel cells is a promising alternative for petroleum based fuels [1.6]. Methanol is found to be a favorable candidate since it is one of the largest bulk chemicals with a production capacity of several million tons per year, it is miscible with water, and it can be activated at relatively low temperatures ( $T < 250$  °C). Methanol steam reforming reaction (Eq. 1.4) yields in a relative high ratio of hydrogen to carbon dioxide of 3:1 in the product gas [1.7]. One of the main drawbacks of methanol steam reforming is the formation of CO as a by-product to the major products hydrogen and carbon dioxide which, at least for Cu/ZnO/Al<sub>2</sub>O<sub>3</sub> catalysts, is mainly produced by



the reverse WGS reaction (reverse of Eq. 1.3; [1.8]). Especially low temperature fuel cells such as proton exchange membrane (PEM) fuel cells for small scale applications impose high purity requirements of the hydrogen since the electrodes are very sensitive to poisoning by CO [1.9].



Methanol synthesis (Eq. 1.1 and 1.2), methanol steam reforming (Eq. 1.4) and the (reverse) WGS reaction (Eq. 1.3) have many similarities, not least that copper catalysts are effective in all three reactions. Here, commercially employed catalysts containing copper metal, zinc oxide and alumina constitute an important system for methanol chemistry. The activity of these Cu based catalysts has been shown to be nearly linearly dependent on the overall copper surface area indicating that metallic copper represents the active phase in methanol chemistry [1.10]. Nevertheless, additional parameters such as geometric and electronic defects on the surface and/ or in the bulk in the copper phase also determine the catalytic performance of Cu/ZnO/Al<sub>2</sub>O<sub>3</sub> catalysts in methanol chemistry [1.11-1.15]. In order to enhance the activity and stability, commercially employed copper catalysts are promoted with ZnO and Al<sub>2</sub>O<sub>3</sub> [1.16]. Although ZnO has some activity for methanol synthesis, which is much less than that of Cu, it has been suggested to be an inert diluent. Accordingly, a rough geometric relationship [1.17] between the diameter of the metal and ZnO stabilizer particles, and the volumes of metal and stabilizer has been observed. The smaller the diameter of the refractory spacers, the higher was the practical Cu loading and consequently the higher the activity. Contrarily, ZnO has been supposed to exhibit a promoting effect either as a provider of atomic spillover hydrogen for further hydrogenation of adsorbed reaction intermediates on Cu sites [1.18] or as a structure-directing support controlling dispersion, morphology, and specific activity of the copper metal particles [1.14, 1.19-1.23]. Strong interaction between the metal and the ZnO phase, especially in the case of a large lattice mismatch, is known to cause strain in the metal particles, to which an increase in catalytic performance has been attributed [1.24-1.27]. The role of alumina is less clear than the one of ZnO in Cu/ZnO/Al<sub>2</sub>O<sub>3</sub> catalysts. On the one hand, it has been empirically found that addition of alumina positively influences the stability of Cu/ZnO catalysts during methanol chemistry (methanol synthesis, WGS reaction, methanol steam reforming). Accordingly, alumina reduced the likelihood of sintering, enhanced the mechanical strength of the catalyst pellet and minimized the pellet shrinkage that occurs during catalyst activation [1.28]. On the other hand, Cu/ZnO/Al<sub>2</sub>O<sub>3</sub> catalysts have been found to exhibit a higher intrinsic activity (activity per Cu surface area) than the homologous Cu/ZnO catalysts [1.29]. Consistently, it has been stated that addition of aluminum as a third component to a Cu/ZnO methanol synthesis catalyst considerably increases the solubility of Cu<sup>2+</sup> ions in the ZnO host lattice during catalyst formulation which is required for a superior activity [1.30].

The steam reforming of methanol (Eq. 1.4) represents the reverse of methanol synthesis from CO<sub>2</sub> and H<sub>2</sub> (Eq. 1.2). Therefore, it is reasonable to assume that the methanol synthesis catalyst also exhibits high activity in the reverse reaction (“principle of microscopic reversibility”). Differences in the requirements of a methanol steam reforming and a methanol synthesis catalyst arise from different partial pressures of reactants and products. The latter reaction is performed with synthesis gas (syngas) containing a large fraction of CO in addition to H<sub>2</sub> and CO<sub>2</sub> whereas the steam reforming reaction starts

from a methanol/steam feed mixture. Thus, different microstructuring of the Cu particles in the active catalyst may take place by applying different gas feeds during the synthesis and steam reforming of methanol [1.31]. With a different microstructure of the copper component of the working catalyst it is likely that the oxidation state of the surface and of the bulk is also different for the both reactions. This is supported by experimental evidence that the optimum Cu/ZnO/Al<sub>2</sub>O<sub>3</sub> formulations for catalysts for methanol synthesis are not the optimum formulations for methanol steam reforming [1.32].

Usually, copper based catalysts are less aggressive and, hence, more selective in hydrogenation and dehydrogenation reactions than those containing nickel, cobalt, iron or platinum. Accordingly, Cu catalysts do not allow the formation of consecutive by-products, such as higher alcohols, ethers, and hydrocarbons, during methanol synthesis in quantitative amounts and, hence, do not allow the reaction to proceed any further downhill on the thermodynamic free-energy scale. Consistently, steam reforming of methanol over copper catalysts is also carried out with high selectivities to the products: H<sub>2</sub> and CO<sub>2</sub>. CO has been observed as by-product during MSR as a result of the reverse water-gas-shift reaction, occurring when methanol is almost completely converted [1.8]. However, for automotive applications of low temperature proton-exchanged membrane (PEM) fuel cells it has to be taken into consideration that even very small amounts of CO can severely poison the anode of the cell. Here, Cu catalysts are excellent for cleavage of C-O  $\pi$ - bonds but they have negligible activity for cleavage of  $\sigma$ -C-O bonds [1.33, 1.34]. Accordingly, the C-O  $\sigma$ - bond in carbon monoxide, carbon dioxide and methanol remains intact during methanol chemistry. This is most probably the origin of their desirable selectivity compared to other (de) hydrogenation catalysts, but they are often more sensitive towards a variety of deactivation processes [1.35].

Especially from the industrial viewpoint, the fundamental research of Cu/ZnO/Al<sub>2</sub>O<sub>3</sub> catalysts is not only related to activity and selectivity but also to the catalyst stability, i.e. chemical and thermal durability, and poison resistance. Unfortunately, copper metal exhibits a low *Tammann* temperature corresponding to a low melting point of  $T_M = 1080$  °C [1.36]. Consequently, Cu/ZnO/Al<sub>2</sub>O<sub>3</sub> catalysts suffer from thermal deactivation by sintering at temperatures above 300 °C. Thermal stability of copper based catalysts strongly depends on both the preparation procedures used and the chemical composition [1.37]. Hence, the catalyst preparation is a crucial point since thermal degradation can be limited in well formulated catalysts prepared under optimized conditions [1.35]. Principally, deactivation of Cu based catalysts are caused by (1) sintering of copper crystallites, (2) poisoning by impurities, and (3) poisoning and blockage by by-products [1.34].

(1) Cu based catalysts exhibit very fast deactivation despite the presence of ZnO and other “stabilizers” even in the absence of poisons. This initial rapid deactivation mainly corresponds to a loss of Cu surface area due to thermal sintering. Accordingly, highly dispersed Cu particles partially agglomerate which is reflected in a considerable decrease of the overall copper surface area [1.38]. Here, the support oxides play a distinctive role in separating Cu particles from each other preventing them to sinter [1.39]. Thus, industrially employed Cu/ZnO catalysts for methanol chemistry contain additional refractory phases, such as Al<sub>2</sub>O<sub>3</sub> to minimize thermal sintering.

(2) Cu/ZnO/Al<sub>2</sub>O<sub>3</sub> catalysts are very susceptible to poisoning by several contaminants (sulfur, chlorine). Typically, sulfur is chemically bonded as H<sub>2</sub>S, thiophene, and COS. For both, methanol

synthesis and WGS reaction, residual sulfur is present from coal derived synthesis gas. Deactivation of Cu based catalyst is prone even when there are only a few ppm of sulfur present in the gas feed [1.40]. In the presence of ZnO in a Cu based catalyst ZnS is formed at the expense of ZnO. In these catalysts the small crystallite size of ZnO, coming from the method of manufacture, ensures that the kinetics of reactive absorption are very fast [1.41]. No copper sulfide phases are detectable reflecting the fact that at concentrations below 30 ppm of sulfur, neither Cu<sub>2</sub>S nor CuS are thermodynamically stable [1.40]. To retain the long-term activity of Cu catalysts it has been empirically found that gas-phase sulfur concentrations need to be kept below 1 ppm and preferably below 0.1 ppm [1.35]. In contrast to sulfur, chlorine is normally not present in the feed stream during methanol synthesis and WGS reaction. Especially for the steam reforming reaction, chlorines are introduced to the catalyst when unpurified water is used as reaction feed. The enhanced rate of deactivation by chlorine poisoning occurs via sintering of copper particles due to the formation of volatile chlorine compounds [1.37]. The effects of sulfur and chlorine on methanol synthesis catalyst are similar to WGS reaction catalyst [1.37]. Apparently, ZnO prevents Cu sintering and may remove catalyst poisons (i.e. sulfides and halogenides) under working conditions in methanol synthesis as well as steam reforming [1.35, 1.38].

(3) Traces of impurities present in the catalyst, such as alkali ions (K<sup>+</sup>, Cs<sup>+</sup>), produces higher hydrocarbons which are thermodynamically favored products during hydrogenation of CO/ CO<sub>2</sub> mixtures during methanol synthesis [1.33]. These higher hydrocarbons would deposit on the catalyst surface and thus, destroy the pore structure of the catalyst [1.42]. Additionally, volatile metal carbonyls of Fe or Ni present in the feed gas would decompose at the catalyst surface and block the active sites or provide unwanted catalytic activities leading to wax or carbon formation [1.43].

The main reason for deactivation is, additionally, dependent on the chemical reaction which has to be catalyzed by the Cu/ZnO/Al<sub>2</sub>O<sub>3</sub> catalysts (methanol synthesis, water-gas-shift reaction, methanol steam reforming). In methanol synthesis involving Cu/ZnO/Al<sub>2</sub>O<sub>3</sub> catalysts neither poisoning by contaminants of the feed gas nor coking is normally a significant source of deactivation. The main cause of deactivation represents thermal sintering of the copper phase present. In contrast, catalyst poisoning and coking have been observed in methanol decomposition and methanol steam reforming reactions [1.35].

### **1.3 Outline of work**

Previous investigations on binary Cu/ZnO catalysts for methanol chemistry (methanol synthesis and methanol steam reforming) have shown that in superior catalysts Cu has to be supported in an appropriate manner to obtain a homogenous microstructure of nanosized and well-intermixed Cu and ZnO particles. The latter are required to maintain the active copper phase in optimal dispersion without allowing segregation. Lattice strain in the metallic copper as the result of an intimate Cu/ZnO interface was found to be an essential modification of bulk copper to achieve superior activity in methanol chemistry [1.13, 1.24, 1.26, and 1.27]. The modification occurs during thermal treatment of the precursor and can be adjusted by either the chemical composition [1.13, 1.24] or by a proper preparation procedure at a constant chemical composition [1.26, 1.27]. In addition, each step in the catalyst preparation

(precipitation, aging, calcination) greatly affects the microstructure and is reflected in the catalytic performance of the final catalyst (“chemical memory” effect).

The objective of this work was a comprehensive microstructural analysis of the even more complex ternary Cu/ZnO/Al<sub>2</sub>O<sub>3</sub> catalysts with alumina as an additional refractory phase under reaction conditions. The goal was to elucidate structure - activity correlations of Cu/ZnO/Al<sub>2</sub>O<sub>3</sub> catalysts employed for the methanol synthesis and the methanol steam reforming. Therefore differently prepared Cu/ZnO/Al<sub>2</sub>O<sub>3</sub> catalysts have been investigated by *in situ* bulk techniques, X-ray diffraction (XRD), and X-ray absorption spectroscopy (XAS). Additionally, microscopic and morphological characteristics of the local structure were examined by electron microscopy (TEM). Temperature programmed techniques (TPR, TPO) were used to study the reducibility of the derived catalysts. These methods are described in chapter 2 in more detail.

In chapter 3 correlations between the defective bulk structure and the methanol steam reforming activity of Cu/ZnO/Al<sub>2</sub>O<sub>3</sub> catalysts were revealed. The catalysts studied exhibited a similar elementary composition of Cu/Zn/Al and were prepared similar to the technical system.

In chapter 4 the results of the microstructural analysis obtained in the previous chapter have been verified for Cu/ZnO/Al<sub>2</sub>O<sub>3</sub> catalysts subjected to the methanol synthesis reaction which, at least formally, represents the reverse of the methanol steam reforming reaction. Methanol synthesis conditions have been chosen very close to the commercially employed process. Additionally, the redox behavior of a methanol synthesis catalyst upon cyclic reduction and re-oxidation has been studied.

In chapter 5, both binary Cu/Zn- and ternary Cu/Zn/Al- hydroxycarbonate precursors were structurally modified by calcination in carbon dioxide. The derived Cu/ZnO/(Al<sub>2</sub>O<sub>3</sub>) catalysts have been tested under methanol synthesis and methanol steam reforming conditions. Catalytic performances obtained from the samples were related to microstructural modifications derived by the calcination atmosphere.

Reliable structure - activity relationships for copper catalysts in methanol chemistry that are prerequisites for a knowledge-based design of improved catalytic materials remain rare. Especially for “real” Cu/ZnO/Al<sub>2</sub>O<sub>3</sub> catalysts with the optimized and commercially employed composition of Cu/Zn/Al = 60:30:10 there were only a few contributions dealing with the microstructure of the catalysts. In this thesis a combination of various analytical methods, *in situ* X-ray absorption spectroscopy (XAS), *in situ* X-ray diffraction (XRD), transmission electron spectroscopy (TEM), and temperature programmed techniques (TPR, TPO) were employed to elucidate correlations between activity, selectivity, and stability and the microstructural characteristics of differently prepared Cu/ZnO/(Al<sub>2</sub>O<sub>3</sub>) with and without alumina as an additional refractory phase to be applied for both methanol synthesis and methanol steam reforming.

#### 1.4 *References cited*

- [1.1] J.B. Hansen, Handbook of Heterogeneous Catalysis, Vol. 4, Editors: G. Ertl, H. Knözinger, J. Weitkamp, VCH Weinheim (1997) pp. 1857.
- [1.2] S. Ahmed, M. Krumpelt, Int. J. Hydrogen Energy, 26 (2001) 291.
- [1.3] J.P. Lange, Catal. Today, 64 (2001) 3.
- [1.4] P.J.A. Tijm, F.J. Waller, D.M. Brown, Appl. Catal. A, 221 (2001) 275.
- [1.5] J.R. Ladebeck, J.P. Wagner, Handbook of Fuel Cells - Fundamentals, Technology and Applications, Vol. 3, Part 2, pp. 190.
- [1.6] P.J. de Wild, M.J.F.M. Vernaak, Catal. Today, 60 (2000) 3.
- [1.7] J. Agrell, B. Lindström, L.J. Petterson, S.G. Järas, Catal., 16 (2002) 67.
- [1.8] H. Purnama, T. Ressler, R.E. Jentoft, H. Soerijanto, R. Schlögl, R. Schomäcker, Appl. Catal. A, 259 (2004) 83.
- [1.9] C. Lamy, A. Lima, V. LeRhun, F. Delime, C. Counteaceau, J.M. Léger, J. Power Sources, 105 (2002) 283.
- [1.10] G.C. Chinchin, K.C. Waugh, D.A. Whan, Appl. Catal., 25 (1986) 101.
- [1.11] N.Y. Topsøe, H. Topsøe, Top. Catal., 8 (1999) 267.
- [1.12] Y. Choi, K. Futagami, T. Fujitani, J. Nakamura, Appl. Catal. A, 208 (2001) 163.
- [1.13] M.M. Günther, T. Ressler, R.E. Jentoft, B. Bems, J. Catal., 203 (2001) 133.
- [1.14] P.L. Hansen, J.B. Wagner, S. Helveg, J.R. Rostrup-Nielsen, B.S. Clausen, H. Topsøe, Science, 295 (2002) 2053.
- [1.15] X.R. Zhang, L.C. Wang, Y. Cao, W.L. Dai, H.Y. He, K.N. Fan, Chem. Commun., 32 (2005) 4104.
- [1.16] J.C.J. Bart, R.P.A. Sneeden, Catal. Today, 2 (1987) 1.
- [1.17] S.P.S. Andrew, Chem. Eng. Sci., 36 (1981) 1431.
- [1.18] R. Burch, S.E. Golunski, M.S. Spencer, J. Chem. Soc. Faraday Trans., 86 (1990) 2683.
- [1.19] J. Yoshihara, C.T. Campbell, J. Catal., 161 (1996) 776.
- [1.20] C.V. Ovesen, B.S. Clausen, J. Schiøtz, P. Stoltze, H. Topsøe, J.K. Nørskov, J. Catal., 168 (1997) 133.
- [1.21] T. Fujitani, J. Nakamura, Catal. Lett., 56 (1998) 119.
- [1.22] N.Y. Topsoe, H. Topsoe, J. Mol. Catal. A, 141 (1999) 95.
- [1.23] J.D. Grunwaldt, A.M. Molenbroek, N.Y. Topsøe, H. Topsøe, B.S. Clausen, J. Catal., 194 (2000) 452.
- [1.24] M.M. Günther, T. Ressler, B. Bems, C. Büscher, T. Genger, O. Hindrichsen, M. Muhler, R. Schlögl, Catal. Lett., 71 (2001) 37.
- [1.25] J.B. Wagner, P.L. Hansen, A.M. Molenbroek, H. Topsøe, B.S. Clausen, S.J. Helveg, J. Phys. Chem. B, 107 (2003) 7753.
- [1.26] B.L. Kniep, F. Girgsdies, T. Ressler, J. Catal., 236 (2005) 34.
- [1.27] T. Ressler, B.L. Kniep, I. Kasatkin, R. Schlögl, Angew. Chem. Int. Ed., 44 (2005) 4704.
- [1.28] C. Rhodes, G.J. Hutchings, A.M. Ward, Catal. Today, 23 (1995) 43.
- [1.29] M. Kurtz, N. Bauer, C. Büscher, H. Wilmer, O. Hinrichsen, R. Becker, S. Rabe, K. Merz, M. Driess, R. A. Fischer, M. Muhler, Catal. Lett., 92 (2004) 49.
- [1.30] T.M. Yurieva, T.P. Minyukova, React. Kinet. Catal. Lett., 29 (1985) 55.
- [1.31] B.S. Clausen, J. Schiøtz, L. Grabaek, C.V. Ovesen, K.W. Jacobsen, J.K. Nørskov, H. Topsoe, Topics Catal., 1 (1994) 367.
- [1.32] W.H. Cheng, Appl. Catal. A, 130 (1995) 13.
- [1.33] K. Klier, Adv. Catal., 31 (1982) 243.
- [1.34] G.C. Chinchin, K. Marsfield, M.S. Spencer, Chemtech., 20 (1990) 682.
- [1.35] M.V. Twigg, M.S. Spencer, Topics Catal., 22 (2003) 191.
- [1.36] J.A. Moulijn, A.E. van Diepen, F. Kapteijn, Appl. Catal. A, 212 (2001) 3.

- [1.37] J.S. Campbell, *Ind. Eng. Chem. Proc. Devel.*, 9 (1970) 588.
- [1.38] M.V. Twigg, M.S. Spencer, *Appl. Catal. A*, 212 (2001) 161.
- [1.39] J. Sloczynski, *Chem. Eng. Sci.*, 49 (1994) 115
- [1.40] B.J. Wood, W.E. Ward, *Canad. J. Chem. Eng.*, 68 (1990) 702.
- [1.41] L. Lloyd, D.E. Ridler, M.V. Twigg, *Catalyst Handbook*, 2<sup>nd</sup> edition, Editors: M.V. Twigg, Manson Publishing, London (1996) p. 283.
- [1.42] K.J. Smith, R.B. Anderson, *Canad. J. Chem. Eng.*, 61 (1983) 40.
- [1.43] H.H. Kung, *Catal. Today*, 11 (1992) 443.

## Chapter Two

### Fundamentals and theoretical details

#### 2.1 X-ray diffraction [2.1-2.2]

X-ray diffraction occurs by elastic scattering of X-ray photons by electrons of atoms. The three-dimensional arrangement in a periodic lattice of the atoms in a crystal structure acts as a suitable grating for diffraction of the X-ray photons. The scattered monochromatic X-rays of each lattice plane that are in phase give constructive interference where the direction of the latter is given by Bragg's law:

$$n\lambda = 2d_{hkl} \sin \theta \quad (2-1)$$

Here,  $\lambda$  is the wavelength of the X-ray photons,  $d$  is the distance between lattice planes ( $hkl$ ),  $\theta$  is the angle between the incoming X-rays and the normal to the reflection lattice plane, and  $n$  is an integer which represents the diffraction order. Scanning different scattering angles result in an interference pattern which is characteristic for a given compound. A typical powder diffraction pattern is shown in Fig. 2-1.

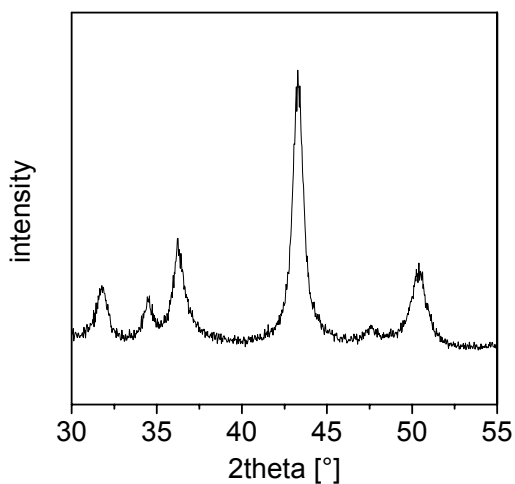


**Fig. 2-1:** Powder X-ray diffraction pattern of a Cu/ZnO/Al<sub>2</sub>O<sub>3</sub> methanol synthesis catalyst measured at ambient temperature.

The position of certain reflections in a XRD pattern describes the geometry of the lattice cell by lattice constants, whereas the intensity accounts for the electron density distribution and, hence, is characteristic for the atomic positions and the identity of an atom in the lattice cell. Additionally, analysis of the reflection peak shape give detailed information on the physical structure of crystallites. Accordingly, the broadening of diffraction lines originates from non-ideal optics of the instrument, wavelength distributions of the X-ray photons and, especially in the case of nanostructured materials, from structural imperfections of the material. Broadening due to lattice imperfections are mainly caused by size effects due to a finite size of crystallites (Eq. 2.2) which give rise to an incoherent diffraction and lattice strain effects (Eq. 2.3) due to varying displacements of atoms relative to their reference position. The latter originate from dislocations, contract or tensile stress, and stacking faults.

$$D_{hkl} = \frac{K \lambda}{B \cos \theta_{hkl}} \quad (2.2)$$

$$\varepsilon_{hkl} = \frac{B}{4 \tan \theta_{hkl}} \quad (2.3)$$

Here,  $D_{hkl}$  is the mean crystallite size,  $\varepsilon$  is the mean lattice strain,  $\lambda$  the wavelength,  $B$  is the broadening of the reflection peak,  $\theta$  is the material characteristic angle in the diffraction pattern,  $K$  is a constant that depends on the crystallite shape and how the broadening of the reflection was quantified. Additionally, the stacking fault probability  $\alpha$  can be determined from the measurements of intervals between the adjacent reflection peaks in the XRD patterns, such as  $(111)$  and  $(200)$  of face centered cubic ( $fcc$ ) metals (Cu, Ag etc.), which are known to progressively shift in opposite directions as  $\alpha$  increases (Eq. 2.4). The overall faulting probability comprising stacking faults and twinning in  $fcc$  metals ( $1.5\alpha+\beta$ ) can be estimated from the comparison of apparent crystallite sizes determined by the shape analysis of different peaks (Eq. 2.5), where  $\alpha$  is the stacking fault probability,  $(1.5\alpha+\beta)$  is the overall faulting probability,  $D$  is the mean crystallite size, and  $a$  is the lattice constant of the corresponding  $fcc$  metal.

$$\alpha = 8.3 \left( \frac{2}{\sqrt{3}} - \frac{\sin \theta_{200}}{\sin \theta_{111}} \right) \quad (2.4)$$

$$1.5\alpha + \beta = a \left( \frac{\frac{1}{D_{200}} - \frac{1}{D_{111}}}{1 - \frac{\sqrt{3}}{2}} \right) \quad (2.5)$$

In summary, X-ray diffraction is a non-destructive technique widely applied for characterization of crystalline materials. In catalyst research XRD is applied on a routine basis for phase identification, quantitative analysis, and quantification of structural imperfections. Due to the relatively high penetration



power of X-rays photons, XRD can be also used for studying the microstructure of catalysts under working conditions (*in situ*).

## 2.2 X-ray absorption spectroscopy [2.3-2.5]

In an X-ray absorption process, a core level electron is excited to an empty state above the Fermi level, probing the unoccupied part of the electronic structure of a system. Interference effects of the created photoelectrons of the absorber atom with the nearby, backscattering atoms give detailed information on local structure of a catalyst. The absorption,  $\mu(E) \cdot x$ , of X-ray photons which passes through a material is defined by the *Lambert-Beer* law:

$$\mu(E) \cdot x = \log\left(\frac{I_0}{I_t}\right) \quad (2.6)$$

where  $\mu(E)$  is the linear absorption coefficient,  $x$  is the thickness of the sample,  $I_0$  the intensity of the incident photons, and  $I_t$  the intensity of the transmitted photons. The linear absorption coefficient is proportional to the transition probability of the photoelectric effect and the latter is defined according to *Fermi's Golden Rule* (Eq. 2.7). The linear absorption coefficient is proportional to a dipole matrix element ( $\hat{e} \cdot r$ ) coupling with the initial ( $\psi_i$ ) and final-state ( $\psi_f$ ) wave functions. The  $\delta$ -function takes care about conservation of the energy.

$$\mu(E) = C \left| \langle \psi_f | \hat{e} r | \psi_i \rangle \right|^2 \delta_{(E_f - E_i - h\nu)} \quad (2.7)$$

X-ray fluorescence and Auger emission are competing processes which significantly depends on the atomic number of the absorber atom. Approximately, in light elements Auger emission is more probable than in heavy elements, where fluorescence becomes more likely. Accordingly, the fluorescence is rather used than transmission mode for analysis of heavy atoms, which represents a minor fraction of the total adsorption of the sample. Here, the signal can be easily discriminated from the background signal consisting mainly of elastic and (inelastic) *Compton* scattering.

When the X-ray photon energy is tuned to the binding energy of the core level of a constituent element, an increase in the absorption coefficient  $\mu(E)$ , denoted as the absorption edge, occurs (Fig. 2-2). X-ray absorption spectrum exemplarily shown in Fig. 2-2 can be separated in two different regions: The X-ray absorption near edge structure (XANES) and the extended X-ray absorption fine structure (EXAFS). The XANES region which ranges approximately 50 eV below and above the absorption edge is dominated by the local atomic resonance and multiple scattering at neighboring atoms, whereas the EXAFS region is determined by single and multiple scattering events at neighboring atoms (see Fig. 2-2).

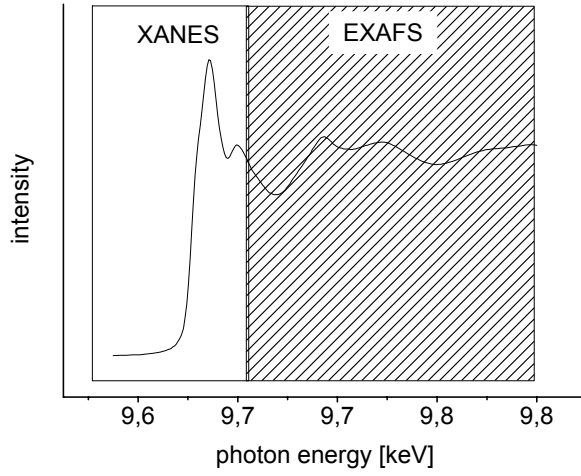


**Fig. 2-2:** X-ray absorption spectra (XAS) of a Cu/ZnO/Al<sub>2</sub>O<sub>3</sub> methanol synthesis catalyst measured at the Zn K -edge ( $E = 9.659$  keV).

Accordingly, the EXAFS region is characterized by modulations of the absorption coefficient above the absorption edge. The EXAFS function,  $\chi(k)$ , is commonly described as the relative difference between the measured absorption,  $\mu(k)$ , and the atomic absorption,  $\mu_0(k)$ :

$$\chi(k) = \frac{\mu(E) - \mu_0(E)}{\mu_0(E)} \quad (2.8)$$

The atomic absorption is the adsorption of photons of an ideal, single atomic gas without any scattering effects due to nearby atoms. The physical basics behind the EXAFS function are given by a semi-phenomenological expression:

$$\chi(k) = \sum_j^{shells} (A_j(k) \cdot \sin(\delta_j(k))) \quad (2.9)$$

with the amplitude function:

$$A_j(k) = N_j S_0^2 \frac{F_j(k)}{kR_j^2} \exp\left(\frac{-2R_j}{\lambda(k)}\right) \cdot \exp(-2k^2 \sigma_j^2) \quad (2.10)$$

and the phase function:

$$\sin(\delta_j(k)) = \sin((2kR_j + \varphi_j(k))) \quad (2.11)$$

where  $N$  is the number of backscattering atoms of type  $j$  at the distance  $R$  from the absorber atom,  $F(k)$  is the amplitude of the backscattering wave from atom  $j$ ,  $S_0$  is a corrective amplitude reduction factor accounting for multi-body effects,  $k$  is the photoelectron wave number, and  $\lambda$  is the mean free path of the electron.

The impact of local static and thermal disorder of adsorbed and backscattered atom on the EXAFS function is accounted by a specific *Debye-Waller* factor (DWF;  $\sigma^2$ ). Accordingly, temperature dependent EXAFS measurements can provide information on the local vibrational dynamics and the local distortions of solids. Both the backscattering amplitude,  $F_j(k)$ , and the phase shift,  $\delta_j(k)$ , for the absorber-neighbor pair can be extracted from the EXAFS of reference compounds or can be theoretically calculated using *ab-initio* based program codes (e.g. *FEFF* [2.6]). These experimentally or theoretically determined parameters, finally, enable the identification of local environment of the probed element. A *Fourier*-transformation of the EXAFS function corresponds to a (pseudo, non phase shift corrected) radial distribution function (RDF) around the probed element (see Fig. 2-2).

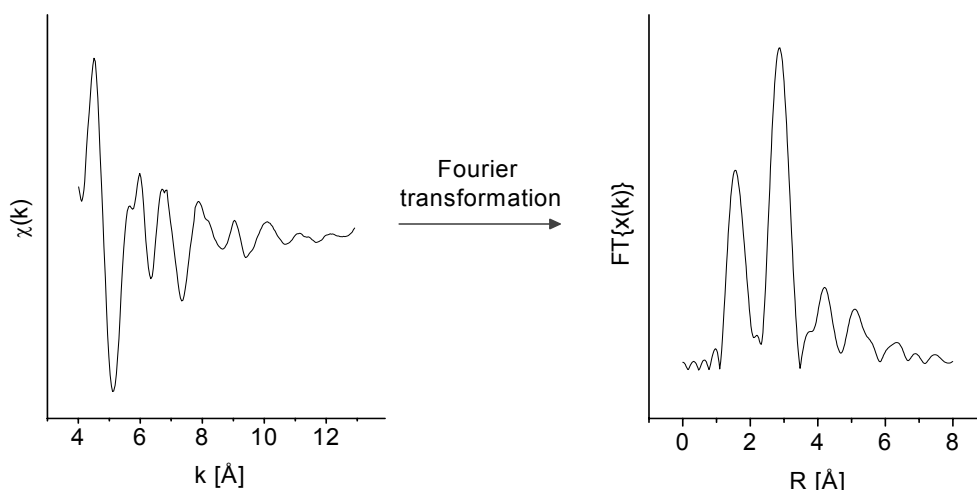


**Fig. 2-3:** Measured EXAFS function,  $\chi(k)$ , of a Cu/ZnO/Al<sub>2</sub>O<sub>3</sub> methanol synthesis catalyst measured at the Zn K-edge (left) and the corresponding pseudo radial distribution function (FT{ $\chi(k)$ }) obtained after Fourier-transformation (right).

In summary, X-ray absorption spectroscopy is an element specific method that provides information regarding the valence, local coordination geometry, number and identity of neighboring atoms of the absorbing atom. Furthermore, the advantage of XAS is that catalysts can be studied under working conditions (*in situ*). Conversely, the application of *in situ* X-ray absorption is limited since the latter provides a bulk average characterization of a catalyst material which is intrinsically non-uniform in particle size, composition and morphology. Additionally, catalysis takes place at the surface of a catalyst which is not (directly) probed by XAS.

### 2.3 *Temperature programmed techniques* [2.7-2.12]

Temperature programmed reduction (TPR) is a convenient technique for the qualitative characterization of supported and non-supported solid oxide catalysts. Generally, TPR is applied for studying the influence of pretreatment procedures during catalyst formulation, the role of support materials, and the application of promoters on the reducibility of metal oxides. Typically, a metal oxide catalyst is subjected to a linear heating rate and reduction is followed by monitoring the corresponding hydrogen uptake from the reducing gas mixture. The information which can be directly gained from TPR measurements includes the overall consumption of hydrogen, the temperature of the maximal reduction rate, and the shape of the TPR profile which qualitatively contains information on the mechanism of the underlying reduction process. The use of conventional linear heating rates in temperature programmed techniques gives rise to non-uniform reaction conditions and, consequently, results in a relatively restricted resolution of the corresponding TPR profile. Furthermore, the shape, temperature of maximal hydrogen consumption and the resolution of TPR profiles are very sensitive towards small variations in experimental parameters employed, i.e. initial amount of reducible species, heating rate, hydrogen concentration, and total flow rate. Accordingly, reaction conditions have to be chosen carefully in order to obtain consistent results within a series of TPR experiments. Similarly to TPR, the oxidation behavior of a catalyst can be studied by means of temperature programmed oxidation (TPO). TPO experiments are commonly employed for studying the oxidation reactivity, for determination of optimal calcination temperatures, and for quantification of carbonaceous deposits on a catalyst surface. Additionally, the latter method is often used complementary to TPR experiments in order to study the reversibility of reduction and re-oxidation cycles of a catalyst.

Kinetic studies of solid state reactions during TPR (TPO) are ordinary performed under either isothermal, at a constant temperature, or under non-isothermal conditions where the temperature is a linear function of the time (constant heating rate). The kinetics of solid state reactions under both isothermal and non-isothermal conditions can be expressed by Equation 2.12:

$$\frac{d\alpha}{dt} = A \cdot \exp\left(-\frac{E_A}{RT}\right) \cdot f(\alpha) \quad (2.12)$$

Here,  $f(\alpha)$  is the reaction model,  $\alpha$  the extent of conversion,  $T$  the temperature,  $t$  the time,  $A$  the pre-exponential factor, and  $E_A$  the activation energy. The function  $f(\alpha)$  represents the mathematical expression of a kinetic model and can be described with a ordinary kinetic power law as  $f(\alpha) = (1-\alpha)^n$ . With dynamic techniques, temperature rate  $dT/dt$  is set to be a constant of the heating rate ( $\beta$ ). Thus, the kinetic equation of non-isothermal heterogeneous reaction is obtained as follows:

$$\frac{d\alpha}{dT} = \frac{A}{\beta} \cdot \exp\left(-\frac{E_A}{RT}\right) \cdot f(\alpha) \quad (2.13)$$

Apparent activation energies can be determined irrespectively of the specific reduction (oxidation) mechanism from the displacement of the maximal temperature ( $T_m$ ) in dependence of different employed heating rates ( $\beta$ ) according to a modified temperature programmed “*Arrhenius* plot” (Eq. 2-14):

$$\frac{d \ln \left( \frac{d\alpha}{dt} \right)}{dT^{-1}} = -\frac{E_A}{R} \quad (2.14)$$

Since reduction (oxidation) is almost not a single step reaction, the effective activation energy computed may vary with the extent of conversion. The behavior originates from complex processes comprising competing and/ or independent reactions during reduction (oxidation). Thus, revealing the dependence of  $E_A$  on  $\alpha$  is sufficient to gain an insight into the reaction mechanism. Model-free isoconversional methods based on the isoconversional principle, which states that the reaction rate at a constant extent of conversion is only a function of the temperature, allow evaluation of *Arrhenius* parameters without choosing a reaction model. From Equation 2.14, the differential isoconversional method of *Friedman* and the integral isoconversional method of *Flynn-Wall-Ozawa* (FWO) can be obtained as Equation 2.15 and Equation 2.16, respectively.

$$\ln \left( \frac{d\alpha}{dt} \right) = \text{const.} - \frac{E_A}{RT} \quad (2.15)$$

$$\ln \beta = \text{const.} - \frac{E_A}{RT} \quad (2.16)$$

These two methods are usually used to calculate activation energy. *Friedman* method is very sensitive to experimental noise, and tends to be numerically unstable because of employing instantaneous rate value. On the other hand FWO method produces a systematic error in  $E_A$  when varies with  $\alpha$ . This error does not appear in *Friedman* method.

## 2.4 **Transmission electron microscopy** [2.13]

In addition to the bulk structural methods, such as XAS and XRD, which yield bulk structural information, electron microscopy is used for investigations of the local elemental composition, structure and morphology of nanoparticles. In transmission electron microscopy (TEM) a primary electron beam of high energy (usually 100 keV to 200 keV) and high intensity passes through a sample while the attenuation of the beam depends on the density and the thickness of the sample investigated. Elastic scattering of electrons by atoms of the sample refract the primary electron beam and, consequently, the diffracted beam intensity increases at the expense of the intensity of the primary electron beam. The fraction of elastically scattered electrons depends on the crystal orientation, the structure, the chemical composition, and structural defects of the sample. Accordingly, the diffracted electrons are used to obtain

structural information. The transmitted electron beam forms an image, which represents a two-dimensional projection of a three-dimensional sample in direction of the electron beam (Fig. 2-4). In addition to the recorded TEM images, the corresponding power spectra (PS) are calculated in order to obtain netplane distances and plane angles for phase identification. The power spectra correspond to the square of the *Fourier*-transform of the image (see Fig. 2-4).

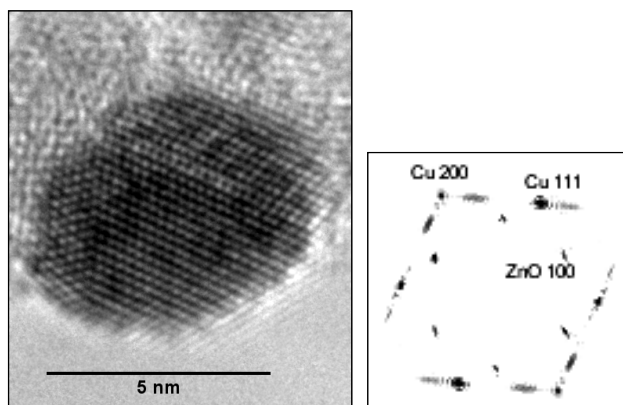


**Fig. 2-4:** High resolution transmission electron microscopic image of a Cu particle (left) and the corresponding power spectrum (right).

Inelastic scattering during penetration of electron beam through the sample can result in absorption phenomena (i.e. X-ray fluorescence) which can be used for element analysis. Due to the relatively small mean free path length of the electrons the technique has to be operated under vacuum condition ( $p \approx 10^{-6}$  mbar). Thus, TEM is not a technique which can be intrinsically used for *in situ* investigation of catalysts.

## 2.5 References cited

- [2.1] B.E. Warren, X-ray Diffraction, Dover Publications, New York (1990) pp. 275.
- [2.2] J.W. Niemantsverdriet, Spectroscopy in Catalysis, 2<sup>nd</sup> edition, Wiley-VCH, Weinheim, New York, Chichester, Brisbane, Singapore, Toronto (2000) pp. 137.
- [2-3] E.A. Stern, Theory of EXAFS, X-ray Absorption, Principles Applications, Techniques of EXAFS, SEXAFS and XANES, Editors: D.C. Koningsberger, R. Prins, John Wiley & Sons, New York Chichester, Brisbane, Toronto, Singapore (1988) pp. 3.
- [2.4] D.C. Koningsberger, B.L. Mojet, G.E. van Dorssen, and D. E. Ramaker, Topics Catal., 10 (2000), 143.
- [2-5] F. de Groot, Chem. Rev., 101 (2001) 1779.
- [2.6] A.L. Ankudinov, B. Ravel, J.J. Rehr, S.D. Conradson, Phys. Rev. B, 58 (1998) 7565.
- [2.7] H.L. Friedman, J. Polym. Sci. Part C, 6 (1963) 183.
- [2.8] T. Ozawa, Bull. Chem. Soc. Jpn., 38 (1965) 1881.
- [2.9] J.H. Flynn and L.A. Wall, J. Polym. Sci. Part B, 4 (1966) 323.
- [2.10] O.J. Wimmers, P. Arnoldy, J.A. Moulin, J. Phys. Chem., 90 (1986) 1331.
- [2.11] S. Vyazovkin, J. Comput. Chem., 22 (2001) 178.

- 
- [2.12] H. Knözinger, Temperature programmed reduction, Handbook of Heterogeneous Catalysis; Editors: G. Ertl, H. Knözinger, J. Weitkamp, VCH Weinheim (2008) Part 2, pp. 1080.
- [2.13] J.W. Niemantsverdriet, Spectroscopy in Catalysis, 2<sup>nd</sup> edition, Wiley-VCH, Weinheim, New York, Chichester, Brisbane, Singapore, Toronto (2000) pp. 169.

## Chapter Three

### Role of Defects in Cu/ZnO/Al<sub>2</sub>O<sub>3</sub> Catalysts for Methanol Steam Reforming

#### 3.1 Introduction

Cu catalysts supported on ZnO-Al<sub>2</sub>O<sub>3</sub> mixed oxides are known to be active in methanol steam reforming (MSR). Methanol, as a chemical carrier of hydrogen to be applied in fuel cells is a promising alternative for petroleum based fuels [3.1]. Especially low temperature fuel cells such as proton exchange membrane (PEM) fuel cells for small scale applications impose high purity requirements of the hydrogen since the electrodes are very sensitive to poisoning by several contaminants (CO, sulfur) [3.2, 3.3]. Integration of a supported membrane with a steam reformer exhibits considerable promise for generating high purity hydrogen [3.4]. Desired Cu/ZnO/Al<sub>2</sub>O<sub>3</sub> steam reforming catalysts combine high activity with high selectivity towards hydrogen even at moderate temperatures (473 K - 573 K). Moreover, they show a suitable chemical and thermal stability under MSR reaction conditions. In order to elucidate synthesis pathways to the active “real” structure, a fundamental understanding of the relation between both bulk and surface structure and the catalytic performance is required (structure - activity relationship).

It is generally accepted that a high copper surface area is a prerequisite for superior Cu/ZnO/Al<sub>2</sub>O<sub>3</sub> catalysts in methanol chemistry. Deviations from a linear correlation between the overall copper metal surface area and the catalytic activity have been frequently reported in the recent literature on Cu based Zn-, Al-oxides [3.5-3.9]. Hence, additional parameters such as geometric and electronic defects on the surface and in the bulk also determine the catalytic performance of copper catalysts in methanol chemistry. Recently it was shown that methanol steam reforming activities of binary Cu/ZnO model catalysts with varying molar ratios of the metals correlate with lattice strain in the copper particles [3.6, 3.10]. Ultraviolet photoelectron spectroscopy (UPS) investigations on thin copper films on silicon model systems revealed that thermally induced strain influences the Cu d band and, hence, the electronic structure of the surface [3.11]. Moreover, microstructural investigations of Cu/ZnO model catalysts for MSR by *in situ* XRD, *in situ* XAS, <sup>63</sup>Cu-NMR as well as HRTEM revealed a positive correlation between strained copper particles and a homogeneous microstructure of the final catalyst. The characteristic defect structure is accompanied by an improved catalytic performance in steam reforming of methanol [3.12-



3.14]. Lattice strain in the copper phase as the result of an intimate Cu-ZnO interface is an indicator of a homogeneous microstructure of superior Cu/ZnO model catalysts [3.13].

The more complex ternary Cu/ZnO/Al<sub>2</sub>O<sub>3</sub> catalysts are currently industrially established for low pressure and temperature regimes in methanol chemistry (steam reforming, synthesis) and in the water-gas-shift (WGS) reaction. The solid-state chemistry of the preparation and structure - activity correlations are highly complex. Compared to the role of ZnO as a structural promoter in Cu/ZnO/Al<sub>2</sub>O<sub>3</sub> catalysts [3.12-3.21], alumina is known to inhibit thermal sintering of metal particles and, therefore, imparts chemical and thermal stability required for an industrially used catalyst [3.22-3.24]. The precursor preparation is governing the electronic and structural properties of the final copper catalyst ("chemical memory" effect [3.25]). Here, the microstructural and catalytic characteristics of various laboratory prepared ternary Cu/ZnO/Al<sub>2</sub>O<sub>3</sub> catalysts under MSR conditions were presented. A commercial CuO/ZnO/Al<sub>2</sub>O<sub>3</sub> methanol synthesis catalyst was employed for comparison. Complementary *in situ* bulk techniques, X-ray diffraction (XRD), and X-ray absorption spectroscopy (XAS), were used for bulk structural investigations of Cu/ZnO/Al<sub>2</sub>O<sub>3</sub> catalysts under working conditions in methanol steam reforming. Additionally, microscopic and morphological characteristics of the local structure were examined by electron microscopy (TEM).

## 3.2 *Experimental*

### 3.2.1 Sample preparation

Various (Cu,Zn,Al)- mixed oxide precursors (CZA) were prepared on a laboratory scale according to patented procedures. Hydroxycarbonates were precipitated from metal nitrate solutions and subsequently washed, dried and calcined. All chemicals employed were obtained from *Fluka Chemicals* and were used without further purification.

CZA-1: A commercial Cu/ZnO/Al<sub>2</sub>O<sub>3</sub> catalyst for methanol synthesis provided by *Süd-Chemie AG* was employed as reference.

CZA-2: 3600 g Cu(NO<sub>3</sub>)<sub>2</sub>·3H<sub>2</sub>O, 733 g Zn(NO<sub>3</sub>)<sub>2</sub>·6H<sub>2</sub>O and 2089 g Al(NO<sub>3</sub>)<sub>3</sub>·9H<sub>2</sub>O were dissolved in 15 L of deionized water. A solution of 2500 g (NH<sub>4</sub>)<sub>2</sub>CO<sub>3</sub> in 63.5 L deionized water was employed as precipitation reagent. The precipitation process occurred at 303 K under vigorous stirring (dosing rate: 2.2 L·min<sup>-1</sup>). The entire basic solution was added in about 30 min and the final pH-value of the suspension was adjusted to 6.8 ± 0.1. The precipitate was aged in the mother liquid for 2 h, filtered off, washed, and dried in a drying oven at 393 K for 36 h. Finally, the precursor material was calcined at 673 K for 2h [3.26].

CZA-3: The preparation sequence used was similar to that of sample CZA-2 (precipitating, washing, calcination). Unlike sample CZA-2, a different drying procedure was applied (spray-drying of a 5 wt.-% suspension).

CZA-4: 5.8 g Cu(NO<sub>3</sub>)<sub>2</sub>·3H<sub>2</sub>O, 1 g Zn(NO<sub>3</sub>)<sub>2</sub>·6H<sub>2</sub>O and 3.53 g Al(NO<sub>3</sub>)<sub>3</sub>·9H<sub>2</sub>O were dissolved in 1 L of deionized water. A premixed solution of 53 g Na<sub>2</sub>CO<sub>3</sub> in 1 L deionized water was added under

vigorous stirring at ambient temperature (dosing rate: 2.5 L·min<sup>-1</sup>). The resulting precipitate was repeatedly washed to remove sodium ions. The solid phase was recovered by filtration, dried at 353 K for 12 h, and finally calcined at 573 K for 1 hour [3.27].

CZA-5 and CZA-6: Additionally, sample CZA-4 was 45 times (CZA-5) and 225 times (CZA-6) up scaled.

The amount of copper, zinc, and aluminum in the prepared catalysts was determined by X-ray fluorescence analysis (XRF). About 50 mg of calcined catalyst was used in the analysis of each sample. The accuracy obtained was estimated to be  $\pm 1\%$ .

### 3.2.2 Activity screening and Cu surface area determination

In order to achieve comparable reaction conditions for all CZA catalysts a standard procedure of catalyst handling was applied. An amount of 300 mg of a homogeneous mixture (sieve fraction 300  $\mu\text{m}$  to 450  $\mu\text{m}$ ) of 50 mg of the CZA catalyst and 250 mg of hexagonal boron nitride (BN, *Alfa Aesar*) was placed into a fixed-bed micro reactor consisting of a quartz tube (7 mm i.d.) with a thermocouple located in the catalyst bed. The activity measurements were conducted in the following sequence for all CZA catalysts. Prior to each experiment the catalyst was activated by heating in 5 vol.-% H<sub>2</sub> in He with a total flow of 80 ml·min<sup>-1</sup> to 523 K and with a temperature ramp of 6 K·min<sup>-1</sup> and an isothermal period of 1 h at 523 K before cooling down to room temperature. Methanol and water were supplied by saturating He carries in two sets of saturators ( $T_{\text{Saturator}} = 298 \text{ K}$ ). The reactor feed contained 3.5 vol.-% water, 3.5 vol.-% methanol, and balance helium. Total flow was kept at 100 ml·min<sup>-1</sup> by mass flow controllers. Steady state activities were determined at 523 K (heating rate: 6 K·min<sup>-1</sup>) by on-line GC analysis (*Varian MicroGC 4900*) equipped with a TCD detector using a PPU column and a Molsieve 5 Å column for separating polar products, such as water, methanol and CO<sub>2</sub> and the gaseous products, such as H<sub>2</sub>, He, and CO, respectively. A blank run conducted with an empty reactor did not show any detectable activity. Selectivity's were calculated at the basis of carbon.

The specific Cu<sup>0</sup> surface area of the catalysts was measured by the dissociative chemisorption of nitrous oxide (N<sub>2</sub>O-RFC [3.28]). The experiments were performed in quartz micro-reactor at 303 K to avoid subsurface oxidation [3.29]. Prior to each experiment the catalysts were reduced in 5 vol.-% H<sub>2</sub> (He) at 523 K. Subsequently, the reactor was purged for 1 hour with He and cooled down to ambient temperature to achieve an adsorbate-free reduced Cu surface. The measurement was started by switching from pure He to 1 vol.-% N<sub>2</sub>O in He (*Messer Griesheim*) by means of a four way valve. The evolved gas atmosphere was monitored using a quadrupole mass spectrometer (*OMNISTAR, Pfeiffer*). The amount of nitrogen formed was quantified from the time interval of the frontal chromatogram of N<sub>2</sub> (i.e. the time interval between the onset of appearance of N<sub>2</sub> and the breakthrough of N<sub>2</sub>O). The Cu surface area was calculated assuming a molar stoichiometry of Cu<sub>s</sub>/N<sub>2</sub> = 2 and a value of 1.46·10<sup>-19</sup> copper atoms m<sup>-2</sup> [3.30].

### 3.2.3 Temperature programmed reduction

Temperature programmed reduction (TPR) studies have been conducted on a TPD/R/O 1100 instrument (*CEInstruments*). TPR studies were carried out by passing 5 vol.-% H<sub>2</sub> (Ar) at a total flow of 80 ml·min<sup>-1</sup> over 40 mg of the catalyst sample contained in a quartz tube. The temperature was increased to 523 K with a linear heating ramp of 6 K·min<sup>-1</sup> and maintained isothermal at 523 K for 1 h. Hydrogen consumption was calculated quantitatively from the integrated TPR signal, calibrated with CuO (*Sigma Aldrich*) as a standard. The TPR studies were performed according to the criterion of *Monti & Baiker* [3.31] and *Maleta & Caballero* [3.32]. Prior to a measurement the sample was purged in an argon flow (10 ml·min<sup>-1</sup>) up to 423 K to ensure an adsorbate-free Cu surface of the corresponding Cu/ZnO/Al<sub>2</sub>O<sub>3</sub> catalysts.

### 3.2.4 Transmission electron microscopy

Immediate transfer of the reduced Cu/ZnO/Al<sub>2</sub>O<sub>3</sub> catalyst (see chapter 3.2.3) into a glove box prevented exposure to air. Afterwards, the samples were dispersed in acetone and deposited on a vacuum transfer sample holder. High resolution transmission electron microscopy (HRTEM) experiments of the reduced catalysts were performed on a *Philips* CM 200 FEG microscope equipped with a *Gatan* imaging filter operating at 200 kV ( $C_s = 1.35$  mm). The information limit was better than 0.18 nm. The experimental micrographs were digitalized using a CCD camera. In addition to the computed images, selected areas were processed to obtain their power spectra (PS) which is the square of the *Fourier*-transform of the image. The power spectra were used for measuring netplane distances ( $\pm 0.5$  %) and angles ( $\pm 0.5$  degree) for phase identification. Since the electron beam is capable to introduce irreversible structural changes in especially small particles, they have never been irradiated for longer than 3 min - the time required to record a series of HRTEM images.

### 3.2.5 *In situ* X-ray diffraction

*In situ* X-ray diffraction (XRD) experiments were performed on a *STOE* Theta/Theta diffractometer (Cu-K $\alpha$  radiation, secondary monochromator, scintillation counter) operating at 50 kV and 30 mA in a reflection scan mode. The diffractometer was equipped with a *Paar* XRK 900 high temperature cell. 80 mg of the calcined catalyst precursor were used for *in situ* measurements. XRD patterns were recorded at 523 K in reducing atmosphere (5 vol.-% H<sub>2</sub>) and under MSR conditions (3.5 vol.-% methanol, 3.5 vol.-% water). XRD pattern were measured in the 2 $\theta$  range from 10 ° to 100 ° with a step size of 0.04 ° and a time/step of 2 s. The gases were pre-mixed by mass flow controllers and introduced in the reaction cell with a total flow of 150 ml·min<sup>-1</sup>. The gas phase composition was monitored using a *Pfeiffer* quadrupole mass spectrometer (*OMNISTAR*).

Microstructural changes of the Cu/ZnO/Al<sub>2</sub>O<sub>3</sub> catalyst under working conditions were elucidated by a detailed line profile analysis of the corresponding X-ray diffraction patterns. With a sum of pseudo-

*Voigt*-profile functions and an appropriate background function (polynomial 3<sup>rd</sup> degree) X-ray diffraction pattern were refined [3.33]. Diffraction line profile analysis was conducted by means of the integral breath method for size and lattice strain (*Pawley* method). This is reasonable because trends in microstructural changes can be identified by comparing a series of similar treated catalysts [3.34]. Refined parameters were lattice constants, peak intensities, *Lorentzian* and *Gaussian* parts of the profile of each individual *hkl* line, a linear zero shift in the  $2\theta$  scale and four coefficients for the background polynomial. A correction for instrumental broadening was omitted because the full width at half maximum (FWHM) of each peak was more than ten times the instrumental broadening.

### 3.2.6 *In situ* X-ray absorption spectroscopy

*In situ* X-ray absorption spectroscopy (XAS) experiments were performed at the Hamburg synchrotron radiation laboratory, HASYLAB, at beamline X1 (Germany) at the Cu K -edge ( $E = 8979$  eV) and the Zn K -edge ( $E = 9659$  eV) in the transmission mode. 3 mg of the catalyst precursor and 30 mg BN (< 325 mesh, *Alfa Aesar*) were physically mixed and pressed at a force of 1 ton into a pellet with 5 mm in diameter. The amount of material in the pellets was calculated to yield an absorber optical thickness of about 1.5 absorption lengths. Temperature programmed reduction (TPR) runs were performed with 5 vol.-% H<sub>2</sub> (He) at a flow of 10 ml·min<sup>-1</sup> by heating linearly to 523 K with a ramp of 5 K·min<sup>-1</sup>, and an isothermal period at 523 K of 1 h. Catalytic activity in methanol steam reforming was determined as described above. The gas phase composition was analyzed by mass spectrometry (*OMNISTAR*, *Pfeiffer*). Analysis of the XAS spectra was performed with the software package *WinXAS 3.1* [3.35]. A general data analysis procedure of the measured absorption spectra consists of energy calibration according to a copper reference foil, background subtraction by using two polynomials, and normalization. After transformation into the  $k$  space, an atomic background  $\mu_0(k)$  was determined using a cubic spline function. The radial distribution function (RDF) was obtained by *Fourier*- transformation of the  $k^3$  weighted experimental spectrum  $\chi(k)$  ( $k$  range from 3 Å<sup>-1</sup> to 13 Å<sup>-1</sup> for Cu K -edge and from 3 Å<sup>-1</sup> to 11.9 Å<sup>-1</sup> for Zn K -edge) multiplied by a Bessel window into the  $R$  space. Theoretical backscattering phases and amplitudes for single and multiple scattering paths were calculated up to 6 Å for cubic Cu metal, monoclinic CuO, and hexagonal ZnO using the *ab-initio* multiple-scattering code *FEFF 7* [3.36]. Refinement of the Cu, CuO, and ZnO model structure to the experimental EXAFS spectrum by a least-squares method was conducted in the  $R$  space. Structural parameters refined were the single scattering shell distances ( $R$ ), the *Debye-Waller* factors of the single scattering paths ( $\sigma^2$ ), and one overall  $E_0$  shift. The coordination numbers (CN) were kept invariant because of the rather large Cu, CuO, and ZnO crystallite sizes, respectively.

### 3.3 Results

#### 3.3.1 Catalytic activity in methanol steam reforming

The steady state activities measured for all catalysts in MSR are summarized in Table 3-1. Steam reforming of methanol over Cu/ZnO/Al<sub>2</sub>O<sub>3</sub> catalysts resulted in the formation of hydrogen and carbon dioxide in a ratio of 3 to 1 under the experimental conditions used. CO was most likely produced by reverse WGS reaction [3.37]. Other by-products such as formaldehyde, formic acid, methyl formate, and dimethyl ether formed during reaction of methanol on Cu/ZnO/Al<sub>2</sub>O<sub>3</sub> catalysts could not be detected under the reaction conditions applied [3.38]. The trends in activity measured in the micro-reactor were also reflected in the *in situ* experiments (Fig. 3-1). For comparison, the methanol conversion was determined for all experiments at constant reaction temperature (523 K) and similar space velocities ( $WHSV_{MeOH} = [86-96] s^{-1}$ ). Overall methanol conversions determined in the *in situ* cells were approximately 5 % to 10 % for the *in situ* XAS experiments and 15 % to 30 % for the *in situ* XRD experiments. The equilibrium conversion of methanol in MSR calculated according to Hess's law from the standard formation enthalpies and entropies of the involved substances [3.39] under the conditions employed amounts to  $X^{Equilibrium} = 98.8 \%$ . The *in situ* measurements were performed under differential conditions in the kinetically controlled regime. Thus, it can be concluded that the *in situ* experiments permit deducing reliable structure activity relationships.

**Table 3-1:** Methanol conversion and product composition for methanol steam reforming over various Cu/ZnO/Al<sub>2</sub>O<sub>3</sub> (CZA) catalysts determined in a fixed-bed reactor (reaction temperature 523 K; ambient pressure; catalyst mass 0.05 g; total gas flow rate 100 ml·min<sup>-1</sup>; feed concentration: 3.5 vol.-% CH<sub>3</sub>OH + 3.5 vol.-% H<sub>2</sub>O).

| sample       | X(MeOH)<br>[%] | Product composition [%] |                |      | H <sub>2</sub> production rate<br>[ $\mu mol s^{-1} m_{Cu}^{-2}$ ] |
|--------------|----------------|-------------------------|----------------|------|--|
|              |                | CO <sub>2</sub>         | H <sub>2</sub> | CO   |  |
| <b>CZA-1</b> | 84.4           | 24.67                   | 75.23          | 0.11 | 130  |
| <b>CZA-2</b> | 43.4           | 24.90                   | 75.02          | 0.08 | 204  |
| <b>CZA-3</b> | 59.5           | 25.02                   | 74.90          | 0.08 | 166  |
| <b>CZA-4</b> | 57.8           | 24.95                   | 74.92          | 0.13 | 176  |
| <b>CZA-5</b> | 25.4           | 24.91                   | 74.97          | 0.13 | 142  |
| <b>CZA-6</b> | 16.2           | 25.82                   | 74.07          | 0.10 | 74   |

The catalytic activity measured was mainly determined by the specific copper surface area. For the catalysts studied, hydrogen production rate per gram catalyst appeared to increase with the Cu surface area (see Fig. 3-2). Best performance in MSR in terms of methanol conversion was determined for CZA-1 exhibiting the highest overall Cu surface area and highest Cu dispersion (Table 3-3). Contrarily, this

sample did not exhibit the highest intrinsic activity in MSR reaction. The intrinsic activity, the H<sub>2</sub> production rate per  $m_{\text{Cu}}^2$ , of sample CZA-1 was roughly half of sample CZA-2 (see Table 3-1). The lowest activity was determined for the sample CZA-6 ( $5.7 m_{\text{Cu}}^2 \cdot \text{g}_{\text{cat}}^{-1}$ ). Interestingly, this catalyst exhibited a similar Cu surface area than the much more active catalyst CZA-2 (see Fig. 3-2). The activity of sample CZA-2 was roughly three times in activity of CZA-6 (Table 3-1).

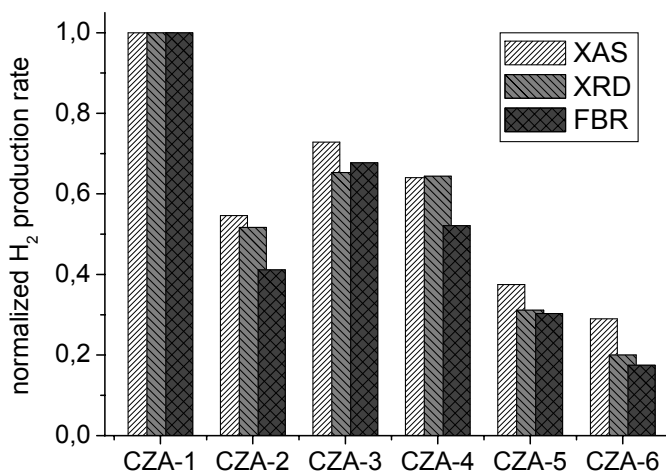


**Fig. 3-1:** Comparison of the normalized H<sub>2</sub> production rates obtained from in situ experiments (XRD, XAS) and measured in a fixed bed micro-reactor (FBR) at 523 K,  $\text{WHSV}_{\text{MeOH}} = (86-96) \text{ s}^{-1}$ .

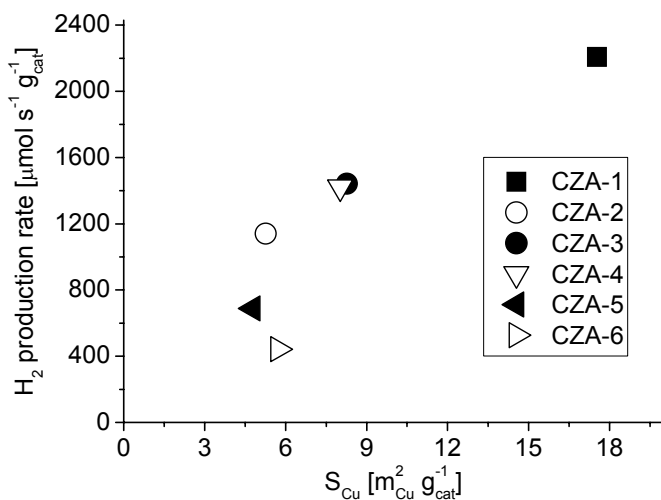


**Fig. 3-2:** H<sub>2</sub> production rate obtained in a fixed-bed reactor in dependence on the specific copper surface area determined by N<sub>2</sub>O surface titration (RFC).

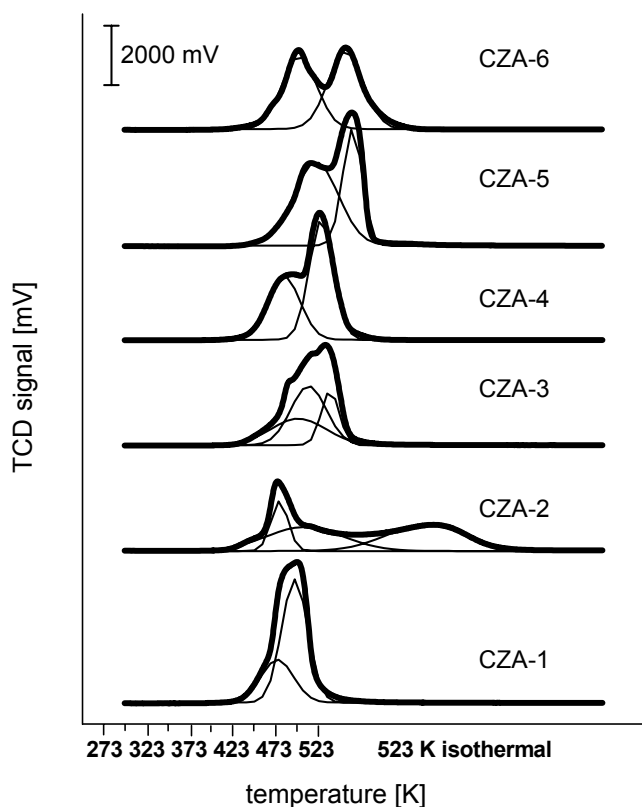


**Fig. 3-3:** Hydrogen consumption during temperature programmed reduction (TPR) of the CZA catalysts. Bold lines are experimental curves and thin lines are deconvoluted curves.

### 3.3.2 General characterization of Cu/ZnO/Al<sub>2</sub>O<sub>3</sub> catalysts

The bulk metal compositions of all investigated catalysts examined by X-ray fluorescence spectroscopy (XRF) are given in Table 3-2. Different Zn and Al contents were found for the various CZA catalysts whereas the copper loadings {(62-65) wt.-%} were relatively similar. The overall Cu to Zn ratio in the catalysts investigated has been confirmed by XAS (see Table 3-2). Fig. 3-3 compares the hydrogen consumption profiles during temperature programmed reduction (TPR) of the CuO/ZnO/Al<sub>2</sub>O<sub>3</sub> precursors. All investigated oxide precursors showed an onset of reduction between 423 K and 453 K. The maxima of the reduction peaks obtained were located at about 483 K to 523 K (Fig. 3-3). Pure CuO was reduced at considerable higher temperature (563 K). Pure ZnO and alumina are not reduced under these conditions [3.40]. The reduction of CZA-1 was completed at the lowest reduction temperature of all catalysts studied. The characteristic TPR profile and the peak maximum temperature of 498 K indicate a homogeneous size distribution of CuO particles present in that sample. This result correlates well with the measured specific Cu<sup>0</sup> surface area, where the highest dispersion was found for the CZA-1 catalyst (Table 3-3). A very different behavior was found for the other catalysts. The TPR profiles of CZA 2–6 were considerable broader and shifted to higher reduction temperatures. Moreover, the reduction profiles of

CZA 2, CZA 4-6 showed two or even three regions of reduction. While a small reduction peak was observed at a similar temperature as for sample CZA-1 - with the maximum between 483 K and 498 K - most of the reduction occurred during the isothermal period of the reduction at 523 K (see Fig. 3-3).

**Table 3-2:** Metal composition of the investigated CZA catalysts determined by X-ray fluorescence analysis (XRF) and Cu to Zn ratio determined from the edge jump at the Cu K and the Zn K -edge (XAS).

| sample | Cu [wt.-%] | Zn [wt.-%] | Al [wt.-%] | Cu/ Zn ratio <sup>a</sup> | Cu/ Zn ratio <sup>b</sup> |
|--------|------------|------------|------------|---------------------------|---------------------------|
| CZA-1  | 61.7       | 29.7       | 8.6        | 2.08                      | 2.35                      |
| CZA-2  | 65.1       | 18.0       | 16.7       | 3.62                      | 3.57                      |
| CZA-3  | 64.5       | 17.1       | 18.4       | 3.77                      | 3.80                      |
| CZA-4  | 62.5       | 17.2       | 20.3       | 3.64                      | 3.64                      |
| CZA-5  | 62.3       | 14.8       | 22.9       | 4.21                      | 4.18                      |
| CZA-6  | 65.0       | 10.6       | 24.4       | 6.13                      | 6.05                      |

<sup>a</sup> determined from XRF

<sup>b</sup> determined from XAS

**Table 3-3:** Specific Cu surface area determined by N<sub>2</sub>O frontal chromatography (RFC) and bulk structural characteristics of the reduced Cu/ZnO/Al<sub>2</sub>O<sub>3</sub> catalysts determined by XRD: Cu crystallite size, Cu lattice strain, and Cu dispersion.

| sample | Cu surface area [m <sup>2</sup> ·g <sup>-1</sup> ] <sup>a</sup> | Cu crystallite size [Å] <sup>b</sup> | Cu surface area [m <sup>2</sup> ·g <sup>-1</sup> ] <sup>b, c</sup> | Cu lattice strain [%] <sup>b</sup> | Cu dispersion [%] |
|--------|---|--------------------------------------|--|------------------------------------|-------------------|
| CZA-1  | 17.5 ± 2.1  | 51                                   | 17.2   | 0.39                               | 4.9               |
| CZA-2  | 5.3 ± 0.7   | 45                                   | 20.1   | -                                  | 1.5               |
| CZA-3  | 8.3 ± 1.1   | 54                                   | 16.4   | -                                  | 2.4               |
| CZA-4  | 8.0 ± 0.8   | 65                                   | 17.9   | -                                  | 1.8               |
| CZA-5  | 4.8 ± 0.6   | 73                                   | 14.5   | -                                  | 1.1               |
| CZA-6  | 5.7 ± 0.8   | 77                                   | 14.4   | -                                  | 1.4               |

<sup>a</sup> determined by N<sub>2</sub>O chemisorption (RFC).

<sup>b</sup> calculated from XRD pattern line broadening of most prominent Cu (111) reflection.

<sup>c</sup> calculated assuming hemisphere-like Cu particles on the surface.

Fig. 3-4 shows transmission electron micrographs of the Cu/ZnO/Al<sub>2</sub>O<sub>3</sub> catalysts obtained after reduction in hydrogen. Electron energy loss spectroscopy (EELS) identified only metallic Cu as copper phase in all samples studied. However, HRTEM analysis of selected areas evidenced the presence of minute amounts of Cu<sub>2</sub>O, brass, ZnO<sub>1-x</sub> and amorphous materials in addition to the main phases: Cu and ZnO. Aluminum was hardly detected and mainly found as amorphous phase. In rare cases Al has been



identified as crystalline  $\alpha$ -Al<sub>2</sub>O<sub>3</sub> by HRTEM. Various morphologies of Cu particles were detected for the Cu/ZnO/Al<sub>2</sub>O<sub>3</sub> catalysts, such as round and irregular shaped Cu particles (plates, needles). In contrast to sample CZA-1, large copper particles (up to 150 nm i.d.) were found for samples CZA 2-6 catalysts. Additionally, the latter samples exhibited inhomogeneous particle shapes which tended to agglomerate forming distinct plate- and needle-like structures (see Fig. 3-4 a-f).

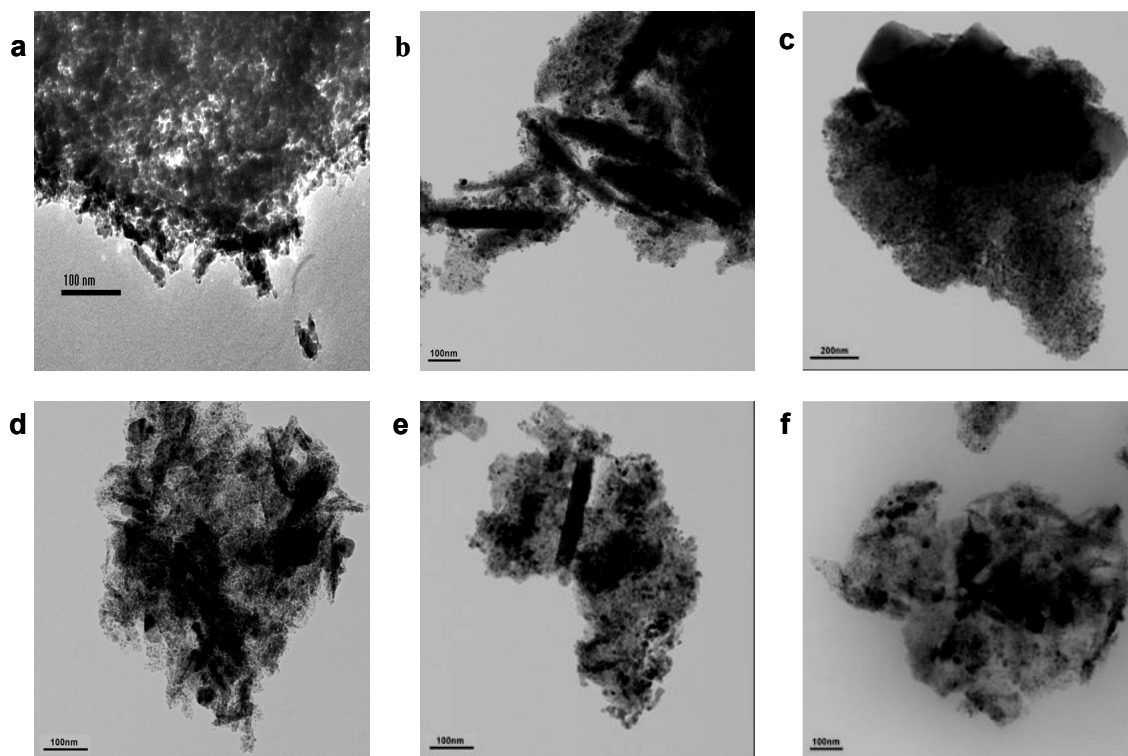


**Fig. 3-4:** Bright field transmission electron micrographs of the in hydrogen activated Cu/ZnO/Al<sub>2</sub>O<sub>3</sub> catalysts: (a) CZA-1, (b) CZA-2, (c) CZA-3, (d) CZA-4, (e) CZA-5, and (f) CZA-6.

High resolution electron micrographs of a “good” (CZA-1) as well as of a “very poor” catalyst (CZA-5) obtained after reduction are depicted in Fig. 3-5. The HRTEM images of the CZA-1 catalyst exhibited a marked interface between the Cu and ZnO particles. The majority of Cu particles were round-shaped and the surfaces of the metal particles were typically covered with smaller ZnO particles (see Fig. 3-5). Additionally, the Cu particles were relatively homogeneous, small-sized, and exhibited a Gaussian like size distribution with a mean diameter of 8 nm (Fig. 3-5c). Conversely, a detailed particle size analysis of sample CZA-5 exhibited a broad log-normal distribution of relatively small (5 nm to 25 nm i.d.) as well as very large (> 40 nm i.d.) Cu particles (see Fig. 3-5d). This distinct bimodal particle size distribution was in accordance with TPR results where two pronounced reduction events have been observed (see Fig. 3-3). Typically for that sample, small rounded Cu particles were embedded in an amorphous matrix (see Fig. 3-5). Sintering of Cu particles in various orientations resulted in dislocations at the interface (indicated with an arrow in Fig. 3-5b). A characteristic Cu-ZnO interface, such as that found in the CZA-1 catalyst (Fig. 3-5a), was not detected in the CZA-5 catalyst.

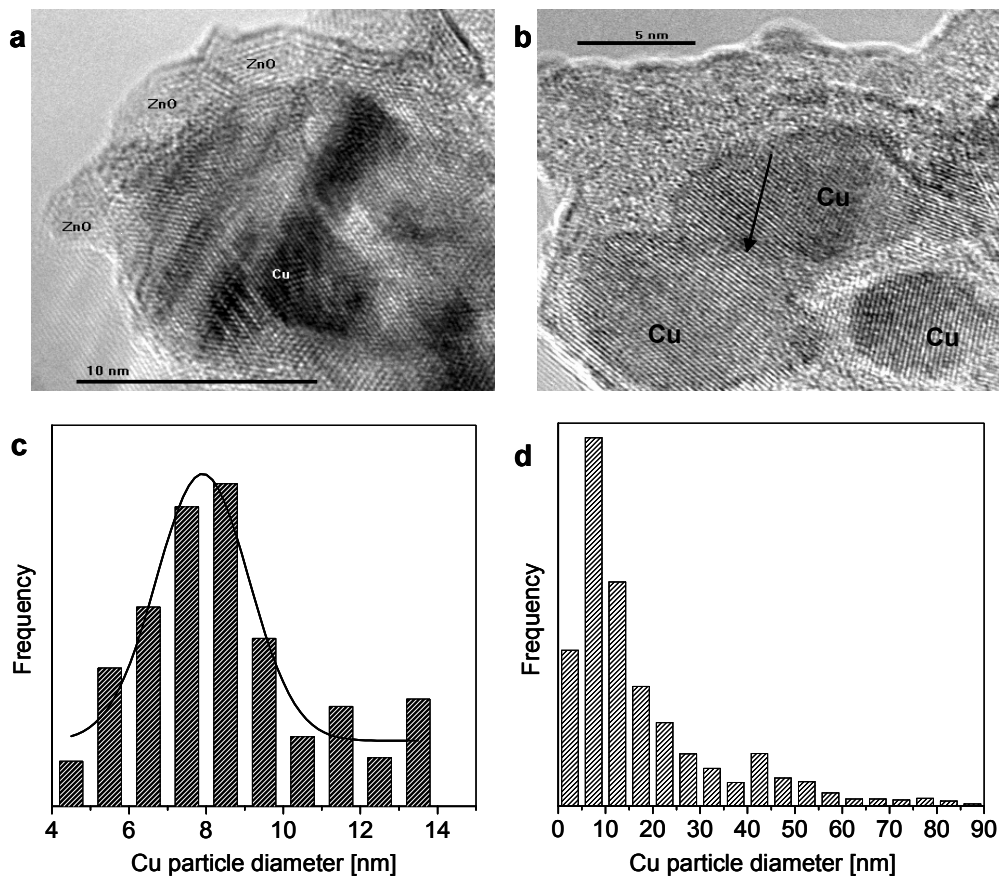


**Fig. 3-5:** Characteristic high resolution electron micrograph (scale bars: 10 nm and 5 nm) and detailed Cu particle size distribution obtained for the activated (reduced) Cu/ZnO/Al<sub>2</sub>O<sub>3</sub> catalysts: CZA-1 (a and c) and CZA-5 (b and d).

**Table 3-4:** Comparison of Cu lattice constant  $a$  (*in situ* XRD), Cu K-edge position  $E_0$ , Cu-Cu distance  $R$ , and the *Debye Waller* factor ( $\sigma_{Cu}^2$ ) obtained from fitting theoretical *fcc* Cu to the experimental EXAFS of the 1<sup>st</sup> Cu-Cu shell (*in situ* XAS) measured under working conditions (MSR feed, 523 K).

| Sample | $a_{Cu}$ XRD [ $\text{\AA}$ ] <sup>a</sup> | $E_0$ [keV] <sup>b</sup> | $R$ 1 <sup>st</sup> Cu-Cu [ $\text{\AA}$ ] | $\sigma^2$ 1 <sup>st</sup> Cu-Cu [ $\text{\AA}^2$ ] |
|--------|--|--------------------------|--|---|
| CZA-1  | 3.615                                      | 8.978(7)                 | 2.53                                       | 0.0170  |
| CZA-2  | 3.615                                      | 8.978(7)                 | 2.54                                       | 0.0176  |
| CZA-3  | 3.615                                      | 8.978(6)                 | 2.53                                       | 0.0168  |
| CZA-4  | 3.615                                      | 8.978(6)                 | 2.53                                       | 0.0199  |
| CZA-5  | 3.614                                      | 8.978(7)                 | 2.54                                       | 0.0187  |
| CZA-6  | 3.615                                      | 8.978(8)                 | 2.53                                       | 0.0184  |

<sup>a</sup>  $a(\text{Cu}_{fcc}) = 3.615 \text{ \AA}$  (ICDD-PDF 4-836).

<sup>b</sup> Energy offset determined as the position of the inflection point of the continuum.

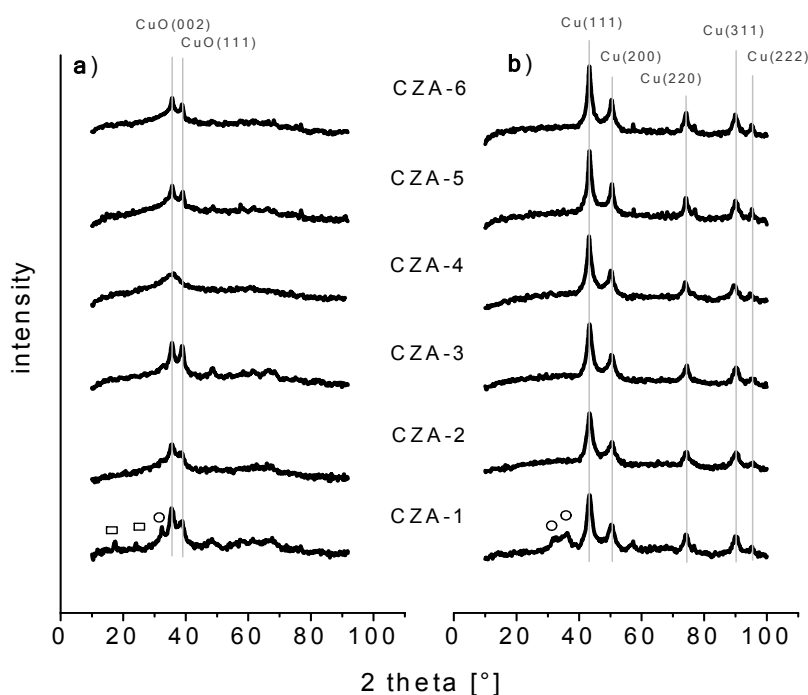


**Fig. 3-6:** *In situ* powder X-ray diffraction patterns recorded at ambient temperature of the (a) calcined precursors, and (b) of the reduced catalysts ( $\circ$  ZnO;  $\square$  Malachite  $\{\text{Cu}_2\text{CO}_3(\text{OH})_2\}$ ).

### 3.3.3 Bulk structural *in situ* investigations

The bulk structure of copper in the various ternary Cu/ZnO/Al<sub>2</sub>O<sub>3</sub> catalysts was studied under reduction and steam reforming conditions by *in situ* XRD. The XRD powder patterns of the calcined precursors are depicted in Fig. 3-6a. All precursors showed broad diffraction lines corresponding to monoclinic CuO (ICDD-PDF 45-937). ZnO appeared to be almost X-ray amorphous. Only for the sample CZA-1 diffraction lines of ZnO (ICDD-PDF 36-1451) were present. For samples CZA 2-6 there was an increased background in the  $2\theta$  region between  $30^\circ$  to  $37^\circ$  which indicates the presence of either highly nano-crystalline or X-ray amorphous ZnO (Fig. 3-6a). A crystalline Malachite like phase ( $\text{Cu}_2\text{CO}_3(\text{OH})_2$ ; ICDD-PDF 41-1390) was clearly observed for sample CZA-1 at lower  $2\theta$  angles (see Fig. 3-6a). On-line MS analysis of the evolved gas atmosphere during the reduction of the calcined precursors revealed that the oxide precursors of samples CZA 2-6 also contained residual  $\text{OH}^-$  and  $\text{CO}_3^{2-}$ . In contrast to CZA-1, the corresponding components appeared to be X-ray amorphous for the other CZA oxide precursors (see Fig. 3-6a). No diffractions lines corresponding to Al compounds were observed. This suggests that the Al compounds were either amorphous or highly dispersed in the catalysts. After reduction in hydrogen, CuO was completely reduced to copper metal as it can be deduced from XRD investigations (Fig. 3-6b). The XRD pattern of the reduced catalysts could be very well simulated by a mixture of hexagonal ZnO and cubic Cu. A refinement of the corresponding ICSD model structures to the experimental pattern (*Pawley* method) resulted in a phase composition of approximately 70 % to 80 % cubic Cu and 20 % to 30 % hexagonal ZnO. Bulk structural parameters such as mean Cu crystallite size and mean Cu lattice strain

after reduction are given in Table 3-3. The averaged Cu crystallite sizes calculated from line broadening of Cu(*111*) reflection range from 45 Å to 77 Å. However, in the set of catalysts studied, only the sample CZA-1 exhibited lattice strained Cu particles (Table 3-3). Exposure to the steam reforming feed had no significant influence on the diffraction pattern and the corresponding bulk structural characteristics, such as phase composition, crystallite size, and lattice strain. Accordingly, lattice constants were in agreement with bulk *fcc* copper (Table 3-4). Consistently, the adsorption edge positions determined as the position of the inflection point of the Cu K -edge absorption spectra of the catalysts investigated matched with bulk metallic copper (see Table 3-4).

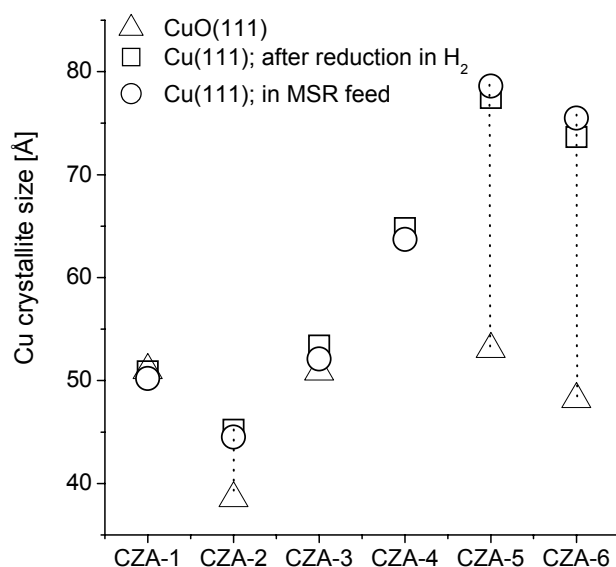


**Fig. 3-7:** Crystallite sizes of CuO and Cu determined from the XRD line broadening of the calcined precursor, the reduced and the Cu/Zn/Al- catalyst under MSR conditions.

The copper phase crystallite sizes calculated from the integral breadth of the CuO(*111*) and Cu(*111*) reflections after the various treatments (i.e. calcined precursor, reduced catalysts, and catalyst under MSR conditions) are summarized in Fig. 3-7. A comparison of the crystallite sizes, determined before and after reduction, revealed that during the reduction process the crystallite sizes for the samples CZA-2 and especially for CZA-5 and -6 increased. Due to the highly amorphous XRD spectra of sample CZA-4 in the calcined state no CuO crystallite sizes have been calculated (see Fig. 3-6a). Conversely to CZA -2, -5 and -6, no changes in crystallite size were determined for the CZA-1 catalyst. Exposure to the steam reforming feed had no significant influence on the crystallite size for any of the catalysts investigated (see Fig. 3-7).

Analysis of the extended fine structure of the experimental spectra (EXAFS) measured under reaction conditions at the Cu K -edge and Zn K -edge revealed changes in the short range order structure of the catalysts. The resulting pseudo radial distribution functions (RDF) measured at the Cu K -edge,  $FT(\chi(k) \cdot k^3)$ , after reduction of all catalysts are depicted in Fig. 3-8. Deviations of the  $FT(\chi(k) \cdot k^3)$  of the various catalysts were most pronounced for the amplitude of the 1<sup>st</sup> Cu-Cu shell ( $R \approx 2.5$  Å). This has

been also found for the spectra recorded in MSR feed under reaction conditions (see  $\sigma_{\text{Cu}}^2$  in Table 3-4). MSR activities determined in the XAS cell coincided with the trend in activity obtained in the *in situ* XRD cell and in the fixed-bed micro reactor (Fig. 3-1). A structural refinement of a theoretical spectrum of bulk *fcc* Cu to the experimental spectra revealed no shift of the distance of the first copper metal shell which indicates that no additional Cu containing phases, such as brass are detectable in the bulk. This is in agreement with the obtained lattice constants of Cu (see Table 3-4).

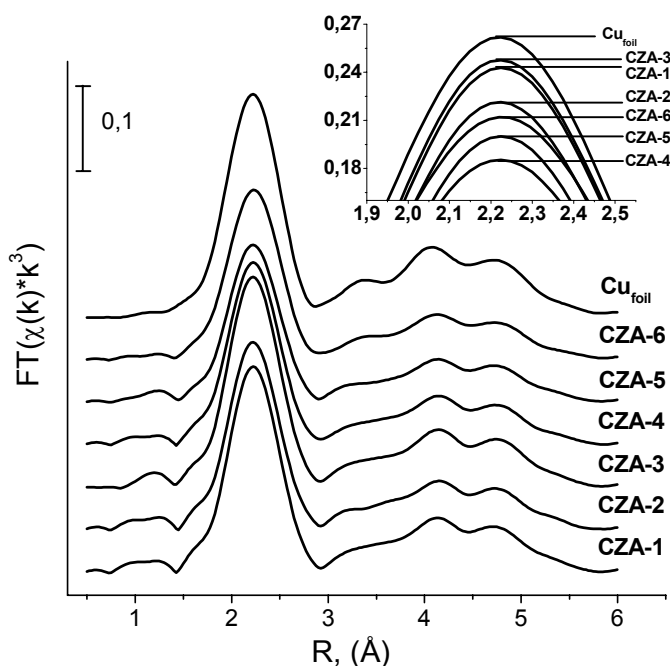


**Fig. 3-8:** Experimental Cu K -edge  $\text{FT}(\chi(k) \cdot k^3)$  of the in 5 vol.-% H<sub>2</sub> (He) reduced Cu/ZnO/Al<sub>2</sub>O<sub>3</sub> catalysts recorded at ambient temperature. The inset shows the real amplitude of the 1<sup>st</sup> Cu-Cu shell (without offset).

In Fig. 3-9 the results of a refinement of a theoretical Cu EXAFS function to an experimental  $\text{FT}(\chi(k) \cdot k^3)$  of sample CZA-1 at 313 K after MSR reaction conditions is depicted. A good agreement between experimental and theoretical data can be seen. The structural parameters of the single scattering paths obtained from a refinement of theoretical bulk copper to the experimental Cu K -edge EXAFS for all CZA catalysts studied are summarized in Table 3-5. The obtained variation of the amplitude of the 1<sup>st</sup> metal-metal shell, shown in Fig. 3-8, corresponded to a different structural disorder (*Debye-Waller* factor,  $\sigma^2$ ) in the Cu phase within the CZA series. The DWF obtained depends on the Cu crystallite size determined from XRD. The smaller the Cu crystallite size the higher the structural disorder in the Cu phase (Fig. 3-10). However, two groups of catalysts have been identified: Samples CZA 1-3 on the one and CZA 4-6 on the other hand. Within each group a linear correlation between the obtained DWF and the Cu crystallite size of the Cu(111) reflection was observed (see Fig. 3-10). Confidence limit of the DWF of the first Cu-Cu shell was estimated to be about 0.0001 Å<sup>2</sup>. Hence, error bars in Fig. 3-10 were in the order of the thickness of the symbols used.

**Table 3-5:** Structural parameters obtained from refinement of theoretical *fcc* copper metal to the experimental Cu K -edge EXAFS function recorded after MSR reaction at 313 K ( $k = 3 \text{ \AA}^{-1}$  to  $13 \text{ \AA}^{-1}$ ;  $R = 1.7 \text{ \AA}$  to  $6 \text{ \AA}$ ; Refinement includes 5 single and 9 multi scattering paths;  $N_{\text{ind}} = 27$ ;  $N_{\text{free}} = 11$ ).

| sample       | Shell    | CN <sup>a</sup> | R [ $\text{\AA}$ ] | $\sigma^2$ [ $\text{\AA}^2$ ] | $\Delta\sigma^2_{\text{foil}}$ [ $\text{\AA}^2$ ] |
|--------------|----------|-----------------|--------------------|-------------------------------|---|
| <b>CZA-1</b> | 1. Cu-Cu | 12              | 2.53(4)            | 0.0110                        | -0.0009   |
|              | 2. Cu-Cu | 6               | 3.62(2)            | 0.0171                        | -0.0013   |
|              | 3. Cu-Cu | 24              | 4.41(7)            | 0.0173                        | -0.0029   |
|              | 4. Cu-Cu | 12              | 5.08(0)            | 0.0273                        | -0.0050   |
|              | 5. Cu-Cu | 24              | 5.78(0)            | 0.0315                        | -0.0065   |
| <b>CZA-2</b> | 1. Cu-Cu | 12              | 2.53(4)            | 0.0116                        | -0.0015   |
|              | 2. Cu-Cu | 6               | 3.61(6)            | 0.0183                        | -0.0025   |
|              | 3. Cu-Cu | 24              | 4.40(7)            | 0.0182                        | -0.0038   |
|              | 4. Cu-Cu | 12              | 5.07(2)            | 0.0275                        | -0.0052   |
|              | 5. Cu-Cu | 24              | 5.74(7)            | 0.0317                        | -0.0067   |
| <b>CZA-3</b> | 1. Cu-Cu | 12              | 2.53(7)            | 0.0108                        | -0.0007   |
|              | 2. Cu-Cu | 6               | 3.63(6)            | 0.0171                        | -0.0013   |
|              | 3. Cu-Cu | 24              | 4.41(6)            | 0.0169                        | -0.0025   |
|              | 4. Cu-Cu | 12              | 5.08(1)            | 0.0262                        | -0.0039   |
|              | 5. Cu-Cu | 24              | 5.76(8)            | 0.0322                        | -0.0072   |
| <b>CZA-4</b> | 1. Cu-Cu | 12              | 2.54(1)            | 0.0135                        | -0.0034   |
|              | 2. Cu-Cu | 6               | 3.63(6)            | 0.0196                        | -0.0038   |
|              | 3. Cu-Cu | 24              | 4.41(6)            | 0.0192                        | -0.0048   |
|              | 4. Cu-Cu | 12              | 5.08(3)            | 0.0298                        | -0.0075   |
|              | 5. Cu-Cu | 24              | 5.76(8)            | 0.0367                        | -0.0116   |
| <b>CZA-5</b> | 1. Cu-Cu | 12              | 2.54(0)            | 0.0127                        | -0.0028   |
|              | 2. Cu-Cu | 6               | 3.63(3)            | 0.0187                        | -0.0029   |
|              | 3. Cu-Cu | 24              | 4.42(0)            | 0.0189                        | -0.0045   |
|              | 4. Cu-Cu | 12              | 5.07(9)            | 0.0310                        | -0.0087   |
|              | 5. Cu-Cu | 24              | 5.77(8)            | 0.0353                        | -0.0103   |
| <b>CZA-6</b> | 1. Cu-Cu | 12              | 2.53(9)            | 0.0122                        | -0.0020   |
|              | 2. Cu-Cu | 6               | 3.62(9)            | 0.0183                        | -0.0025   |
|              | 3. Cu-Cu | 24              | 4.41(8)            | 0.0183                        | -0.0039   |
|              | 4. Cu-Cu | 12              | 5.08(0)            | 0.0298                        | -0.0075   |
|              | 5. Cu-Cu | 24              | 5.78(1)            | 0.0351                        | -0.0103   |

<sup>a</sup> non refined parameter (fixed)

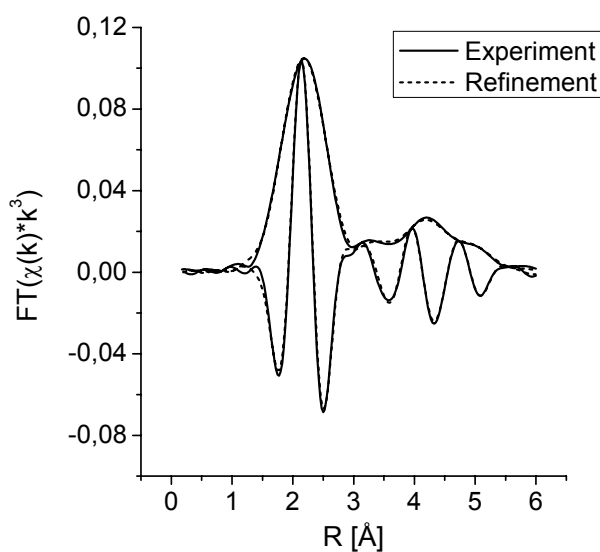


**Fig. 3-9:** Refinement of theoretical Cu EXAFS function (dashed line) to the experimental Cu K -edge  $FT(\chi(k) \cdot k^3)$  (solid line) of CZA-1 catalyst measured after MSR reaction at 313 K.

**Table 3-6:** Zn K -edge position ( $E_0$ ) of the calcined precursor (313 K), the reduced catalyst (523 K), and the catalyst under MSR conditions (523 K). Energy offset has been determined as the position of the inflection point of the continuum absorption curve. The edge position of macro-crystalline ZnO measured as reference amounts to  $E_0 = 9.662$  keV.

| sample | $E_0$ ZnO [keV] |          |                      |
|--------|-----------------|----------|----------------------|
|        | calcined        | reduced  | under MSR conditions |
| CZA-1  | 9.658(5)        | 9.662(3) | 9.662(4)             |
| CZA-2  | 9.658(8)        | 9.662(8) | 9.662(7)             |
| CZA-3  | 9.658(4)        | 9.662(9) | 9.662(9)             |
| CZA-4  | 9.658(8)        | 9.662(4) | 9.662(2)             |
| CZA-5  | 9.658(6)        | 9.663(2) | 9.663(0)             |
| CZA-6  | 9.658(6)        | 9.662(9) | 9.662(7)             |

In Fig. 3-11 the  $FT(\chi(k) \cdot k^3)$  measured at the Zn K -edge in reducing atmosphere after the activation procedure at ambient temperature are depicted. The first peak,  $R = (1-2)$  Å, attributed to Zn in a distorted tetrahedral coordination by oxygen was also visible for the measured ZnO reference. Differences compared to a crystalline ZnO reference were found at distances above 2 Å. For the catalysts investigated the peak located at 3 Å in the corresponding RDF (Fig. 3-11) attributed to the 1<sup>st</sup> Zn-Zn shell in a ZnO crystal was diminished relative to the ZnO reference. Apparently, the Zn K -edge EXAFS indicates the presence of a zinc species different from bulk crystalline ZnO.

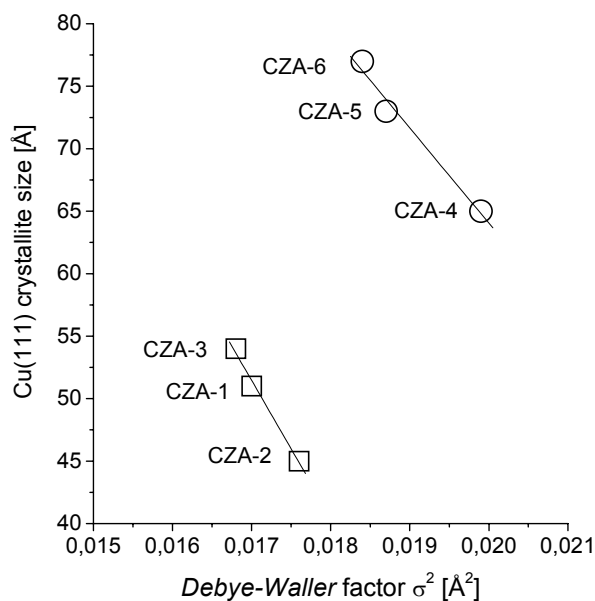


**Fig. 3-10:** Correlation of Cu crystallite size (XRD) with the DWF of the 1<sup>st</sup> Cu-Cu shell (XAS) derived from a refinement of theoretical Cu functions to the corresponding experimental data.

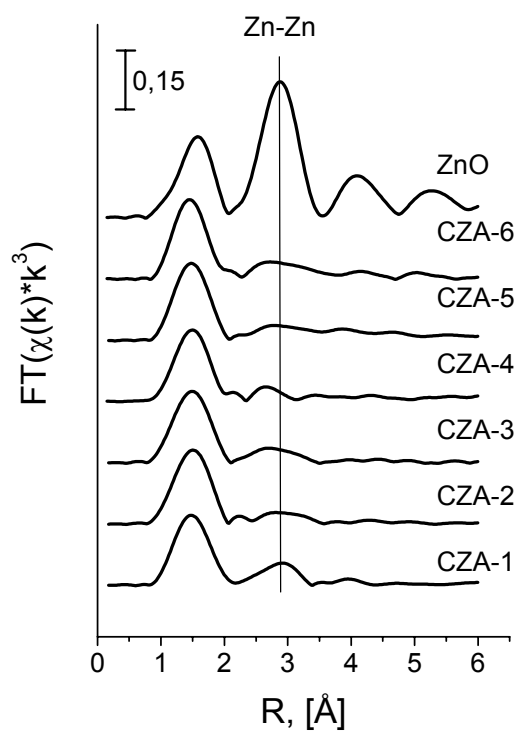


**Fig. 3-11:** Experimental  $FT(\chi(k) \cdot k^3)$  of the Cu/ZnO/Al<sub>2</sub>O<sub>3</sub> catalysts measured after the reduction (activation) treatment at ambient temperature. For comparison the Radial Distribution Function (RDF) of ZnO measured as reference is also depicted.



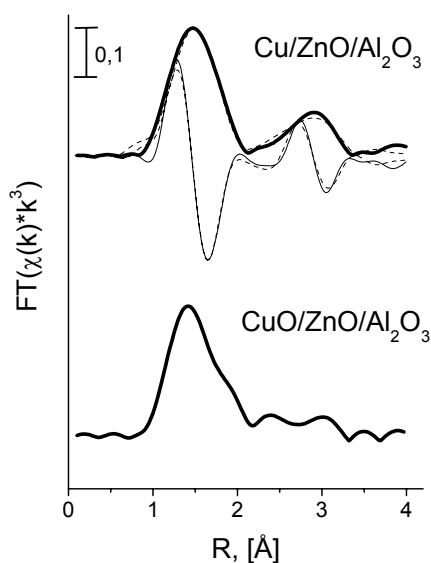


**Fig. 3-12:** Experimental Zn K -edge  $FT(\chi(k) \cdot k^3)$  measured before and after reduction in hydrogen of the sample CZA-1: calcined oxide precursor (bottom) and reduced catalyst (top) with refinement of theoretical ZnO EXAFS function (dashed line) to the experimental Zn K -edge  $FT(\chi(k) \cdot k^3)$  (solid line).

In Fig. 3-12 the Zn  $FT(\chi(k) \cdot k^3)$  of the calcined CZA-1 precursor is compared to the RDF obtained after reduction in hydrogen. The amplitude of the first zinc metal shell ( $R = 2.9 \text{ \AA}$ ) of the reduced CZA-1 catalyst was barely half of the first Zn-O peak ( $R = 1.5 \text{ \AA}$ ). According to the analysis of the evolved gas phase, decomposition of a Zn containing hydroxycarbonate precursor material took place during reduction. A refinement of a theoretical ZnO model structure to the experimental Zn  $FT(\chi(k) \cdot k^3)$  obtained after reduction revealed a highly defect rich ZnO phase for sample CZA-1 (see Fig. 3-12). Conversely, the refinement of the ZnO model structure to the experimental RDF of samples CZA 2-6 after reduction alone resulted in a high Fit residual. No structural differences in regard to Zn-O as well as Zn-Zn distances and the corresponding DWF's have been found between the reduced catalysts and the catalysts under MSR reaction conditions. Accordingly, the absorption edge position of the Zn K -edge did not change by switching from reduction atmosphere to MSR feed (Table 3-6).

### 3.4 Discussion

#### 3.4.1 Microstructure of Cu in Cu/ZnO/Al<sub>2</sub>O<sub>3</sub> catalysts

The catalysts investigated exhibit considerable differences in their MSR activities. This emphasizes the eminent relevance of the catalyst preparation for the electronic and structural properties of the resulting solids (see Fig. 3-1). Conversions of methanol on the catalysts studied can certainly be enhanced to the thermodynamic equilibrium by decreasing the space velocity (WHSV). However, an optimization of the catalytic performance with respect to a complete methanol conversion was not the objective of this study. Here, catalytic performance in MSR was mainly determined by the overall surface area of the

copper phase in the Cu/ZnO/Al<sub>2</sub>O<sub>3</sub> catalysts studied (Fig. 3-2). However, a significant deviation from a linear correlation between copper surface area and activity has been found. This deviation was most pronounced for samples CZA-2, -5 and -6, which exhibited a similar Cu surface area of about 5 m<sup>2</sup><sub>Cu</sub>·g<sup>-1</sup> but still differed considerably in the catalytic activity (see Fig. 3-2). Strained copper particles were detected only for the catalyst CZA-1 which also exhibited the highest specific Cu surface area of all catalysts studied (Table 3-3). Highest intrinsic activities (activity per m<sup>2</sup><sub>Cu</sub>) have been found for the sample CZA-2. Catalyst CZA-1 exhibited even less activity per m<sup>2</sup><sub>Cu</sub> than the samples CZA 2-6 (see Table 3-1). Obviously, lattice strain appeared to be the consequence of the high Cu dispersion and a high Cu surface area found in CZA-1 (see Table 3-3). This confirms previous investigations of binary Cu/ZnO model catalysts concerning the relevance of bulk structural defects in stabilization of a high Cu surface area in methanol chemistry [3.10]. The high degree of disorder in the Cu nanoparticles found for sample CZA-1 may result from an increased interface area between Cu and ZnO [3.6, 3.9-3.10, 3.12-3.14, and 3.21]. This is confirmed by HRTEM investigations of CZA-1 which revealed a variety of both epitaxial and irregular arrangements of, in most cases, relatively smooth Cu-ZnO interfaces (Fig. 3-5a). The existence of subsurface oxygen at the Cu-O-Zn interface which also has been ascribed to cause disorder in the Cu particles can not ruled out for the Cu/ZnO/Al<sub>2</sub>O<sub>3</sub> catalysts investigated [3.41].

The catalyst CZA-1 exhibited the lowest reduction temperature and a rather narrow and symmetrical TPR peak compared to the other samples. By means of temperature programmed XANES investigations at the Cu K -edge the shoulder which appeared at lower temperature side in the TPR signal (Fig. 3-3) was assigned to the appearance of Cu<sub>2</sub>O as an intermediate phase during the reduction of Cu(II) to Cu(0) as it was also found for other Cu based mixed oxides [3.42]. Previous investigations concerning the reducibility of copper based catalysts for methanol chemistry have revealed that a “good” reducibility is associated with a high activity of the corresponding catalyst [3.43, 3.44]. In addition to the low reduction temperature, the shape of the TPR profile of sample CZA-1 indicate a homogeneous microstructure of small and uniformly distributed copper particles [3.14]. Conversely, the samples CZA-2 to -6 exhibited a heterogeneous mixture of large and isolated copper agglomerates (see Fig. 3-4). The pronounced bimodal particle size distribution of small and large Cu agglomerates (5 nm - 150 nm) observed by electron microscopy was also reflected in the TPR profiles. A shift to higher reduction temperatures as well as a pronounced broadening of the reduction peaks indicate large and less dispersed copper particles in those catalysts (see Fig. 3-3). Apparently, the main fraction of CuO was less accessible to hydrogen during the reduction procedure and therefore may also less accessible to the reactants MeOH and H<sub>2</sub>O during MSR reaction. Consistently, the copper surface area calculated from XRD line broadening was much larger than the surface area measured by RFC. Only for CZA-1 the calculated Cu surface area for all diffraction domains matched the RFC results (Table 3-3). Deviations found for the samples CZA 2-6 may originate from non-spherical copper particles or from different activities of individual copper lattice planes exposed at the surface. More likely though, it is the agglomeration of copper particles which reduces the accessible Cu surface area. Apparently, the large copper particles in samples CZA 2-6 were composed of mosaic crystals with smaller domains. Thus, the accessible surface area was noticeable lower than the total surface area calculated for all diffraction domains. In opposite to CZA-1, samples CZA 2-6 partially consist of isolated Cu particles in the ZnO/Al<sub>2</sub>O<sub>3</sub> matrix (see Fig. 3-5). Hence, determining the

reducibility of the copper species in terms of reduction temperature and reduction profile is well suited as indicator for the catalytic performance of the present Cu/ZnO/Al<sub>2</sub>O<sub>3</sub> samples.

No variations in lattice cell parameters (XRD) and in distance of the 1<sup>st</sup> Cu-Cu shell (XAS) of Cu were observed for all samples. This indicates that no brass or other Cu sub-oxides were formed in the bulk (Table 3-4). Conversely, an increasing Cu-Zn(ZnO<sub>1-x</sub>) alloying abundance in the bulk was found to be accompanied by a decrease in MSR activity [3.14]. Conversely, HRTEM investigations confirmed the presence of minute amounts of Cu<sub>2</sub>O and brass in the reduced Cu/ZnO/Al<sub>2</sub>O<sub>3</sub> catalysts. Since the bulk sensitive techniques such as XRD and XAS did not observe any lattice expansion of Cu within the detection limit (Table 3-4) it is most probably that these species originates from traces of oxygen during TEM sample preparation in the glove box or from incomplete reduction of the Cu/Zn/Al- catalyst during TPR. The averaged crystallite sizes determined by X-ray diffraction line profile analysis and particle sizes obtained from TEM investigations classified copper as a nano-crystalline material. These copper particles exhibited a certain disorder in short and medium range order as it can be deduced from the high *Debye-Waller* factor (DWF) of copper compared to “ideal” bulk copper (Table 3-4, Table 3-5). The differences of the DWF observed within the series of CZA catalysts did not coincide with the calculated lattice strain in the Cu crystallites. The observed variation in amplitude of the single scattering Cu-Cu shells might be caused by size effects of the Cu phase present (Fig. 3-12). Generally, the temperature independent (static) disorder is increased in a nano-crystalline sample with respect to a macro-crystalline bulk like particle. The elevated static disorder reflects an incoherent bond length distribution within the nano-crystals [3.45]. Two groups of catalysts, which have been identified, exhibited a different dependency of the DWF on the Cu crystallite size. Apparently, the samples CZA 1-3 exhibited less structural disorder in the Cu crystallites under MSR reaction conditions than samples CZA 4-6 (Fig. 3-10). However, the different dependencies, observed within the CZA series, did not coincide with the catalytic performance of the catalysts investigated. Only samples CZA 4-6 exhibited a linear correlation between static structural disorder in the Cu lattice obtained from *in situ* XAS studies and the measured activity in the *in situ* cell. Those samples have been prepared in an equal manner. Obviously, this linear trend was caused by the observed specific Cu surface area of the three corresponding catalysts. The determined Cu crystallite sizes of samples CZA 4-6 coincided with the measured Cu surface area and were also reflected in the catalytic activity (see Table 3-3). Apparently, Cu/ZnO/Al<sub>2</sub>O<sub>3</sub> catalysts prepared under nearly similar conditions gave rise to a linear Cu surface area - activity correlation in MSR reaction. Conversely, samples CZA 1-3, which were differently prepared, did not show a distinct dependency of the overall Cu surface area and the activity in MSR. This clearly indicates that the observed DWF contained complex information which strongly depends on the kind of preparation of the catalyst. Obviously, lattice strain determined by XRD and structural disorder (DWF) determined by XAS in the Cu phase of the Cu/ZnO/Al<sub>2</sub>O<sub>3</sub> catalysts under working conditions are different microstructural features. Hence, lattice strain in the copper particles was not the primary origin of the structural disorder, quantified by the *Debye-Waller* factor in the corresponding RDF, observed. It can be speculated that lattice oxygen diversely (qualitative and/ or quantitative) intercalated in the Cu particles of the Cu/ZnO/Al<sub>2</sub>O<sub>3</sub> catalysts studied were the reason for the different DWF's obtained [41]. This Cu-O sub-surface phase consists of covalently bonded atomic oxygen species without participation of the Cu d- bands which form the main bonding contribution in

bulk copper oxides [42]. In that case, bulk structural determination techniques used in this study, i.e. X-ray diffraction and X-ray absorption spectroscopy, would merely detect zero-valent copper to be present. However, the physical origin of structural disorder determined in the Cu phase remains unclear.

Crystallites, which are significantly smaller than 10 nm, exhibit a disproportionately high fraction of surface atoms relative to the bulk. Accordingly, due to inharmonic, non Gaussian pair distribution function the corresponding RDF will result in a reduction in the averaged coordination number [3.46]. During the fit procedure, employed the coordination numbers of Cu were kept constant at the values of bulk copper (CN = 12). Here, the copper crystallite sizes of the Cu/ZnO/Al<sub>2</sub>O<sub>3</sub> catalysts studied range from 5 nm to 8 nm (Table 3-3). Thus, both size effects due to the nanosized Cu crystallites and structural disorder may account for the reduction in amplitude observed for 1<sup>st</sup> Cu-Cu shell (Fig. 3-8). However, an EXAFS refinement with the *Debye-Waller* factor fixed to those of Cu bulk afforded an apparent coordination number of 8 to 9 for copper. Here the coordination number was treated as a fitting parameter with DWF's fixed to those of Cu foil measured as reference. Based on molecular dynamics simulations averaged coordination numbers of nanosized copper with an crystallite size of 5 nm to 8 nm has been calculated to be 11 to 11.5 [3.47]. The considerably lower coordination number of Cu (CN = 8-9) determined from experimental EXAFS indicates that a disproportionately high fraction of Cu atoms located on the surface with respect to the bulk only played a minor role for the observed reduction of the amplitude in the RDF. Accordingly, the measured Cu surface area as result of a more or less pronounced dispersion of Cu (Table 3-3) was not reflected in the observed variation of the amplitude in the radial distribution function. Both size effects due to reduction in the CN to a minor and (static) structural disorder in the copper crystallites to a major part accounted for the observed reduction of the amplitude in the FT( $\chi(k)$ ) in a cumulative manner.

### 3.4.2 Microstructure of ZnO and Al<sub>2</sub>O<sub>3</sub> in Cu/ZnO/Al<sub>2</sub>O<sub>3</sub> catalysts

The role of ZnO in copper based catalysts for methanol chemistry has been controversially debated in the literature. Apparently, ZnO prevents Cu sintering and remove catalyst poisons, i.e. sulfides and halogenides, under working conditions in methanol synthesis as well as steam reforming [3.24, 3.48]. In semi-conductor science it is well established that the electronic properties of highly defective, nano-scaled zinc oxide, such as the band gap size, significantly differ those of macro-crystalline ZnO [3.49]. Decomposition of appropriate CuZn(Al)- hydroxycarbonates is believed to result in a particular zinc oxide modified by ad-mixed OH<sup>-</sup> and CO<sub>3</sub><sup>2-</sup> groups [3.50]. Such a modified zinc oxide serves as a growth inhibitor of copper particles [3.25, 3.51-3.52]. Hence, mild reduction in hydrogen results in copper dissolved in ZnO and copper metal particles bonded epitaxially to the surface of the ZnO matrix [3.50]. Here, EXAFS investigations of various calcined CuO/ZnO/Al<sub>2</sub>O<sub>3</sub> precursors at the Zn K -edge indicated the presence of zinc phases different from ZnO. This indicates the presence of additional Zn species other than ZnO in the non reduced catalyst state (see Fig. 3-12). The increase in XAS amplitude of the 1<sup>st</sup> Zn-Zn shell of sample CZA-1 during reduction imply that ZnO undergoes a microstructural ordering in the medium range structure (Fig. 3-12). Consistently, the determined Zn K -edge position shifted of about 4 eV during reduction compared to the calcined sample (Table 3-6). Analysis of the MS data revealed that

the observed shift in the Zn K -edge position during reduction coincided with a release of H<sub>2</sub>O and CO<sub>2</sub>. After reduction, *in situ* XRD investigations exhibited crystalline ZnO with a mean crystallite size of about 39 Å for CZA-1 (Fig. 3-6b). Additionally, electron microscopy investigations on the sample CZA-1 confirmed a highly defect rich microstructure of crystalline ZnO including dislocations, bent lattice planes, and a rough surface morphology. For that sample, ZnO appeared roughly spherical shaped with an averaged diameter of  $d_{\text{ZnO}} = 7$  nm (Fig. 3-5a). However, the presence of oxygen deficit ZnO which has been found in rare cases by HRTEM investigations has not been confirmed by analysis of the Zn K -edge position in the reduced state as well as under MSR reaction conditions (Table 3-6). This indicates that either the abundance of ZnO<sub>1-x</sub> is negligible in the CZA-1 catalysts or that the absorption K -edge of Zn is dominated by different Zn<sup>2+</sup> species. The short range order structure (< 2 Å) of this resulting ZnO phase mainly corresponds to disordered ZnO. Nevertheless, hydroxide and carbonate species may persist after mild thermal treatment (calcination, reduction) in the catalytically active catalyst [3.25]. Thus, the diminished amplitude of the 1<sup>st</sup> Zn-Zn shell obtained after reduction of sample CZA-1 might be caused by a superimposition of the spectra of different Zn species in addition to a highly disordered ZnO phase (Fig. 3-12). The presence of these species located at the zinc centers should result in a modified microstructure at the Zn-O-Cu interface which causes the detected lattice strain in the copper nanoparticles [3.50]. Conversely, the presence of crystalline hydroxycarbonates has not been confirmed by XRD for the reduced CZA-1 (Fig. 3-6b). Apparently, Zn K -edge EXAFS probes the amorphous part of the catalysts which is not observable by XRD. Consistently, TEM revealed the presence of amorphous structures in the reduced CZA-1 catalyst. EXAFS spectra measured at the Zn K -edge of the samples CZA-2 to 6 showed no microstructural changes as those observed for sample CZA-1 during reduction in hydrogen (Fig. 3-11). In good agreement with these results, no long range ordered ZnO phase was detectable by X-ray diffraction for samples CZA 2-6. Consistently, HRTEM investigations did not reveal the presence of nano-crystalline ZnO sticks to Cu particles as it was found for CZA-1. Typically for those CZA samples, Cu particles were found to be embedded in an amorphous matrix which shapes large plate or needle like structures (see Fig. 3-4). Apparently, even after reduction in hydrogen, “ZnO” remains in an amorphous state similar to that of the calcined precursors. Thus, differences found in RDF with respect to CZA-1 were most probably due to an unfavored texture of ZnO in samples CZA 2-6. In contrast to CZA-1, the diminished amplitude of the 1<sup>st</sup> Zn-Zn shell obtained after reduction may be caused by a highly amorphous texture of ZnO. The pronounced loss of structural coherence above 2 Å in the Zn K -edge FT( $\chi(k) \cdot k^3$ ) corresponded to a highly amorphous texture of ZnO in these catalysts [3.53]. The highly non-ordered character of ZnO in the bulk of catalysts CZA 2-6 was confirmed by *in situ* XRD (Fig. 3-6). Consistently, TEM investigations exhibited a less pronounced nanostructuring of intimately mixed ZnO and Cu particles with respect to CZA-1 (Fig. 3-5). In consequence of that, samples CZA 2-6 exhibited Cu surface areas of less than 9 m<sup>2</sup><sub>Cu</sub>·g<sup>-1</sup> (Table 3-3). Apparently, ZnO was required to maintain the active copper phase in optimal dispersion without allowing segregation. Thus, ZnO is not just a support but integral part of the active copper based catalyst. The bulk structure and, hence, the catalytically active surface was determined by an advanced Cu-ZnO interface.

Alumina did not appear as a separate phase detectable by X-ray diffraction and TEM investigations. Only in rare cases Al has been identified as crystalline  $\alpha$ -Al<sub>2</sub>O<sub>3</sub> by HRTEM. Cu-Al interactions in

Cu/ZnO/Al<sub>2</sub>O<sub>3</sub> catalysts have been suggested by *Figueiredo et al.* [3.54]. However, the addition of aluminum in the precipitation process significantly changes the precursor chemistry according to the structural and electronic properties of ternary Cu/ZnO/Al<sub>2</sub>O<sub>3</sub> compared to binary Cu/ZnO catalysts. Thus, superior activities have been described for Cu/ZnO/Al<sub>2</sub>O<sub>3</sub> catalysts exhibiting a similar copper surface area as comparable Cu/ZnO catalysts [3.55, 3.56].

### 3.4.3 Thermal stability of Cu/ZnO/Al<sub>2</sub>O<sub>3</sub> catalysts

Copper metal exhibits a low *Tammann* temperature corresponding to a low melting point of  $T_M = 1356$  K [3.57]. Therefore, Cu/ZnO/Al<sub>2</sub>O<sub>3</sub> catalysts suffer from thermal deactivation by sintering at temperatures above 523 K (see Fig. 3-7). Thermal stability of copper based catalysts strongly depends on both the preparation procedures used and the chemical composition [3.24]. Thus catalyst preparation represents a crucial point since thermal degradation can be limited in well formulated catalysts prepared under optimized conditions [3.48]. During *in situ* reduction of the catalysts sintering occurred for the samples CZA 2-6 resulting in an increase in Cu crystallite sizes compared to crystallite sizes of the corresponding oxides (Fig. 3-7). Sintering accompanied by loss of Cu surface area was highly pronounced for the samples CZA-5 and CZA-6 and was reflected in a “poor” hydrogen production rate obtained in MSR (see Table 3-1). Degradation was less pronounced for the samples CZA-2 and CZA-3 (Fig. 3-7). Subsequent exposure to MSR conditions caused no further sintering indicating that, in this study, the reduction process was the crucial step with respect to catalyst degradation [3.58]. The commercial CZA-1 catalyst exhibited no sintering process, neither during the reduction process nor under MSR working conditions. Apparently, the tendency for sintering depends on the interaction of copper particles and the ZnO/Al<sub>2</sub>O<sub>3</sub> matrix. Thus, it can be concluded that the enhanced stability observed for the commercial Cu/ZnO/Al<sub>2</sub>O<sub>3</sub> catalysts compared to the laboratory prepared catalysts (CZA 2-6) was closely related to the increased structural disorder (lattice strain) in the Cu particles. Lattice strain in the copper particles was a consequence of the homogeneous nanostructuring of Cu metal and ZnO/Al<sub>2</sub>O<sub>3</sub> support. The latter kept the Cu crystallites in a meta-stable state and thus maintained a high active surface area. While maintaining a similar copper surface area, the strained CZA sample revealed a significantly increased chemical and thermal stability during catalyst treatment (reduction, MSR).

The superior activities obtained for ternary Cu/ZnO/Al<sub>2</sub>O<sub>3</sub> catalysts compared to binary Cu/ZnO catalysts exhibiting a similar copper surface area may be originating from the more complex precursor chemistry of these catalysts during the precipitation process [3.56]. Addition of aluminum as a third cationic component will change the electronic and structural properties of the final catalyst and may result in an enhanced activity. Nevertheless, structural and catalytically relevant differences obtained from the binary Cu/ZnO model system can be reliably extrapolated to Cu/ZnO/Al<sub>2</sub>O<sub>3</sub> catalysts. Correlations found for the binary system [3.6, 3.10, and 3.12-3.14], such as phase composition, reduction characteristics, crystallinity, homogeneity of microstructure and structural disorder are also valid for the more complex Cu/ZnO/Al<sub>2</sub>O<sub>3</sub> system.

### 3.5 Summary

Various ternary Cu/ZnO/Al<sub>2</sub>O<sub>3</sub> catalysts were tested for methanol steam reforming activity (MSR). Consistent with previous investigations of binary Cu/ZnO model systems, the hydrogen production rate exhibited no linear correlation with the overall specific copper surface area. The catalytic activity and stability (thermal, chemical) under MSR reaction conditions was also influenced by structural defects in the bulk of the materials. Lattice strain in the copper particles was a consequence of the homogeneous nanostructuring observed of Cu component and ZnO/Al<sub>2</sub>O<sub>3</sub> matrix. ZnO kept the Cu crystallites in a meta-stable state and, hence, maintained a high active surface area.

Differences in the microstructure obtained for the binary Cu/ZnO model system has been also identified for “real” Cu/ZnO/Al<sub>2</sub>O<sub>3</sub> catalysts. Thus, structure activity correlations drawn for the binary system such as phase composition, reduction characteristics, crystallinity, homogeneity of microstructure and structural disorder are also valid for “real” Cu/ZnO/Al<sub>2</sub>O<sub>3</sub> catalysts. Therefore, these specific microstructural characteristics of the Cu and the ZnO/Al<sub>2</sub>O<sub>3</sub> matrix - in addition to a high copper surface area - have to be achieved for superior Cu/ZnO/Al<sub>2</sub>O<sub>3</sub> catalysts for methanol steam reforming.

### 3.6 References cited

- [3.1] P.J. de Wild, M.J.F.M. Vernaak, *Catal. Today*, 60 (2000) 3.
- [3.2] C. Lamy, A. Lima, V. LeRhun, F. Delime, C. Counteaceau, J.M. Léger, *J. Power Sources*, 105 (2002) 283.
- [3.3] M. Krumpelt, T. Krause, J.D. Carter, J.P. Kopasz, S. Ahmed, *Catal. Today*, 77 (2002) 3.
- [3.4] Y.M. Lin, M.H. Rei, *Int. J. Hydrogen Energy*, 25 (2000) 211.
- [3.5] K.C. Waugh, *Catal. Lett.*, 58 (1999) 163.
- [3.6] M.M. Günther, T. Ressler, R.E. Jentoft, B. Bems, *J. Catal.*, 203 (2001) 133.
- [3.7] M. Kurtz, H. Wilmer, T. Genger, O. Hinrichsen, M. Muhler, *Catal. Lett.*, 86 (2003) 77.
- [3.8] J. Agrell, H. Birgersson, M. Boutonnet, I. Melian-Cabrera, R.M. Navarro, J.L.G. Fierro, *J. Catal.*, 219 (2003) 389.
- [3.9] X.R. Zhang, L.C. Wang, Y. Cao, W.L. Dai, H.Y. He, K.N. Fan, *Chem. Commun.*, 32 (2005) 4104.
- [3.10] M.M. Günther, T. Ressler, B. Bems, C. Büscher, T. Genger, O. Hinrichsen, M. Muhler, R. Schlögl, *Catal. Lett.*, 71 (2001) 37.
- [3.11] F. Girgsdies, T. Ressler, U. Wild, T. Wübben, T.J. Balk, G. Dehm, L. Zhou, S. Günther, E. Arzt, R. Imbihl, R. Schlögl, *Catal. Lett.*, 102 (2005) 91.
- [3.12] B.L. Kniep, T. Ressler, A. Rabis, F. Girgsdies, M. Baenitz, F. Steglich, R. Schlögl, *Angew. Chem. Int. Ed.*, 43 (2004) 112.
- [3.13] T. Ressler, B.L. Kniep, I. Kassatkine, R. Schlögl, *Angew. Chem. Int. Ed.*, 44 (2005) 4704.
- [3.14] B.L. Kniep, F. Girgsdies, T. Ressler, *J. Catal.*, 236 (2005) 34.
- [3.15] K. Klier, *Adv. Catal.*, 31 (1982) 243.
- [3.16] G.C. Chinchin, K.C. Waugh, W. Da, *Appl. Catal.*, 25 (1986) 101.
- [3.17] R. Burch, S.E. Golunski, M.S. Spencer, *J. Chem. Soc. Faraday Trans.*, 86 (2000) 1990.
- [3.18] T. Fujitani, J. Nakamura, *Catal. Lett.*, 56 (1998) 119.
- [3.19] N.Y. Topsøe, H. Topsøe, *J. Mol. Catal. A*, 141 (1999) 95.
- [3.20] M.S. Spencer, *Catal. Lett.*, 66 (2000) 255.

- [3.21] J.B. Wagner, P.L. Hansen, A.M. Molenbroek, H. Topsøe, B.S. Clausen, S. Helveg, *J. Phys. Chem. B*, 107 (2003) 7753.
- [3.22] S. Velu, K. Suzuki, T. Osaki, *Catal. Lett.*, 62 (1999) 159.
- [3.23] J. Breen, R.H. Ross, *Catal. Today*, 51 (1999) 521.
- [3.24] M.V. Twigg, M.S. Spencer, *Appl. Catal. A*, 212 (2001) 161.
- [3.25] B. Bems, M. Schur, A. Dassenoy, H. Junkes, D. Herein, R. Schlögl, *Chem. Eur. J.*, 9 (2003) 2039.
- [3.26] A.B. Stiles, German patent, DE 2320 192 (1973), to DuPont company.
- [3.27] H. Fukui, M. Kobayashi, T. Yamaguchi, H. Arakawa, K. Okabe, K. Sayama, H. Kusama, European patent, EP 0 868 943 B1 (2002), to YKK cooperation.
- [3.28] G.C. Chinchin, K.C. Waugh, W. Da, *J. Catal.*, 103 (1987) 79.
- [3.29] O. Hinrichsen, T. Genger, M. Muhler, *Chem. Eng. Technol.*, 23 (2000) 11.
- [3.30] R.M. Dell, F.S. Stone, P.F. Tiley, *Trans. Faraday Soc.*, 49 (1953) 195.
- [3.31] D.A.M. Monti, A. Baiker, *J. Catal.*, 83 (1983) 323.
- [3.32] P. Malet, A. Caballero, *J. Chem. Soc. Trans. Faraday Trans. 1*, 84 (1988) 2369.
- [3.33] G.S. Pawley, *J. Appl. Cryst.*, 14 (1981) 357.
- [3.34] P. Scardi, M. Leoni, R. Delhez, *J. Appl. Cryst.*, 37 (2004) 381.
- [3.35] T. Ressler, *J. Syn. Rad.*, 5 (1998) 118.
- [3.36] A.L. Ankudinov, B. Ravel, J.J. Rehr, S.D. Conradson, *Phys. Rev. B*, 58 (1998) 7565.
- [3.37] H. Purnama, T. Ressler, R.E. Jentoft, H. Soerijanto, R. Schlögl, R. Schomäcker, *Appl. Catal. A*, 259 (2004) 83.
- [3.38] Y. Choi, H.G. Stenger, *Appl. Catal. B*, 38 (2002) 259.
- [3.39] R.C. Weast (Editor), *Handbook of Chemistry and Physics*, 57<sup>th</sup> edition, CRC Press Inc., Cleveland, 1976.
- [3.40] S. Velu, K. Suzuki, M. Okazaki, M.P. Kapoor, T. Osaki, F. Ohashi, *J. Catal.*, 194 (2000) 337.
- [3.41] I. Böttger, T. Schedel-Niedrig, O. Timpe, R. Gottschall, M. Hävecker, T. Ressler, R. Schlögl, *Chem. Eur. J.*, 6 (2000) 1870.
- [3.42] M.M. Günther, B. Bems, R. Schlögl, T. Ressler, *J. Syn. Rad.*, 8 (2001) 619.
- [3.43] G. Fierro, M.L. Jacono, M. Inversi, P. Porta, F. Cioci, R. Lavecchia, *Appl. Catal.*, 76 (1991) 117.
- [3.44] Y. Kawamura, K. Yamamoto, N. Ogura, T. Katsumata, A. Igarashi, *J. Power Sources*, 150 (2005) 20.
- [3.45] J. Rockenberger, L. Tröger, A.L. Rogach, M. Tischer, M. Grundmann, A. Eychmüller, H. Weller, *J. Chem. Phys.*, 108 (1998) 7807.
- [3.46] B.S. Clausen, L. Gråbæk, H. Topsøe, L.B. Hansen, P. Stolze, J.K. Nørskov, O.H. Nielsen, *J. Catal.*, 141 (1993) 368.
- [3.47] B.S. Clausen, J.K. Nørskov, *Topics Catal.*, 10 (2000) 221.
- [3.48] M.V. Twigg, M.S. Spencer, *Topics Catal.*, 22 (2003) 191.
- [3.49] V. Ischenko, S. Polarz, D. Grote, V. Stavarche, K. Fink, M. Driess, *Adv. Func. Mater.*, 15 (2005) 1945.
- [3.50] M. Yurieva, L.M. Plyasova, V.I. Zaikovskii, T.P. Minyukova, A. Bliet, J.C. van den Heuvel, L.P. Davydova, I. Molina, M.P. Demeshkina, A.A. Khassin, E.D. Batyrev, *Phys. Chem. Chem. Phys.*, 6 (2004) 4522.
- [3.51] G.C. Chinchin, P.J. Denny, J.R. Jennings, M.S. Spencer, K.C. Waugh, *Appl. Catal.*, 36 (1988) 1.
- [3.52] M.S. Spencer, *Topics Catal.*, 8 (1999) 259.
- [3.53] B. Gilbert, F. Huang, H. Zhang, G.A. Waychunas, J.F. Banfield, *Science*, 305 (2004) 651.
- [3.54] R.T. Figueiredo, A. Martinez-Arias, M.L. Granados, J.L.G. Fierro, *J. Catal.*, 178 (1998) 146.
- [3.55] M. Kurtz, N. Bauer, H. Wilmer, O. Hinrichsen, M. Muhler, *Chem. Ing. Tech.*, 76 (2004) 42.
- [3.56] M. Kurtz, N. Bauer, C. Büscher, H. Wilmer, O. Hinrichsen, R. Becker, S. Rabe, K. Merz, M. Driess, R.A. Fischer, M. Muhler, *Catal. Lett.*, 92 (2004) 49.
- [3.57] J.A. Moulijn, A.E. van Diepen, F. Kapteijn, *Appl. Catal. A*, 212 (2001) 3.



- [3.58] S. Fujita, S. Moribe, Y. Kanamori, N. Takezawa, *React. Kinet. Catal. Lett.*, 70 (2000) 11.

## Chapter Four

### Role of Defects in Cu/ZnO/Al<sub>2</sub>O<sub>3</sub> Catalysts for Methanol Synthesis

#### 4.1 *Role of defects in the activated Cu/ZnO/Al<sub>2</sub>O<sub>3</sub> catalyst*

##### 4.1.1 Introduction

The synthesis of methanol from CO/ CO<sub>2</sub>/ H<sub>2</sub> mixtures over Cu/ZnO/Al<sub>2</sub>O<sub>3</sub> catalysts at low reaction temperature and low pressure is an important industrial process. Although this reaction has been intensively studied over the last decades, the nature of the active sites and, hence, the microstructural requirements of a superior Cu/ZnO/Al<sub>2</sub>O<sub>3</sub> methanol synthesis catalyst are still under debate. There is a common agreement that the reaction occurs exclusively on the Cu component. Thus, activity has been suggested to be dependent on the overall Cu surface area of the methanol synthesis catalysts [4.1]. In this respect, the support phases, ZnO/Al<sub>2</sub>O<sub>3</sub>, only act as a mechanical spacer of the Cu phase ensuring an optimal Cu surface area [4.2]. Conversely, deviations from an explicit linear behavior between the activity in methanol synthesis and the overall Cu surface area of Cu/ZnO/Al<sub>2</sub>O<sub>3</sub> catalysts have been frequently reported in the recent literature. Accordingly, the interaction of metal and support phases was shown to have a significant role in determining the morphology, size, and distribution of the active Cu phase [4.3-4.7].

A series of Cu/ZnO/Al<sub>2</sub>O<sub>3</sub> catalysts exhibiting different catalytic activities in methanol synthesis was analyzed by means of transmission electron microscopy (TEM) and X-ray diffraction (XRD). Here, the nature of the Cu species present in the activated, reduced Cu/ZnO/Al<sub>2</sub>O<sub>3</sub> catalysts was in the main focus of the investigation. Activities observed in methanol synthesis reaction were correlated to the microstructure observed for the different Cu/Zn/Al- catalysts studied.

##### 4.1.2 Experimental details

CuO/ZnO/Al<sub>2</sub>O<sub>3</sub> catalyst precursors studied were conventionally prepared by co-precipitation of hydroxycarbonates from metal nitrate solutions and, subsequently, washed, dried, and calcined [4.8]. Temperature programmed reduction was carried out by passing 5 vol.-% H<sub>2</sub> (Ar) at a flow of 80 ml·min<sup>-1</sup> over 40 mg of the catalyst sample contained in a quartz tube. The temperature was increased linearly to

250 °C with a heating ramp of 6 K·min<sup>-1</sup> and maintained isothermal at 250 °C for 1 h. Immediate transfer of the reduced catalyst into a glove box prevented exposure to air. Afterwards, the samples were dispersed in acetone and deposited on a vacuum TEM transfer sample holder.

High resolution transmission electron microscopy (HRTEM) studies of the activated, reduced Cu/ZnO/Al<sub>2</sub>O<sub>3</sub> catalysts were performed according to procedure described in chapter 3.2.4.

*In situ* X-ray diffraction (XRD) experiments were employed for studying the bulk structure of the reduced Cu/ZnO/Al<sub>2</sub>O<sub>3</sub>. The experimental details have been already described in chapter 3.2.5. Profiles of the Cu (111) and (222) reflections were analyzed within the 2θ intervals of (38 - 49)° and of (90 - 100)°, respectively, to determine mean Cu crystallite size, Cu crystallite size distribution, and Cu lattice strain. Therefore, an adopted model was used to simulate the peak profiles from first principles by double summation of interference functions over different column lengths and over different lattice spacings according to the corresponding distribution functions [4.9]. A trial-and-error procedure was used to determine approximate values, which were further refined with a least-square procedure in the final step. The applied model did not impose any restrictions on the mathematical dependency of both lattice spacing and crystallite size distribution (normal, log-normal, etc.). The size-distribution shape was described by a polynomial function whose coefficients were refined during simulation. A correction for instrumental broadening was omitted because the full width at half maximum (FWHM) of each peak was more than ten times the instrumental broadening.

The Cu/ZnO/Al<sub>2</sub>O<sub>3</sub> catalysts investigated were tested in methanol synthesis at a temperature of 210 °C and a pressure of 60 bar. The feed was composed of 72 vol.-% H<sub>2</sub>, 10 vol.-% CO, 4 vol.-% CO<sub>2</sub>, and balance He.

### 4.1.3 Results and discussion

The transmission electron micrographs, shown in Fig. 4-1a, illustrate the microstructure which was typical of the activated (reduced) Cu/ZnO/Al<sub>2</sub>O<sub>3</sub> methanol synthesis catalysts investigated. The local microstructure considerably differed with respect to its morphology, i.e. well dispersed, round particles, needles, and rod-shaped agglomerates were found (see Fig. 4-1a). Generally, the reduced Cu/ZnO/Al<sub>2</sub>O<sub>3</sub> catalysts exhibited a porous framework which also locally varied in its Cu particle size distribution (Fig. 4-1b) and in its metal composition (Fig. 4-1c). The averaged elementary composition of all Cu/Zn/Al-catalysts studied has been determined by Energy Disperse X-ray spectroscopy (EDX) and amounted to Cu: (62.7 ± 7.2) at.-%, Zn: (26.7 ± 4.2) at.-%, and Al: (10.6 ± 4.5) at.-% (see Fig. 4-2). This molar ratio of roughly Cu/Zn/Al = 60:30:10 corresponds to the optimized metal composition and is characteristic for commercially employed methanol synthesis catalysts [4.10]. Typically, nanosized Cu and ZnO particles were separated by each other forming a well nanostructured arrangement of the latter phases (Fig. 4-3 a). In certain cases the copper surface was partially or even completely covered by ZnO (Fig. 4-3b). Additionally, Cu particles which were in intimate contact with smaller ZnO particles displayed a marked, smooth interface (Fig. 4-3 a-b). This wetting phenomenon of the Cu particles by ZnO indicates a relatively strong interaction of the two phases. Apparently, ZnO particles served as spacers between

individual Cu particles and, hence, prevent them from sintering [4.11]. Additionally, surfaces of Cu were partially covered by thin layers of unidentified, amorphous species. These species might be ZnO, Al<sub>2</sub>O<sub>3</sub> and/or residual Cu/Zn/Al- hydroxycarbonates. It is well known that Cu/Zn/Al- hydroxycarbonates partially persist the mild thermal treatment applied during catalyst calcination and subsequent reduction [4.12]. The OH<sup>-</sup> and CO<sub>3</sub><sup>2-</sup> groups present in the Cu/Zn/Al- hydroxycarbonates were assumed to chemically stabilize the active Cu phase on the ZnO/Al<sub>2</sub>O<sub>3</sub> support matrix [4.13]. This stabilization of metal Cu by the anion-modified ZnO/Al<sub>2</sub>O<sub>3</sub> phase occurred on an atomic scale and, hence, the joint Cu-ZnO/(Al<sub>2</sub>O<sub>3</sub>) interface appeared relatively smooth in the corresponding HRTEM micrographs (see Fig. 4-3 a-b).

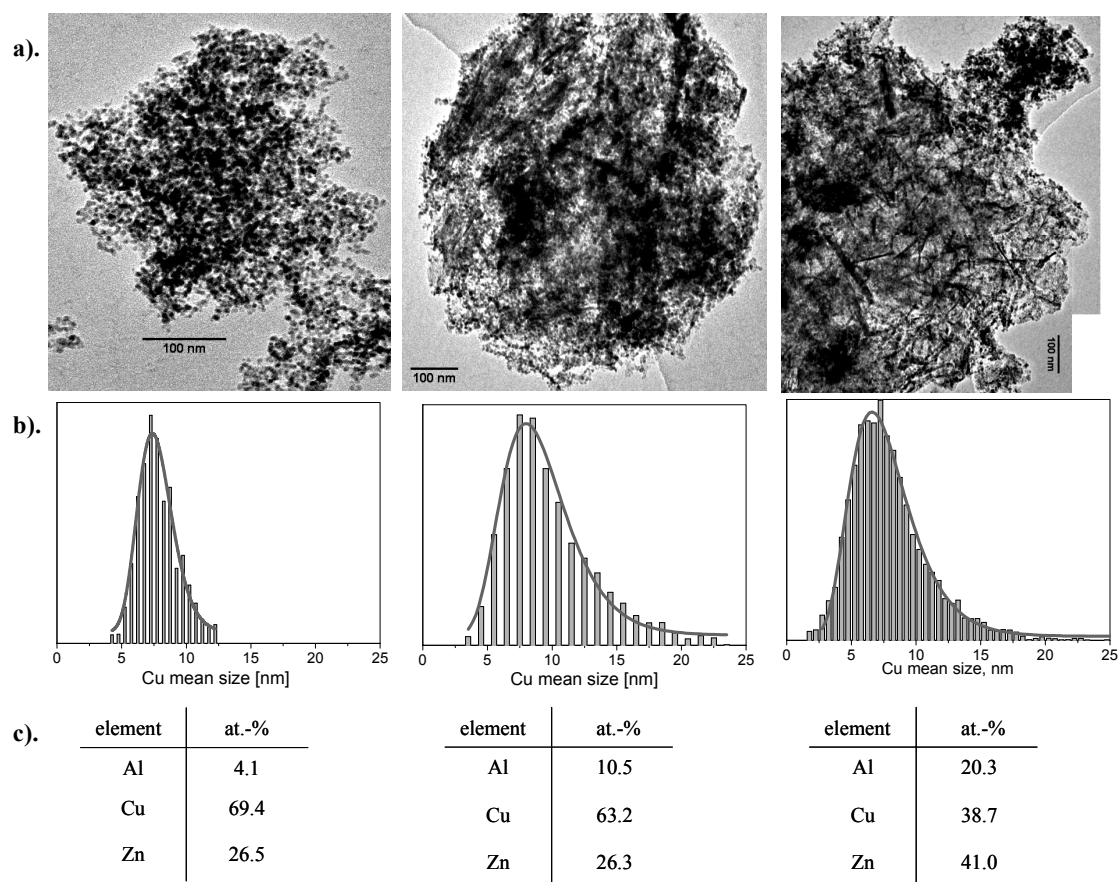


**Fig. 4-1:** Characteristic TEM overview images (a), and the corresponding Cu particle size distribution (b), and Cu/Zn/Al- elementary composition (c) of an activated (reduced) Cu/ZnO/Al<sub>2</sub>O<sub>3</sub> catalyst.

Conversely to ZnO, alumina was present in different structures. It tended to segregate, and it occurred in mixed oxide particles. Accordingly, agglomerated masses of amorphous material, comparable in size with clusters of the Cu/ZnO nanoparticles observed, were found (see Fig. 4-3c). These agglomerates featured only traces of Cu and Zn. In addition, amorphous or poorly crystallized alumina was found to be intermixed with Cu and ZnO particles. Only in rare cases HRTEM images revealed small regions of better crystallized particles (Fig. 4-3e). The corresponding power spectrum, shown in the inset of Fig. 4-3e, allowed identification of a Spinel like cubic structure with the corresponding lattice distances

$d_{111}$ ,  $d_{311}$ ,  $d_{220}$  markedly closer to those of ZnAl<sub>2</sub>O<sub>4</sub> [4.14] than of pure cubic Al<sub>2</sub>O<sub>3</sub> [4.15]. Thereby, the positive correlation between the concentrations of Al and Zn locally determined with EDX within all samples supports the hypothesis on the formation of ZnAl<sub>2</sub>O<sub>4</sub> Spinel in the catalysts (Fig. 4-4). The latter phase has been suggested to significantly increase the stability of Cu supported ZnO/Al<sub>2</sub>O<sub>3</sub> methanol synthesis catalysts [4.16].

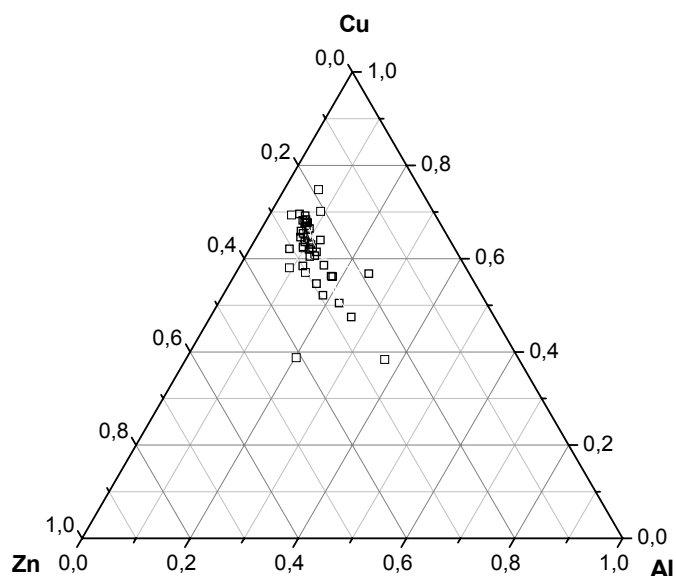


**Fig. 4-2:** Metal composition determined by Energy Disperse X-ray spectroscopy (EDX) of the activated Cu/ZnO/Al<sub>2</sub>O<sub>3</sub> catalysts studied.

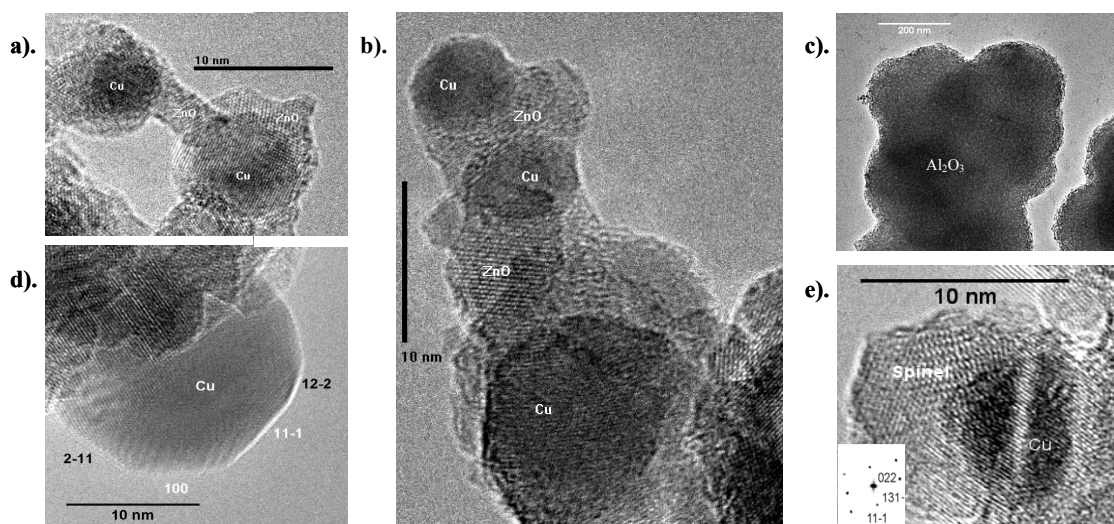


**Fig. 4-3:** Typical morphologies of Cu and ZnO particles of the Cu/ZnO/Al<sub>2</sub>O<sub>3</sub> catalysts investigated by means of high resolution electron microscopy (HRTEM).

Cu particles were often round, non-equilibrium formed exhibiting elliptic or spherical shapes which are sometimes truncated with  $\{111\}$ ,  $\{100\}$  or higher index facets (Fig. 4-3d). The mean Cu particle size in the catalysts studied was determined by measuring projected areas of individual particles in the TEM

images and calculating the equivalent diameter, which corresponded to the diameter of a circle with the same area (Fig. 4-5). The total number of Cu particles measured varied from 5060 to 24200 in the different samples. Redundant measurements performed to check that further increase in the number of measured particles did change neither the mean size nor the shape of the distribution curve revealed statistically meaningful results of the Cu particle size distribution. Conversely, ZnO and, especially, Al<sub>2</sub>O<sub>3</sub> were not well-shaped and separated from one another (see Fig. 4-3). Additionally, the oxide particles exhibited a lower degree of structural ordering (crystallinity) than Cu. Thus, a reliable determination of their mean sizes in TEM projections was not possible with the same accuracy as for the Cu phase.

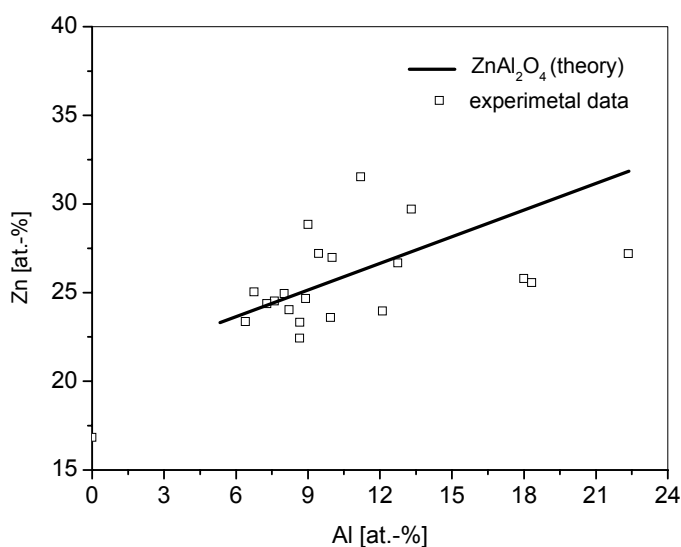


**Fig. 4-4:** Dependency of the local Zn concentration on the Al content in the analyzed TEM images, shown in Fig. 4-1a. The bold line corresponds to a theoretical Zn to Al ratio which is characteristic for ZnAl<sub>2</sub>O<sub>4</sub> Spinel.

Mean contact angles of Cu on ZnO measured were almost similar for all Cu/ZnO/Al<sub>2</sub>O<sub>3</sub> catalysts investigated. Generally, contact angles determined decreased with decreasing Cu particle size. Apparent work of adhesion calculated for Cu particles of similar sizes were significantly higher for the Cu/ZnO/Al<sub>2</sub>O<sub>3</sub> catalyst studied ( $W_{adh} = 1.68 \text{ J}\cdot\text{m}^{-2}$  for a 4 nm particle) than for a binary Cu/ZnO catalyst ( $W_{adh} = 1.39 \text{ J}\cdot\text{m}^{-2}$  [4.17]) without alumina as a stabilizing phase (Fig. 4-6). Apparently, the interaction between Cu and the support phase is much more intensive in a Cu/ZnO/Al<sub>2</sub>O<sub>3</sub> catalyst compared to a homologous binary Cu/ZnO catalyst. Accordingly, superior activities have been described for Cu/ZnO/Al<sub>2</sub>O<sub>3</sub> catalysts exhibiting a similar copper surface area like comparable Cu/ZnO catalysts [4.18].

Catalytic performance in methanol synthesis (MS) was roughly determined by the surface area of the active copper phase (Fig. 4-5a). Accordingly, the most active catalyst exhibited the highest Cu surface area and vice versa. However, a considerable deviation from a linear correlation between copper surface area and activity has been found (see Fig. 4-5a). The calculations of the Cu surface area were based on particle size considerations. Here, the effect of decreasing fraction of open surface with decreasing

particle size due to the stronger wetting of small Cu particles was taken into account, but not the coverage of Cu surface by smaller ZnO particles (Fig. 4-3 a-b). Nevertheless, the specific Cu surface area measured by N<sub>2</sub>O surface titration and the calculated surface area exhibited a similar trend within the Cu/ZnO/Al<sub>2</sub>O<sub>3</sub> catalysts investigated (Fig. 4-5). This supports the applicability of Cu surface area determination based on HRTEM investigations.

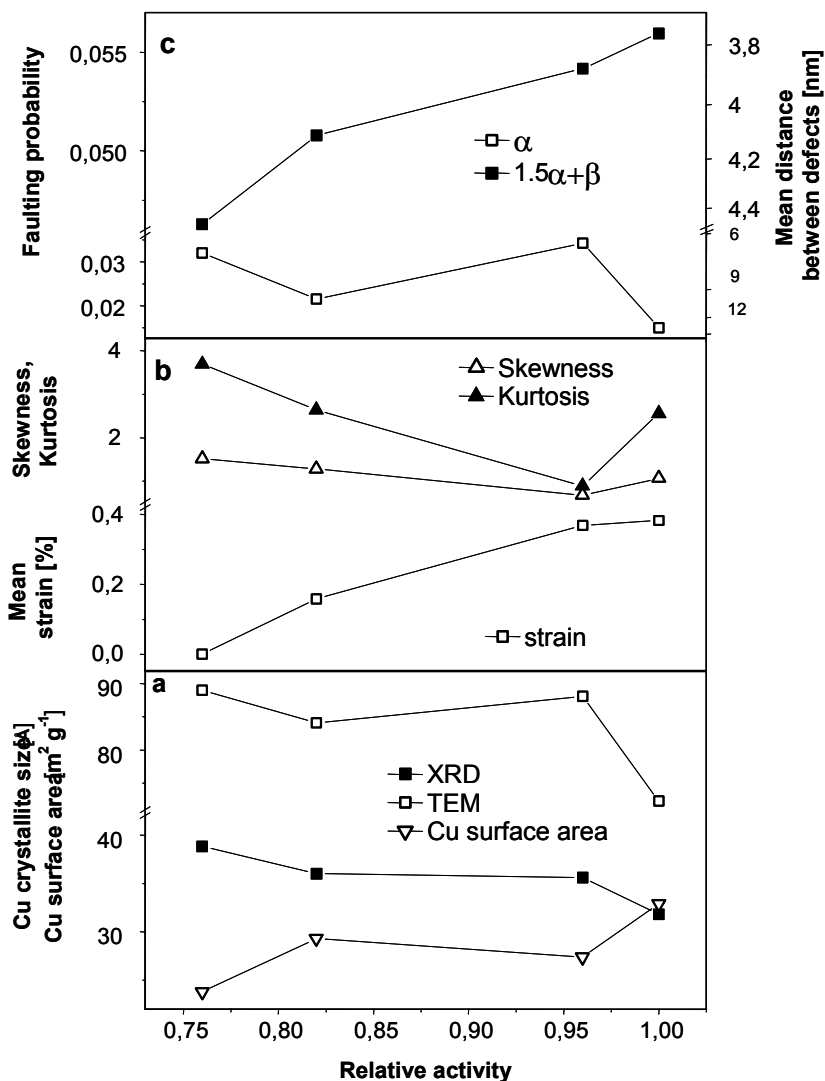


**Fig. 4-5:** Microstructural parameters of the Cu phase obtained by TEM and XRD in dependence on the relative catalytic activity in methanol synthesis.

The symmetry of the Cu particle size distribution (see Fig. 4-1b) observed for all catalysts in terms of skewness and kurtosis is shown in Fig. 4-5b. Here, the skewness accounts for the “tailoring” and the kurtosis accounts for the “flatness” of the corresponding Cu particles size distributions. With the exception of the most active material, the skewness and kurtosis of the Cu particle size distribution correlated with the catalytic activity in methanol synthesis. This indicates that in addition to the overall Cu surface area (averaged Cu particle size) the degree of symmetry of the Cu particle size distribution -

the homogeneity of the microstructure - also affected the activity. The skewness (kurtosis) of an ideal *Gaussian* distribution function amounts to 0 (3), respectively. A pronounced asymmetry of the particle size distribution may result from sintering of smaller Cu particles during catalyst activation indicating an unfavorable microstructure of the methanol synthesis catalyst. Accordingly, a highly symmetrical, *Gaussian* like Cu particle size distribution was reflected in a superior catalytic activity of the Cu/ZnO/Al<sub>2</sub>O<sub>3</sub> catalysts studied (see Fig. 4-5b).

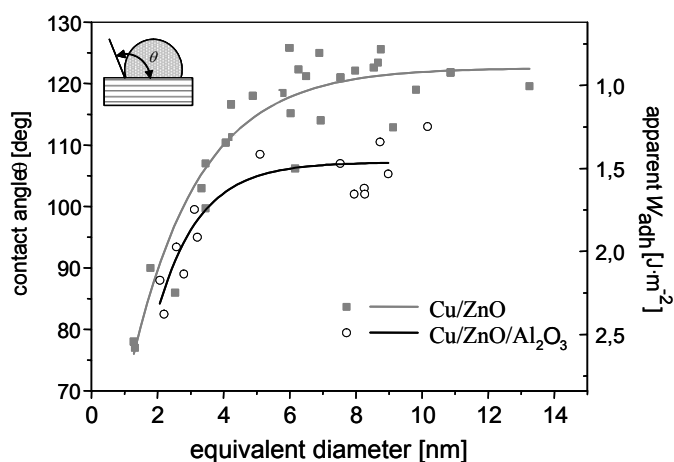


**Fig. 4-6:** Measured contact angle  $\theta$  as a function of the size of Cu particles supported on ZnO (black symbols) and on ZnO/Al<sub>2</sub>O<sub>3</sub> (open symbols). Right axis shows the apparent work of adhesion:  $W_{adh} = \gamma_{Cu} \cdot (1 + \cos\theta)$ , where  $\gamma_{Cu}$  is the surface energy of the Cu phase [4.17].

Cu particles, especially those larger than 5 nm, contained various structural imperfections, among which the most typical were twins and stacking faults. Fig. 4-7 a-b displays, exemplarily, a twin boundary ( $\beta$ ) and a stacking fault ( $\alpha$ ) in a Cu particle, respectively. Here, the stacking fault probability ( $\alpha$ ) in the Cu crystallites has been quantified from the degree of displacement of adjacent peaks in the XRD patterns in such pairs as  $(111)$ - $(200)$  (see Fig. 4-8), which are known to progressively shift in opposite directions, as  $\alpha$  increases [4.19]. Apparently, the stacking fault probability determined for all catalysts did not correlate with the activity, but scaled with the TEM particle size. Thus, smaller Cu crystallites contained fewer defects than larger ones (see Fig. 4-5). Mean distance between the defects were calculated as  $l = d_{111}/\alpha$  or  $l = d_{111}/1.5\alpha + \beta$ , where  $\beta$  represents the twinning probability in the Cu crystallites. Here, the mean distance between the defects was in the same range as the averaged Cu particle size determined by TEM (compare Fig. 4-5 a and c). This observation can be interpreted by a geometrical point of view: At a given mean distance between the defects, the larger particles contained defects with higher probability than the smaller ones. The overall faulting probability ( $1.5\alpha + \beta$ ) could be estimated from the comparison of apparent crystallite sizes determined by the shape analysis of different peaks. Due to a low intensity of higher XRD reflections of Cu other than  $(111)$  a detailed analysis was not possible. Therefore, a quantification of the overall faulting probability was done by a combined analysis of XRD and TEM data obtained. Here, the presence of stacking faults and twin boundaries was assumed to be solely responsible for the smaller domain size determined by XRD (Fig. 4-5a, filled squares) compared to the mean particle



size calculated by TEM (Fig. 4-5a, open squares). This assumption is reasonable since it is known that the presence of structural defects, such as stacking faults and twin boundaries, may account for this discrepancy [4.19]. Additionally, a spherical shape of the Cu particles has been assumed, which was supported by the TEM investigations (see Fig. 4-3).

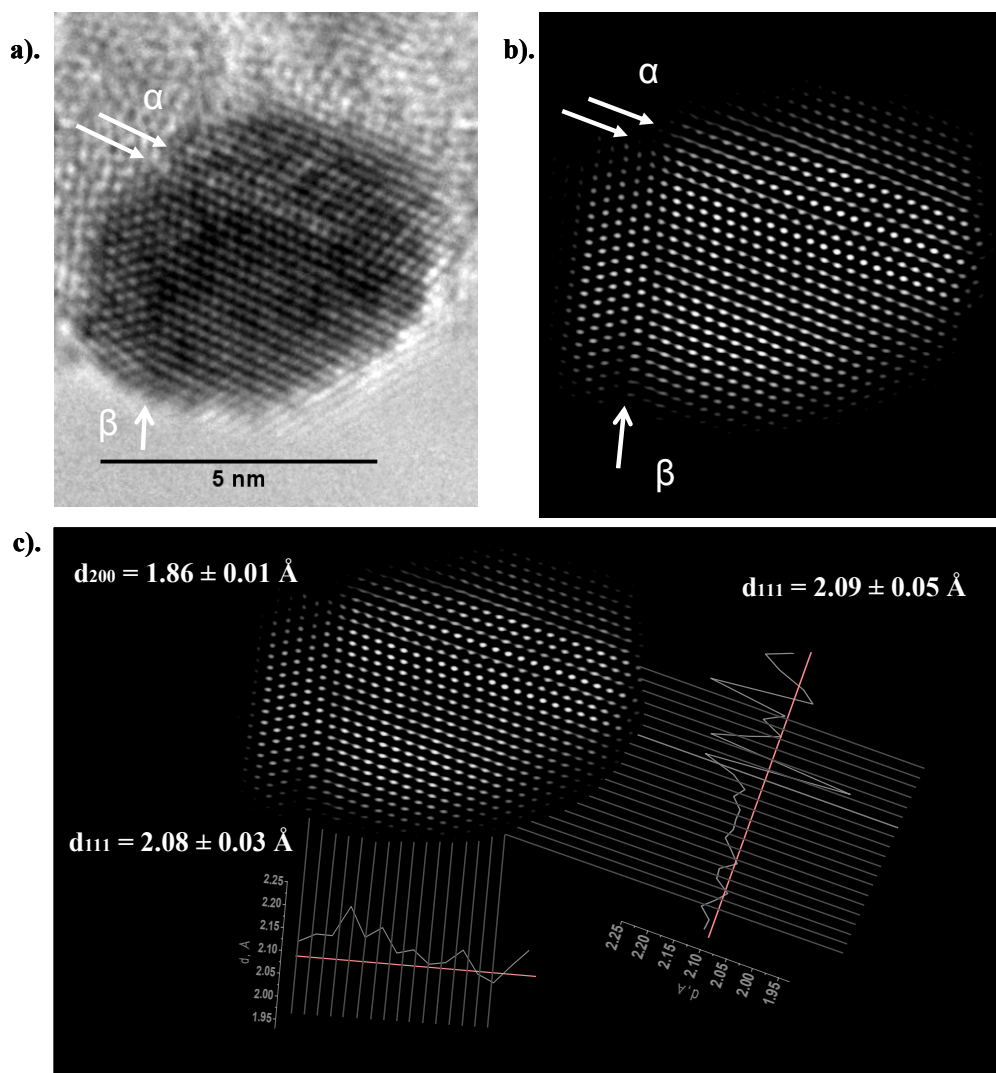


**Fig. 4-7:** (a) High resolution TEM image of a typical Cu particle in the Cu/ZnO/Al<sub>2</sub>O<sub>3</sub> catalysts exhibiting a stacking faults ( $\alpha$ ) in the  $(111)$  direction and a twin boundary ( $\beta$ ) between the  $(111)$  and  $(200)$  direction, (b) corresponding *Fourier-filtered* TEM image, and (c) corresponding d-spacing of the Cu phase present.

The results of the quantification of the overall defect probability ( $1.5\alpha + \beta$ ) in the Cu crystallites obtained by the combined analysis of the series of TEM and XRD data are shown in Fig. 4-5c. The activity clearly scaled with the overall faulting probability  $1.5\alpha + \beta$  (Fig. 4-5c). Since the methods of determination of  $1.5\alpha + \beta$  and  $\alpha$  were different, conclusion on the dominating role of twin boundaries in increasing activity of the Cu/ZnO/Al<sub>2</sub>O<sub>3</sub> catalysts studied may be doubtful (see Fig. 4-5c). Nevertheless,

the impact of planar defects in the Cu phase - without any differentiation - on the catalytic activity in the synthesis of methanol seemed to be obvious.

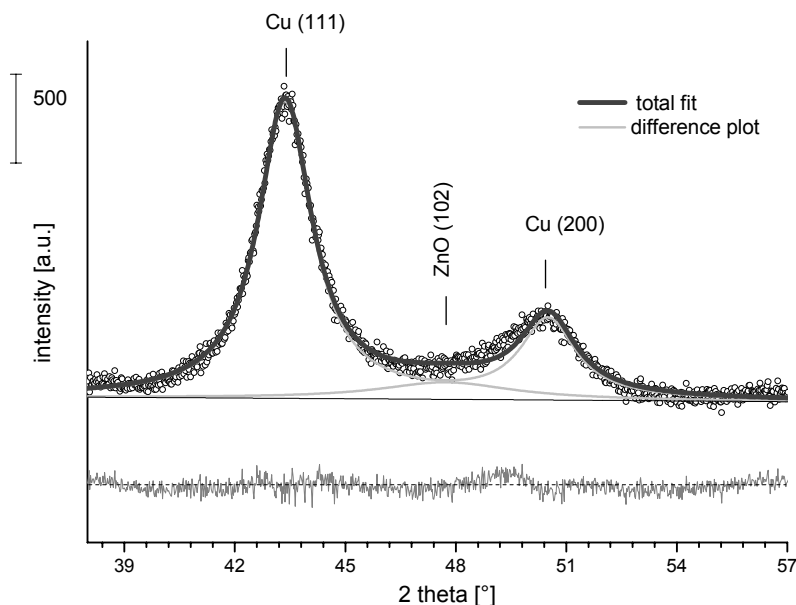


**Fig. 4-8:** Refinement of the corresponding ICSD model structures of *fcc* Cu and *hcp* ZnO to the experimental XRD pattern of a reduced Cu/ZnO/Al<sub>2</sub>O<sub>3</sub> catalyst.

Moreover, the activity correlated with the strain in Cu crystallites (Fig. 4-5b). The local d-spacing deviation (lattice strain) observed in the Cu particles is illustrated in Fig. 4-7c. The d-spacing of macro-crystalline *fcc* Cu amounts to  $d_{111} = 2.08 \text{ \AA}$ . Thus, Cu was present as metal and was not transferred into brass or copper oxides. The high degree of disorder in the Cu phase observed may result from an increased interface area between Cu and ZnO [4.20-4.21]. Accordingly, lattice strain was a consequence of the nanostructuring of Cu and ZnO in the activated Cu/ZnO/Al<sub>2</sub>O<sub>3</sub> catalysts studied (see Fig. 4-3 a-b). This is confirmed by HRTEM investigations which revealed a variety of both epitaxial and irregular arrangements of, in most cases, relatively smooth Cu-ZnO interfaces (Fig. 4-3 a-b). However, the parallelism observed between the lattice strain and the overall faulting probability may indicate the presence of a causal interconnection between both parameters. Moreover, the presence of twin boundaries, stacking faults and lattice strain in the Cu particles was assumed to affect surface properties of copper. Thus, the trends shown here clearly emphasize the essential role of structural imperfections in the Cu lattice on the activity of Cu/ZnO/Al<sub>2</sub>O<sub>3</sub> catalysts in methanol synthesis.

The Cu/ZnO/Al<sub>2</sub>O<sub>3</sub> catalysts investigated have been only analyzed in their reduced (activated) catalyst state. Thus, bulk structural defects, i.e. stacking faults, twin boundaries, and lattice strain, derived for the Cu phase of the reduced Cu/ZnO/Al<sub>2</sub>O<sub>3</sub> catalysts may basically differ from the corresponding Cu phase present under methanol synthesis conditions. Considering the strong linear correlation of the fraction of bulk structural imperfections in the reduced Cu/ZnO/Al<sub>2</sub>O<sub>3</sub> catalysts and the final activity obtained in methanol synthesis (Fig. 4-5 b-c) it seems to be reasonable to assume that the microstructure

of the reduced Cu/ZnO/Al<sub>2</sub>O<sub>3</sub> catalysts was also present under methanol synthesis conditions. Accordingly, the microstructural feature of “defective” Cu in the reduced catalyst state has been preserved under methanol synthesis conditions and, hence, the structure - activity correlations drawn were physically meaningful.

#### 4.1.4 Summary

A series of Cu/ZnO/Al<sub>2</sub>O<sub>3</sub> methanol synthesis catalysts with a metal composition close to the technical system were analyzed by a combination of electron microscopy (TEM) and X-ray diffraction (XRD). Structure - function relations obtained correlated with those derived from Cu/ZnO model systems [4.21]. Accordingly, the existence of structural imperfections in addition to the overall Cu surface area was positively related to the activity of Cu/ZnO/Al<sub>2</sub>O<sub>3</sub> catalysts in the synthesis of methanol. Here, the structural defects in the Cu nanoparticles have been found to be (i) planar defects, such as stacking faults, and twin boundaries, and (ii) lattice strain. These non-equilibrium structures seemed, however, to be strongly interrelated and, hence, a discrimination of the implication among the latter on the catalytic activity was not possible. Thus, the active sites in a Cu/ZnO/Al<sub>2</sub>O<sub>3</sub> methanol synthesis catalyst must be found predominantly in these structural elements without excluding that the regular surfaces (“perfect” or modified with line and point defects) will also contain some active centers, allowing single crystals of Cu or ZnO to exhibit some catalytic activity.

## 4.2 *Redox behavior of Cu/ZnO/Al<sub>2</sub>O<sub>3</sub> methanol synthesis catalyst*

### 4.2.1 Introduction

Since the interaction of Cu with the support oxides is known to affect not only particle morphologies but also the catalytic properties, the active copper phase has to be supported in an appropriate manner to obtain an optimal dispersion in the Cu/ZnO/Al<sub>2</sub>O<sub>3</sub> catalyst without allowing segregation of the Cu phase [4.11]. Thus, the catalytic activity and particular the thermal stability of Cu based methanol synthesis catalysts strongly depends on both the catalyst preparation [4.22] and the chemical composition [4.4].

Temperature programmed reduction (TPR) is a commonly used method for investigations of the influence of pretreatment procedures on the reducibility of catalysts [4.23, 4.24], the role of metal additives as promoter of reduction [4.25, 4.26], and the impact of certain phases in a multi-component system on the reducibility of a specific component [4.27]. The combination of temperature programmed reduction and subsequent re-oxidation (TPR/TPO) has been shown to be powerful technique for studying metal-support interactions in Cu based catalyst [4.28-4.32]. Generally, both TPR and TPO profiles are critically influenced by the experimental parameters applied, such as heating rate, flow rate, concentration of hydrogen (oxygen), and the amount of catalyst. Inappropriate experimental conditions cause a loss of peak resolution for multi-step processes leading to significantly different TPR (TPO) profiles. Hence,

experimental parameters employed during TPR/O have to be chosen carefully in order to achieve meaningful and reproducible data [4.33, 4.34].

This chapter focuses on the structural evolution of Cu phase in a Cu/ZnO/Al<sub>2</sub>O<sub>3</sub> methanol synthesis catalyst with an industrial relevant composition of Cu/Zn/Al = 60/30/10 at.-% [4.10] during successive reduction and re-oxidation. Complementary bulk *in situ* techniques (i.e. X-ray diffraction, and X-ray absorption spectroscopy), in combination with on-line mass spectrometry are employed to gain direct evidence for the Cu-ZnO/Al<sub>2</sub>O<sub>3</sub> synergisms in a methanol synthesis catalyst. Finally, in order to reveal structure - activity correlations the Cu/ZnO/Al<sub>2</sub>O<sub>3</sub> catalyst obtained after each redox cycle has been tested in methanol synthesis.

### 4.2.2 Experimental techniques

Cu/ZnO/Al<sub>2</sub>O<sub>3</sub> catalyst employed in this study was conventionally prepared by co-precipitation of hydroxycarbonates from metal nitrate solutions, and subsequently washed and dried [4.8]. Afterwards the precursor obtained has been calcined by heating linearly up to 330 °C with a rate of 5 K·min<sup>-1</sup> and an isothermal period of 3 h in synthetic air (100 ml·min<sup>-1</sup>). The amount of copper, zinc, and aluminum in the Cu/ZnO/Al<sub>2</sub>O<sub>3</sub> catalyst was determined by X-ray fluorescence (XRF) using a wavelength dispersive X-ray spectrometer (*S4 pioneer, Bruker AXS*). About 0.5 g of the calcined catalyst was physically mixed with 7 g of H<sub>3</sub>BO<sub>3</sub> (*Alfa Aesar*) and pressed at a force of 10 tons into a pellet with 35 mm in diameter. The accuracy obtained was estimated to be ± 1 at.-%.

Temperature programmed reduction and re-oxidation were done in a cyclic mode, in which a calcined CuO/ZnO/Al<sub>2</sub>O<sub>3</sub> methanol synthesis catalyst was subjected to reduction (TPR-1). The resulting Cu/ZnO/Al<sub>2</sub>O<sub>3</sub> catalyst was then subjected to re-oxidation (TPO-1). During the second cycle, the re-oxidized catalyst, present as a Cu/Zn/Al- mixed metal oxide, was re-subjected to reduction (TPR-2), and the reduced species was subsequently subjected to re-oxidation (TPO-2). Finally, the obtained sample has been reduced for a third time (TPR-3).

Thermogravimetric measurements (TG/MS) have been conducted on a *NETZSCH STA 449C* thermo balance to quantify the fraction of residual carbonates in the catalyst after the each reduction and oxidation process. Evolution of the corresponding gas phase was monitored on-line using an *OMNISTAR* mass spectrometer (*Pfeiffer*). Approximately 10 mg of the catalyst material were put into an alumina crucible and positioned onto the TG sample holder. The residual carbonate abundance in the calcined CuO/ZnO/Al<sub>2</sub>O<sub>3</sub> catalyst has been determined by heating to 1000 °C with a heating rate of 6 K·min<sup>-1</sup> in an argon flow (100 ml·min<sup>-1</sup>). Carbonate fraction of the reduced/ re-oxidized samples were quantified from the difference of the residual carbonate abundance of the freshly calcined sample and the CO<sub>2</sub> amount released during reduction (TPR) and re-oxidation (TPO) from calibrated mass spectra.

Sequential temperature programmed reduction (TPR) and oxidation (TPO) studies have been conducted on a TPD/R/O 1100 instrument (*CE Instruments*). Prior to the initial measurement the sample was purged in an Ar flow (10 ml·min<sup>-1</sup>) up to 150 °C to ensure an adsorbate free surface. TPR studies were performed according to the criteria of *Monti & Baiker* [4.33] and *Maleta & Caballero* [4.34].

Accordingly, TPR studies were carried out by passing 5 vol.-% H<sub>2</sub> (Ar) at a flow of 80 ml·min<sup>-1</sup> over 40 mg of the calcined catalyst sample contained in a quartz tube. The temperature was increased linearly to 300 °C with a heating ramp of 2 K·min<sup>-1</sup> and maintained isothermal for 0.5 h at 300 °C. Subsequent temperature programmed re-oxidation of the reduced samples (TPO) was performed by heating up to 330 °C with a rate of 5 K·min<sup>-1</sup> under a flow of 5 vol.-% O<sub>2</sub> in He (50 ml·min<sup>-1</sup>), and held at 330 °C for 3 h to maintain a complete oxidation. This temperature program during re-oxidation was identical to the calcination performed for that sample. Hydrogen (oxygen) consumption was measured by a thermal conductivity detector (TCD). Water and CO<sub>2</sub> formed during the redox cycles were trapped using soda lime (*Fluka*) to avoid interference with the measured TCD signal.

*In situ* X-ray absorption spectroscopy (XAS) experiments were performed at the Hamburg synchrotron radiation laboratory, HASYLAB (Germany), at beamline X1 at the Cu K -edge (E = 8979 eV) and the Zn K -edge (E = 9659 eV) in the transmission mode. XANES spectra were measured at the Cu K -edge with a time resolution of 2 min per spectrum (8959 eV - 9200 eV) during sequential reduction and re-oxidation cycles. TPR runs were performed with 5 vol.-% H<sub>2</sub> (He) at a flow of 10 ml·min<sup>-1</sup> by heating linearly to 250 °C with a ramp of 5 K·min<sup>-1</sup>, and an isothermal period of 1 h. Subsequent TPO runs were performed in a flow of 5 vol.-% O<sub>2</sub> (He) by heating up to 330 °C and an isothermal period of 3 h. *In situ* EXAFS spectra were measured after reduction and re-oxidation at ambient temperature to reveal microstructural changes of the Cu and Zn phases present. The gas phase composition was analyzed by mass spectrometry (*OMNISTAR, Pfeiffer*).

Analysis of the EXAFS spectra was performed according to the procedure described in chapter 3.2.6. Time resolved Cu K -edge XANES data were analyzed to reveal qualitative and quantitative information on the copper bulk phases during TPR and TPO conditions. Identification of the number of Cu phases was achieved by principal component analysis (PCA) of the experimental XANES spectra. Reference spectra for these phases were then used in a least squares fitting procedure of the time resolved spectra to determine the fraction of each phase present [4.35].

*In situ* X-ray diffraction (XRD) experiments during reduction and re-oxidation and data possessing were performed according to the procedure described in chapter 3.2.6. The *in situ* cell was loaded with approximately 80 mg of the as prepared catalyst. Generally, TPR studies were done in 5 vol.-% H<sub>2</sub> (He) at a total gas flow of 150 ml·min<sup>-1</sup> by heating linearly to 250 °C with a ramp of 6 K·min<sup>-1</sup>, and an isothermal period of 1 h. Subsequent TPO runs were performed in a flow of 5 vol.-% O<sub>2</sub> in He (150 ml·min<sup>-1</sup>) by heating up to 330 °C and an isothermal period of 3 h.

Methanol synthesis employing the calcined and the re-oxidized samples was carried out in a fixed bed micro reactor with an inner diameter of 2 mm filled with 180 mg of the sieve fraction (100-200) μm. Prior to the activity measurements, the samples were activated by reduction in H<sub>2</sub>. The samples were first treated for 12 h in a mixture of 5 vol.-% H<sub>2</sub> in He at 250 °C using a heating rate of 0.3 K·min<sup>-1</sup> and then for 4 h in pure H<sub>2</sub> at 250 °C. Methanol synthesis was performed at total pressure of 60 bar at different temperatures. The synthesis gas was composed of 59.5 vol.-% H<sub>2</sub>, 19.5 vol.-% CH<sub>4</sub>, 8 vol.-% CO<sub>2</sub>, 6 vol.-% CO, and balance N<sub>2</sub>. Total flow was kept at 60 ml·min<sup>-1</sup> by mass flow controllers. Methanol synthesis activity was measured under steady state conditions. Therefore, the sample has been aged for 48 h at 250

°C at 60 bar. Afterwards, steady state activities were determined for each temperature (250 °C, 230 °C, 210°C) after 24 h on stream by on-line GC analysis (*Varian MicroGC 4900*) equipped with a TCD detector using a PPU column, a COx column, and a Molsieve 5 Å column for separating polar products, such as water, methanol, CO<sub>2</sub> and CO, and the non polar products, such as He, H<sub>2</sub>, and CH<sub>4</sub>, respectively. A blank run conducted with a reactor filled with inert Al<sub>2</sub>O<sub>3</sub> (*Acros*) of the same sieve fraction did not show any detectable activity.

The specific Cu<sup>0</sup> surface area of the CuO/ZnO/Al<sub>2</sub>O<sub>3</sub> catalysts was measured by the dissociative chemisorption of nitrous oxide [4.36]. N<sub>2</sub>O pulse titration experiments were performed in quartz reactor at 30 °C under atmospheric pressure to avoid subsurface oxidation [4.37]. Prior to each experiment the catalysts was reduced in 5 vol.-% H<sub>2</sub> (N<sub>2</sub>) at 250 °C. Subsequently, the reactor was purged and cooled down to ambient temperature in a N<sub>2</sub> stream to achieve an adsorbate free reduced Cu surface. Pulses of N<sub>2</sub>O (99.5 vol.-%) were then introduced successively into the nitrogen stream. After each pulse the effluent gas was analyzed using a thermal conductivity detector (TCD). Titration continues until no further conversion of N<sub>2</sub>O has been observed. Cu surface area was calculated assuming a molar stoichiometry of Cu<sub>s</sub>/N<sub>2</sub> = 2 and a value of 1.46·10<sup>-19</sup> copper atoms per m<sup>2</sup> [4.38].

### 4.2.3 Results

The TPR profiles of the calcined (TPR-1) and re-oxidized catalysts (TPR-2, TPR-3) are shown in Fig. 4-9. The profiles corresponded to the reduction of CuO to metallic Cu. The TPR profile of the calcined, non treated sample consisted of at least two overlapping peaks. The onset of reduction appeared at 145 °C and reduction reached its maximal rate at 184 °C. Unexpectedly, the re-oxidized catalyst (TPR-2) required a lower reduction temperature than the non treated sample. The downshift in temperature of about 2 K was accompanied by a considerable change of the reduction profile shape (Fig. 4-9). The shoulder appeared at lower temperature side of the re-oxidized sample became more pronounced than in the TPR-1. Consistently, the onset of reduction for the re-oxidized sample was shifted to 125 °C. The reduction profile of the re-oxidized sample (TPR-2) was similar to that of the re-re-oxidized catalyst (TPR-3) in terms of reduction profile shape, and reduction temperature (see Fig. 4-9). The characteristics of the TPR profiles obtained during the redox treatment of the Cu/ZnO/Al<sub>2</sub>O<sub>3</sub> catalyst are summarized in Table 4-1. In addition to the change in the reduction profile shape, and the reduction temperature, the amount of hydrogen consumed during reduction was also different comparing the calcined (TPR-1) with the re-oxidized catalysts (TPR-2, TPR-3). The overall CuO content of the calcined sample has been determined by XRF to be (64.3 ± 0.8) at.-%. Thus, approximately 2 at.-% of CuO were not reduced during TPR-1. Conversely, during reduction of the re-oxidized samples all CuO present was completely reduced to metallic Cu which has been quantified from the amount of hydrogen consumed during reduction for TPR-2, and TPR-3 (Table 4-1). The amount of carbonates released during reduction has been computed based on thermogravimetric measurements (TG/MS). There was a certain amount of residual carbonates present in the catalyst, which persisted the mild thermal treatment employed during calcination, reduction and re-oxidation. Thereby, the abundance of residual carbonates continuously

decreased with cyclic TPR/ O applied, whereas the major fraction of CO<sub>2</sub> was released during TPR-1 (see Table 4-1).

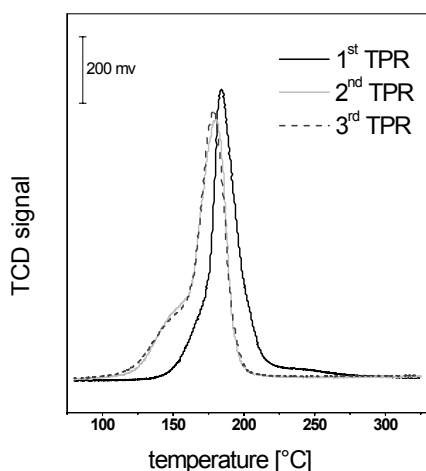


**Fig. 4-9:** Hydrogen consumption during temperature programmed reduction (TPR) of the calcined and re-oxidized CuO/ZnO/Al<sub>2</sub>O<sub>3</sub> catalysts (TPR-TPO-TPR-TPO-TPR).

**Table 4-1:** Comparison of the characteristics of the temperature programmed reduction profile obtained by conventional TPR, and by *in situ* studies (XRD, XAS), and abundance of CO<sub>2</sub> released during reduction of the derived Cu/Zn/Al- catalysts.

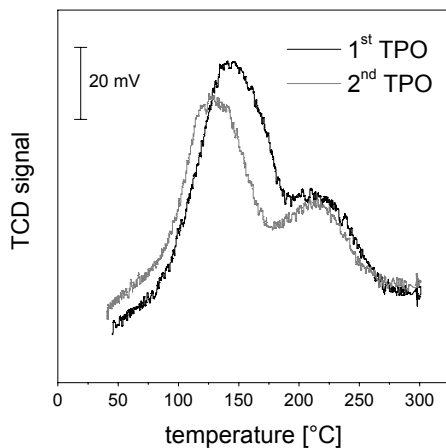
| sample | TPR                   |                        |  | XAS                   | XRD                   |
|--------|-----------------------|------------------------|--|-----------------------|-----------------------|
|        | T <sub>max</sub> [°C] | at.-% CuO <sup>1</sup> | Released CO <sub>2</sub> [ml] <sup>2</sup> | T <sub>max</sub> [°C] | T <sub>max</sub> [°C] |
| TPR-1  | 184 ± 1               | 62.5 ± 0.2             | -0.193                                     | 261 ± 3               | 179 ± 1               |
| TPR-2  | 180 ± 1               | 65.0 ± 0.1             | -0.068                                     | 200 ± 3               | 163 ± 3               |
| TPR-3  | 178 ± 1               | 64.8 ± 0.2             | -0.034                                     | 190 ± 3               | 163 ± 1               |

1 Calculated from the amount of hydrogen consumed during TPR.

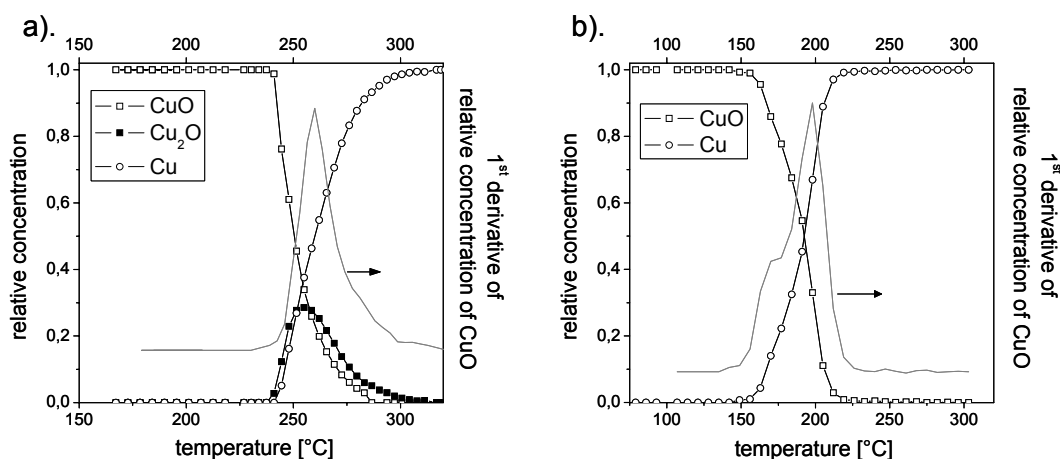
2 Released abundance of CO<sub>2</sub> has been determined by TG/MS.

Fig. 4-10 shows the TPO profiles of the previously reduced Cu/ZnO/Al<sub>2</sub>O<sub>3</sub> catalyst. Oxidation was characterized by two main peaks which were located at 141 °C and 218 °C for TPO-1, and at 130 °C and 212 °C for TPO-2, respectively (see Fig. 4-10). During TPO Cu was re-oxidized to CuO. *In situ* X-ray absorption spectroscopy was performed at the Cu K -edge to determine the evolution of the copper phases present during successive reduction and re-oxidation. A principal component analysis of the Cu K -edge XANES spectra revealed that three primary components were necessary to reconstruct the experimental XANES spectra obtained during TPR-1. The results of a least-squares fit procedure using probable reference compounds, i.e., Cu, Cu(I) oxide, Cu(II) oxide, during TPR-1 are shown in Fig. 4-11a. From these investigation it is evident that the shoulder in the TPR profile at lower temperature side corresponded to the appearance of Cu(I) oxide as an intermediate during the reduction of CuO to

metallic Cu (Fig. 4-11a). Conversely, the shoulder at lower temperature side in the TPR profile for TPR-2 (TPR-3) corresponded to a direct reduction of parts of Cu(II) oxide to metallic Cu indicating the presence of two types of bulk Cu. Cu(I) oxide as an intermediate was not detectable (see Fig. 4-11b).



**Fig. 4-10:** Oxygen consumption during temperature programmed oxidation (TPO) of the reduced Cu/ZnO/Al<sub>2</sub>O<sub>3</sub> catalysts (TPR-TPO-TPR-TPO-TPR).



**Fig. 4-11:** Evolution of copper phase during (a) TPR of the calcined catalyst (TPR-1), and (b) during TPR of the re-oxidized sample (TPR-2). The TPR profiles have been calculated by differentiation of the concentration profile (as a function of the temperature) of the CuO phase. The quantitative phase analysis is based on a least-squares fit of Cu K -edge XANES during TPR using suitable reference spectra of Cu, Cu<sub>2</sub>O, and CuO as described in the text.

The evolution of the Cu K -edge XANES position during re-oxidation (TPR-TPO) and re-re-oxidation (TPR-TPO-TPR-TPO) is shown in Fig. 4-12. During re-oxidation Cu was transformed to bulk CuO. The maxima of the oxidation rate were located at 130 °C (255 °C) for TPO-1 and 113 °C (207 °C) for TPO-2, respectively. This was qualitatively consistent with the results obtained from conventional TPO (compare Fig. 4-10 and Fig. 4-12). Fig. 4-13a (Fig. 4-13b) compares the Cu K -edge FT( $\chi(k)$ ·k<sup>3</sup>) measured directly after each oxidation step observed during TPO-1 (TPO-2), respectively. From the



measured EXAFS spectra it is evident that the two oxidation events observed during TPO-1 (TPO-2) corresponded to the oxidation of metallic copper to Cu(II) oxide, respectively (see Fig. 4-13a and b). Analysis of the extended fine structure (EXAFS) of the experimental XAFS spectra measured under TPR conditions at the Cu K -edge and Zn K -edge revealed changes in the short range order structure of the catalysts. The resulting pseudo radial distribution functions (RDF) at the Cu K -edge recorded after each reduction cycle are depicted in Fig. 4-14a. Deviations of the  $FT(\chi(k) \cdot k^3)$  of the treated catalyst were most pronounced for the amplitude of the 1<sup>st</sup> Cu-Cu shell ( $R < 3 \text{ \AA}$ ). A structural refinement of a theoretical spectrum of bulk *fcc* Cu to the experimental spectra revealed no shift of the distances of the copper metal shells after each reduction cycle (Table 4-2).

**Table 4-2:** Structural parameters obtained from refinement of theoretical Cu model structure to the experimental Cu K -edge EXAFS function measured for the calcined and re-oxidized samples at ambient temperature.

| Pair    | CN | R [ $\text{\AA}$ ] |       |       |                    |
|---------|----|--------------------|-------|-------|--------------------|
|         |    | TPR-1              | TPR-2 | TPR-3 | Cu <sub>ref.</sub> |
| Cu – Cu | 12 | 2.54               | 2.54  | 2.54  | 2.56               |
| Cu – Cu | 6  | 3.61               | 3.61  | 3.61  | 3.61               |
| Cu – Cu | 24 | 4.44               | 4.44  | 4.43  | 4.42               |
| Cu – Cu | 12 | 5.20               | 5.19  | 5.19  | 5.11               |
| Cu – Cu | 24 | 5.56               | 5.56  | 5.56  | 5.72               |

Results of a structural refinement of a theoretical spectrum of CuO to the experimental spectra obtained for the calcined and re-oxidized samples are summarized in Table 4-3. There was a considerable change in the characteristic local structure of the oxidized samples in comparison to the non treated (as prepared) sample. Apparently, during the initial redox cycle (TPR-1 followed by TPO-1) the distances of Cu-O as well as Cu-Cu are slightly decreased indicating a contraction of the CuO lattice cell after the first redox cycle. Further reduction and re-oxidation (TPR-TPO-TPR-TPO) resulted in a similar short range order structure of CuO for TPO-2 as obtained after TPO-1 (see Table 4-3). The RDF's measured at the Zn K -edge after each TPR cycle are depicted in Fig. 4-14b. The first peak,  $R = (1 - 2) \text{ \AA}$ , in the RDF corresponded to the 1<sup>st</sup> Zn-O shell present in bulk ZnO. Differences between the reduced samples were pronounced at distances above 2  $\text{\AA}$ . For the re-reduced catalysts the intensity of the peak located at 3  $\text{\AA}$  was significantly increased compared to the spectra measured after TPR-1. This peak corresponded to the 1<sup>st</sup> Zn-Zn shell in a ZnO crystal. Table 4-4 summarizes the results of structural refinement of a ZnO model structure to the experimental Zn K -edge  $FT(\chi(k) \cdot k^3)$  obtained for the as prepared sample, after reduction, and after re-oxidation. The local structure of ZnO phase present considerably changed after the initial reduction. The distinct increase of the Zn-O distances observed indicates an expansion of the ZnO unit cell after TPR-1 (see Table 4-4).

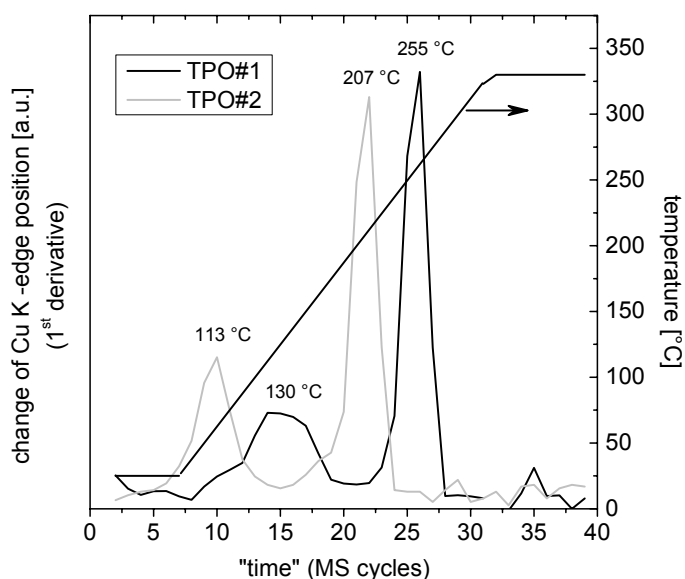


**Fig. 4-12:** Evolution of the Cu K -edge XANES position obtained from its first derivative during temperature programmed oxidation (TPO). The energy offset (edge position) has been determined as the position of the inflection point of the continuum.

**Table 4-3:** Structural parameters obtained from refinement of theoretical CuO model structure to the experimental Cu K -edge EXAFS function measured for the calcined and re-oxidized samples at ambient temperature.

| Pair    | CN | R [Å]       |       |       |                     |
|---------|----|-------------|-------|-------|---------------------|
|         |    | as prepared | TPO-1 | TPO-2 | CuO <sub>ref.</sub> |
| Cu – O  | 2  | 1.95        | 1.94  | 1.94  | 1.95                |
| Cu – O  | 2  | 1.95        | 1.96  | 1.96  | 1.96                |
| Cu – O  | 2  | 2.93        | 2.87  | 2.88  | 2.78                |
| Cu – Cu | 4  | 2.96        | 2.91  | 2.92  | 2.90                |
| Cu – Cu | 4  | 3.15        | 3.09  | 3.09  | 3.08                |

Fig. 4-15 shows the background subtracted and normalized XANES spectra measured at the Cu K -edge of the calcined and re-oxidized (TPO-1, TPO-2) samples. XANES spectrum of the calcined sample was distinctly different from those of the re-oxidized samples in terms of edge position, white line intensity, and the XANES profile. Here, the XANES spectra of the re-oxidized samples (TPO-1, TPO-2) corresponded to bulk CuO. Especially the pre-edge features, indicated with an arrow in Fig. 4-15 were characteristic for a distorted square pyramidal environment of copper surrounded by oxygen, such as in

bulk CuO. Contrarily, the calcined, non treated sample did not exhibit this pronounced pre-peak feature in the corresponding Cu K -edge XANES spectrum (see Fig. 4-15).

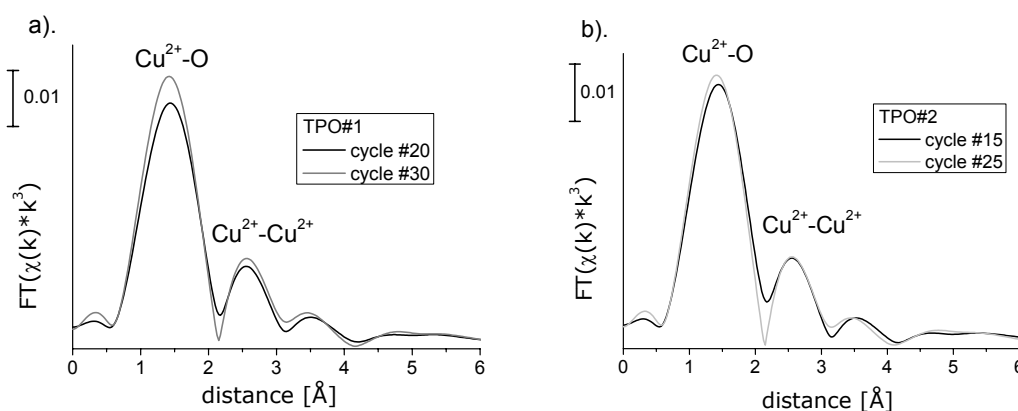


**Fig. 4-13:** Experimental Cu K -edge  $FT(\chi(k) \cdot k^3)$  spectra recorded during temperature programmed oxidation. The spectra were taken after each oxidation event observed during temperature programmed oxidation of (a) the re-oxidized (TPO-1), and (b) re-re-oxidized sample (TPO-2).

**Table 4-4:** Structural parameters obtained from refinement of theoretical ZnO model structure to the experimental Zn K -edge EXAFS function recorded after each reduction and re-oxidation cycle at ambient temperature.

| sample              | R [Å]       |             |              |
|---------------------|-------------|-------------|--------------|
|                     | Zn-O (CN=3) | Zn-O (CN=1) | Zn-Zn (CN=6) |
| as prepared         | 1.94        | 1.99        | -            |
| TPR-1               | 1.95        | 2.05        | 3.21         |
| TPO-1               | 1.94        | 2.04        | 3.22         |
| TPR-2               | 1.96        | 2.03        | 3.23         |
| TPO-2               | 1.94        | 2.03        | 3.24         |
| TPR-3               | 1.96        | 2.01        | 3.25         |
| ZnO <sub>ref.</sub> | 1.97        | 1.98        | 3.25         |

Fig. 4-16a shows the X-ray diffraction pattern of the reduced Cu/ZnO/Al<sub>2</sub>O<sub>3</sub> catalyst recorded after each TPR cycle. The characteristic reflections of Cu and ZnO obtained are indicated in the diffractograms. Due to its highly amorphous character and/ or nanosized crystallites alumina did not appear as a separate phase in the XRD pattern. During reduction in hydrogen, CuO was reduced to copper metal. No Cu<sub>2</sub>O was detectable in the XRD pattern (Fig. 4-16a). The results of a structural refinement of the corresponding ICDD model structures of Cu [4.39] and ZnO [4.40] to the experimental pattern are

summarized in Table 4-5. The lattice constants of Cu were in agreement with macro-crystalline *fcc* Cu. Averaged Cu crystallite sizes calculated from line broadening of Cu (*111*) peak exhibited a continuous increase during the redox treatment. Similar to the Cu phase, the crystallite sizes of ZnO also continuously increased during the redox treatment (Table 4-5). In contrast to the Cu phase, lattice constants of ZnO determined after each reduction cycle were generally lower than for its macro-crystalline form, but tended to approach the bulk value with redox treatment. Accordingly, successive reduction and re-oxidation resulted in a continuous increase in the lattice cell volume of ZnO (see Table 4-5).

**Table 4-5:** Structural parameters of the reduced samples obtained from refinement of theoretical Cu and ZnO model structures to the experimental XRD pattern recorded after each reduction at ambient temperature.

| sample | Cu <sup>1</sup> |                                 |        | ZnO <sup>2</sup> |              |                     |        |
|--------|-----------------|---------------------------------|--------|------------------|--------------|---------------------|--------|
|        | <i>a</i> [Å]    | I( <i>111</i> )/I( <i>220</i> ) | D [nm] | <i>a</i> [Å]     | <i>c</i> [Å] | V [Å <sup>3</sup> ] | D [nm] |
| TPR-1  | 3.615           | 3.9                             | 3.9    | 3.23             | 5.18         | 54.0                | 1.8    |
| TPR-2  | 3.615           | 3.6                             | 5.0    | 3.24             | 5.20         | 54.6                | 2.1    |
| TPR-3  | 3.615           | 3.3                             | 6.1    | 3.24             | 5.24         | 55.0                | 3.8    |

<sup>1</sup>  $a(\text{Cu}_{\text{fcc}}) = 3.6150 \text{ \AA}$ ,  $I(111)/I(220) = 2.2$  [4.39].

<sup>2</sup>  $a(\text{ZnO}) = 3.2495 \text{ \AA}$ ,  $c(\text{ZnO}) = 5.2069 \text{ \AA}$ ,  $V(\text{ZnO}) = 54.98 \text{ \AA}^3$  [4.40].

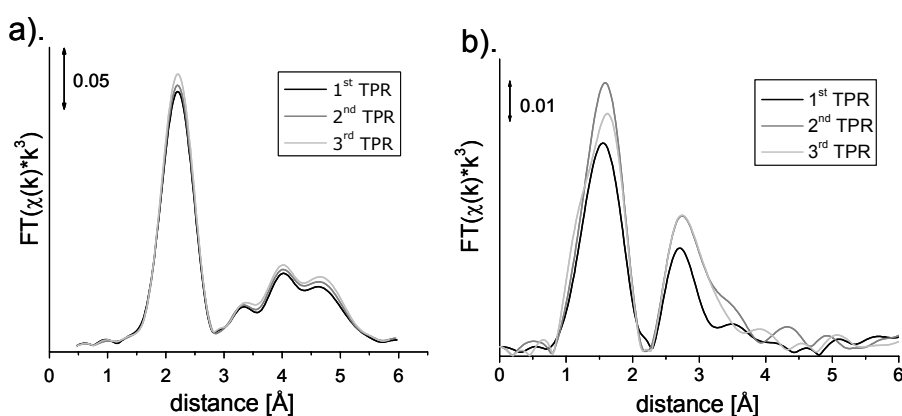


**Fig. 4-14:** Experimental  $\text{FT}(\chi(k) \cdot k^3)$  measured at (a) Cu K-edge, and at (b) Zn K-edge. The spectra were recorded after each temperature programmed reduction cycle at ambient temperature.

Fig. 4-16b shows the XRD pattern of the calcined and the re-oxidized catalysts. The presence of crystalline malachite like phase [4.41] was clearly visible for the calcined, non treated sample (Fig. 4-16b). This phase most probably originated from crystallization and/ or chemisorption of water and CO<sub>2</sub> during storage of this sample under ambient air and, hence, was not a relict due to an improper calcination

temperature employed. Accordingly, optimum calcination temperature with respect to the activity of the Cu/ZnO/Al<sub>2</sub>O<sub>3</sub> catalyst studied has been determined to be 330 °C. The crystalline malachite like phase disappeared during the initial reduction step (see Fig. 4-16a). From the relatively high background between 10° and 25° 2θ obtained for all diffractograms it can be speculated that all samples still contained residual hydroxycarbonates which appeared X-ray amorphous (Fig. 4-16 a-b). This is also evident from analysis of the evolved gas atmosphere during the reduction and re-oxidation cycles, in which a concurrent release of H<sub>2</sub>O and CO<sub>2</sub> has been always observed. During TPO all Cu was oxidized to bulk CuO. No reflections of Cu<sub>2</sub>O or other Cu sub-oxides were visible in the powder diffraction patterns of the re-oxidized catalysts (Fig. 4-16b). Due to the severe overlap of CuO and ZnO reflection a reliable refinement in order to achieve lattice constants was not possible for the oxidized samples.

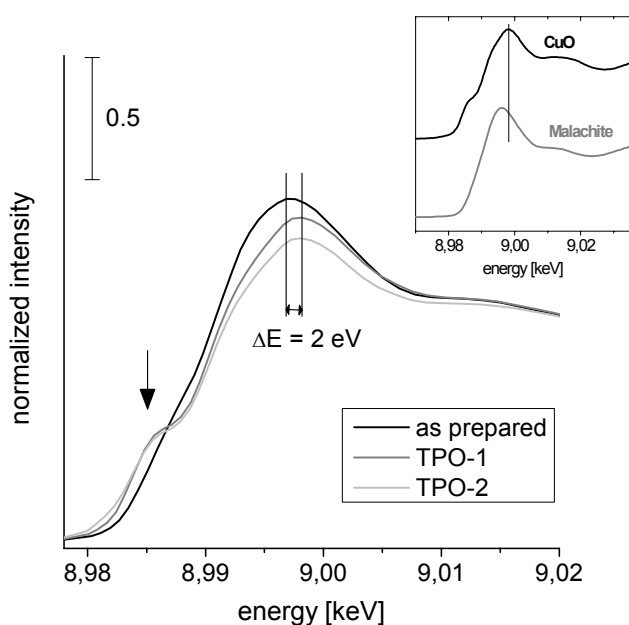


**Fig. 4-15:** Cu K -edge XANES spectra measured at ambient temperature for the calcined (as prepared) and re-oxidized catalysts (TPO-1, TPO-2). Insert shows the Cu K -edge XANES spectra of bulk CuO and Malachite (Cu<sub>2</sub>CO<sub>3</sub>(OH)<sub>2</sub>; [4-41]) measured as references.

Table 4-6 summarizes the normalized weight time yield of methanol (WTY) determined at different temperatures for the calcined (as prepared) and treated Cu/ZnO/Al<sub>2</sub>O<sub>3</sub> catalysts. Highest activity has been observed for the re-oxidized sample (TPO-1). Further reduction and successive re-oxidation (TPO-2) of the latter sample resulted in a slightly lower activity in methanol synthesis. Accordingly, the calcined, non treated sample exhibited the lowest methanol synthesis activity of all catalysts studied. Error bars have been determined to be approximately 1 % to 3 % of the weight time yield obtained (Table 4-6). Thus, the differences in methanol synthesis activity determined at reaction temperatures  $\leq 230$  °C diminished comparing the calcined with sample TPO-2, and comparing sample TPO-1 with sample TPO-2. Conversely, even at low reaction temperatures sample TPO-1 exhibited a considerable higher activity than the calcined, non treated sample (Table 4-6). The observed activities in methanol synthesis were not

reflected in the specific Cu surface areas determined for all samples. Intuitively, successive reduction and re-oxidation was accompanied by a continuous loss of the overall Cu surface area (see Table 4-6).

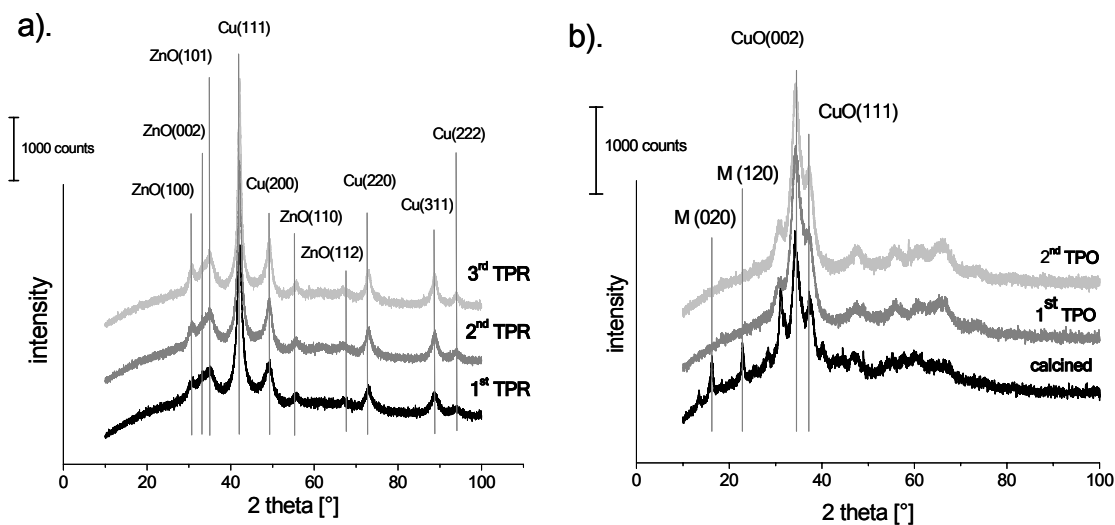


**Fig. 4-16:** Powder X-ray diffraction patterns recorded at ambient temperature after (a) reduction (TPR-1, TPR-2, TPR-3), and (b) of the calcined and re-oxidized (TPO-1, TPO-2) catalyst (M: Malachite  $\{(\text{Cu}_2\text{CO}_3(\text{OH})_2)\}$  [4-41]).

**Table 4-6:** Specific Cu surface areas,  $S_0(\text{Cu})$ , determined from  $\text{N}_2\text{O}$  titration and normalized reaction rate in methanol synthesis determined at different temperatures, and 60 bar of the calcined and re-oxidized  $\text{CuO}/\text{ZnO}/\text{Al}_2\text{O}_3$  catalysts. The rates in methanol synthesis were normalized to the rate of the as prepared  $\text{Cu}/\text{ZnO}/\text{Al}_2\text{O}_3$  catalyst. Prior to the catalytic testing, the derived  $\text{CuO}/\text{ZnO}/\text{Al}_2\text{O}_3$  catalysts have been *in situ* reduced according to the procedure described in chapter 4.2.2.

| Sample                 | $S_0(\text{Cu})$<br>[ $m_{\text{Cu}}^2 \text{ g}_{\text{cat.}}^{-1}$ ] | normalized rate |                 |                 |
|------------------------|--|-----------------|-----------------|-----------------|
|                        |  | 250 °C          | 230 °C          | 210 °C          |
| as prepared            | 26.1   | = 1             | $0.64 \pm 0.01$ | $0.33 \pm 0.01$ |
| Re-oxidized (TPO-1)    | 24.5   | $1.08 \pm 0.01$ | $0.72 \pm 0.02$ | $0.36 \pm 0.01$ |
| Re-re-oxidized (TPO-2) | 22.0   | $1.03 \pm 0.01$ | $0.70 \pm 0.03$ | $0.34 \pm 0.01$ |

#### 4.2.4 Discussion

Successive reduction and re-oxidation by conventional TPR/ O was employed for studying the  $\text{Cu}/\text{ZnO}/\text{Al}_2\text{O}_3$  interaction of an industrial relevant methanol synthesis catalyst. All experimental findings point to the fact that the microstructure of the calcined sample in its initial, as prepared state and after reduction (TPR-1) was considerably different from the re-oxidized (TPO-1, -2) and re-reduced (TPR-2, -3) samples, respectively. The second and third TPR profiles (TPR-2, -3) unexpectedly appeared at lower

temperature than the TPR-1. The shift in temperature observed was accompanied by a considerable change of the TPR profile shape indicative of a two-stage procedure (Fig. 4-9, Fig. 4-10), while further re-oxidation (TPO-2) and reduction (TPR-3) revealed only marginal differences to the previous reduction in terms of profile shapes, peak positions, and of the amount of H<sub>2</sub> (O<sub>2</sub>) consumed reduction (oxidation). Furthermore, after TPR-1 the calcined catalyst exhibited an incomplete reduction of CuO to metallic Cu, whereas subsequent re-reduction (TPR-2) led to a complete reduction (Table 4-1). These differences can be related to the unique microstructural and structural properties of the copper and Zn/Al- oxide phases directly after preparation and to their change upon redox cycling. In order to gain a detailed insight in the evolution of the phases present complementary investigations by *in situ* X-ray diffraction and absorption spectroscopy have been conducted. Additionally, the treated samples have been subjected to methanol synthesis reaction.

Temperature programmed XANES investigations at the Cu K -edge during reduction of the calcined, non treated sample revealed that the shoulder observed at lower temperature side in the TPR signal originated from the appearance of Cu<sub>2</sub>O as an intermediate phase during the reduction of CuO to metallic Cu (Fig. 4-11a). Thus, the TPR-1 profile indicates a homogeneous microstructure of the CuO phase in the calcined catalyst, which was reduced via an intermediate Cu(I) phase. This was in accordance with previous investigations of Cu based catalysts [4.32, 4.42]. After reduction, however, *in situ* XANES experiments during TPO-1 revealed that two different types of Cu were present, which were oxidized to CuO in independent, successive steps (Fig. 4-12, and Fig. 4-13a). This is in contrast to *Li* and *Imui* [4.43] who ascribed the two oxidation steps during re-oxidation of a Cu/ZnO/Al<sub>2</sub>O<sub>3</sub> catalyst to a stepwise oxidation of Cu(0) over Cu(I) oxide to Cu(II) oxide. Moreover, TEM investigations of the reduced Cu/ZnO/Al<sub>2</sub>O<sub>3</sub> catalyst obtained after TPR-1 exhibited a homogeneous microstructure of the Cu phase present (sample CZA-1 in chapter 3.2.2.). Thus, the two distinct oxidation steps observed during re-oxidation of the reduced Cu/ZnO/Al<sub>2</sub>O<sub>3</sub> catalysts (TPO-1) were not caused by a bimodal particle size distribution of the Cu phase present after TPR-1. The formation of Cu(II) oxide with different rates supports speculations that parts of the copper interacted differently with the ZnO/Al<sub>2</sub>O<sub>3</sub> matrix [4.28]. Conversely to TPR-1, reduction of the re-oxidized sample occurred without Cu(I) oxide as a detectable intermediate for the two different CuO species present. The two different Cu(II) species corresponded well to the two Cu<sup>0</sup> species observed during the previous oxidation (TPO-1). Apparently, reduction and subsequent re-oxidation had a significant impact on the microstructure of the Cu/Zn/Al- catalyst studied. These changes of the microstructure might be caused by the decomposition of residual Cu containing carbonates, which persisted the mild thermal treatment applied during calcination (Fig. 4-16b). Consistently, TG/MS investigations revealed that the major fraction of carbonates was decomposed during TPR-1 (Table 4-1). The presence of residual carbonates may also explain the differences observed in the white lines of the Cu K -edge XANES spectra of the re-oxidized samples, which were less broadened compared to the as prepared sample (Fig. 4-15). The shift of the continuous line position of about 2 eV to higher absorption energy observed for the re-oxidized samples (8.998 keV) compared to the calcined sample (8.996 keV) could not be attributed to the presence of reduced Cu species, such as Cu<sub>2</sub>O or even Cu, but rather to the presence of a carbonate phase in the non treated sample. Here, this microstructure directing effect observed after TPR-1 is rather ascribed to an amorphous carbonate phase,

which formed during calcination and remained in the oxides than to the crystalline Malachite like phase observed in the XRD pattern of the calcined sample. Since the calcination temperature of 330 °C was optimized in terms of complete decomposition of crystalline hydroxycarbonate precursors, the latter phase is assumed to have formed by chemisorption of carbon dioxide and water from air upon storage of the catalyst at ambient conditions. The presence of crystalline hydroxycarbonate phases is suggested to exhibit no beneficial effect on the catalytic performance of the Cu/ZnO/Al<sub>2</sub>O<sub>3</sub> catalyst studied. Conversely, residual amorphous carbonate phases have often been observed in Cu based catalysts [4.44] and a decisive role on the catalytic properties has been discussed [4.45]. Therefore, the effects of the amorphous carbonate phase on the microstructure and catalytic performance are assumed to outweigh the influence of the crystalline hydroxycarbonate formed by chemisorption.

Apparently, the re-oxidized samples resembled more to the bulk phases of CuO and ZnO than the calcined sample indicating a trend to the equilibrium properties with repeated redox treatment of the catalyst. Accordingly, the distances of the coordination shells around Cu and Zn and the lattice constants of ZnO approached values expected for the bulk phases with re-oxidation and re-reduction (see Table 4-3, Table 4-4, and Table 4-5). The change of the short as well as the long range order observed in both phases during the first redox cycle proceeded step-like and was evidenced by a contraction of the CuO and an expansion of the ZnO phase. The unique properties of the calcined sample differed significantly from the bulk phases and are known to critically depend on the various synthesis parameters during the preparation of a Cu/ZnO/Al<sub>2</sub>O<sub>3</sub> catalyst. This phenomenon is termed the “chemical memory” of the system. Obviously, this “memory” is abruptly lost upon redox cycling, which, again, can be related to the microstructural effect of the decomposition of residual carbonate present in the calcined sample. Thus, the different reduction behavior of the re-oxidized sample (TPR-2) compared to TPR-1 may be attributed to an irreversible change of the microstructure of the catalyst during the first reduction and re-oxidation. Structural changes during further re-oxidation (TPO-2) and subsequent reduction (TPR-3) did not change as significantly as during the initial redox cycles (Table 4-3). Apparently, the reduction behavior did not change applying further TPR/ O cycles and, consequently, the treated samples exhibited almost similar TPR (TPO) profiles (Fig. 4-9 and Fig. 4-10). Another gradual process related to thermal sintering was observed to be superimposed on the abrupt microstructural change happening during the first redox cycle. A higher averaged crystallite size due to particle growth is evidenced by decreasing XRD line widths, decreasing preferred orientation of Cu [4.46] (Table 4-5) and a loss of the overall Cu surface area (Table 4-6), but can also explain the slight decrease of the white line intensity observed for sample TPO-2 compared to sample TPO-1 (Fig. 4-15). A similar microstructural alteration during reduction of the calcined CuO/ZnO/Al<sub>2</sub>O<sub>3</sub> catalysts (TPR-1) has been also observed for the ZnO component in the catalysts studied (sample CZA-1 in chapter 3.4.2).

Independently on the number of reduction steps (TPR-1, -2, -3) employed, the copper component in the bulk was present as metallic copper which was not transferred into other phases, such as bulk oxides or alloys. Accordingly, no variations in lattice cell parameter (Table 4-5) and in distance of the individual metal-metal shells (Table 4-2) of Cu were observed. However, severe variations were observed for the oxides. Generally, ZnO can be considered as defect rich phase as suggested by the disproportional broadening of higher ZnO reflections with 2 theta in relation to the (100), (002), and (110) reflections



(Fig. 4-16a). Theoretically, it has been shown that stacking faults in *hcp* crystals, such as ZnO, cause a broadening of peaks of certain crystallographic directions. This broadening effect is symmetric and, hence, does not result in a shift in reflection positions [4.47]. Due to the low intensity of higher reflections in ZnO present in the reduced Cu/ZnO/Al<sub>2</sub>O<sub>3</sub> catalyst a quantification of the stacking fault probability was not possible (see Fig. 4-16a). The ZnO lattice became significantly contracted after TPR-1 compared to the re-reduced samples (TPR-2, TPR-3). Thereby, the latter samples exhibited a similar lattice cell volume of ZnO as its macro-crystalline form (Table 4-5). The changes in the ZnO lattice observed were clearly anisotropic, with a much higher enlargement for the *c* parameter upon reduction (see Table 4-5). Apparently, reduction of the re-oxidized sample (TPR-2) resulted in an increase of the ZnO lattice cell volume. Here, the smaller ZnO lattice cell volume obtained after TPR-1 indicates that Zn<sup>2+</sup> ions in the ZnO lattice were partially substituted by Cu<sup>2+</sup> and/ or Al<sup>3+</sup> reflecting the *Shanon* ionic radii for Zn<sup>2+</sup> (0.074 nm), Cu<sup>2+</sup> (0.073 nm), and Al<sup>3+</sup> (0.054 nm) [4.48]. The maximal concentration of Cu<sup>2+</sup> ions dissolved in well crystallized ZnO is limited and has been found to be less than 1 at.-% [4.49]. But, addition of aluminum during Cu/Zn/Al- catalyst formulation has been stated to considerably increase the solubility of Cu<sup>2+</sup> ions in the ZnO lattice [4.50]. Quantification of the amount of hydrogen consumed during TPR-1 revealed that approximately 2 at.-% of the copper remained unreduced (Table 4-1) and, as it was evident from the corresponding ZnO cell volumina determined after each TPR cycle, were dissolved in ZnO. Consistently, several examples of Cu<sub>x</sub>Zn<sub>1-x</sub>O phases formed during the preparation of Cu/ZnO catalysts have already been reported in the literature [4.51-4.54]. Here, most likely, Cu<sup>2+</sup> (and Al<sup>3+</sup> ions) dissolved in the ZnO host lattice were formed in the course of low temperature decomposition of residual Cu/Zn/(Al)- hydroxycarbonates upon reduction (TPR-1). This was accompanied by a considerable change of microstructure (Table 4-3 and Table 4-4). During reduction of the re-oxidized sample (TPR-2) the copper dissolved in the ZnO lattice was finally reduced to its metallic form (Table 4-1).

The specific Cu surface area measured by dissociative N<sub>2</sub>O chemisorption did not correlate with the activity observed for the treated Cu/ZnO/Al<sub>2</sub>O<sub>3</sub> catalysts. Despite a lower Cu surface area, the catalysts obtained after the reduction and re-oxidation (after TPO-1 and after TPO-2) exhibited a significantly higher activity than the non treated (as prepared) sample (see Table 4-6). Thus, in addition to the overall Cu surface area the activity is also dependent on other intrinsic factors like the morphology of the Cu particles [4.3, 4.4, 4.6, and 4.17]. Apparently, metallic Cu formed by reduction of {Cu(Al)}<sub>x</sub>Zn<sub>1-x</sub>O pseudo solid solution exhibited a significantly higher intrinsic activity (activity per Cu surface area) than Cu formed by reduction of primary CuO particles (Table 4-6). Consistently, an increase in the intrinsic activity during methanol steam reforming reaction, which formally represents the reverse of the methanol synthesis, has been observed for Cu/ZnO catalysts with extending number of oxidation/ reduction cycles by temporary addition of molecular oxygen to the reaction feed [4.55]. During reduction of the re-oxidized sample Cu migrated out of the ZnO host lattice, was reduced to its metallic form, and was preferentially located in the vicinity of stacking faults present on the ZnO surface [4.56]. Consequently, metallic Cu formed by reduction of {Cu(Al)}<sub>x</sub>Zn<sub>1-x</sub>O exhibited very strong Cu-support interactions reflected by a complex wetting of the Cu particles on the support oxide phases and, hence, higher intrinsic activities of Cu/ZnO/Al<sub>2</sub>O<sub>3</sub> methanol synthesis catalysts were observed [4.13, 4.21, 4.49, and 4.57]. The

slight decrease in activity observed after TPO-2 compared to TPO-1 was caused by thermal sintering of the copper but without suffering the structural alteration as it was observed during reduction of the calcined sample (Table 4-6). Accordingly, a similar microstructure of both Cu (CuO) and ZnO has been determined for these treated samples (see Table 4-2, Table 4-3, and Table 4-4). Thus, formation of a highly active copper phase obtained after TPO-1 was able to preserve its microstructure upon reduction and re-oxidation and, hence, exhibited similar intrinsic activities in methanol synthesis [4.58].

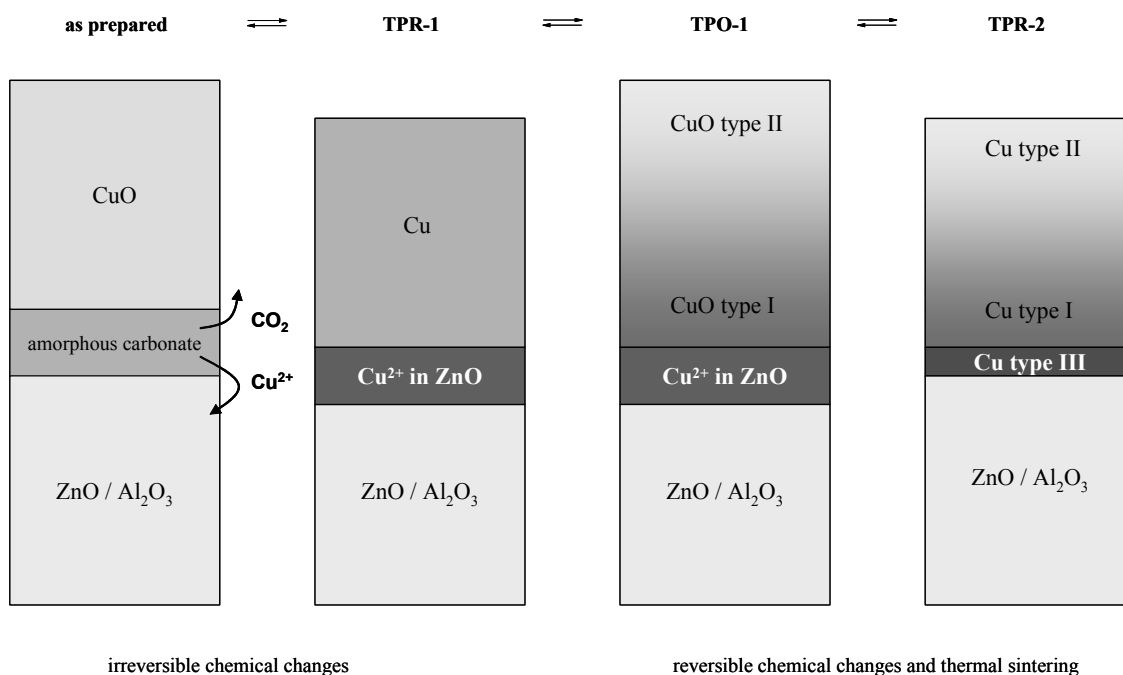


**Fig. 4-17:** Schematic model for the impact of successive reduction and re-oxidation (TPR/ O) on the microstructure of the derived Cu/Zn/Al- catalysts. Reduction of the as prepared CuO/ZnO/Al<sub>2</sub>O<sub>3</sub> catalyst (TPR-1) results in a reduction of copper from primary CuO particles and, in addition, in a decomposition of residual Cu/Zn/(Al)- hydroxycarbonates which is accompanied by a considerable change of the microstructure of the derived Cu/ZnO/Al<sub>2</sub>O<sub>3</sub> catalyst. Consequently, a {Cu(Al)}<sub>x</sub>Zn<sub>1-x</sub>O pseudo solid solution is formed. Finally, during TPR-2 the copper dissolved in the ZnO host lattice is reduced to its metallic form resulting in a superior interface between this Cu fraction and the ZnO/(Al<sub>2</sub>O<sub>3</sub>) matrix. Conversely to TPR-1, further re-oxidation and subsequent reduction (TPR-3) only results in reversible changes and some thermal sintering leading to a decreased overall Cu surface area.

The effect of successive reduction and re-oxidation (TPR/ O) on the microstructure of the derived Cu/ZnO/Al<sub>2</sub>O<sub>3</sub> catalysts is schematically depicted in Fig. 4-17. Reduction of the calcined (as prepared) CuO/ZnO/Al<sub>2</sub>O<sub>3</sub> catalyst results in a reduction of copper from primary CuO particles and, in addition, in a thermal decomposition of residual Cu/Zn/(Al)- carbonates, which are suggested to be located at the grain boundaries between CuO and ZnO/Al<sub>2</sub>O<sub>3</sub> particles, acting like a buffer layer. The decomposition is accompanied by a considerable change of the microstructure of the derived Cu/ZnO/Al<sub>2</sub>O<sub>3</sub> catalyst. Moreover, upon decomposition of the amorphous carbonate, fresh Cu-ZnO/(Al<sub>2</sub>O<sub>3</sub>) interfaces are created enabling interfacial reactions leading to the formation of a {Cu(Al)}<sub>x</sub>Zn<sub>1-x</sub>O pseudo solid solution.

Subsequent re-oxidation (TPO-1) occurred via a two-stage oxidation of two different Cu(0) species to bulk Cu(II) oxide. Thereby, the two oxidation steps observed were not caused by pronounced bimodal particle size distribution of the Cu phase present after TPR-1. The two distinct oxidation events observed in the corresponding TPO profile are rather caused by two different copper species exhibiting a different degree of interaction with the ZnO/Al<sub>2</sub>O<sub>3</sub> matrix. The latter species are denoted as Cu type I and Cu type II in the Fig. 4-17. Here, the differently pronounced support interaction of the primary CuO after TPO-1 (Cu after TPR-2), respectively, is schematically illustrated by a color gradient in the corresponding copper phase shown in Fig. 4-17.

Re-oxidation and subsequent reduction (TPR-2), finally, results in a reduction of the copper (Cu type III) dissolved in the ZnO lattice. This fraction of copper is thereby characterized by a superior interface with the ZnO/Al<sub>2</sub>O<sub>3</sub> matrix. An increase of the metal-support interaction for a part of the Cu phase (Cu type III) might be explained by the freshly created interfaces due to elimination of the carbonate buffer layer. It can be speculated that the formed copper is preferentially located in the vicinity of stacking faults present on the ZnO surface [4.56]. Due to this complex wetting of parts of the Cu particles on the Zn/Al-support oxides higher intrinsic activities, activity per Cu surface area, of the derived Cu/ZnO/Al<sub>2</sub>O<sub>3</sub> catalysts are observed in methanol synthesis. During further re-oxidation and subsequent reduction (TPR-3) the Cu/ZnO/Al<sub>2</sub>O<sub>3</sub> catalyst is thermally and chemically stressed leading to a considerable decrease of the overall Cu surface. The latter is a consequence of thermal sintering and, hence, rather a physical phenomenon, since in addition to the reversible redox chemistry, no further irreversible chemical events take place. Consistently, similar intrinsic activities in methanol synthesis have been observed for the re-oxidized Cu/ZnO/Al<sub>2</sub>O<sub>3</sub> catalysts (TPR-2 and -3). The initial processes happening during the first redox cycle comprise irreversible chemical reactions, i.e. the decomposition of residual carbonates. The change of the microstructure and, consequently, the implication for catalysis, due to this latter chemical phenomenon is much more pronounced compared to the physical events happening during repeated redox cycles.

#### 4.2.5 Conclusions

Evolution of bulk phases of a Cu/ZnO/Al<sub>2</sub>O<sub>3</sub> methanol synthesis catalyst during successive reduction and oxidation was monitored by *in situ* X-ray diffraction and *in situ* X-ray absorption spectroscopy. Based on these investigations the following can be concluded:

(i). Reduction of the calcined CuO/ZnO/Al<sub>2</sub>O<sub>3</sub> catalyst occurred via reduction of copper from primary CuO particles with Cu(I) oxide as an intermediate species according to a two step reduction process ( $\text{CuO} \rightarrow [\text{Cu}_2\text{O}] \rightarrow \text{Cu}$ ). Accordingly, a homogeneous microstructure of the Cu phase was found in the reduced Cu/ZnO/Al<sub>2</sub>O<sub>3</sub> catalyst. Additionally, during TPR-1 residual Cu/Zn/(Al)- carbonates were decomposed leading to the formation of a  $\{\text{Cu}(\text{Al})\}_x\text{Zn}_{1-x}\text{O}$  pseudo solid solution in which  $\text{Cu}^{2+}$  ( $\text{Al}^{3+}$ ) ions were partially dissolved in the ZnO lattice. This is accompanied by a considerable change of the microstructure of the derived Cu/ZnO/Al<sub>2</sub>O<sub>3</sub> catalyst.

(ii). Subsequent re-oxidation occurred via a two-stage oxidation of two different Cu(0) species to bulk Cu(II) oxide. The two oxidation steps observed were not caused by pronounced bimodal particle size

distribution of the Cu phase present after TPR-1. The formation of Cu(II) oxide with different rates rather supports the speculation that parts of the copper differently interact with the ZnO/Al<sub>2</sub>O<sub>3</sub> matrix. Here, Cu(I) oxide intermediates were not detected.

(iii). Successive reduction of the re-oxidized sample resulted in a downshift of reduction temperature which is accompanied by a significant change of the TPR profile. In contrast to the initial reduction, no intermediate Cu<sub>2</sub>O phase was detected. The two TPR events observed corresponded to the different types of CuO which have been also identified for the previous oxidation. Here, reduction of Cu occurred from two different crystalline CuO particles and, in contrast to the initial reduction, from the {Cu(Al)}<sub>x</sub>Zn<sub>1-x</sub>O phase present. The latter Cu phase was, thereby, characterized by an intimate Cu-support interaction.

(iv). Structural properties, i.e. phase evolution, microstructure of Cu (CuO) and ZnO, during further re-oxidation and reduction were similar to the previous redox cycle. Thus, Cu phase present after the initial redox treatment was able to preserve its microstructure in response to reduction and re-oxidation. Consequently, similar TPR (TPO) profiles were observed.

(v). During successive reduction and re-oxidation the Cu/ZnO/Al<sub>2</sub>O<sub>3</sub> catalyst investigated was chemically and thermally stressed and, consequently, suffered a considerable loss of the overall Cu surface area. Despite the lower Cu surface area, the catalysts obtained after the reduction and re-oxidation exhibited a significantly higher activity than the non treated Cu/ZnO/Al<sub>2</sub>O<sub>3</sub> catalyst in methanol synthesis. This superior intrinsic activity, activity per Cu surface area, was attributed to Cu formed by reduction from a certain {Cu(Al)}<sub>x</sub>Zn<sub>1-x</sub>O solid solution.

In summary successive TPR/ O cycles in combination with *in situ* techniques, X-ray diffraction and absorption spectroscopy are suitable methods for investigation of Cu-ZnO/Al<sub>2</sub>O<sub>3</sub> interactions in a methanol synthesis catalyst. Additionally, TPR/ O prior to the catalyst activation may be a novel extension to the classical preparation of Cu/ZnO/Al<sub>2</sub>O<sub>3</sub> catalysts in order to obtain superior activities in methanol synthesis.

### 4.3 References cited

- [4.1] G.C. Chinchin, K.C. Waugh, D.A. Whan, *Appl. Catal.*, 25 (1986) 101.
- [4.2] J. Soczynski, *Chem. Eng. Sci.*, 49 (1994) 115.
- [4.3] G.J.J. Bartley, R. Burch, *Appl. Catal.*, 43 (1988) 141.
- [4.4] M. Kurtz, H. Wilmer, T. Genger, O. Hinrichsen, M. Muhler, *Catal. Lett.*, 86 (2003) 77.
- [4.5] J. Agrell, H. Birgersson, M. Boutonnet, I. Melian-Cabrera, R.M. Navarro, J.L.G. Fierro, *J. Catal.* 219 (2003) 389.
- [4.6] B.L. Kniep, F. Girgadies, T. Ressler, *J. Catal.*, 236 (2005) 34.
- [4.7] X.R. Zhang, L.C. Wang, Y. Cao, W.L. Dai, H.Y. He, K.N. Fan, *Chem. Commun.*, 32 (2005) 4104.
- [4.8] J.C.J. Bart, R.P.A. Sneed, *Catal. Today*, 2 (1987) 1.
- [4.9] I.A. Kasatkin, T.I. Ivanova, *Crystallogr. Rep.*, 43 (1998) 1015.
- [4.10] P.J.A. Tijm, F.J. Waller, D.M. Brown, *Appl. Catal. A*, 221 (2001) 275.
- [4.11] M.V. Twigg, M.S. Spencer, *Appl. Catal. A*, 212 (2001) 161.
- [4.12] M.J.L. Gines, N. Amadeo, M. Laborde, C.R. Apesteguia, *Appl. Catal. A*, 131 (1995) 283.

- [4.13] T.M. Yurieva, L.M. Plyasova, V.I. Zaikovskii, T.P. Minyukova, A. Blik, J.C. van den Heuvel, L.P. Davydova, I.Y. Molina, M.P. Demeshkina, A.A. Khassina, E.D. Batyrevb, *Phys. Chem. Chem. Phys.*, 6 (2004) 4522.
- [4.14] ICDD-PDF 5-669.
- [4.15] ICDD-PDF 47-1292.
- [4.16] K. Klier, *Adv. Catal.*, 31 (1982) p. 292.
- [4.17] I. Kasatkin, B. Kniep, T. Ressler, *Phys. Chem. Chem. Phys.*, 9 (2007) 878.
- [4.18] M. Kurtz, N. Bauer, C. Büscher, H. Wilmer, O. Hinrichsen, R. Becker, S. Rabe, K. Merz, M. Driess, R.A. Fischer, M. Muhler, *Catal. Lett.*, 92 (2004) 49.
- [4.19] B.E. Warren, *X-ray Diffraction*, Dover Publications, New York (1990).
- [4.20] M.M. Günther, T. Ressler, B. Bems, C. Büscher, T. Genger, O. Hinrichsen, M. Muhler, R. Schlögl, *Catal. Lett.* 71 (2001) 37.
- [4.21] T. Ressler, B.L. Kniep, I. Kasatkin, R. Schlögl, *Angew. Chem. Int. Ed.*, 44 (2005) 4704.
- [4.22] M.V. Twigg, M.S. Spencer, *Appl. Catal. A*, 212 (2001) 161.
- [4.23] N. Wagstaff, R. Prins, *J. Catal.*, 59 (1979) 434.
- [4.24] B.H. Isaacs, E.E. Peterson, *J. Catal.*, 77 (1982) 43.
- [4.25] S.J. Gentry, N.W. Hurst, A. Jones, *J. Chem. Soc., Faraday Trans. 1*, 77 (1981) 603.
- [4.26] B.A. Sexton, A.E. Hughes, T.W. Turney, *J. Catal.*, 97 (1986) 390.
- [4.27] R. Brown, M.E. Cooper, D.A. Whan, *Appl. Catal. A*, 3 (1982) 177.
- [4.28] Y. Okamoto, K. Fukino, T. Imanaka, S. Teranishi, *J. Phys. Chem.*, 87 (1983) 3740.
- [4.29] G. Fierro, M. Lo Jacono, M. Inversi, P. Porta, F. Cioci and R. Lavecchia, *Appl. Catal. A*, 137 (1996) 327.
- [4.30] S. Kannan, A. Dubey, H. Knözinger, *J. Catal.*, 231 (2005) 381.
- [4.31] V.V. Pelipenko, D.I. Kochubey, A.A. Khassin, T.M. Yurieva, *React. Kinet. Catal. Lett.*, 86 (2005) 307.
- [4.32] I. Ritzkopf, S. Vukojevic, C. Weidenthaler, J.D. Grunwaldt, F. Schüth, *Appl. Catal. A*, 302 (2006) 215.
- [4.33] D.A.M. Monti, A. Baiker, *J. Catal.*, 83 (1983) 323.
- [4.34] P. Malet, A. Caballero, *J. Chem. Soc., Faraday Trans. 1*, 84 (1988) 2369.
- [4.35] T. Ressler, J. Wong; J. Roos, I.L. Smith, *Environ. Science Tech.*, 34 (2000) 950.
- [4.36] J.W. Evans, M.S. Wainwright, A.J. Bridgewater, D.J. Young, *Appl. Catal.*, 7 (1983) 75.
- [4.37] O. Hinrichsen, T. Genger, M. Muhler, *Chem. Eng. Technol.*, 23 (2000) 11.
- [4.38] R.M. Dell, F.S. Stone, P.F. Tiley, *Trans. Faraday Soc.*, 49 (1953) 201.
- [4.39] ICDD-PDF 4-836.
- [4.40] R.B. Heller, J. McGannon, A.H. Weber, *J. Appl. Phys.*, 21 (1950) 1283.
- [4.41] ICDD-PDF 41-1390.
- [4.42] M.M. Günther, B. Bems, R. Schlögl, T. Ressler, *J. Syn. Rad.*, 8 (2001) 619.
- [4.43] J.L. Li, T. Inui, *Appl. Catal. A*, 137 (1996) 105.
- [4.44] B. Bems, M. Schur, A. Dassenoy, H. Junkes, D. Herein, R. Schlögl, *Chem. Eur. J.*, 9 (2003) 2039.
- [4-45] M. Schur, B. Bems, A. Dassenoy, I. Kasatkine, J. Urban, H. Wilmes, O. Hinrichsen, M. Muhler, R. Schlögl, *Angew. Chem. Int. Ed.*, 42 (2003) 3815.
- [4.46] Y.N. Wen, J.M. Zhang, *Solid State Commun.*, 144 (2007) 163.
- [4.47] B.E. Warren, *X-ray diffraction*, Reading MA, Addison Wesley (1969), pp. 251-315.
- [4.48] R.D. Shanon, *Acta Crystallogr. A*, 32 (1976) 751.
- [4.49] A.A. Khassin, V.V. Pelipenko, T.P. Minyukova, V.I. Zaikovskii, D.I. Kochubey, T.M. Yurieva, *Catal. Today*, 112 (2006) 143.
- [4.50] T. M. Yurieva, T.P. Minyukova, *React. Kinet. Catal. Lett.*, 29 (1985) 55.
- [4.51] J.W. Andreasen, F. Berg Rasmussen, S. Hilveg, A. Molenbroek, K. Ståhl, M. Meedom Nielson, R. Feidenhans'l, *J. Appl. Cryst.*, 39 (2006) 209.

- [4.52] S. Ketchik, T. Minyukova, L. Kuznetsova, L. Plyasova, T. Yurieva, G. Boreskov, *React. Kinet. Catal. Lett.*, 19 (1982) 345.
- [4.53] J.B. Bulko, R.G. Herman, K. Klier, G.W. Simmons, *J. Phys. Chem.*, 83 (1979) 3118.
- [4.54] D. Grandjean, H.L. Castricum, J.C. van den Heuvel, B.M. Weckhuysen, *J. Phys. Chem. B*, 110 (2006) 16892.
- [4.55] M.M. Günter, T. Ressler, R.E. Jentoft, B. Bems, *J. Catal.*, 203 (2001) 133.
- [4.56] D.O. Klenov, G.N. Kryukova, L.M. Plyasova, *J. Mater. Chem.*, 8 (1998) 1665.
- [5.57] I. Kasatkin, P. Kurr, B.L. Kniep, A. Trunschke, R. Schlögl, *Angew. Chem.*, 119 (2007) 7465.
- [4.58] J.D. Grunwaldt, A.M. Molenbroek, N.-Y. Topsøe, H. Topsøe, B.S. Clausen, *J. Catal.*, 194 (2000) 452.
- [4.59] B. Bems, M. Schur, A. Dassenoy, H. Junkes, D. Herein, R. Schlögl, *Chem. Eur. J.*, 9 (2003) 2039.
- [4-60] M. Schur, B. Bems, A. Dassenoy, I. Kasatkine, J. Urban, H. Wilmes, O. Hinrichsen, M. Muhler, R. Schlögl, *Angew. Chem. Int. Ed.*, 42 (2003) 3815.

## Chapter Five

### Catalyst Modification by Carbon Dioxide Calcination

#### 5.1 Introduction

Mixed copper-zinc-aluminum hydroxycarbonates are well established for the formation of catalysts employed for methanol steam reforming, methanol synthesis, and water-gas-shift reaction. Classically, Cu/ZnO/(Al<sub>2</sub>O<sub>3</sub>) catalysts are prepared by co-precipitation of the metal nitrates with sodium carbonate as precipitation agent [5.1]. The calcination of appropriate Cu/Zn/Al- hydroxycarbonates to the mixed oxides is a crucial step in catalyst preparation. Optimum calcination temperatures with respect to activity roughly range from 300 °C to 400 °C and are confined on the basis of sintering restrictions of the copper phase present [5.2-5.5]. It is assumed that during calcination at mild temperatures CuO and ZnO are modified by residual OH<sup>-</sup> and CO<sub>3</sub><sup>2-</sup> groups [5.6]. These ad-mixed groups may serve as growth inhibitors of defect rich Cu particles in the final catalyst required for superior activity in methanol chemistry [5.7]. Accordingly, higher calcination temperatures cause sintering of the CuO phase, with attendant loss of activity due to a reduction of the Cu surface area of the derived Cu/ZnO catalysts [5.8]. Conventionally, calcination is conducted in an oxidizing atmosphere, i.e. air or oxygen. Earlier investigations revealed that calcination in the presence of carbon dioxide result in superior activities of the derived Cu- based catalysts in methanol decomposition [5.9] and methanol synthesis reaction [5.10]. Due to a higher partial pressure calcination in carbon dioxide may retain some particular ad-mixed carboxyl groups hindering the sintering process of the active copper phase and, hence, may result in an enhanced catalytic performance, i.e. activity, stability, of the derived Cu/Zn/(Al)- catalysts.

Here, a comprehensive study of the effect of carbon dioxide calcination on the microstructure and on the catalytic behavior in methanol chemistry of Cu/ZnO catalysts was performed. Therefore, Cu/Zn-hydroxycarbonate catalyst precursor was conventionally prepared by co-precipitation followed by calcination under different atmospheres: oxygen, carbon dioxide, a mixture of oxygen and carbon dioxide, and for comparison pure nitrogen. Complementary *in situ* bulk techniques, X-ray diffraction (XRD), and X-ray absorption spectroscopy (XAS), as well as thermal gravimetry (TG/MS) were used for bulk structural investigations of Cu/ZnO catalysts obtained. In order to reveal structure activity correlations the differently calcined Cu/ZnO catalysts were tested in both methanol steam reforming and methanol synthesis reaction. Additionally, calcination in carbon dioxide was performed on a homologous ternary Cu/Zn/Al- hydroxycarbonate precursor. The derived Cu/ZnO/Al<sub>2</sub>O<sub>3</sub> catalysts with alumina as an

additional refractory phase have been, similar to the binary Cu/ZnO catalysts, tested in methanol steam reforming and methanol synthesis reaction.

## 5.2 Experimental details

Cu/ZnO catalyst with a molar ratio of Cu:Zn = 70:30 was prepared by co-precipitation of (Cu,Zn)-hydroxycarbonates from metal nitrate solution. Precipitation occurred at 65 °C in an automated laboratory reactor system (*LabMax*®, *METTLER-TOLEDO*). Here, 500 ml of a premixed Cu/Zn nitrate solution (total 1.0 M) and a 1.6 M Na<sub>2</sub>CO<sub>3</sub> solution were dosed simultaneously to 400 ml distilled H<sub>2</sub>O. The nitrate solution was added with a constant dosing rate of 25 ml·min<sup>-1</sup> whereas the dosing rate of the precipitation agent was used to adjust the pH-value of the mother liquid to 7.0. After complete addition of the solutions, the resulting precipitates were aged under continuous stirring for 15 min in the mother liquor at 80 °C, filtered off, and washed with five portions of 400 ml of deionized water to lower the sodium content to acceptable levels (conductivity < 0.5 mS·cm<sup>-1</sup>). Afterwards, the resulting precipitate has been dried in a *Büchi-190* laboratory spray-dryer (inlet temperature: 200 °C; outlet temperature: 122 °C, air flow: 600 l·h<sup>-1</sup>). Different batches of calcination has been conducted in a rotating furnace (*XERION*) loaded with, in each case, 5 g of the catalyst precursor under the following gas phase compositions in:

- (i) synthetic air (**CZ-1**),
- (ii) 10 vol.-% O<sub>2</sub>/10% vol.-% CO<sub>2</sub>/ N<sub>2</sub> (**CZ-2**),
- (iii) 20%vol.-% CO<sub>2</sub>/ N<sub>2</sub> (**CZ-3**), and
- (iv) pure N<sub>2</sub> (**CZ-4**).

The total gas flow during the calcination experiments were kept at 100 ml·min<sup>-1</sup>. Calcination was performed by heating linearly up to 330 °C with a heating rate of 2 K·min<sup>-1</sup>, and holding isothermally at 330 °C for 3 h.

*In situ* X-ray diffraction (XRD) experiments during reduction of the differently calcined catalysts were performed according to the procedure described in chapter 3.2.6.

*In situ* EXAFS spectra were measured before and after each reduction treatment of the differently calcined catalysts to reveal structural changes of the Cu phases present in the derived catalysts. The experimental details and data processing has been already described in chapter 3.2.7.

Thermogravimetric measurements (TG/MS) have been conducted on a *NETZSCH STA 449C* thermo balance to quantify the fraction of residual carbonates of the derived Cu/Zn/Al- catalysts. Evolution of the corresponding gas phase was monitored on-line using an *OMNISTAR* mass spectrometer (*Pfeiffer*). Approximately 10 mg of the catalyst material were put into an alumina crucible and positioned onto the TG sample holder. The residual carbonate abundance in the calcined CuO/ZnO catalysts has been determined by heating to 1000 °C with a heating rate of 6 K·min<sup>-1</sup> in an argon flow (100 ml·min<sup>-1</sup>). This elevated temperature ensures that all residual carbonates decompose and are converted to the “true”



Cu/Zn- oxides. Carbonate fraction of the reduced samples were quantified from the difference of the residual carbonate abundance of the freshly calcined sample and the CO<sub>2</sub> amount released during reduction by evaluation of calibrated mass spectra.

Multiple heating rate experiments during catalyst reduction (1, 2, 4, and 6 K·min<sup>-1</sup>) were conducted for analysis of the reducibility of the derived CuO/ZnO catalysts. Therefore, the isoconversional method has been employed to elucidate kinetics of the catalyst activation process using *Thermokinetics* software (*NETZSCH*) [5.11]. Effective activation energies and frequency factors were calculated on the basis of differential isoconversional method of *Friedman* [5.12], and the corresponding integral method of *Flynn-Wall* [5.13] and *Ozawa* [5.14], respectively.

Steam reforming of methanol (MSR) was studied in a down-stream fixed bed stainless steel reactor (10 mm i.d.) with a thermocouple located in the catalyst bed. Approximately 300 mg of the (200-300) μm sieve fraction of a physical mixture of 50 mg of the freshly calcined catalyst and 250 mg BN (*Alfa Aesar*) were placed into the reactor. For better flow conditioning and heat transfer the catalyst bed was fixed between two layers of inert *Pyrex* beads (d = 500 μm). Prior to the activity measurement, the catalysts were activated *in situ* in 5 vol.-% H<sub>2</sub> (He) at 250 °C for 1 h. Catalytic measurements started by introducing an equimolar mixture of methanol (*Roth*, HPLC grade, > 99.9% purity) and distilled water by means of a HPLC pump (*Dionex HPLC 580*) into the reactor. Steady state activities were determined after a catalyst aging period of 48 h under MSR conditions at ambient pressure. In order to remove unconverted water and methanol, the product mixture leaving the reactor was passed through two condensers cooled to 0 °C and -20 °C, respectively, Dry product gas mixture achieved then passed a mass flow meter calibrated with a 3:1 H<sub>2</sub>:CO<sub>2</sub> mixture for conversion measurement. Composition of the dry product gas stream was monitored on-line using a *Varian 3800* gas chromatograph equipped with a thermal conductivity detector (TCD). Helium was applied as a carrier gas and separation was achieved using a 25 m x 0.53 mm *CarboPLOT P7* column heated to 30 °C. A blank run conducted with an reactor, solely filled with *Pyrex* beads, did not show any detectable activity. Selectivities were calculated at the basis of carbon.

Methanol synthesis data has been obtained from the differently calcined catalysts under industrially related conditions. The experimental details are given in chapter 4.2.2.

The specific Cu<sup>0</sup> surface area of the catalysts obtained was measured by the dissociative chemisorption of nitrous oxide (N<sub>2</sub>O- RFC) according to the procedure described in chapter 3.2.2.

## 5.3 Results and Discussion

### 5.3.1 Microstructure of the derived CuO/ZnO catalysts

The powder XRD pattern of the precipitated, washed, and subsequently dried precursor material shown in Fig. 5-1 corresponded to those of Rosasite, (Cu,Zn)<sub>2</sub>(OH)<sub>2</sub>CO<sub>3</sub> [5.15], and Aurichalcite, (Cu,Zn)<sub>5</sub>(OH)<sub>6</sub>(CO<sub>3</sub>)<sub>2</sub> [5.16]. After drying the sample has been subjected to calcination. Thereby, sample CZ-1 has been obtained by conventional calcination in synthetic air. Successively, the oxygen during

calcination has been partially (CZ-2), and completely (CZ-3) replaced by carbon dioxide. For comparison calcination has been alternatively conducted in pure nitrogen (CZ-4). XRD patterns obtained after calcination are summarized in Fig. 5-2a. Bulk phase analysis of the corresponding XRD pattern indicates that independent of the gas atmosphere applied the hydroxycarbonates in the bulk were transformed into the bivalent oxides (Fig. 5-2 a-c). No reflections corresponding to crystalline hydroxycarbonates were visible in the corresponding XRD pattern (Fig. 5-2a). The diffractograms only differed in the relative intensity of the CuO and ZnO reflections. The highest crystallinity qualified by comparison of the relative intensity of the reflections in the XRD pattern has been found for sample CZ-4 which was calcined in pure nitrogen. Poorest crystallinity has been obtained for CZ-1 (see Fig. 5-2a).

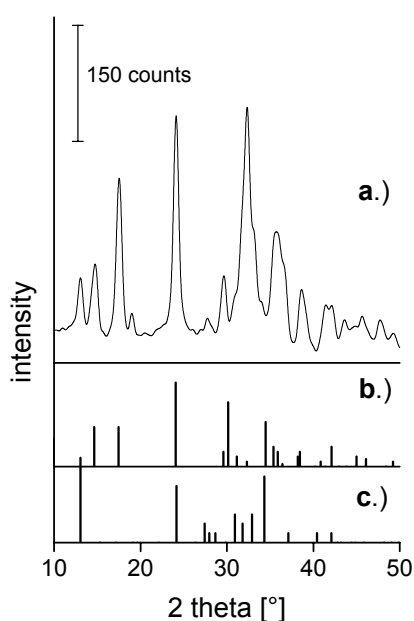


**Fig. 5-1:** XRD pattern of the precipitated, washed, and subsequently dried (Cu,Zn)- hydroxycarbonate precursor material used for the calcination experiments: (a) as prepared (Cu,Zn)- precursor, (b) powder X-ray diffraction file of Rosasite,  $(\text{Cu,Zn})_2(\text{OH})_2\text{CO}_3$ , and (c) powder X-ray diffraction file of Aurichalcite,  $(\text{Cu,Zn})_3(\text{OH})_6(\text{CO}_3)_2$ .

After catalyst activation in hydrogen (5 vol.-% H<sub>2</sub>), bulk CuO was reduced to copper metal which can be inferred from Fig. 5-2d. The results of a refinement of the corresponding ICDD model structures of *fcc* Cu [5.17] and ZnO [5.18] to the experimental pattern obtained after catalyst reduction are summarized in Table 5-1. Lattice constants of Cu were in agreement with ideal crystalline *fcc* Cu. This indicates that the bulk consisted of metallic copper which was not transferred into other phases, such as bulk oxides or Cu/Zn- alloys. Averaged Cu crystallite sizes calculated from line broadening of the most prominent Cu(*111*) reflection located at  $2\theta = 43.3^\circ$  (see Fig. 5-2d) nonlinearly increased with increasing CO<sub>2</sub> partial pressure during calcination. Apparently, carbon dioxide calcination resulted in higher mean Cu crystallite sizes of the derived Cu/ZnO catalysts than conventional calcination in synthetic air. Here, highest mean crystallite size of copper within all Cu/ZnO catalysts investigated has been determined for sample CZ-4 (Table 5-1). Additionally, the activated (reduced) Cu/ZnO catalysts revealed different

relative intensities of the high-index reflections of the Cu phase present, such as the Cu(311) reflection located at  $2\theta = 89.9^\circ$  (see Fig. 5-2d). Here, sample CZ-2 (CZ-4) exhibited the highest (lowest) intensity ratio of the Cu(111) to Cu(311) reflection, respectively (see Table 5-1). This clearly indicates that both the crystallite size of Cu and the morphology of the Cu phase could be manipulated by the calcination atmosphere.

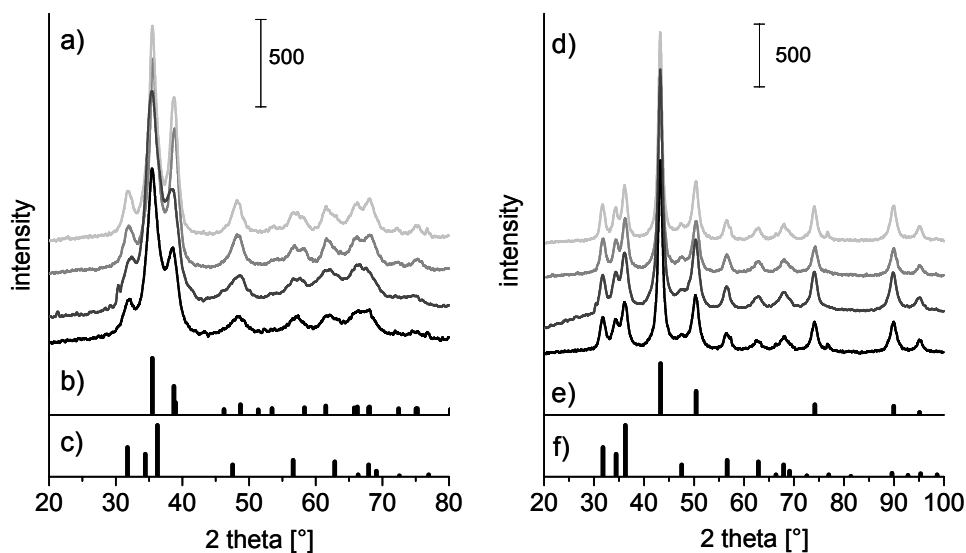


**Fig. 5-2:** XRD pattern of the differently calcined and *in situ* reduced Cu/Zn catalysts: (a) calcined CuO/ZnO catalyst precursors (from bottom to top: CZ-1, CZ-2, CZ-3, CZ-4), (b) powder X-ray diffraction file of CuO, (c) powder X-ray diffraction file of ZnO, (d) reduced Cu/ZnO catalysts (from bottom to top: CZ-1, CZ-2, CZ-3, CZ-4), (e) powder X-ray diffraction file of Cu, and (f) powder X-ray diffraction file of ZnO.

**Table 5-1:** Structural parameters, i.e. lattice constants, mean crystallite sizes of the Cu and ZnO phases present and characteristic intensity ratio of the Cu (111) to Cu (311) Bragg diffraction reflexes, of the reduced Cu/ZnO catalysts obtained from a refinement of theoretical Cu and ZnO model structures to the experimental XRD pattern recorded at ambient temperature.

| sample | $a$ (Cu)<br>[Å] <sup>a</sup> | D Cu(111)<br>[nm] | I(111)/I(311)<br>[-] <sup>a</sup> | $a$ (ZnO)<br>[Å] <sup>b</sup> | $c$ (ZnO)<br>[Å] <sup>b</sup> | D ZnO(100)<br>[nm] |
|--------|------------------------------|-------------------|-----------------------------------|-------------------------------|-------------------------------|--------------------|
| CZ-1   | 3.615                        | 6.1               | 2.4                               | 3.246                         | 5.217                         | 5.7                |
| CZ-2   | 3.615                        | 6.2               | 2.8                               | 3.248                         | 5.211                         | 5.4                |
| CZ-3   | 3.615                        | 6.6               | 2.6                               | 3.247                         | 5.213                         | 5.7                |
| CZ-4   | 3.615                        | 7.3               | 2.3                               | 3.248                         | 5.211                         | 6.5                |

<sup>a</sup>.  $a$  (Cu) = 3.615 Å, I(111):I(311) = 5.88 [5.17].

<sup>b</sup>.  $a$  (ZnO) = 3.249 Å,  $c$  (ZnO) = 5.207 Å [5.18].

Lattice parameters determined for the ZnO phase present in the activated Cu/ZnO catalysts were also in agreement with its macro-crystalline form (Table 5-1). Mean crystallite sizes of ZnO were slightly affected by carbon dioxide calcination and subsequent reduction. Consistently to the Cu phase in the activated Cu/ZnO catalysts, calcination in nitrogen (CZ-4) resulted in the largest crystallite size of ZnO. However, smallest averaged ZnO crystallite size has been obtained for sample CZ-2 which was calcined in a 1:1 mixture of oxygen and carbon dioxide (see Table 5-1). Apparently, calcination atmosphere has been also strongly influenced the texture of the ZnO phase present in the Cu/ZnO catalysts.

The effect of carbon dioxide on the microstructure of Cu phase in the Cu/ZnO catalysts was also investigated by X-ray absorption spectroscopy. The corresponding pseudo radial distribution functions (RDF) measured for the calcined catalysts are shown in Fig. 5-3 a-d. Here, the bulk mainly corresponded to CuO indicating that, consistently to the XRD investigations (Fig. 5-2a), the hydroxycarbonate precursor were transformed to the corresponding bivalent oxides upon calcination. Accordingly, the first peak, located at  $R \approx 1.6 \text{ \AA}$  in the  $FT\{\chi(k) \cdot k^3\}$ , can be attributed to Cu surrounded by oxygen in a square planar coordination, and the second peak, located at  $R \approx 2.6 \text{ \AA}$ , can be attributed to the first metal-metal shell in CuO. Deviations from bulk CuO were most pronounced for higher distances in the *Fourier*-transformed spectra at  $R > 3 \text{ \AA}$  (see Fig. 5-3 a-e) and mostly originated from the significantly smaller CuO crystallite sizes in the CuO/ZnO catalysts compared to macro-crystalline CuO measured as reference [5.19].

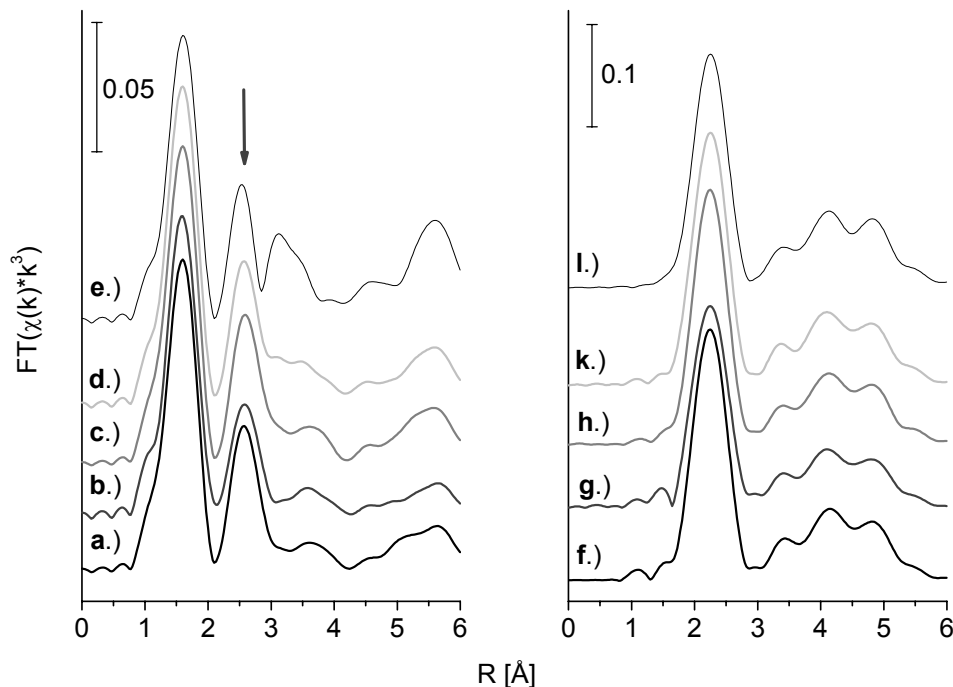


**Fig. 5-3:** Experimental Cu K -edge *Fourier*- transformed spectra,  $FT\{\chi(k) \cdot k^3\}$ , of the differently calcined (left), and subsequently reduced (right) Cu/ZnO catalysts. CZ-1: a) and f); CZ-2: b) and g); CZ-3: c) and h); CZ-4: d) and k); macro-crystalline CuO: e); and macro-crystalline Cu: l).

Additionally, the overall distance of the peak located at  $R \approx 2.6 \text{ \AA}$  in the corresponding RDF (indicated with an arrow in Fig. 5-3 a-e) of the calcined samples exhibited a slight displacement compared to macro-crystalline CuO measured as reference. The displacement found in the medium range order of the Cu phase in the differently calcined samples has been found to correlate linearly with the fraction of CO<sub>2</sub> employed upon catalyst calcination (Fig. 5-4a). Conversely, the displacement was not related to the fraction of oxygen used during calcination. Samples CZ-1 and CZ-4 exhibited a similar displacement in their (pseudo) RDF although they have been calcined under completely different atmospheres (see Fig. 5-4a). Generally, Malachite, a Cu containing hydroxyl-carbonate ( $\text{Cu}_2\text{CO}_3(\text{OH})_2$ ), exhibits a considerable higher distance of the 2<sup>nd</sup> Cu-O shell ( $R = 2.67 \text{ \AA}$ ) than bulk CuO ( $R = 2.53 \text{ \AA}$ ) in the corresponding RDF (see inset in Fig. 5-4b). Obviously, the pronounced displacement of the 2<sup>nd</sup> Cu-O shell observed for the calcined CuO/ZnO catalyst precursors indicates that with increasing fraction of CO<sub>2</sub> upon calcination and, hence, with increasing partial pressure of CO<sub>2</sub> the medium short range order in the  $\text{FT}(\chi(k) \cdot k^3)$  equaled more to Malachite than to bulk CuO. Thus, it can be concluded that calcination in carbon dioxide resulted in an incorporation of CO<sub>2</sub> into the CuO lattice, which was proportional to the partial pressure of CO<sub>2</sub> employed during calcination (see Fig. 5-4).

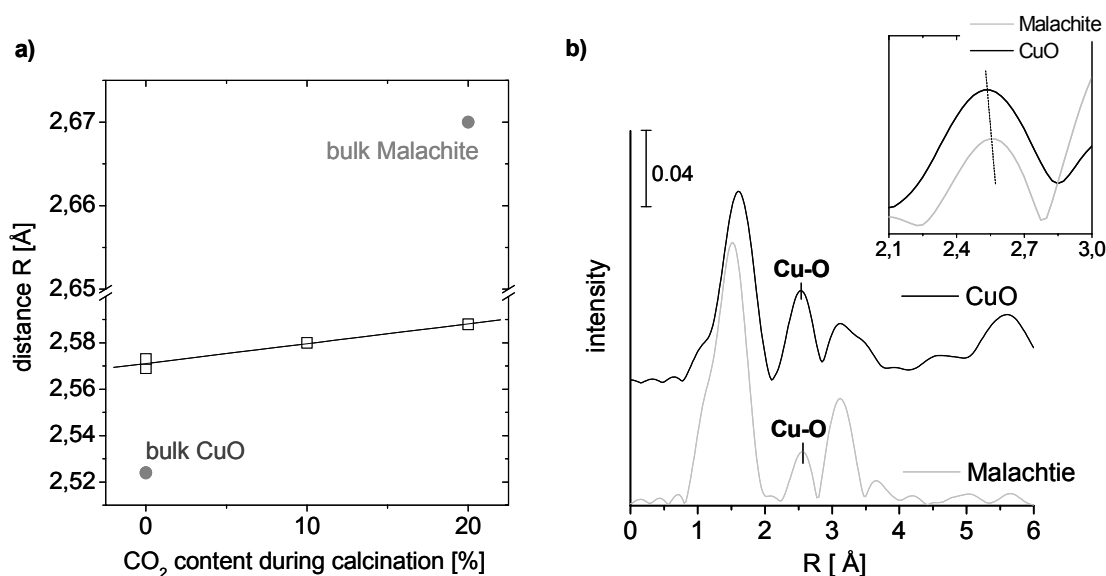


**Fig. 5-4:** (a) Dependency of the overall distance of the 2<sup>nd</sup> Cu-O shell of the Cu K -edge  $\text{FT}(\chi(k) \cdot k^3)$  of the differently calcined catalysts on the fraction of CO<sub>2</sub> employed during catalyst calcination. The corresponding Cu-O shell is indicated by an arrow in Fig. 5-3 a-e. (b) Cu K -edge  $\text{FT}(\chi(k) \cdot k^3)$  of bulk CuO and Malachite  $\{\text{Cu}_2\text{CO}_3(\text{OH})_2\}$  measured as references. The characteristic displacement of the corresponding Cu-O shell, located at  $R \approx 2.5 \text{ \AA}$  in the RDF, is highlighted in the inset.

After catalyst activation in hydrogen, bulk CuO was transformed to metallic Cu (Fig. 5-3 f-k). Metal-metal distances obtained from a refinement of theoretical Cu model structure to the experimental Cu K -edge EXAFS function were similar to bulk *fcc* copper within all Cu/ZnO catalysts studied. This was in accordance with the corresponding lattice constants extracted from the XRD data (Table 5-1). Conversely, *Debye-Waller* factors (DWF) determined for the individual Cu-Cu shells exhibited a

maximum for sample CZ-2 (Fig. 5-5). Lowest DWF has been determined for sample CZ-4, which was close to the value obtained for macro-crystalline Cu measured as reference. Apparently, structural disorder in the Cu phase of the derived Cu/ZnO catalysts was strongly influenced by the gas phase employed during calcination (“chemical memory” effect [5.1]). This effect was most pronounced for the medium range order structure ( $R > 5 \text{ \AA}$ ) of the copper phase (see Fig. 5-5). Generally, DWF’s are interrelated to the crystallite size: the smaller the crystallite size the higher the corresponding structural disorder (DWF). Here, Cu crystallite sizes determined were in the same range, except for sample CZ-4, within all Cu/ZnO catalyst investigated (see Table 5-1). Thus, different DWF’s obtained were rather caused by structural disorder in the Cu phase than a size effect.

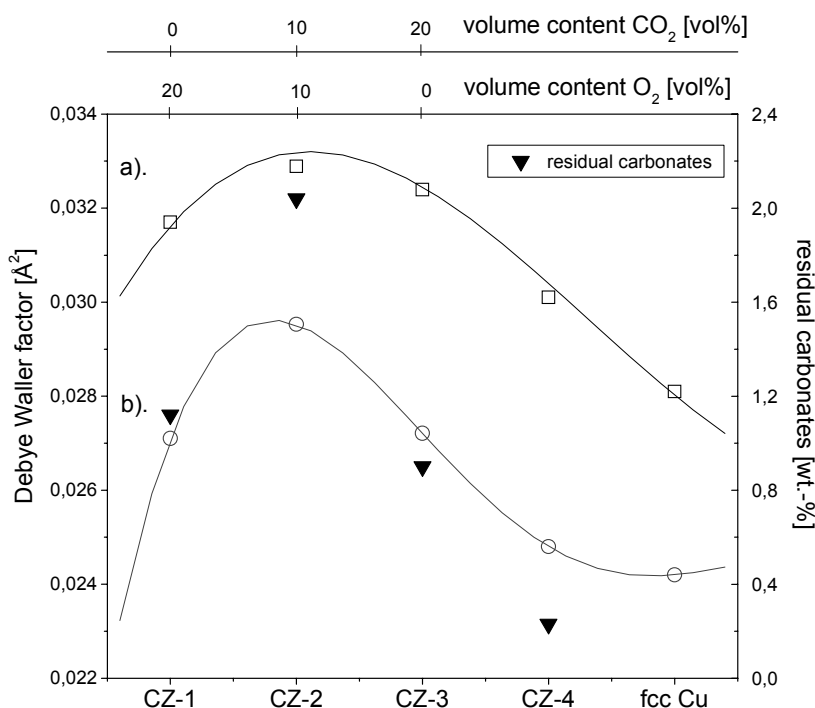


**Fig. 5-5:** Dependency of the *Debye-Waller* factors (DWF) determined for the (a) 4<sup>th</sup> ( $R_{\text{Cu-Cu}} = 5.1 \text{ \AA}$ ), (b) 5<sup>th</sup> ( $R_{\text{Cu-Cu}} = 5.8 \text{ \AA}$ ) Cu-Cu shell, and fraction of residual carbonates in the activated (reduced) Cu/ZnO catalysts on the fraction of CO<sub>2</sub> (O<sub>2</sub>) employed during catalyst calcinations, respectively. DWF’s have been determined from refinement of theoretical Cu model structure to the experimental Cu K -edge EXAFS function measured for the *in situ* reduced Cu/ZnO catalysts.

### 5.3.2 Reducibility of the derived CuO/ZnO catalysts

The ease of reduction of Cu/ZnO catalysts has been shown to be an important parameter for valuation of the activity of Cu- based catalysts for methanol chemistry (methanol steam reforming, methanol synthesis). Roughly, it has been found that the lower the reduction temperature during catalysts activation the higher the activity of the derived catalysts [5.20-5.21]. Thus, the reducibility of the differently

calcined CuO/ZnO catalysts has been investigated by temperature programmed reduction (TPR) and thermal gravimetry (TG). Apparent activation energies for the catalyst activation were derived by measuring the displacement of the maximal reduction temperature in the corresponding TPR profile as a function of different heating rates [5.22]. The activation energies determined are listed in Table 5-2.

**Table 5-2:** Characteristics, such as specific Cu surface area, overall abundance of residual carbonates and apparent activation energies for the activation process, of the activated (reduced) Cu/ZnO catalysts studied.

| sample      | Cu surface area                                  | Residual carbonate | E <sub>A</sub> (Reduction) |
|-------------|--|--------------------|----------------------------|
|             | [m <sup>2</sup> <sub>Cu</sub> ·g <sup>-1</sup> ] | [wt.-%]            | [kJ·mol <sup>-1</sup> ]    |
| <b>CZ-1</b> | 19.5 ± 1.5                                       | 1.12               | 58.0 ± 2.2                 |
| <b>CZ-2</b> | 18.0 ± 1.1                                       | 2.04               | 53.1 ± 2.1                 |
| <b>CZ-3</b> | 18.4 ± 1.7                                       | 0.90               | 56.0 ± 2.0                 |
| <b>CZ-4</b> | 16.1 ± 1.2                                       | 0.23               | 55.9 ± 2.5                 |

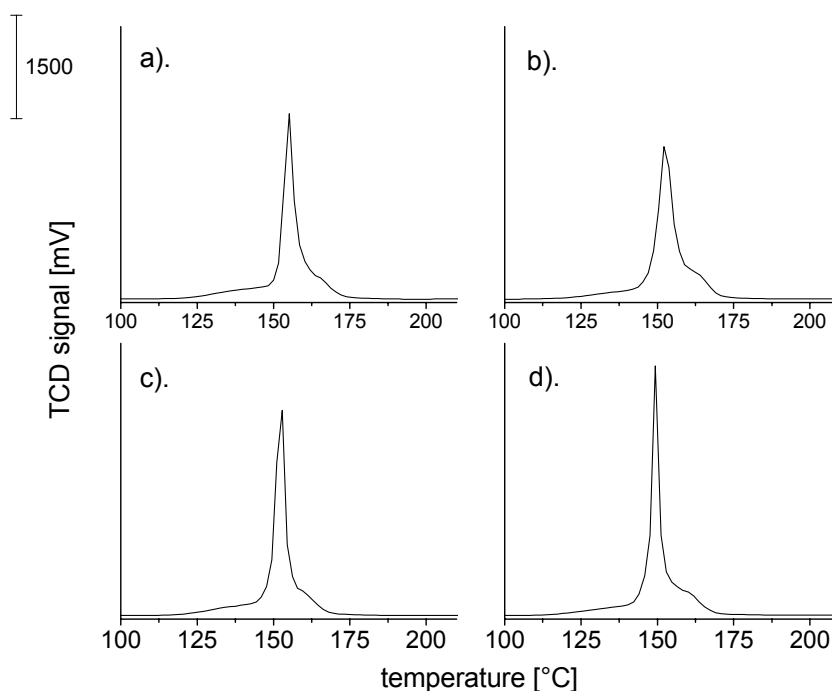


**Fig. 5-6:** Temperature programmed reduction (TPR) profiles obtained during catalyst activation in 5 vol.-% H<sub>2</sub> ( $\beta = 2 \text{ K}\cdot\text{min}^{-1}$ ) of the differently calcined CuO/ZnO catalysts: a). CZ-1, b). CZ-2, c). CZ-3, and d). CZ-4.

The values obtained for the effective activation energies are characteristic for the reduction of bivalent CuO to its metallic form [5.23]. However, apparent activation energies determined were quite similar for all Cu/ZnO catalysts and, hence, were barely affected by the gas phase employed upon calcination (Table 5-2). This indicates that there was no significant change in catalyst reduction mechanism due to carbon dioxide calcination. Generally, reduction of CuO/ZnO catalysts is a multi-step process and, hence, is not characterized by a single TPR peak. Accordingly, reduction of the CuO has been found to occur via a meta-stable Cu<sub>2</sub>O species which appeared as an intermediate during reduction of bulk CuO to its metallic form [5.24]. The activation energy of this step could not be determined because its peak, the shoulder at lower temperature side in the corresponding TPR profile, was not distinguishable from the main reduction step (see Fig. 5-6).

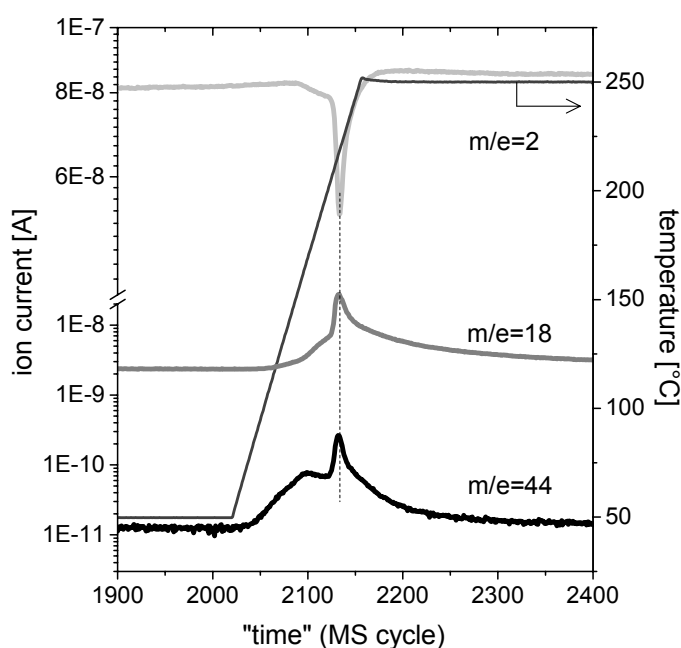
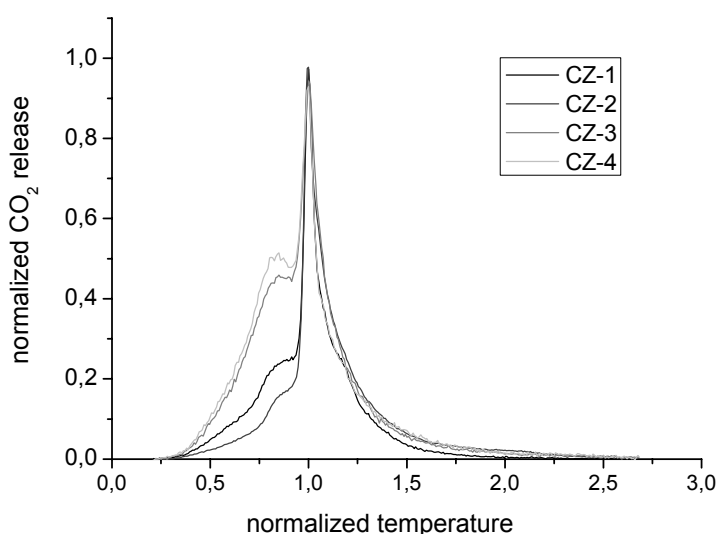


**Fig. 5-7:** MS spectra obtained during temperature programmed reduction (TPR) of sample CZ-1 ( $\beta = 6 \text{ K}\cdot\text{min}^{-1}$ ). The mass-to-charge:  $m/e = 2$  corresponds to hydrogen,  $m/e = 18$  corresponds to water, and  $m/e = 44$  corresponds to carbon dioxide.

Calcination temperature,  $T = 330 \text{ }^\circ\text{C}$ , of the Cu/Zn- catalyst studied was chosen on the basis of TG/MS investigation which exhibited a maximum of the weight loss at this certain temperature during linear heating in synthetic air. The latter temperature was, thereby, not affected by the gas phase applied during calcinations. Thus, irrespective of the atmosphere the optimum calcination temperature for the catalysts investigated amounted to  $T = 330 \text{ }^\circ\text{C}$ . This calcination temperature is in accordance with the temperature range given in the literature [5.2-5.5]. At these mild calcination temperatures not all (hydroxyl)-carbonates present in the Cu/Zn- precursor were decomposed to the oxides. Only at significantly higher temperatures during catalyst treatment upon calcination and subsequent catalyst activation, Cu/ZnO catalysts lose the strongly bonded  $\text{CO}_3^{2-}$  and, hence, were completely decarbonated, leading to the formation of the final bivalent oxides [5.1]. Accordingly, TG/MS investigations revealed



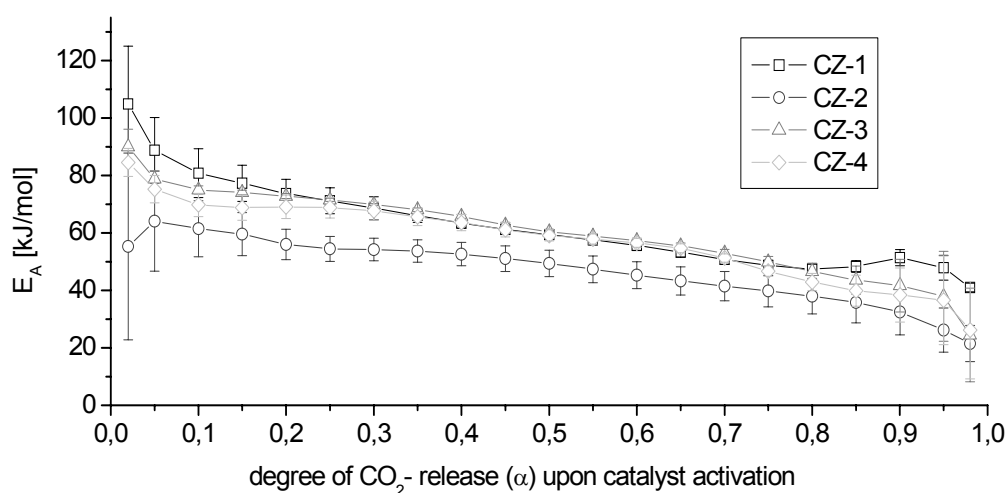
the presence of a considerable fraction of residual carbonates in the activated (reduced) Cu/ZnO catalysts. The abundance of residual carbonates determined in the reduced Cu/ZnO catalysts is summarized in Table 5-2. Here, highest fraction of residual carbonates has been found for sample CZ-2, whereas sample CZ-4 exhibited the lowest residual carbonate fraction of the catalysts studied. It has been proposed that appropriate carbonates present in the reduced Cu- based catalysts form a proper buffer layer between the grains hindering the sintering process of the Cu phase [5.7]. Consistently, it has been shown that a total loss of residual carbonates in a Cu/ZnO/Al<sub>2</sub>O<sub>3</sub> catalyst achieved by treating the catalyst at elevated temperatures ( $T > 600$  °C) is accompanied by a profuse sintering of the Cu phase [5.4]. However, there was no discrete positive relation between the overall Cu surface area and the fraction of residual carbonates in the reduced Cu/ZnO catalysts (see Table 5-2). This indicates that there is no general causality between the entire bulk of residual carbonates and the overall Cu surface area of the derived Cu/ZnO catalysts. Conversely, the fraction of residual carbonates has been found to coincide with the structural disorder in the Cu phases probed by Cu K -edge EXAFS (Fig. 5-5). Apparently, residual carbonates present in the activated Cu/ZnO catalysts caused structural disorder in the Cu phase. This modification of the Cu phase could be, thereby, tuned by the gas phase employed upon catalyst calcination.



**Fig. 5-8:** Evolved CO<sub>2</sub> profiles observed during reduction (TPR) of the differently calcined Cu/ZnO catalysts ( $\beta = 6$  K·min<sup>-1</sup>). For comparison the spectra were normalized to the maximum of the CO<sub>2</sub>-release during catalyst activation.

During catalyst activation CO<sub>2</sub> always appeared in the corresponding MS spectra (Fig. 5-7). Thereby, the maximum of the MS signal of carbon dioxide typically coincided with the corresponding maxima of hydrogen and water (see Fig. 5-7). This indicates that during catalysts activation CO<sub>2</sub> originated from decomposition/ reduction of parts of the residual (hydroxyl-) carbonates present in the CuO/ZnO catalysts studied. Nevertheless, there was still a considerable fraction of carbonates present in the reduced Cu/ZnO catalysts obtained after the activation procedure (see Table 5-2). Since the catalysts studied have been

treated by different gas atmospheres, analysis of CO<sub>2</sub> evolution during catalyst activation may provide a more detailed picture of the impact of calcination atmosphere on the reducibility of the derived Cu/ZnO catalysts. The corresponding evolved gas analysis (EGA) traces of CO<sub>2</sub> obtained during reduction of all CuO/ZnO catalysts studied are shown in Fig. 5-8. For comparison all spectra were normalized to the maximum of their CO<sub>2</sub>- release. As it is evident from inspection of Fig. 5-8, the CO<sub>2</sub>- EGA profiles and, hence the reducibility of the derived CuO/ZnO catalysts was influenced by calcination in carbon dioxide. The differences were most pronounced for the shoulder, which appeared at lower temperature side in the corresponding CO<sub>2</sub>- EGA profiles (see Fig. 5-8).

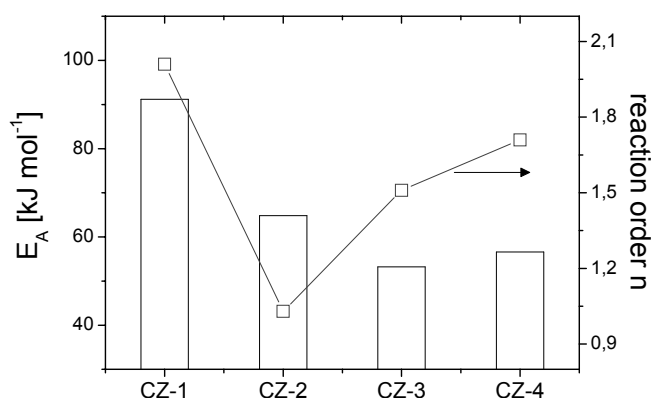


**Fig. 5-9:** Apparent activation energy as a function of the degree of CO<sub>2</sub>- release upon catalyst activation of the differently calcined CuO/ZnO catalysts. The EGA profiles of CO<sub>2</sub> during reduction (TPR) are shown in Figure 5-8. The activation energy has been determined by model-free isoconversional method according to *Friedman* [5.12].

A series of temperature programmed experiments at different heating rates (1, 2, 4, and 6 K·min<sup>-1</sup>) were performed to determine apparent activation energies ( $E_A$ ), and any dependence of  $E_A$  on the extent of CO<sub>2</sub> release during catalyst activation for the corresponding CO<sub>2</sub>- EGA profiles. The two steps, which have been observed for the EGA profiles of CO<sub>2</sub> during reduction (Fig. 5-8), were also evident from analysis of the dependency of the activation energy on the degree of the CO<sub>2</sub>- release upon catalyst activation (Fig. 5-9). Here, effective activation energies determined for the reduction process ranged from 40 kJ·mol<sup>-1</sup> to 100 kJ·mol<sup>-1</sup> and decreased monotonously with increasing degree of CO<sub>2</sub>- release ( $\alpha$ ) upon activation. The characteristic dependency of  $E_A$  on  $\alpha$  is sufficient to reveal information of the reaction mechanism and helps to predict its kinetics [5.25]. The evolution of activation energy with the extent of the CO<sub>2</sub>- release ( $\alpha$ ) upon reduction, shown in Fig. 5-9, has been found to be characteristic for a two-stage consecutive reaction according to  $A \rightarrow B \rightarrow C$  [5.26]. Apparently, the process started with a reaction ( $A \rightarrow B$ ) exhibiting the slower rate (in the isolated state) and the higher activation energy. This reaction corresponded to the formation of an intermediate species (B) during the reduction process.

**Table 5-3:** Kinetic parameters determined from a refinement of a series of MS spectra of the CO<sub>2</sub>- release during TPR of the differently calcined Cu/ZnO catalysts measured with different heating rates.

| sample | f( $\alpha$ )                                       | E <sub>A</sub> [kJ·mol <sup>-1</sup> ] | lg(A) [s <sup>-1</sup> ] | n    | a    |
|--------|---|--|--------------------------|------|------|
| CZ-1   | (1- $\alpha$ ) <sup>n</sup>                         | 91.2 ± 1.8                             | 8.24                     | 2.01 | -    |
|        | (1- $\alpha$ ) <sup>n</sup> · $\alpha$ <sup>a</sup> | 61.0 ± 0.5                             | 5.51                     | 1    | 1    |
| CZ-2   | (1- $\alpha$ ) <sup>n</sup>                         | 64.8 ± 1.5                             | 5.07                     | 1.03 | -    |
|        | (1- $\alpha$ ) <sup>n</sup> · $\alpha$ <sup>a</sup> | 57.3 ± 1.4                             | 5.03                     | 1.12 | 0.99 |
| CZ-3   | (1- $\alpha$ ) <sup>n</sup>                         | 53.2 ± 1.2                             | 3.69                     | 1.51 | -    |
|        | (1- $\alpha$ ) <sup>n</sup> · $\alpha$ <sup>a</sup> | 58.9 ± 0.5                             | 5.18                     | 1.15 | 0.96 |
| CZ-4   | (1- $\alpha$ ) <sup>n</sup>                         | 56.6 ± 0.7                             | 4.66                     | 1.71 | -    |
|        | (1- $\alpha$ ) <sup>n</sup> · $\alpha$ <sup>a</sup> | 60.1 ± 0.9                             | 5.23                     | 1.33 | 0.98 |

**Fig. 5-10:** Apparent activation energies and order of reactions of the first step in the CO<sub>2</sub>- release upon catalyst reduction (see Fig. 5-8). The kinetic parameters derived from a refinement of a series of CO<sub>2</sub>-EGA spectra during catalyst activation are summarized in Table 5-3.

In a second reaction step, the intermediate was consecutively transformed into the final species (B → C). The latter reaction was, thereby, characterized by the faster reaction rate (in the isolated state) and the lower activation energy. The limiting role of the first reaction step was kept up to the end of the reduction process. The slight increase of activation energy observed at nearly completed CO<sub>2</sub>- release ( $\alpha \approx 0.85 - 1.0$ ) was, thereby, most probably caused by mass transfer limitations. Accordingly, at higher heating rates the effect of diffusion of the gas phase to the catalyst surface dominated the reaction rate (see Fig. 5-9). For determination of characteristic kinetic parameters according to a two-stage, consecutive reaction (A → B → C), a model free kinetic model was utilized using the *NETZSCH Thermokinetics* software

package. Therefore, sixteen commonly used [5.27] models have been fitted to the experimental data obtained from the multiple heating rate experiments (see Fig. 5-8). Here, the best fitted model was  $F_n$  { $n^{\text{th}}$  order reaction with the corresponding function:  $f(\alpha) = (1 - \alpha)^n$ } for the first and  $B_{na}$  {*Prout-Tompkins* equation, autocatalytic  $n^{\text{th}}$  order reaction with the corresponding function:  $f(\alpha) = (1 - \alpha)^n \alpha^a$ } for the second reaction step. The estimated values of the apparent activation energy, pre-exponential factor, and reaction orders are summarized in Table 5-3.

During catalyst activation (reduction) CO<sub>2</sub> originated from partial decomposition of residual carbonates which persisted the calcination treatment. Accordingly, during this initial step of the CO<sub>2</sub>-release no H<sub>2</sub> consumption has been observed in the corresponding mass spectra (see Fig. 5-7). Thereby, the initial thermal decomposition of parts of the residual Cu containing (hydroxyl-) carbonates represented the rate determining step. Activation energies determined for this initial decomposition step were very different for all catalysts studied and strongly depended on the gas phase employed upon calcination (see Table 5-3). The higher the fraction of carbon dioxide employed during calcination the lower was the apparent activation energy of the initial CO<sub>2</sub>-decomposition step (Fig. 5-10). Moreover, reaction orders ( $n$ ) determined for this step exhibited a volcano behavior for the catalysts studied which inversely correlated with fraction of residual carbonates and with the structural disorder determined in the Cu phase (see Fig. 5-10 and Table 5-2). Apparently, reaction order, activation energy of this certain step, the fraction of residual carbonates and the structural disorder in the copper phase of the derived Cu/ZnO catalysts were, somehow, interrelated and dependent on the gas phase employed during calcination.

Conversely, the second TPR step, shown in Fig. 5-8, corresponded to an autocatalytic reduction of bulk CuO to its metallic form. In the reduction of oxides, autocatalysis can occur in which adsorption of molecular hydrogen on the metal gives rise to chemisorbed hydrogen atoms, which further facilitate the reduction of adjacent oxide particles [5.28]. CuO reduction occurred most readily at the Cu-CuO interface which considerably increased after formation of initial Cu metal nuclei [5.29]. Here, CO<sub>2</sub> was most probably evolved (Fig. 5-7) by lattice rearrangement accompanied by the formation of Cu metal nuclei upon catalyst reduction. Thus, the monotonous decrease in the activation energy observed probably originated from this autocatalytic/ nucleation effects (see Fig. 5-9). The activation energies determined from the second step in the corresponding EGA profiles of CO<sub>2</sub> during catalysts activation exhibited similar values as obtained from the H<sub>2</sub>-TPR profiles (see Table 5-2 and Table 5-3). Analogous to the activation energies of this autocatalytic reaction step, the reaction orders ( $n$ ,  $a$ ) were also relatively similar for all catalysts studied (see Table 5-3). This was in consistence with effective activation energies determined from the H<sub>2</sub>-TPR profiles (Table 5-2).

In summary, the results of analysis of the H<sub>2</sub>-TPR and CO<sub>2</sub>- EGA profiles during catalyst activation clearly emphasize that the copper reactivity towards reduction in a Cu/ZnO catalyst was slightly dependent on the gas phase applied upon calcination. Accordingly, calcination in carbon dioxide affected the CO<sub>2</sub>- EGA profiles and, additionally, the kinetics (apparent activation energies, orders of reaction) of the CO<sub>2</sub>-release during reduction of the derived CuO/ZnO catalysts.

### 5.3.3 Effect of CO<sub>2</sub> calcination on methanol steam reforming activity

The activity in methanol steam reforming (MSR) reaction of the differently calcined Cu/ZnO catalysts is shown in Fig. 5-11. Increasing of the residence time, the reciprocal space velocity (WHSV<sup>-1</sup>), resulted in a continuous increase of the methanol conversion. Maximal methanol conversion under the reaction conditions employed is given by the thermodynamic equilibrium and amounted to  $X^{\text{Equilibrium}} \approx 99\%$ . The catalytic activity measured was mainly determined by the specific copper surface area (Table 5-2) of the derived Cu/ZnO catalysts. Accordingly, samples CZ-1 to -3 exhibited almost similar specific Cu surface areas and, hence, showed a similar activity in the steam reforming of methanol. Due to a considerable lower Cu surface area sample CZ-4 exhibited a significantly lower activity than the other Cu/ZnO catalysts studied (Fig. 5-11). Obviously, Cu/ZnO catalysts prepared under identical preparation conditions give rise to discrete Cu surface area - activity relations [5.30]. Effective activation energies determined during methanol steam reforming reaction were similar for all samples investigated (Table 5-4). The activation energies determined for Cu/ZnO catalysts in the methanol steam reforming reaction corresponded to the values already cited in the recent literature [5.31]. The similar activation energies obtained indicates that the reaction mechanism was not affected by the different calcination procedure employed.

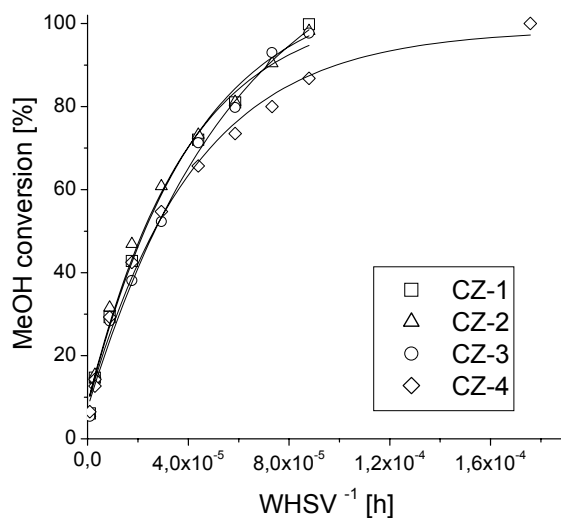


**Fig. 5-11:** Dependency of the MeOH conversion on the residence time (WHSV<sup>-1</sup>) in methanol steam reforming reaction of the differently calcined Cu/ZnO catalysts (T = 250 °C; p = 1 bar; H<sub>2</sub>O/MeOH = 1).

CO has been found as an undesired by-product in the reaction gas mixture and was most likely produced by reverse WGS reaction [5.32]. Here, CO production has been found to differ considerably for the catalysts studied (Fig. 5-12). Apparently, calcination in carbon dioxide resulted in an improved H<sub>2</sub> selectivity (declined CO selectivity) of the derived catalysts, respectively. Under nearly complete methanol conversion sample CZ-2, which has been calcined in a 1:1 mixture of CO<sub>2</sub> and O<sub>2</sub>, exhibited the lowest CO fraction in the reaction mixture (Table 5-4). Highest CO fraction in the effluent gas has been

found for sample CZ-4 which, in addition, exhibited the lowest activity in methanol steam reforming reaction of all Cu/ZnO catalysts studied (see Fig. 5-11 and Fig. 5-12). Generally, CO levels observed at all reaction temperatures (210 °C to 300 °C) were far below those predicted by thermodynamic equilibrium calculations.

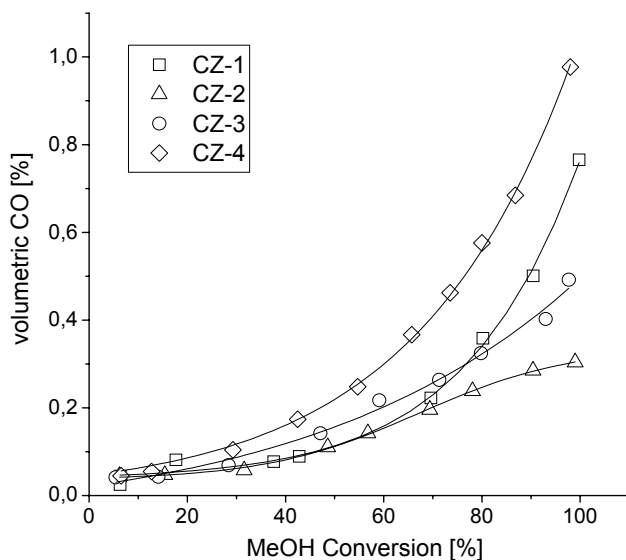


**Fig. 5-12:** Dependency of the CO concentration at the reactor outlet on MeOH conversion during methanol steam reforming reaction of the differently calcined Cu/ZnO catalysts ( $T = 250\text{ °C}$ ;  $p = 1\text{ bar}$ ;  $\text{H}_2\text{O}/\text{MeOH} = 1$ ).

**Table 5-4:** Apparent activation energies ( $E_A$ ), frequency factors ( $A$ ) determined for methanol steam reforming of the differently calcined Cu/ZnO catalysts obtained from *Arrhenius* plot, normalized reaction rate, and hydrogen yield during methanol steam reforming reaction. The rates obtained in methanol steam reforming were normalized to the rate of the Cu/ZnO catalyst which was derived by conventional calcination in synthetic air (CZ-1).

| sample | $\lg(A)$<br>[s <sup>-1</sup> ] | $E_A$<br>[kJ·mol <sup>-1</sup> ] | normalized<br>rate <sup>a</sup> | H <sub>2</sub> Yield<br>[%] <sup>a</sup> |
|--------|--------------------------------|----------------------------------|---------------------------------|--|
| CZ-1   | 8.86                           | 80.6 ± 0.8                       | = 1                             | 98.0 ± 0.01                              |
| CZ-2   | 8.76                           | 80.4 ± 1.2                       | 0.99 ± 0.02                     | 98.5 ± 0.02                              |
| CZ-3   | 8.39                           | 76.8 ± 0.6                       | 0.98 ± 0.03                     | 98.3 ± 0.01                              |
| CZ-4   | 8.94                           | 82.2 ± 1.6                       | 0.84 ± 0.03                     | 84.3 ± 0.02                              |

<sup>a</sup> This has been determined at thermodynamic equilibrium of methanol conversion ( $T = 250\text{ °C}$ ;  $p = 1\text{ bar}$ ;  $\text{H}_2\text{O}/\text{MeOH} = 1$ ;  $\text{WHSV} = 9.0 \cdot 10^{-5}\text{ h}$ ;  $X^{\text{Equilibrium}} = 98.8\%$ ).

### 5.3.4 Effect of CO<sub>2</sub> calcination on methanol synthesis activity

Since there is a common agreement that methanol during methanol synthesis reaction on, at least, Cu- based catalysts is mainly produced by hydrogenation of CO<sub>2</sub> [5.51], it can be speculated that carbon dioxide calcination during catalyst preparation may influence the activity in the synthesis of methanol [5.33-5.34]. Accordingly, a positive effect of carbon dioxide calcination on methanol synthesis rate has been already found for Cu/ZnO catalysts prepared by ball milling technique [5.10]. There, the positive impact of carbon dioxide calcination on the activity has been attributed to a higher Cu surface area of the derived Cu/ZnO catalysts. In order to verify the effect of CO<sub>2</sub> calcination on the methanol synthesis activity, the differently calcined Cu/ZnO catalysts have been subjected to methanol synthesis conditions. Here, the reaction pressure, temperature and feed composition (see chapter 4.2.2) during the synthesis of methanol were chosen very close to the technical conditions. The results obtained are summarized in Table 5-5. As it is evident from Table 5-5, dioxide calcination resulted in a considerable decrease of activity in methanol synthesis of the derived Cu/ZnO catalysts. Additionally, sample CZ-4, which has been calcined in inert gas (N<sub>2</sub>), exhibited a similar reaction rate than the samples CZ-2 and -3, which were obtained from calcination in CO<sub>2</sub> with or without additional O<sub>2</sub> (Table 5-5). Apparently, high activity of Cu/ZnO catalysts in methanol synthesis reaction performed under severe, industrial related reaction conditions (see chapter 4.2.2) required calcination in synthetic air. Effective activation energies determined were similar for all catalysts studied (Table 5-5). The difference in activity compared to the benchmark sample (CZ-1) probably originated from an improper microstructure of the derived Cu/ZnO for methanol synthesis than by a change in reaction mechanism. Accordingly, similar apparent activation energies have been determined for all investigated catalysts (see Table 5-5).

**Table 5-5:** Normalized reaction rate and apparent activation energy in methanol synthesis obtained from the differently calcined Cu/ZnO catalysts (T = 250 °C; p = 60 bar; feed: 59.5 vol.-% H<sub>2</sub>, 19.5 vol.-% CH<sub>4</sub>, 8 vol.-% CO<sub>2</sub>, 6 vol.-% CO, and balance N<sub>2</sub>). The rates in methanol synthesis were normalized to the rate of the Cu/ZnO catalyst which was derived by conventional calcination in synthetic air (CZ-1).

| atmosphere<br>(in vol.-%; balance N <sub>2</sub> ) | Cu/ZnO | normalized<br>rate | E <sub>A</sub><br>[kJ·mol <sup>-1</sup> ] |
|--|--------|--------------------|---|
| 20 % O <sub>2</sub>                                | CZ-1   | = 1                | 58.2 ± 0.8                                |
| 10 % O <sub>2</sub> + 10 % CO <sub>2</sub>         | CZ-2   | 0.82 ± 0.01        | 56.5 ± 0.7                                |
| 20 % CO <sub>2</sub>                               | CZ-3   | 0.82 ± 0.01        | 57.7 ± 1.1                                |
| N <sub>2</sub>                                     | CZ-4   | 0.83 ± 0.01        | 61.4 ± 1.8                                |

Generally, Cu/ZnO catalysts are less aggressive and, hence, more selective in hydrogenation reactions of CO/CO<sub>2</sub> mixtures than those catalysts containing nickel, cobalt, iron or platinum. Here, under the reaction conditions employed no difference in the selectivity behavior of the derived Cu/ZnO catalysts

has been detected ( $S^{\text{MeOH}} \approx 99.9\%$ ). This beneficial selectivity behavior observed for the derived Cu/ZnO catalysts is, typically, at the expense of a higher sensitivity towards a variety of deactivation processes [5.35]. Accordingly, all Cu/ZnO catalysts investigated suffered a considerable loss of approximately 40 % of the initial reaction rate during the first thirty hours on stream. The initial rapid deactivation observed was similar for all catalysts studied. Thus, there was no improvement of catalysts stability under methanol synthesis reaction conditions by carbon dioxide calcination.

#### ***5.4 Implication of carbon dioxide calcination on ternary Cu/ZnO/Al<sub>2</sub>O<sub>3</sub> catalysts: methanol steam reforming vs. methanol synthesis***

In order to verify the effect of carbon dioxide calcination observed for the Cu/ZnO catalysts on ternary Cu/ZnO/Al<sub>2</sub>O<sub>3</sub> catalysts with alumina as an additional refractory phase a similar calcination procedure has been applied before catalyst testing in both methanol steam reforming and methanol synthesis reaction. The Cu/Zn/Al- catalysts precursor employed for this study has been obtained by conventionally co-precipitation of hydroxycarbonates from the corresponding metal nitrate solutions, and was subsequently washed and dried [5.36]. The calcination as well the catalytic testing was conducted in a similar manner as for the binary Cu/ZnO catalysts described above (see chapter 5.2). Afterwards the derived Cu/Zn/Al- mixed oxide catalysts have been - similar to the binary Cu/Zn catalysts - activated in 5 vol.-% H<sub>2</sub> and, afterwards, subjected to reaction conditions. The testing results in methanol steam reforming reaction are summarized in Table 5-6. Apparently, calcination in carbon dioxide did not improve the catalytic activity in methanol steam reforming reaction. Calcination in 20 vol.-% CO<sub>2</sub> resulted rather in a decreased activity of the latter Cu/ZnO/Al<sub>2</sub>O<sub>3</sub> catalyst. Roughly, a similar trend as for the corresponding binary Cu/ZnO catalysts has been achieved with respect to the yield of hydrogen. The highest H<sub>2</sub> yield in methanol steam reforming has been obtained for the catalyst derived by calcination in a 1:1 mixture of oxygen and carbon dioxide (Table 5-6). This improvement of the selectivity behavior was also found for the binary catalysts, although, in contrast to the latter, the ternary catalyst which was calcined in 20 vol.-% CO<sub>2</sub> exhibited a considerable lower H<sub>2</sub> yield than the homologous Cu/ZnO catalyst (compare Table 5-4 and Table 5-6). Apparently, Cu/Zn- and Cu/Zn/Al- catalysts exhibited a slightly different dependency of the selectivity behavior in MSR on the calcination atmosphere.

The effect of carbon dioxide calcination on the activity of ternary Cu/ZnO/Al<sub>2</sub>O<sub>3</sub> catalysts in methanol synthesis reaction is summarized in Table 5-7. Here, two sets of calcination experiments have been performed which differed in the time interval between catalysts preparation (calcination) and catalytic testing of the derived Cu/Zn/Al- mixed oxide catalyst in methanol synthesis reaction. The freshly calcined and immediately tested Cu/ZnO/Al<sub>2</sub>O<sub>3</sub> catalysts exhibited a significant higher activity than the conventionally calcined benchmark catalyst. This effect observed appeared to be independent of the fraction of carbon dioxide employed upon catalyst calcination. However, during storage of the catalysts at ambient air over a period of approximately 6 months the positive effect observed for the catalyst activity entirely vanished (see Table 5-7). Apparently Cu/Zn/Al- catalysts studied significantly aged in the presence of ambient air leading to an irreversible change of the microstructure. Generally, Cu- based



catalysts prepared by co-precipitation are susceptible to chemisorption of H<sub>2</sub>O and CO<sub>2</sub> from ambient air. The interference with air moisture during catalyst storing resulted in an irreversible alteration of parts of the residual hydroxycarbonates [5.36]. This altering phenomenon is not reflected in the apparent activation energies determined in methanol synthesis for the differently calcined Cu/ZnO/Al<sub>2</sub>O<sub>3</sub> catalysts (Table 5-7). Apparently, there was no change in the overall reaction mechanism in methanol synthesis reaction of the freshly prepared and immediately used and stored Cu/Zn/Al- catalysts.

**Table 5-6:** Apparent activation energies, normalized reaction rate, and H<sub>2</sub> yield in MSR reaction obtained from the differently calcined Cu/ZnO/Al<sub>2</sub>O<sub>3</sub> catalysts (T = 250 °C; p = 1 bar; WHSV = 9.0·10<sup>-5</sup> h; H<sub>2</sub>O/MeOH = 1). The rates in MSR were normalized to the rate of the Cu/ZnO/Al<sub>2</sub>O<sub>3</sub> catalyst which was derived by conventional calcination in synthetic air (20 vol.-% O<sub>2</sub> in N<sub>2</sub>).

| atmosphere<br>(in vol.-%; balance N <sub>2</sub> ) | E <sub>A</sub><br>[kJ·mol <sup>-1</sup> ] | normalized<br>rate <sup>a</sup> | H <sub>2</sub> Yield<br>[%] <sup>a</sup> |
|--|---|---------------------------------|--|
| 20 % O <sub>2</sub>                                | 78.6 +/- 1.2                              | = 1                             | 98.2 ± 0.01                              |
| 10 % O <sub>2</sub> + 10 % CO <sub>2</sub>         | 79.2 +/- 0.9                              | 1 ± 0.02                        | 98.4 ± 0.01                              |
| 20 % CO <sub>2</sub>                               | 78.4 +/- 1.0                              | 0.92 ± 0.02                     | 93.4 ± 0.01                              |

<sup>a</sup> H<sub>2</sub> yield at the reactor outlet has been determined at thermodynamic equilibrium of methanol conversion (T = 250 °C; p = 1 bar; H<sub>2</sub>O/MeOH = 1; WHSV = 9.0·10<sup>-5</sup> h; X<sup>Equilibrium</sup> = 98.8 %).

The altering phenomenon during catalysts storage observed was also evident from the specific copper surface areas determined of the freshly prepared and immediately tested on the one, and the aged (stored) Cu/ZnO/Al<sub>2</sub>O<sub>3</sub> catalysts on the other hand (Table 5-8). The overall Cu surface area measured of the latter samples was very different compared to the homologous freshly calcined sample. Apparently, Cu surface area of the catalysts derived by carbon dioxide nominally increased during catalyst storage at ambient air. But, the considerable increase in surface area observed was not reflected in an enhancement of the activity in methanol synthesis (see Table 5-7). Conversely, Cu surface areas determined for the sample, which was conventionally calcined in synthetic air, did not show this deterioration phenomenon. Here, the Cu surface area which has been re-measured after a storage period of approximately 6 month was almost similar as for the freshly calcined sample. Obviously, the microstructure and, hence, the overall Cu surface areas of the differently calcined Cu/ZnO/Al<sub>2</sub>O<sub>3</sub> catalysts were only maintained for the latter, the conventionally calcined, catalyst (see Table 5-8). Consistently, there were no differences in the methanol synthesis activity of that specific sample after storage at ambient air (see Table 5-7). At this point it is speculated that the higher Cu surface area measured for the stored Cu/Zn/Al- catalysts originated from a considerable different surface texture of the Cu phase of the corresponding catalysts before and after catalyst storage. This surface texture might be different in the distribution of exposed Cu planes at the surface, in the distribution of equilibrated, less by the ZnO/Al<sub>2</sub>O<sub>3</sub> matrix stabilized Cu particles which were more susceptible to surface oxidation by N<sub>2</sub>O or by the presence of crystallized residual hydroxycarbonates after catalyst storage. Thus, the nominally increased Cu surface areas seemed rather to

be caused by an inherent and, hence, a systematic error of the determination method using N<sub>2</sub>O surface titration (RFC, see chapter 3.2.2) than a “real” effect during Cu/ZnO/Al<sub>2</sub>O<sub>3</sub> catalyst storage at ambient air.

**Table 5-7:** Normalized reaction rates and apparent activation energies ( $E_A$ ) obtained in methanol synthesis of the differently calcined Cu/ZnO/Al<sub>2</sub>O<sub>3</sub> catalysts (T = 250 °C; p = 60 bar; feed: 59.5 vol.-% H<sub>2</sub>, 19.5 vol.-% CH<sub>4</sub>, 8 vol.-% CO<sub>2</sub>, 6 vol.-% CO, and balance N<sub>2</sub>). The rates in methanol synthesis were normalized to the rate of the Cu/ZnO/Al<sub>2</sub>O<sub>3</sub> catalyst which was derived by conventional calcination in synthetic air (20 vol.-% O<sub>2</sub> in N<sub>2</sub>).

| atmosphere<br>(in vol.-%; balance N <sub>2</sub> ) | normalized<br>rate <sup>a</sup> | $E_A$<br>[kJ·mol <sup>-1</sup> ] <sup>a</sup> | normalized<br>rate <sup>b</sup> | $E_A$<br>[kJ·mol <sup>-1</sup> ] <sup>b</sup> |
|--|---------------------------------|---|---------------------------------|---|
| 20.0 % O <sub>2</sub>                              | = 1                             | 58.1 ± 0.8                                    | 1.00 ± 0.01                     | 59.2 ± 1.1                                    |
| 17.5 % O <sub>2</sub> + 2.5 % CO <sub>2</sub>      | 1.07 ± 0.02                     | 56.1 ± 0.9                                    | -                               | -   |
| 12.5 % O <sub>2</sub> + 7.5 % CO <sub>2</sub>      | 1.06 ± 0.01                     | 58.9 ± 1.0                                    | -                               | -   |
| 10.0 % O <sub>2</sub> + 10.0% CO <sub>2</sub>      | -                               | -   | 0.99 ± 0.01                     | 57.3 ± 0.9                                    |
| 7.5 % O <sub>2</sub> + 12.5 % CO <sub>2</sub>      | 1.05 ± 0.01                     | 57.5 ± 1.2                                    | -                               | -   |
| 2.5 % O <sub>2</sub> + 17.5 % CO <sub>2</sub>      | 1.05 ± 0.01                     | 55.2 ± 1.1                                    | -                               | -   |
| 20.0 % CO <sub>2</sub>                             | -                               | -   | 1.01 ± 0.01                     | 56.7 ± 1.3                                    |

<sup>a</sup> Freshly calcined samples which were immediately tested in methanol synthesis.

<sup>b</sup> Samples which were tested after a storage period of approximately 6 months at ambient air before catalytic testing.

**Table 5-8:** Specific Cu surface area of the differently calcined Cu/ZnO/Al<sub>2</sub>O<sub>3</sub> catalysts measured by N<sub>2</sub>O surface titration (RFC). Prior to each experiment the catalysts were *in situ* reduced in 5 vol.-% H<sub>2</sub> (He) at 523 K.

| atmosphere<br>(in vol.-%; balance N <sub>2</sub> ) | Cu surface area <sup>a</sup><br>[m <sub>Cu</sub> <sup>2</sup> · g <sub>cat.</sub> <sup>-1</sup> ] | Cu surface area <sup>b</sup><br>[m <sub>Cu</sub> <sup>2</sup> · g <sub>cat.</sub> <sup>-1</sup> ] |
|--|---|---|
| 20% O <sub>2</sub>                                 | 24.6 ± 2.1  | 21.2 ± 2.0  |
| 10% O <sub>2</sub> + 10% CO <sub>2</sub>           | 11.0 ± 1.2  | 23.1 ± 2.1  |
| 20% CO <sub>2</sub>                                | 15.4 ± 1.4  | 20.2 ± 2.0  |

<sup>a</sup> Freshly calcined samples which were immediately subjected to Cu surface area determination.

<sup>b</sup> Samples which were only subjected to Cu surface area determination after a storage period of approximately 6 months of the calcined CuO/ZnO/Al<sub>2</sub>O<sub>3</sub> catalysts at ambient air before surface area determination.

### ***5.5 Mechanistic considerations of the effect of carbon dioxide calcination on methanol steam reforming and synthesis reaction***

The structural differences obtained by carbon dioxide calcination of Cu/ZnO catalysts were not reflected in activity in methanol steam reforming (MSR) reaction (Fig. 5-11). Consistently, ternary Cu/ZnO/Al<sub>2</sub>O<sub>3</sub> catalysts with alumina as an additional refractory phase exhibited a similar catalytic behavior in MSR as the homologous binary catalysts (Table 5-6). Obviously, methanol steam reforming was a less sensitive reaction to the structural modifications of Cu/ZnO/(Al<sub>2</sub>O<sub>3</sub>) catalysts obtained by calcination in carbon dioxide. Accordingly, effective activation energies determined were irrespective of the calcination atmosphere for all Cu/ZnO/(Al<sub>2</sub>O<sub>3</sub>) catalysts studied similar (see Table 5-4 and Table 5-6). Conversely to the activity, considerable differences have been found in the selectivity of the derived Cu/ZnO and Cu/ZnO/Al<sub>2</sub>O<sub>3</sub> catalysts during MSR reaction. The desired low selectivity towards CO (high selectivity towards H<sub>2</sub>) observed during methanol steam reforming is attributed to a lower activity of the Cu/ZnO/(Al<sub>2</sub>O<sub>3</sub>) catalysts for the reverse water-gas-shift (rWSG) reaction, which constitute a consecutive side-reaction during MSR [5.32-5.33]. Consequently, CO formation during methanol steam reforming reaction might be positively correlated with pore diffusion limitation and, hence, with the sieve fraction of the catalyst employed [5.33-5.34]. Here, estimation of the influence of pore diffusion limitations on the reaction rate according to the *Weisz-Prater* criterion indicated no mass transport limitations for the chosen reaction conditions. Accordingly, different batches of MSR reaction performed with varying sieve fractions of the same catalyst, (100-200) μm, (200-300) μm, and (300-450) μm, exhibited no influence of the overall reaction rate on intra-particle mass transport limitations. Thus, no pore diffusion limitations of the CO formation during methanol steam reforming have been experimentally found indicating that the reaction was gradient-free under the condition employed. Apparently, Cu/ZnO/(Al<sub>2</sub>O<sub>3</sub>) catalysts derived by calcination in a 1:1 mixture of carbon dioxide and oxygen exhibited a significantly decreased activity in the reverse WGS reaction and, hence, a significantly enhanced selectivity in MSR than those derived by conventional calcination (see Table 5-4 and Table 5-6). This indicates that the rWGS reaction was, in contrast to the MSR reaction, a structure sensitive reaction towards the modifications of the catalyst structure derived by calcination in carbon dioxide. Accordingly, investigations of oxygen labeled, i.e. <sup>18</sup>O, Cu/ZnO/Al<sub>2</sub>O<sub>3</sub> catalysts in the methanol steam reforming reaction imply that there is a separate reaction path for the CO producing reaction (rWGS) that, unlike the CO<sub>2</sub> producing reaction (MSR), does not involve oxygen interchange with the catalyst [5.35]. The reverse WGS reaction is presumed to proceed according a redox mechanism [5.36-5.37]. Here, the rate determining step represents the dissociative chemisorption of gas phase CO<sub>2</sub> producing adsorbed carbon monoxide and a surface oxidized copper [5.38]. Subsequent adsorption of carbon dioxide from the gas phase onto this copper surface, finally, produces carbonate species [5.39-5.40]. Due to its strong binding nature with the copper surface, these carbonate species block active surface sites and, consequently, exhibit a reducing effect on the overall rWGS reaction rate [5.37]. In that regard, the strong bonding carbonate species might be much easier formed on those Cu/ZnO/(Al<sub>2</sub>O<sub>3</sub>) catalysts derived by calcination in the presence of carbon dioxide (with or without additional oxygen). Thus, differences in selectivity observed during methanol steam reforming reaction imply that the surface structures of the active copper crystallites varied by the calcination

methods employed. The different surface modifications may be, however, caused by the considerable different structural disorder and/ or the different fraction of residual carbonates in the bulk of the Cu/Zn/(Al)- catalysts studied. Obviously, the dissociative sticking probability of gas phase CO<sub>2</sub> on the Cu surface during MSR was, however, related to the structural modification obtained upon calcination in an O<sub>2</sub>/CO<sub>2</sub> mixture. Here, the selectivity towards CO during MSR inversely correlated to the intensity ratio  $I(111)/I(311)$  of the Cu phase (Table 5-1) in the Cu/ZnO catalysts studied. The latter appeared to be structurally defined by the fraction of residual carbonates (Table 5-2) in the reduced Cu/Zn/(Al)-catalysts. Consistently, it has been shown that the activity in rWGS reaction is given by certain surface texture effects of the active copper component [5.41]. For instance, it has been stated that “flat” surfaces, such as Cu (111), are incapable of decomposing gas phase CO<sub>2</sub> [5.38]. Consequently, activity in (reverse) WGS reaction is substantially higher on “open”, such as the Cu (311), than on the more densely packed Cu (111) surface [5.42]. These copper planes offer Cu surface atoms which are more coordinatively unsaturated and, hence, are more conducive to chemisorptive bonding of CO<sub>2</sub> and H<sub>2</sub>O from the gas phase during MSR. In this respect, the very different selectivity to CO in methanol steam reforming reaction may be attributed to a different surface texture of the active Cu phase obtained by the calcination atmosphere. Thus, the Cu/ZnO (Cu/ZnO/Al<sub>2</sub>O<sub>3</sub>) catalysts calcined in a mixture of O<sub>2</sub> and CO<sub>2</sub> exhibited a significant lower reactivity towards CO<sub>2</sub> dissociation, which proceeded preferentially on certain copper, i.e. Cu (311), surfaces (see Table 5-1). In contrast to gas phase CO<sub>2</sub>, methanol interacts very weakly on clean copper planes, such as Cu (100) [5.43], Cu (110) [5.44-5.45], and Cu (111) [5.46] used as model catalysts. But, the sticking probability of methanol on Cu is significantly enhanced at low surface oxygen coverage of the Cu metal indicating that for superior activities in MSR reaction the presence of surface oxygen is required [5.47-5.48]. As already mentioned, these surface oxygen species will also enhance the chemisorption of gas phase CO<sub>2</sub> leading to the formation of surface carbonates. Thus, surface oxygen should not only decrease the rWGS but also increase the MSR activity which was, apparently, not the case for the Cu/ZnO/(Al<sub>2</sub>O<sub>3</sub>) catalysts investigated. Obviously, slight differences in the surface texture and, hence, in the oxygen (and carbonate) coverage of the copper surface during MSR reaction were less reflected in the activity of methanol steam reforming and much more reflected in the activity of the rWGS reaction of the Cu/ZnO/(Al<sub>2</sub>O<sub>3</sub>) catalysts studied (Table 5-4, Table 5-6). Here, the methanol steam reforming reaction performed ran, due to technical reasons, at relative high conversions ( $X^{\text{MeOH}} \geq 5\%$ ) and, consequently, variations in activity obtained by the calcination atmosphere were less pronounced (Fig. 5-11). Conversely, reverse WGS reaction proceeded far below to the thermodynamic equilibrium and, hence, small differences in the microstructure of the Cu/ZnO/(Al<sub>2</sub>O<sub>3</sub>) catalyst obtained by carbon dioxide calcination were highly reflected in its activity (Fig. 5-12).

Since the (forward and reverse) WGS reaction is part of the reaction network occurring in the synthesis of methanol and the latter reaction were performed at thermodynamic equilibrium, a superior (reverse) WSG catalyst should be also a superior methanol synthesis catalyst [5.49]. Correspondingly, hydrogenation of strongly chemisorbed carbonate on the copper surface results in the formation of a surface formate species, which, on further hydrogenation, yields formate, formaldehyde, methoxy species and, finally, methanol [5.50]. Generally, formate species on the Cu catalyst surface represents the longest living intermediate in this reaction sequence and, hence, the rate determining step for methanol synthesis

has been supposed to be the hydrogenation of the formate intermediate [5.51-5.52]. In this respect, carbonate species formed on the Cu surface, which inhibit the reverse WGS reaction during MSR, should be beneficial for methanol synthesis reaction. Accordingly, at least, the freshly prepared and immediately tested Cu/ZnO/Al<sub>2</sub>O<sub>3</sub> catalysts obtained by carbon dioxide calcination exhibited a considerable higher reaction rate in the synthesis of methanol compared to the conventionally calcined benchmark catalyst (Table 5-7). However, there was no dependency of the activity on the fraction of CO<sub>2</sub> employed upon calcination. Furthermore, this positive effect entirely vanished after a certain time of storing of the calcined Cu/ZnO/Al- catalysts at ambient air (see Table 5-7). Conversely, Cu/ZnO catalysts prepared similar to the latter ternary samples exhibited a completely different catalytic behavior in methanol synthesis (Table 5-5). Here, all samples, which were not conventionally calcined in synthetic air, exhibited a considerable lower activity in methanol synthesis reaction. Irrespective of the gas phase upon calcination, i.e. O<sub>2</sub>:CO<sub>2</sub> mixture, CO<sub>2</sub>, and pure N<sub>2</sub>, all Cu/ZnO catalysts exhibited a roughly 20 % lower activity than the conventionally calcined benchmark catalyst (Table 5-5). Furthermore, the latter Cu/ZnO catalyst (CZ-1) only exhibited roughly 60 % of the upper limit given by thermodynamics during methanol synthesis which has been arrived for the homologous ternary system. But, similar effective activation energies have been determined irrespective on the catalysts system (binary, ternary) or gas phase employed upon calcination (Table 5-5, Table 5-7). This indicates that the differences observed were not caused by a change of the overall reaction mechanism. Apparently, modification of Cu phase in the binary Cu/ZnO catalyst achieved by calcination in the presence of CO<sub>2</sub> was not maintained under MS conditions (60 bar; 250°C; “dirty” gas feed: 59.5 vol.-% H<sub>2</sub>, 19.5 vol.-% CH<sub>4</sub>, 8 vol.-% CO<sub>2</sub>, 6 vol.-% CO, and balance N<sub>2</sub>). The difference in the microstructure of the freshly calcined and immediately tested Cu/ZnO/Al<sub>2</sub>O<sub>3</sub> catalysts leading to an improved activity in methanol synthesis compared to the corresponding binary Cu/ZnO catalysts may be attributed to the presence of aluminum as stabilizing component. Obviously, carbon dioxide calcination also affected the microstructure of the ZnO/Al<sub>2</sub>O<sub>3</sub> support which was shown to be essential for maintaining active Cu particles in methanol chemistry (see chapters 3 and 4).

## 5.6 Summary

Calcination in carbon dioxide did not positively affect the activity of both Cu/ZnO and Cu/ZnO/Al<sub>2</sub>O<sub>3</sub> catalysts in the methanol steam reforming reaction. This indicates that the quantity of the active sites were unaffected by carbon dioxide calcination. Conversely, selectivities to the desired product, hydrogen, were significantly improved by calcination in the presence of carbon dioxide. Accordingly, best yields of hydrogen have been gained by calcination in a 1:1 mixture of oxygen and carbon dioxide. This indicates that the quality of the active sites has been considerably changed by carbon dioxide calcination. Structurally, the modification of the quality of the active site seemed to be, however, related to an increased structural disorder in the copper phase, which appeared to originate from the presence of an appropriate fraction of residual carbonates in the catalytically active Cu/ZnO/(Al<sub>2</sub>O<sub>3</sub>)

catalysts. Both the fraction of residual carbonates and the structural disorder could be, thereby, tuned by the calcination atmosphere.

Conversely, the effect of carbon dioxide calcination on the activity in the synthesis of methanol at industrial related reaction conditions was non-uniform comparing Cu/ZnO and the homologous Cu/ZnO/Al<sub>2</sub>O<sub>3</sub> catalysts. Cu/ZnO catalysts derived by carbon dioxide calcination exhibited a considerably lower activity than the conventionally in synthetic air calcined benchmark sample. Here, a loss of activity during methanol synthesis has been observed for all catalysts which were not calcined in synthetic air. Contrarily, ternary Cu/ZnO/Al<sub>2</sub>O<sub>3</sub> catalysts derived by carbon dioxide calcination exhibited a higher activity in methanol synthesis. This positive effect was limited to the freshly calcined and immediately tested Cu/ZnO/Al<sub>2</sub>O<sub>3</sub> catalysts. Accordingly, after storage period of approximately six months at ambient air the superior activities obtained completely vanished. These differences in activity might be attributed to distinct different durability of the microstructure derived by calcination in the presence of CO<sub>2</sub> of Cu/ZnO and Cu/ZnO/Al<sub>2</sub>O<sub>3</sub> catalysts under the severe methanol synthesis condition applied. Consistently, binary catalyst system possessed a CO<sub>2</sub> conversion during methanol synthesis which is only half of the thermodynamic equilibrium under the reaction conditions applied. Ternary Cu/Zn/Al- catalysts met the thermodynamic equilibrium of CO<sub>2</sub> conversion during catalytic testing.

## 5.7 *References cited*

- [5.1] B. Bems, M. Schur, A. Dassenoy, H. Junkes, D. Herein, R. Schlögl, *Chem. Eur. J.*, 9 (2003) 2039.
- [5.2] K. Klier, *Adv. Catal.*, 31 (1982) 243.
- [5.3] G.C. Chinchin, P.J. Jennings, M.S. Spencer, K.C. Waugh, *Appl. Catal.*, 36 (1988) 1.
- [5.4] M.J.L. Gines, N. Amadeo, M. Laborde, C.R. Apesteguia, *Appl. Catal. A*, 131 (1995) 283.
- [5.5] W.H. Cheng, *Mater. Chem. Phys.*, 41 (1995) 36.
- [5.6] M. Yurieva, L.M. Plyasova, V.I. Zaikovskii, T.P. Minyukova, A. Blik, J.C. van den Heuvel, L.P. Davydova, I. Molina, M.P. Demeshkina, A.A. Khassin, E.D. Batyrev, *Phys. Chem. Chem. Phys.*, 6 (2004) 4522.
- [5.7] S.V. Ketchik, T.M. Yurieva, L.M. Plyasova, *React. Kinet. Catal. Lett.*, 19 (1982) 345.
- [5.8] M. Saito, K. Tomoda, I. Takahara, K. Murata, M. Inaba, *Catal. Lett.*, 89 (2003) 11.
- [5.9] W.H. Cheng, United States patent, US 4 826 798 (1989), to E.I. Du Pont de Nemours and Company.
- [5.10] H.L. Castricum, H. Bakker, B. van der Linden, E.K. Poels, *J. Phys. Chem. B*, 105 (2001) 7928.
- [5.11] S. Vyazovkin, *J. Comput. Chem.*, 18 (1997) 393.
- [5.12] H.L. Friedman, *J. Polym. Sci Part C*, 6 (1963) 183.
- [5.13] T. Ozawa, *Bull. Chem. Soc. Jpn.*, 38 (1965) 1881.
- [5.14] J.H. Flynn, L.A. Wall, *J. Polym. Sci. Part B*, 4 (1966) 323.
- [5.15] Powder X-ray diffraction file, ICDD-PDF 36-1475.
- [5.16] Powder X-ray diffraction file, ICDD-PDF 17-743.
- [5.17] Powder X-ray diffraction file, ICDD-PDF 4-836.
- [5.18] Powder X-ray diffraction file, ICDD-PDF 36-1451.
- [5.19] B. Gilbert, F. Huang, H. Zhang, G.A. Waychunas, J.F. Banfield, *Science*, 305 (2004) 651.
- [5.20] G. Fierro, M. Lo Jacono, M. Inversi, P. Porta, F. Cioci, R. Lavecchia, *Appl. Catal. A*, 137 (1996) 327.

- [5.21] Y. Kawamura, K. Yamamoto, N. Ogura, T. Katsumata, A. Igarashi, *J. Power Sources*, 150 (2005) 20.
- [5.22] O.J. Wimmers, P. Arnoldy, J.A. Moulijn; *J. Phys. Chem.*, 90 (1986) 1331.
- [5.23] J.Y. Kim, J.A. Rodriguez, J.C. Hanson, A.I. Frenkel, P.L. Lee, *J. Am. Chem. Soc.*, 125 (2003) 10684.
- [5.24] M.M. Günther, B. Bems, R. Schlögl, T. Ressler, *J. Syn. Rad.*, 8 (2001) 619.
- [5.25] S. Vyazovkin, C.A. Wight, *Annu. Rev. Phys. Chem.*, 48 (1997) 125.
- [5.26] S. Vyazovkin, *Thermochimica Acta*, 236 (1994) 1.
- [5.27] J. Opfermann, *J. Therm. Anal. Calorim.*, 60 (2000) 641.
- [5.28] M.J. Tiernan, P.A. Barnes, G.M.B. Parkes, *J. Phys. Chem. B*, 103 (1999) 338.
- [5.29] R.N. Pease, H.S. Taylor, *J. Am. Chem. Soc.*, 43 (1921) 2179.
- [5.30] R.A. Halden, R.J. Lambert, C. Ranson, *Appl. Catal. A*, 122 (1995) L1.
- [5.31] J.K. Lee, J.B. Bo, D.H. Kim, *Appl. Catal. A*, 278 (2004) 25.
- [5.32] B.A. Peppley, J.C. Amphlett, L.M. Kearns, R.F. Mann, *Appl. Catal. A*, 179 (1999) 21.
- [5.33] H. Purnama, T. Ressler, R.E. Jentoft, H. Soerijanto, R. Schlögl, R. Schomäcker, *Appl. Catal. A*, 259 (2004) 83.
- [5.34] B. Frank, F.C. Jentoft, H. Soerijanto, J. Kröhnert, R. Schlögl, R. Schomäcker, *J. of Catal.*, 246 (2007) 177.
- [5.35] N.E. Vanderborgh, B.E. Goodby, T.E. Springer, *Proceedings of the 32<sup>th</sup> International Power Sources Symposium*, (1986) 623.
- [5.36] G.C. Chinchin and M.S. Spencer, *J. Catal.*, 112 (1988) 325.
- [5.37] K.C. Waugh, *Catal. Today*, 53 (1999) 161.
- [5.38] R.A. Hadden, H.D. Vandervell, K.C. Waugh, G. Webb, *Catal. Lett.*, 1 (1988) 27.
- [5.39] J.M. Campbell, C.T. Campbell, *Surf. Sci.*, 259 (1991) 1.
- [5.40] G.J. Millar, C.H. Rochester, K.C. Waugh, *J. Mol. Phys. Condens. Matter*, 1 SB (1989) 149.
- [5.41] S. Fujita, S. Moribe, Y. Kanamori, M. Kakudate, N. Takezawa, *Appl. Catal. A*, 207 (2001) 121.
- [5.42] J. Nakamura, J.M. Campbell, C.T. Campbell, *J. Chem. Soc. Faraday Trans.*, 86 (1990) 2725.
- [5.43] B. Sexton, *Surf. Sci.*, 88 (1979) 299.
- [5.44] I.E. Wachs, R.J. Madix, *J. Catal.*, 53 (1978) 208.
- [5.45] S.M. Francis, F.M. Leibsle, S. Haq, N. Xiang, M. Bowker, *Surf. Sci.*, 315 (1994) 284.
- [5.46] J.N. Rusell, S.M. Gates, J.T. Yates, *Surf. Sci.*, 163 (1985) 516.
- [5.47] D.B. Clarke, D.K. Lee, M.L. Sandoval, A.T. Bell, *J. Catal.*, 150, (1994) 81.
- [5.48] M. Bowker, *Top. Catal.*, 3 (1996) 461.
- [5.49] K.C. Waugh, *Catal. Today*, 53 (1999) 161.
- [5.50] G.J. Millar, C.H. Rochester, K.C. Waugh, *J. Mol. Phys.*, 76 (1991) 833.
- [5.51] A. Ya Rozokovskii, *Russ. Chem. Rev.*, 58 (1989) 41.
- [5.52] P.A. Taylor, P.B. Rasmussen, I. Chorkendorff, *J. Chem. Soc. Faraday Trans.*, 91 (1995) 1267.

## Chapter Six

### Conclusions

#### 6.1 *Methanol steam reforming vs. Methanol synthesis*

##### 6.1.1 **Role of the defects and the support in Cu/ZnO/Al<sub>2</sub>O<sub>3</sub> catalysts**

Cu/ZnO/Al<sub>2</sub>O<sub>3</sub> catalysts represent a versatile catalyst system for methanol chemistry, including the synthesis and steam reforming of methanol [6.1]. Formally, the steam reforming of methanol (MSR) is the reverse of methanol synthesis from CO<sub>2</sub> and H<sub>2</sub>. Accordingly, the utility of copper catalysts may originate from a favorable adsorption chemistry of methoxy and formate species which represent common reaction intermediates in both reactions. Therefore, it is reasonable to assume that the superior methanol synthesis catalyst also exhibits a high activity in the reverse reaction (“principle of microscopic reversibility”). Differences between methanol synthesis and methanol steam reforming have two reasons. First, the partial pressures of reactants and products during MSR considerably differ from those in methanol synthesis. The latter reaction is performed with synthesis gas containing a large fraction of CO in addition to H<sub>2</sub> and CO<sub>2</sub>. Second, the reaction mechanism is probably different from that of the reverse synthesis reaction in that methyl formate is a molecular intermediate [6.2-6.5]. With a different reaction mechanism the working catalyst is likely to be different, e.g. with respect to the extent of surface and bulk oxidation. This is supported by empirical evidence that the optimum Cu/ZnO/Al<sub>2</sub>O<sub>3</sub> formulations for methanol synthesis catalysts are not the inherent optimum formulations for methanol steam reforming catalysts [6.6]. Consistently, deactivation behavior of Cu/ZnO/Al<sub>2</sub>O<sub>3</sub> catalysts is also different for the two reactions. In methanol synthesis the main cause of deactivation is thermal sintering, whereas catalyst degradation by poisoning and by coking have been identified in methanol steam reforming reactions [6.7]. Thus, catalytic activity in both reactions requires different properties of the active sites. It has been shown that copper particles dynamically respond to the chemical potential of the gas feed, i.e. the copper particle shape and, hence, the exposed surface area strongly depend on the feed conditions applied [6.8]. The positive change of the *Gibbs* free-energy during methanol synthesis at chemisorption of the gas phase reactants indicates that equilibrium surface coverage is relatively small. Thus, methanol is formed on essentially oxygen-free copper surface in the methanol synthesis reaction [6.9, 6.10], whereas during methanol steam reforming surface oxidized copper is more favored [6.11]. The activity of copper metal in Cu/ZnO/Al<sub>2</sub>O<sub>3</sub> catalysts in the two different reactions may be related to the existence of various Cu



species which differ in their surface oxidation state without forming stoichiometric oxide phases, but still considerably differ from macro-crystalline metal Cu.

In this thesis, it has been shown that in both reactions studied, activity was almost linearly related to the overall Cu surface area. Thus, metal copper is the active phase in the methanol synthesis and methanol steam reforming reaction. This was strongly supported by earlier investigations of Cu based catalysts in methanol chemistry [6.12-6.15]. Deviations observed from a linear Cu surface area - activity relation are caused by the fact that there is only an “active fraction” of copper responsible for the activity obtained in methanol chemistry. The latter term appears to be more applicable than the term “active phase” since it does not contain any assumption about the required physiochemical form of copper. Accordingly, active copper in methanol chemistry significantly differed from “ideal”, equilibrated bulk copper metal. Superior Cu/ZnO/Al<sub>2</sub>O<sub>3</sub> catalysts in both, methanol synthesis and methanol steam reforming, exhibited lattice strain in the copper phase. Apparently, lattice strain was a consequence of a high dispersion and, hence, a high Cu surface area in the Cu/ZnO/Al<sub>2</sub>O<sub>3</sub> catalysts. This confirms previous investigations concerning the relevance of bulk structural imperfections in stabilization of active copper in methanol chemistry [6.16-6.18]. The high degree of disorder observed in the Cu phase seemed to result from an increased interface area between Cu and ZnO as it is evident from HRTEM investigation of the activated Cu/ZnO/Al<sub>2</sub>O<sub>3</sub> catalysts. Accordingly, a variety of both epitaxial and irregular arrangements of, in most cases, relatively smooth Cu-ZnO interfaces has been found. The microstructural model in which ZnO acts as a spacer of Cu nanoparticles may be the physical explanation of the ability of ZnO to stabilize a relatively high Cu surface area and, hence, to limit sintering of the copper phase under reaction conditions. This favored microstructuring of Cu and ZnO has also been found, at least partially, for less active Cu/ZnO/Al<sub>2</sub>O<sub>3</sub> catalysts which, qualitatively, exhibited a more heterogeneous morphology of Cu and ZnO, i.e. large and isolated Cu and ZnO particles. Conversely, alumina did not appear as a separate phase. Alumina is known to be a structural promoter reducing the likelihood of sintering of Cu/ZnO/Al<sub>2</sub>O<sub>3</sub> catalysts in methanol chemistry [6.19]. This positive behavior may be related to an increased solubility of copper ions in the ZnO host lattice in the calcined state achieved by adding aluminum as a third cationic component during preparation leading to a favored metal-support interaction between Cu and ZnO/Al<sub>2</sub>O<sub>3</sub> after catalysts activation [6.20]. Accordingly, apparent work of adhesion calculated for Cu particles of similar sizes were found to be significantly higher for the Cu/ZnO/Al<sub>2</sub>O<sub>3</sub> catalyst studied than for a homologous binary Cu/ZnO catalyst without aluminum as a stabilizing component [6.21]. Apparently, dynamic restructuring of the Cu particles and, hence, the tendency for sintering depends in addition to the gas feed composition on the quality of interaction of the copper particles and the ZnO/Al<sub>2</sub>O<sub>3</sub> matrix [6.22].

Since strain in the Cu lattice seemed to be the dominant bulk structural feature affecting the catalytic properties in those catalysts, which exhibit a relatively homogeneous microstructure, strain may originate from a pronounced lattice mismatch between Cu and ZnO/(Al<sub>2</sub>O<sub>3</sub>) at the metal-oxide interface [6.23]. Apparently, lattice strain has been found to be one factor which modifies bulk copper, yielding active copper in methanol chemistry. Generally, the degree of lattice strain in copper exhibited beneficial effects on the catalytic performance, but has not been always found to correlate linearly with the activity observed in methanol chemistry. Accordingly, less active Cu/ZnO/Al<sub>2</sub>O<sub>3</sub> catalysts employed in methanol

steam reforming reaction exhibited a different degree of structural disordering in the copper phase without any detectable contributions of lattice strain. Consistently, other microstructural features have to be present, which account for the structural disorder determined. The presence of subsurface oxygen species in the bulk has been suggested to positively influence the adsorption properties of the reactants in methanol chemistry [6.24-6.26]. This subsurface oxygen species do not covalently contribute to the d-band of copper and, consequently, bulk averaged analytical techniques employed in this study (i.e. XRD and XAS) will only detect zero-valent copper. Thus, the reactivity of active copper may be governed by subsurface oxygen and lattice strain in a cumulative manner which guarantees the ability of dynamic reconstructing of the surface of the active copper without allowing agglomeration or transformation of the latter into other phases such as bulk oxides and alloys during the reaction. Consistently, it occurs clearly that the abundance of non-equilibrium structures in Cu, such as planar defects, lattice strain, and subsurface oxygen, properties which are strongly interrelated, correlated with the catalytic activity. The active sites must thus be found predominantly in these structural elements without excluding that the regular surfaces (“perfect” or modified with line and point defects) will also contain some active centers, allowing single crystals of Cu to exhibit some catalytic activity. Thus, the kinetic stabilization of non-equilibrium structures during long-term operation was seen as the physical reason of the kinetic “synergy” between Cu component and ZnO/Al<sub>2</sub>O<sub>3</sub> matrix. This has been already speculated much earlier on the basis of surface science results [6.27].

### 6.1.2 Role of the calcination gas atmosphere

Previous investigations have shown that the microstructure of Cu/ZnO catalysts for methanol chemistry (methanol synthesis and methanol steam reforming) can be positively modified by either the chemical composition [6.28] or by a proper preparation procedure at a constant chemical composition [6.29]. The modification occurred during mild thermal treatment (calcination) of the catalyst precursor and was reflected in the catalytic performance of the final catalyst (“chemical memory” effect [6.30]). Accordingly, calcination of Cu/Zn/Al- hydroxycarbonates to the mixed oxides is a crucial step in the preparation of Cu/ZnO/Al<sub>2</sub>O<sub>3</sub> catalysts for methanol chemistry. Optimum calcination temperatures with respect to activity roughly range from 300 °C to 400 °C and are confined on the basis of sintering restrictions of the CuO phase formed [6.31-6.34]. It is assumed that during calcination at mild temperatures CuO and ZnO were modified by residual hydroxyl and carboxyl groups [6.35]. These ad-mixed groups may serve as growth inhibitors of defect rich Cu particles in the final catalyst required for superior activity in methanol chemistry [6.36]. Accordingly, a total decarboxylation of the catalyst achieved by calcination at higher temperatures ( $T > 600$  °C) caused sintering of the copper phase, which was accompanied by a loss of activity due to a reduction of the Cu surface area of the derived catalysts [6.37]. The thermal decomposition of the hydroxycarbonate precursors should not only be affected by temperature but also by the composition of the gas phase. A higher partial pressure of carbon dioxide during decarboxylation may retain some particular ad-mixed carboxyl groups hindering the sintering process of the active copper and, hence, may result in an enhanced catalytic activity and stability. In order

to verify the impact of carbon dioxide calcination on the catalytic properties calcinations of binary Cu/Zn- and ternary Cu/Zn/Al- hydroxycarbonate precursor were done at different partial pressures of oxygen and carbon dioxide. Afterwards, the derived Cu/ZnO/(Al<sub>2</sub>O<sub>3</sub>) catalysts were tested in methanol synthesis and methanol steam reforming reaction.

Carbon dioxide calcination of the Cu/Zn/(Al)- catalyst precursors has been conducted under different gas phase compositions: (i) synthetic air, (ii) 10 vol.-% O<sub>2</sub>/ 10 vol.-% CO<sub>2</sub> in N<sub>2</sub>, and (iii) 20 vol.-% CO<sub>2</sub> in N<sub>2</sub>. Calcination in carbon dioxide with or without additional oxygen did not positively affect the activity of both Cu/ZnO and Cu/ZnO/Al<sub>2</sub>O<sub>3</sub> catalysts in the methanol steam reforming reaction (MSR). This indicates that the quantity of the active sites were unaffected by carbon dioxide calcination. Conversely, selectivities to the desired product, hydrogen, were significantly improved by carbon dioxide calcination. Accordingly, CO formation were significantly decreased for the Cu/ZnO/(Al<sub>2</sub>O<sub>3</sub>) catalysts derived by calcination in carbon dioxide. The latter was formed according to the reverse water-gas-shift reaction (rWGS), which is part of the reaction network during the steam reforming of methanol. Here, the methanol steam reforming reaction performed ran at relative high conversions of methanol ( $X^{\text{MeOH}} \geq 5\%$ ) and, consequently, minor improvements of the catalysts derived by the calcination atmosphere were less pronounced in the reaction rate. Conversely, reverse WGS reaction proceeded far below its thermodynamic equilibrium and, hence, small differences in the microstructure of the Cu/ZnO/(Al<sub>2</sub>O<sub>3</sub>) catalyst obtained by carbon dioxide calcination were highly reflected in its activity. Best yields of hydrogen have been gained by calcination in a 1:1 mixture of oxygen and carbon dioxide. This indicates that the quality of the active sites has been changed by calcination in carbon dioxide. The desired low selectivity towards CO (high selectivity towards the main products H<sub>2</sub> and CO<sub>2</sub>) observed during methanol steam reforming was attributed to a lower activity of the Cu/ZnO/(Al<sub>2</sub>O<sub>3</sub>) catalysts for the reverse water-gas-shift (rWGS) reaction [6.38]. This reaction is presumed to proceed according to a redox mechanism where the rate determining step is the dissociative chemisorption of gas phase CO<sub>2</sub> producing adsorbed carbon monoxide and a surface oxidized copper [6.39]. Subsequent adsorption of carbon dioxide from the gas phase onto the copper surface produces carbonate species [6.40, 6.41]. Due to its strong binding nature with the copper surface, these carbonate species block active surface sites and, consequently, exhibit a reducing effect on the overall rWGS reaction rate [6.42]. Apparently, the strong bonding carbonate species were much easier formed on the surface of those catalysts, which were derived from calcination in an O<sub>2</sub>/CO<sub>2</sub> mixture - the Cu/ZnO/(Al<sub>2</sub>O<sub>3</sub>) catalysts which exhibited the lowest selectivity to CO during MSR reaction. The dissociative sticking probability of CO<sub>2</sub> on the Cu surface and, hence, the different selectivity behavior of the Cu/ZnO/Al<sub>2</sub>O<sub>3</sub> catalysts studied was related to an increased structural disorder in the copper phase which may originate from the presence of an appropriate fraction of residual carbonates in the catalytically active catalysts. Both the fraction of residual carbonates and the structural disorder affected the local electronic structure of the active copper sites which could be, thereby, tuned by the calcination atmosphere.

The selectivity observed during MSR reaction exhibited a volcano-like dependency on the partial pressures of carbon dioxide and oxygen upon calcination. This behavior may be attributed to an improvement of two different, competing properties, the chemisorption and the activation of gas phase CO<sub>2</sub> during reverse WGS reaction in dependence of a more oxygen or a more carbon dioxide rich

calcination atmosphere [6.43]. Accordingly, best selectivities to  $H_2$  have been obtained by calcination in 1:1 mixture of  $CO_2$  and  $O_2$ . Catalysts derived by calcination in the presence of either oxygen or carbon dioxide resulted in considerable decrease of the  $H_2$ - selectivity (increase of the  $CO$ - selectivity) during methanol steam reforming reaction. Apparently, calcination in a 1:1 mixture of  $O_2$  and  $CO_2$  represent the best compromise with respect to, on the one hand, an improved chemisorption and, on the other hand, an improved activation of gas phase  $CO_2$  of the derived  $Cu/ZnO/(Al_2O_3)$  catalysts. Moreover, the modification of the catalyst upon calcination with regard to an improvement of the gas phase  $CO_2$  chemisorption and activation properties of the derived catalysts was also dependent on the catalyst system studied (binary, ternary). As already mentioned  $Cu/ZnO$  and  $Cu/ZnO/Al_2O_3$  obtained from calcination in a 1:1 mixture of  $CO_2$  and  $O_2$  exhibited the best selectivities in methanol steam reforming. But, binary  $Cu/ZnO$  catalysts conventionally calcined in synthetic air (20 vol.-%  $O_2$  in  $N_2$ ) exhibited a considerable lower selectivity to  $H_2$  than the catalysts which were calcined in 20 vol.-%  $CO_2$  ( $N_2$ ). Contrarily, ternary  $Cu/ZnO/Al_2O_3$  catalysts calcined in synthetic air exhibited a higher selectivity to  $H_2$  than the catalysts which were calcined in 20 vol.-%  $CO_2$  ( $N_2$ ). Apparently,  $Cu/ZnO$  and  $Cu/ZnO/Al_2O_3$  catalysts featured a slightly different dependency of their microstructure and, hence, of the selectivity behavior during MSR on the  $O_2/CO_2$  partial pressure upon calcination. The different catalytic behavior in terms of hydrogen yield obtained in MSR for  $Cu/ZnO/Al_2O_3$  catalysts compared to the homologous  $Cu/ZnO$  catalysts may be originating from the more complex microstructure of the ternary catalyst system. Certainly, addition of aluminum as a third cationic component during catalyst preparation will change the electronic and structural properties of the final  $Cu/Zn/Al$ - catalyst.

$Cu/ZnO/Al_2O_3$  catalysts derived by carbon dioxide calcination exhibited, at least for the freshly calcined catalysts, a higher reaction rate in the synthesis of methanol. However, activity was not dependent on the fraction of  $CO_2$  employed during calcination. Furthermore, this positive effect entirely vanished after a certain time of catalyst storing (6 months) at ambient air. Conversely,  $Cu/ZnO$  catalysts prepared similar to the corresponding ternary samples exhibited a completely different catalytic behavior in methanol synthesis. Here, all samples, which were not calcined in synthetic air, exhibited a considerable loss of activity in methanol synthesis. The most active, conventionally in synthetic air calcined, binary  $Cu/ZnO$  catalyst exhibited roughly 60 % of the upper limit given by thermodynamics during methanol synthesis, which has been arrived for the ternary system. Nevertheless, similar effective activation energies have been determined irrespective on the catalysts system (binary, ternary) or gas phase employed upon calcination. This indicates that the differences observed were not caused by a change of the reaction mechanism. Apparently, the modification of the  $Cu$  phase in  $Cu/ZnO$  catalysts, achieved by  $CO_2$  calcination (incorporation of carbonates and, therefore, enhancement of structural disorder in the  $Cu$  phase), was not stable under the methanol synthesis conditions employed without alumina as an additional refractory phase. The difference in the microstructure of the  $Cu/ZnO/Al_2O_3$  catalysts leading to a, at least temporary, improved activity in methanol synthesis compared to the corresponding binary  $Cu/ZnO$  catalysts may be attributed to the presence of aluminum as stabilizing component.

## 6.2 Summary and perspectives

In this thesis a combination of various analytical methods, *in situ* X-ray absorption spectroscopy (XAS), *in situ* X-ray diffraction (XRD), transmission electron spectroscopy (TEM), and temperature programmed techniques (TPR, TPO), were employed to elucidate correlations between activity and selectivity in dependence on the microstructure of differently prepared Cu/ZnO/Al<sub>2</sub>O<sub>3</sub> catalysts for methanol chemistry (methanol synthesis, methanol steam reforming). The latter reactions are, generally, the domain of copper catalysts which are able to selectively minimize the binding energy required for activation of the carbon-oxygen bond present in carbon monoxide, carbon dioxide, and methanol. In order to limit the complexity of this investigation, the composition of the catalysts studied has not been varied and was chosen to be very close to the technical system of approximately Cu:Zn:Al = 60:30:10.

In summary, catalytically active copper in the Cu/ZnO/Al<sub>2</sub>O<sub>3</sub> catalysts employed in the synthesis and steam reforming of methanol was a highly defective, strained form of the metal. This structural modification of active copper originated from an appropriate nanostructuring of Cu and the ZnO/Al<sub>2</sub>O<sub>3</sub> matrix. The latter accounted for a better “wetting” of copper on the ZnO/Al<sub>2</sub>O<sub>3</sub> matrix compared to the homologous binary Cu/ZnO catalyst without aluminum. Thus, aluminum modified ZnO appeared to be an essential component in stabilizing an appropriate microstructure of copper nanoparticles yielding a marked interface interaction of metal Cu and the support. Accordingly, the role of aluminum has been supposed to be a structural stabilizer of the Cu/ZnO system. Thereby, differences between methanol synthesis and methanol steam reforming arise from considerably different partial pressures of reactants and products during the synthesis and steam reforming reaction. Consequently, working Cu/ZnO/Al<sub>2</sub>O<sub>3</sub> catalysts were likely to be different in the extent of surface oxidized copper in methanol chemistry. Here, methanol was formed on an essentially oxygen-free copper surface, whereas during methanol steam reforming surface oxidized copper was more favored. Thus, the degree of nanostructuring of copper and, hence, the resistance against sintering strongly depends on both the interaction of copper particles with the ZnO/Al<sub>2</sub>O<sub>3</sub> matrix and the gas phase composition under reaction conditions in methanol chemistry. Apparently, the presence of bulk meta-stable states in metal copper, such as planar defects (i.e. stacking faults, twin boundaries), lattice strain and subsurface oxygen, constituted the kinetic barrier for equilibration of the surface in dependence on different gas phase compositions during synthesis and steam reforming of methanol.

Reliable structure-activity relationships for copper catalysts in methanol chemistry that are prerequisites for a rational design of improved catalytic materials remain rare. Cu/ZnO/Al<sub>2</sub>O<sub>3</sub> catalysts exhibit a high microstructural complexity which, unfortunately, can be only probed by a small number of structure sensitive analytical tools. Thus, further investigations should also consider possible reaction mechanism during both methanol synthesis and methanol steam reforming reaction. Since it is established that the surface morphology of “working” copper is strongly affected by changes of the gas phase oxidation potential during catalysis, suitable kinetic models may help to unravel the dynamic microstructure of active copper in methanol chemistry and, hence, may overcome the limitations given by *in situ* spectroscopy in general.

Furthermore, it has been shown that Cu/ZnO with or without alumina as an additional refractory phase could be structurally modified by carbon dioxide calcination. Comprehensive bulk structural analysis of the derived Cu/ZnO catalysts clearly evidenced that by calcination under proper partial pressures of CO<sub>2</sub> and O<sub>2</sub> carbonates could be incorporated into the bulk of the catalyst. The fraction of the incorporated carbonates was, thereby, not linearly dependent on the partial pressure of CO<sub>2</sub> employed upon calcination. Here, highest fraction of carbonates in the activated Cu- catalyst was obtained by calcination in a 1:1 mixture of CO<sub>2</sub>/O<sub>2</sub>. Additionally, the fraction of incorporated carbonates in the bulk has been found to cause structural disorder in the short range order structure of the copper component of the derived Cu/ZnO catalysts. Thus, consistently to previous investigations, the microstructure of Cu/ZnO/(Al<sub>2</sub>O<sub>3</sub>) catalysts and, hence, the catalytic performance in methanol chemistry was highly influenced by the preparation conditions employed. Accordingly, Cu/ZnO/(Al<sub>2</sub>O<sub>3</sub>) catalysts previously calcined in the presence of CO<sub>2</sub> featured a considerably lower selectivity to CO in methanol steam reforming at high methanol conversion. This improved selectivity was caused by a decreased activity of the derived catalysts for the reverse water-gas-shift (rWGS) reaction, which constitutes a consecutive reaction during methanol steam reforming (MSR). Apparently, the dissociative sticking probability of gas phase CO<sub>2</sub> on the Cu surface during MSR reaction, which represents the rate determining step in the rWGS reaction, was, however, determined by an incorporation of carbonates into the bulk, an increased structural disorder in the copper phase and, hence, a different surface texture of the corresponding Cu/ZnO/(Al<sub>2</sub>O<sub>3</sub>) catalyst. Considering the low CO levels obtained by changing the calcination atmosphere it renders carbon dioxide calcination a promising alternative for the preparation of highly selective copper catalysts for methanol steam reforming reaction to be applied for *in situ* H<sub>2</sub> generation from methanol in proton exchanged membrane (PEM) fuel cells. However, carbon dioxide calcination did not improve the activity behavior of methanol synthesis as well as steam reforming reaction of the derived Cu/ZnO/(Al<sub>2</sub>O<sub>3</sub>) catalysts. Due to technical reasons, MSR reactions studied ran at relative high conversions of methanol ( $X^{\text{MeOH}} \geq 5\%$ ) and, hence, small modifications in the microstructure obtained by the calcination atmosphere are less reflected in the activity of the derived Cu/ZnO/(Al<sub>2</sub>O<sub>3</sub>) catalysts.

Calcination performed was not optimized with respect to the positive effect of individual O<sub>2</sub>/CO<sub>2</sub> partial pressures on the selectivity during methanol steam reforming reaction. Here, calcination was only performed in (i) O<sub>2</sub>, (ii) 1:1 mixture of O<sub>2</sub> and CO<sub>2</sub>, and (iii) CO<sub>2</sub>, whereas best selectivities to H<sub>2</sub> in methanol steam reforming were found for the Cu/Zn/(Al)- catalyst derived by calcination in a mixture of O<sub>2</sub> and CO<sub>2</sub>. Due to the different surface and bulk texture of binary Cu/ZnO and ternary Cu/ZnO/Al<sub>2</sub>O<sub>3</sub> catalysts it is believed that optimum calcination atmosphere compositions are different for the both catalyst systems studied. Additionally, carbon dioxide calcination may still enhance the catalytic activity in methanol chemistry of other Cu- supported catalysts than the Cu/ZnO/(Al<sub>2</sub>O<sub>3</sub>) catalyst system studied. At least there are examples given in the literature where carbon dioxide treatment positively influences the activity [6.44, 6.45] or chemical stability [6.46] of the derived Cu catalysts in methanol chemistry.

### 6.3 *References cited*

- [6.1] J. Agrell, B. Lindström, L.J. Petterson, S.G. Järås, *Catal.*, 16 (2002) 67.
- [6.2] K. Takahashi, N. Takezawa, H. Kobayashi, *Appl. Catal.*, 2 (1982) 383.
- [6.3] M.S. Spencer, *Surf. Sci.*, 192 (1987) 323.
- [6.4] C.J. Jiang, D.L. Trimm, M.S. Wainwright, N.W. Cant, *Appl. Catal. A*, 93 (1993) 245.
- [6.5] C.P. Thurgood, J.C. Amphlett, R.F. Mann, B.A. Peppley, *Topics Catal.*, 22 (2003).
- [6.6] W.H. Cheng, *Appl. Catal. A*, 130 (1995) 13.
- [6.7] M.V. Twigg, M.S. Spencer, *Topics Catal.*, 22 (2003) 191.
- [6.8] P.L. Hansen, J.B. Wagner, S. Helveg, J.R. Rostrup-Nielsen, B.S. Clausen, H. Topsøe, *Science*, 295 (2002) 2053.
- [6.9] M. Muhler, E. Törnqvist, L.P. Nielson, B.S. Clausen, H. Topsøe, *Catal. Lett.*, 14 (1992) 241.
- [6.10] T.S. Askgaard, J.K. Nørskov, C.V. Ovesen, P. Stoltze, *J. Catal.*, 156 (1995) 229.
- [6.11] P.H. Matter, U.S. Ozkan, *J. Catal.*, 234 (2005) 463.
- [6.12] G.C. Chinchin, K.C. Waugh, D.A. Whan, *Appl. Catal.*, 25 (1986) 101.
- [6.13] M.S. Spencer, *Catal. Lett.*, 60 (1999) 45.
- [6.14] J.D. Grunwaldt, B.S. Clausen, *Topics Catal.*, 18 (2002) 37.
- [6.15] M. Kurtz, N. Bauer, C. Büscher, H. Wilmer, O. Hinrichsen, R. Becker, S. Rabe, K. Merz, M. Driess, R.A. Fischer, M. Muhler, *Catal. Lett.*, 92 (2004) 49.
- [6.16] M.M. Günther, T. Ressler, R.E. Jentoft, B. Bems, *J. Catal.*, 203 (2001) 133.
- [6.17] X.R. Zhang, L.C. Wang, Y. Cao, W.L. Dai, H.Y. He, K.N. Fan, *Chem. Commun.*, 32 (2005) 4104.
- [6.18] B.L. Kniep, F. Girgadies, T. Ressler, *J. Catal.*, 236 (2005) 34.
- [6.19] C. Rhodes, G.J. Hutchings, A.M. Ward, *Catal. Today*, 23 (1995) 43.
- [6.20] T.M. Yurieva, T.P. Minyukova, *React. Kinet. Catal. Lett.*, 29 (1985) 55.
- [6.21] I. Kasatkin, B.L. Kniep, T. Ressler, *Phys. Chem. Chem. Phys.*, 9 (2007) 878.
- [6.22] B.S. Clausen, J. Schiøtz, L. Gråbaek, C.V. Ovesen, K.W. Jacobsen, J.K. Nørskov, H. Topsøe, *Topics Catal.*, 1 (1994) 367.
- [6.23] T. Ressler, B.L. Kniep, I. Kasatkin, R. Schlögl, *Angew. Chem. Int. Ed.*, 44 (2005) 4704.
- [6.24] X. Bao, M. Muhler, T. Schedel-Niedrig, R. Schlögl, *Phys. Rev. B*, 54 (1994) 2249.
- [6.25] H. Werner, D. Herein, G. Schulz, U. Wild, R. Schlögl, *Catal. Lett.*, 49 (1997) 109.
- [6.26] F. Girgadies, T. Ressler, U. Wild, T. Wübben, T.J. Balk, G. Dehm, L. Zhou, S. Günther, E. Arzt, R. Imbihl, R. Schlögl, *Catal. Lett.*, 102 (2005) 91.
- [6.27] M.S. Spencer, *Catal. Lett.*, 50 (1998) 37.
- [6.28] M.M. Günther, T. Ressler, B. Bems, C. Büscher, T. Genger, O. Hindrichsen, M. Muhler, R. Schlögl, *Catal. Lett.*, 71 (2001) 37.
- [6.29] B.L. Kniep, T. Ressler, A. Rabis, F. Girgadies, M. Baenitz, F. Steglich, R. Schlögl, *Angew. Chem. Int. Ed.*, 43 (2004) 112.
- [6.30] B. Bems, M. Schur, A. Dassenoy, H. Junkes, D. Herein, R. Schlögl, *Chem. Eur. J.*, 9 (2003) 2039.
- [6.31] K. Klier, *Adv. Catal.*, 31 (1982) 243.
- [6.32] G.C. Chinchin, P.J. Jennings, M.S. Spencer, K.C. Waugh, *Appl. Catal.*, 36 (1988) 1.
- [6.33] M.J.L. Gines, N. Amadeo, M. Laborde, C.R. Apesteguia, *Appl. Catal. A*, 131 (1995) 283.
- [6.34] W.H. Cheng, *Mater. Chem. Phys.*, 41 (1995) 36.
- [6.35] T.M. Yurieva, L.M. Plyasova, V.I. Zaikovskii, T.P. Minyukova, A. Bliok, J.C. van den Heuvel, L.P. Davydova, I. Molina, M.P. Demeshkina, A.A. Khassin, E.D. Batyrev, *Phys. Chem. Chem. Phys.*, 6 (2004) 4522.
- [6.36] S.V. Ketchik, T.M. Yurieva, L.M. Plyasova, *React. Kinet. Catal. Lett.*, 19 (1982) 345.
- [6.37] M. Saito, K. Tomoda, I. Takahara, K. Murata, M. Inaba, *Catal. Lett.*, 89 (2003) 11.

- 
- [6.38] B.A. Peppley, J.C. Amphlett, L.M. Kearns, R.F. Mann, *Appl. Catal. A*, 179 (1999) 21.
  - [6.39] R.A. Hadden, H.D. Vandervell, K.C. Waugh, G. Webb, *Catal. Lett.*, 1 (1988) 27.
  - [6.40] J.M. Campbell, C.T. Campbell, *Surf. Sci.*, 259 (1991) 1.
  - [6.41] G.J. Millar, C.H. Rochester, K.C. Waugh, *J. Mol. Phys. Condens. Matter*, 1 SB (1989) 149.
  - [6.42] K.C. Waugh, *Catal. Today*, 53 (1999) 161.
  - [6.43] C.J.H. Jacobsen, S. Dahl, B.S. Clausen, S. Bahn, A. Logadottir, J.K. Nørskov, *J. Am. Chem. Soc.*, 123 (2001) 8404.
  - [6.44] W.H. Cheng, United States patent, US 4 826 798 (1989), to E.I. Du Pont de Nemours and Company.
  - [6.45] H.L. Castricum, H. Bakker, B. van der Linden, E.K. Poels, *J. Phys. Chem. B*, 105 (2001) 7928.
  - [6.46] W.H. Cheng, C.Y. Shiau, T.H. Liu, H.L. Tung, H.H. Chen, J.F. Lu, C.C. Hsu, *Appl. Catal. B*, 18 (1998) 63.



# Appendix

## 7.1 *Curriculum vitae*

### Personal Information:

Name: Patrick Kurr  
Date of birth: 25-04-1979  
Place of birth: Potsdam, Germany

### Education:

01/2005 - 09/2008 Ph.-D. Thesis at the *Fritz-Haber-Institute* of the *Max-Planck-Society*, Department of Inorganic Chemistry, Prof. Dr. R. Schlögl,  
Title: “*Microstructural Investigations of Cu/ZnO/Al<sub>2</sub>O<sub>3</sub> catalysts for the synthesis and steam reforming of methanol*”

04/2004 - 09/2004 Diploma Thesis at the Technical University Berlin, Institute of Technical Chemistry, Prof. Dr. R. Schomäcker,  
Title: “*Comparison of the space time yield of the hydrogenation of  $\alpha$ -Methylstyrene in a membrane reactor, fixed-bed reactor, and a trickle-bed reactor*”

11/2003 - 01/2004 Internship at *Aventis AG*, Frankfurt a.M. (Germany)

12/2003 *Klaus-Koch* Scholarship of the Technical University Berlin

10/1999 - 09/2004 Study of Chemistry at the Technical University Berlin, Major: Chemical Engineering, Grade: summa cum laude

10/1998 - 04/1999 Military Service

09/1992 - 05/1998 Secondary School (Abitur), Grade: 2.2

## 7.2 *Publication index*

H. Purnama, P. Kurr, A. Schmidt, R. Schomäcker, I. Voigt, A. Wolf, R. Warsitz, “ $\alpha$ - Methylstyrene Hydrogenation in a Flow-Through Membrane Reactor”, *AIChE J.*, 52 (2006) 2805.

P. Kurr, T. Ressler; “Cu/ZnO/Al<sub>2</sub>O<sub>3</sub> Catalysts for Steam Reforming of Methanol”, *HASYLAB Annual Report 2005* (2006) 1097.

I. Kasatkin, P. Kurr, B. Kniep, A. Trunschke, R. Schlögl, “Role of Lattice Strain and Defects in Copper Particles on the Activity of Cu/ZnO/Al<sub>2</sub>O<sub>3</sub> Catalysts for Methanol Synthesis”, *Angew. Chem. Int. Ed.*, 119 (2007) 7465.

P. Kurr, A. Furche, A. Trunschke, R. Schlögl, T. Ressler, “*In situ* investigations of Cu/ZnO catalysts during calcination in different gas atmospheres”, *HASYLAB Annual Report 2006* (2007) 1347.

P. Kurr, I. Kasatkin, F. Girgsdies, A. Trunschke, R. Schlögl, T. Ressler, “Microstructural characterization of Cu/ZnO/Al<sub>2</sub>O<sub>3</sub> catalysts for methanol steam reforming - a comparative study”, *Appl. Catal. A*, 348 (2008) 153.

P. Kurr, M. Behrens, A. Trunschke, T. Ressler, R. Schlögl, “Redox behavior of a Cu/ZnO/Al<sub>2</sub>O<sub>3</sub> methanol synthesis catalyst studied by *in situ* X-ray diffraction and absorption spectroscopy”, in preparation

P. Kurr, A. Furche, B. Frank, M. Behrens; A. Trunschke, R. Schomäcker, T. Ressler, R. Schlögl, “Effect of carbon dioxide calcination on the structure of Cu/ZnO catalysts for methanol steam reforming”, in preparation.

... an ending story.